

NUMERICAL SIMULATIONS OF SPATIALLY DEVELOPING MIXING LAYERS

A Thesis

Submitted to the Faculty

of

Purdue University

by

Sai Lakshminarayanan Balakrishnan

In Partial Fulfillment of the

Requirements for the Degree

of

Master of Science in Engineering

May 2020

Purdue University

West Lafayette, Indiana

THE PURDUE UNIVERSITY GRADUATE SCHOOL
STATEMENT OF THESIS APPROVAL

Dr. Gregory A. Blaisdell, Chair

School of Aeronautics and Astronautics

Dr. Jonathan Poggie

School of Aeronautics and Astronautics

Dr. Tom I. Shih

School of Aeronautics and Astronautics

Approved by:

Dr. Gregory A. Blaisdell

Head of the School Graduate Program

Dedicated to my mother, Hemavathy Balakrishnan
and to my father, Balakrishnan Thangiah

ACKNOWLEDGMENTS

Firstly, I would like to express my sincerest gratitude to my advisor, Dr. Gregory Blaisdell, for his immense support, guidance and constant encouragement throughout the course of this work. His exuberant knowledge and patience were unparalleled in their importance to this work and my graduate studies. I would like to express my sincere thanks to Dr. Jonathan Poggie, for serving on my examining committee and for allowing me to use his computational resources, which were critical in the completion of this work. I would like to thank Dr. Tom Shih for serving on my examining committee. I would like to thank the School of Aeronautics and Astronautics and the Department of Computer Science for providing me with a graduate assistantship that helped financially support my graduate studies throughout the course of this work. I would like to thank the past members of the research group, Dr. Shanmukeshwar Rao Vankayala and Dr. Nitin Dhamankar for their help and support during this work. Special thanks to Dr. Shanmukeshwar Rao Vankayala for his valuable time and patience in helping me understand the inhouse LES solver and to use it.

I would like to immensely thank my parents for their everlasting love and innumerable sacrifices that gave me a chance to pursue my dreams. Their constant motivation was the most influential factor that kept me going in the toughest of times. I also would like to thank my uncles and aunts for their support and encouragement. Finally, I would like to thank my friends at Purdue for their moral support and help throughout my graduate studies.

The present work made use of the computational resources at the Rosen Center for Advanced Computing (RCAC) at Purdue and Stampede 2 at the Texas Advanced Computing Center (TACC). I would like to express my gratitude to Dr. Carol Song for providing me access to Stampede 2 for the purpose of this work, through an XSEDE allocation TG-ASC170016.

TABLE OF CONTENTS

	Page
LIST OF TABLES	vii
LIST OF FIGURES	x
SYMBOLS	xvii
ABBREVIATIONS	xx
ABSTRACT	xxi
1 INTRODUCTION	1
1.1 Motivation	1
1.2 Review	4
1.2.1 Experimental Studies	4
1.2.2 Numerical Studies	6
1.3 Thesis Objectives	8
1.4 Organization of the Thesis	8
2 COMPUTATIONAL METHODOLOGY	10
2.1 LES Methodology	11
2.1.1 Governing Equations	11
2.1.2 Numerical Methods	15
2.1.3 Boundary Conditions	16
2.1.4 Initial Conditions	20
2.1.5 Solver Topology, Parallelization and Scaling	20
2.1.6 Solver Performance and Scaling	21
2.2 RANS Methodology	27
3 CODE VERIFICATION AND VALIDATION	32
3.1 Laminar Mixing Layer : Case 1	32
3.1.1 Simulation Details	33
3.1.2 Results and Discussions	37
3.2 Laminar Mixing Layer : Case 2	41
3.2.1 Simulation Details	46
3.2.2 Results and Discussion	47
3.3 LES of an Incompressible Turbulent Mixing Layer	48
3.3.1 Simulation Details	52
3.3.2 Results and Discussion	55
3.4 Summary	90

	Page
4 COMPRESSIBLE MIXING LAYER	99
4.1 Case Details	99
4.2 Precursor RANS Simulations	99
4.2.1 Simulation Details	100
4.2.2 Results and Discussion	107
4.3 LES of the Compressible Mixing Layer	124
4.3.1 Flow Parameters	124
4.3.2 Domain Size	125
4.3.3 Grid Details	128
4.3.4 Boundary Conditions and other Details	131
4.3.5 Simulation Cost	135
4.3.6 LES : Results and Discussion	135
5 CONCLUSION	166
5.1 Summary	166
5.2 Recommendations for Future Work	170
REFERENCES	171
APPENDIX A. ANALYTICAL SOLUTIONS OF THE INCOMPRESSIBLE LAMINAR MIXING LAYERS	176

LIST OF TABLES

Table	Page
2.1 Grid configurations considered for the scaling tests	22
2.2 C1 - strong scaling test on SKX	23
2.3 C1 - strong scaling test on KNL	24
2.4 C5 - strong scaling test on SKX and KNL (W.M.)	24
2.5 Weak scaling with 32^3 pts/core - SKX	31
2.6 Weak scaling with 48^3 pts/core - KNL	31
3.1 Laminar mixing layer : case 1 : superblock extents and grid distribution (total number of grid points \sim 11 million)	38
3.2 Laminar mixing layer : case 1 : superblock boundary conditions	38
3.3 Laminar mixing layer : case 1 : additional simulation settings	39
3.4 Laminar mixing layer : case 1 : mixing layer thickness: error	41
3.5 Laminar mixing layer : case 2 : mixing layer thickness: error computed against the analytical result	48
3.6 Incompressible turbulent mixing layer : case 2 : $\frac{d\delta_\omega}{dx}$ comparison	62
4.1 Compressible mixing layer : case details	100
4.2 Compressible mixing layer : RANS calculations : mesh details	103
4.3 Compressible mixing layer : RANS calculations : grid spacings inside the shear layer	105
4.4 Compressible mixing layer : RANS calculations : maximum streamwise grid stretching ratios	105
4.5 Compressible mixing layer : RANS calculations : maximum cross-stream grid stretching ratios	105
4.6 Compressible mixing layer : RANS calculations : pressure values at the inlet and outlet	106
4.7 Compressible mixing layer : RANS calculations : location of transition from inviscid to viscous wall given as streamwise distance from inflow . .	107

Table	Page
4.8 Compressible mixing layer : RANS calculations : $k - \epsilon$ model : δ and C_f at 5 mm upstream of the splitter plate tip	109
4.9 Compressible mixing layer : RANS calculations : RSM : δ and C_f at 5 mm upstream of the splitter plate tip	109
4.10 Compressible mixing layer : RANS calculations : $\frac{d\delta_b}{dx}$ for the three meshes	109
4.11 Compressible mixing layer : RANS calculations : $k - \epsilon$ simulation : δ compared with the experiment. Here 'l' denotes distance upstream of the splitter plate tip in mm	112
4.12 Compressible mixing layer : RANS calculations : $k - \epsilon$ simulation : C_f compared with the experiment. Here 'l' denotes distance upstream of the splitter plate tip in mm	112
4.13 Compressible mixing layer : RANS calculations : RSM simulation : δ compared with the experiment. Here 'l' denotes distance upstream of the splitter plate tip in mm	113
4.14 Compressible mixing layer : RANS calculations : RSM simulation : C_f compared with the experiment. Here 'l' denotes distance upstream of the splitter plate tip in mm	113
4.15 Compressible mixing layer : RANS calculations : comparison of $\frac{d\delta_b}{dx}$ with the experiment	116
4.16 Compressible mixing layer : RANS calculations : mean freestream velocities U_1 and U_2	123
4.17 Compressible mixing layer : RANS calculations : convective Mach number M_c	123
4.18 Compressible mixing layer : LES calculations : boundary layer thickness at the inflow	128
4.19 Compressible mixing layer : LES calculations : number of grid points in each superblock (total number of grid points ~ 221 million)	130
4.20 Compressible mixing layer : LES calculations : wall y^+ for each of the boundary layers at the inflow	131
4.21 Compressible mixing layer : RANS calculations : sample sizes for analysis of statistical convergence	146
4.22 Compressible mixing layer : LES calculations : δ and C_f at $x/\delta_{99_{ref}} = 0$, obtained using the three different sample sizes	147

Table	Page
4.23 Compressible mixing layer : LES calculations : $\frac{d\delta_b}{dx}$ obtained using the three different sample sizes	150
4.24 Compressible mixing layer : LES calculations : δ compared with the experiment. Here 'l' denotes distance upstream of the splitter plate tip in mm	152
4.25 Compressible mixing layer : LES calculations : C_f compared with the experiment. Here 'l' denotes distance upstream of the splitter plate tip in mm	152
4.26 Compressible mixing layer : LES calculations : U_1, U_2 and M_c at certain streamwise locations	153
4.27 Compressible mixing layer : LES calculations : comparison of $\frac{d\delta_b}{dx}$ with the experiment and the RANS	156
4.28 Compressible mixing layer : LES calculations : comparison of Reynolds stress anisotropy coefficients with the experiment, RANS and DNS of Pantano and Sarkar [18]	160
4.29 Compressible mixing layer : LES calculations : comparison of Reynolds stress correlation coefficient with the experiment and RANS	162

LIST OF FIGURES

Figure	Page
2.1 Strong scaling tests.	25
2.2 Weak scaling tests.	26
2.3 Floating point Performance - strong scaling tests.	28
2.4 Floating point performance - weak scaling tests.	28
3.1 Laminar mixing layer : case 1 : inflow profiles.	34
3.2 Laminar mixing fluid domain: case 1 : 2D view.	35
3.3 Laminar mixing layer : case 1 : grid distribution: showing every 4 th grid point.	35
3.4 Laminar mixing layer : case 1 : velocity profiles. Here $\hat{T} = T \frac{U_1}{\delta_{b0}}$	42
3.5 Laminar mixing layer : case 1 : shear layer thickness δ_b . Here $\hat{T} = T \frac{U_1}{\delta_{b0}}$	42
3.6 Laminar mixing layer : case 1 : contours of the mean of the velocity fluctuations.	43
3.7 Laminar mixing layer : case 1 : self-similar velocity profile.	44
3.8 Laminar mixing layer : case 1 : static pressure variation.	44
3.9 Laminar mixing layer : case 1 : mixing layer thickness: comparison with the analytical solution. ' x_{vo} ' indicates that the solution is plotted with respect to the virtual origin.	45
3.10 Laminar mixing layer : case 1 : linear fit to the square of the mixing layer thicknesses. ' x_{vo} ' indicates that the solution is plotted with respect to the virtual origin.	45
3.11 Laminar mixing layer : case 2 : inflow profiles.	47
3.12 Laminar mixing layer : case 2 : contours of the mean of the velocity fluctuations.	49
3.13 Laminar mixing layer : case 2 : self-similar velocity profile.	50
3.14 Laminar mixing layer : case 2 : mixing layer thickness.	50
3.15 Laminar mixing layer : case 2 : static pressure variation.	51

Figure	Page
3.16 Incompressible turbulent mixing layer : fluid domain: 2D view.	56
3.17 Incompressible turbulent mixing layer : grid distribution : showing every 4 th grid point.	56
3.18 Incompressible turbulent mixing layer : case 2 : vorticity and momentum thickness for three different sample sizes.	57
3.19 Incompressible turbulent mixing layer : case 2 : Reynolds stresses at $\frac{x}{\delta_{\omega_0}}$ = 300 at 6,8,10 FTC's of statistics collection.	58
3.20 Incompressible turbulent mixing layer : case 2 : Reynolds stresses at $\frac{x}{\delta_{\omega_0}}$ = 456 at 6,8,10 FTC's of statistics collection.	59
3.21 Incompressible turbulent mixing layer : case 2 : momentum thickness δ_θ . . .	61
3.22 Incompressible turbulent mixing layer : case 2 : self-similar profile. $U_c =$ $\frac{U_1+U_2}{2}$	62
3.23 Incompressible turbulent mixing layer : case 2 : vorticity thickness δ_ω . . .	63
3.24 Incompressible turbulent mixing layer : case 2 : integral normalized cross- wise component of the turbulent kinetic energy.	64
3.25 Incompressible turbulent mixing layer : case 2 : Reynolds stresses.	66
3.26 Incompressible turbulent mixing layer : case 2 : Reynolds stresses at $\frac{x}{\delta_{\omega_0}}$ = 450 compared against the reference DNS.	67
3.27 Incompressible turbulent mixing layer : case 2 : contours of vorticity magnitude.	68
3.28 Incompressible turbulent mixing layer : case 2 : contours of vorticity magnitude close to the inflow.	69
3.29 Incompressible turbulent mixing layer : case 2 : iso-surface of vorticity magnitude at $ \omega = 0.45 \frac{\Delta U}{\delta_{\omega_0}}$	69
3.30 Incompressible turbulent mixing layer : case 2 : iso-surface of vorticity magnitude at $ \omega = 0.45 \frac{\Delta U}{\delta_{\omega_0}}$: plan view close to the inflow.	70
3.31 Incompressible turbulent mixing layer : comparison of δ_θ for case 1 (TD outflow) and case 2 (Characteristic outflow).	72
3.32 Incompressible turbulent mixing layer : comparison of δ_ω for case 1 (TD outflow) and case 2 (Characteristic outflow).	72
3.33 Incompressible turbulent mixing layer : case 1 : self-similar profile. $U_c =$ $\frac{U_1+U_2}{2}$	73

Figure	Page
3.34 Incompressible turbulent mixing layer : case 1 : Reynolds stresses.	75
3.35 Incompressible turbulent mixing layer : streamwise variation of the peak Reynolds stresses : case 1 (TD outflow) vs case 2 (Characteristic outflow).	76
3.36 Incompressible turbulent mixing layer : Reynolds stresses at $\frac{x}{\delta_{\omega_0}} = 450$: case 1 (TD outflow) compared against case 2 (Characteristic outflow) and the reference DNS.	77
3.37 Incompressible turbulent mixing layer : integral normalized crosswise component of the turbulent kinetic energy : case 1 (TD outflow) and case 2 (Characteristic outflow).	78
3.38 Incompressible turbulent mixing layer : Mean pressure contours : case 1 (TD outflow) vs case 2 (Characteristic outflow). The dash dotted red line indicates the end of the physical zone.	79
3.39 Incompressible turbulent mixing layer : Pressure variation along the centreline $y = 0$: case 1 (TD outflow) vs case 2 (Characteristic outflow).	79
3.40 Incompressible turbulent mixing layer : case 3 : self-similar profile. $U_c = \frac{U_1+U_2}{2}$	81
3.41 Incompressible turbulent mixing layer : case 3 : Reynolds stresses.	82
3.42 Incompressible turbulent mixing layer : momentum thickness : case 2 (White noise Inflow) vs case 3 (Correlated Inflow).	83
3.43 Incompressible turbulent mixing layer : vorticity thickness : case 2 (White noise Inflow) vs case 3 (Correlated Inflow).	83
3.44 Incompressible turbulent mixing layer : streamwise variation of the peak Reynolds stresses : case 2 (White noise Inflow) vs case 3 (Correlated Inflow).	85
3.45 Incompressible turbulent mixing layer : Reynolds stresses at $\frac{x}{\delta_{\omega_0}} = 450$: case 3 (Correlated Inflow) compared against case 2 (White noise Inflow) and the reference DNS.	86
3.46 Incompressible turbulent mixing layer : iso-surface of instantaneous vorticity : $\omega_z = -0.4 \frac{\Delta U}{\delta_{\omega_0}}$ (green), $\omega_x = -0.3 \frac{\Delta U}{\delta_{\omega_0}}$ (blue), $\omega_x = 0.3 \frac{\Delta U}{\delta_{\omega_0}}$ (red).	91
3.47 Incompressible turbulent mixing layer : iso-surface of streamwise vorticity : $\omega_x = -0.3 \frac{\Delta U}{\delta_{\omega_0}}$ (blue) & $\omega_x = 0.3 \frac{\Delta U}{\delta_{\omega_0}}$ (red).	92
3.48 Contours of secondary shear stress $\langle u'w' \rangle$ (taken from [25], used with permission).	93
3.49 Incompressible turbulent mixing layer : secondary shear stress $\langle u'w' \rangle$ at $\frac{x}{\delta_{\omega_0}} = 11$: case 2 (White noise Inflow) vs case 3 (Correlated Inflow).	93

Figure	Page
3.50 Incompressible turbulent mixing layer : secondary shear stress $\langle u'w' \rangle$ at $\frac{x}{\delta_{\omega_0}} = 30$: case 2 (White noise Inflow) vs case 3 (Correlated Inflow). . .	94
3.51 Incompressible turbulent mixing layer : secondary shear stress $\langle u'w' \rangle$ at $\frac{x}{\delta_{\omega_0}} = 54$: case 2 (White noise Inflow) vs case 3 (Correlated Inflow). . .	94
3.52 Incompressible turbulent mixing layer : secondary shear stress $\langle u'w' \rangle$ at $\frac{x}{\delta_{\omega_0}} = 84$: case 2 (White noise Inflow) vs case 3 (Correlated Inflow). . .	95
3.53 Incompressible turbulent mixing layer : secondary shear stress $\langle u'w' \rangle$ at $\frac{x}{\delta_{\omega_0}} = 120$: case 2 (White noise Inflow) vs case 3 (Correlated Inflow). . .	95
3.54 Incompressible turbulent mixing layer : secondary shear stress $\langle u'w' \rangle$ at $\frac{x}{\delta_{\omega_0}} = 200$: case 2 (White noise Inflow) vs case 3 (Correlated Inflow). . .	96
3.55 Incompressible turbulent mixing layer : secondary shear stress $\langle u'w' \rangle$ at $\frac{x}{\delta_{\omega_0}} = 300$: case 2 (White noise Inflow) vs case 3 (Correlated Inflow). . .	96
3.56 Incompressible turbulent mixing layer : secondary shear stress $\langle u'w' \rangle$ at $\frac{x}{\delta_{\omega_0}} = 400$: case 2 (White noise Inflow) vs case 3 (Correlated Inflow). . .	97
3.57 Incompressible turbulent mixing layer : secondary shear stress $\langle u'w' \rangle$ at $\frac{x}{\delta_{\omega_0}} = 440$: case 2 (White noise Inflow) vs case 3 (Correlated Inflow). . .	97
3.58 Incompressible turbulent mixing layer : spanwise wrinkling of $\langle u \rangle$ normalised by its spanwise-averaged value. Here the spanwise averaged value is represented by \bar{u} : case 2 (White noise Inflow) vs case 3 (Correlated Inflow).	98
4.1 Compressible mixing layer : RANS calculations : fluid domain.	102
4.2 Compressible mixing layer : RANS calculations : fine grid (showing every 4 th grid point).	104
4.3 Compressible turbulent mixing layer : RANS studies: velocity profiles at the splitter tip on the secondary section top wall. Here y_w is the distance from the secondary section top wall.	108
4.4 Compressible turbulent mixing layer : RANS studies: shear layer thickness δ_b	110
4.5 Compressible mixing layer : RANS calculations : mean streamwise veloc- ity profiles of the $k - \epsilon$ (red) and RSM (green) simulations compared with the experiments (scatter) at several streamwise locations.	115
4.5 (cont.) Compressible mixing layer : RANS calculations : mean streamwise velocity profiles of the $k - \epsilon$ (red) and RSM (green) simulations compared with the experiments (scatter) at several streamwise locations.	116

Figure	Page
4.6 Compressible turbulent mixing layer : RANS studies: self-similar velocity profile.	117
4.7 Compressible mixing layer : RANS calculations : δ_b comparison with the experiment.	117
4.8 Compressible mixing layer : RANS calculations : comparison of TKE with the experiment.	118
4.9 Compressible mixing layer : RANS calculations : Reynolds stresses. . . .	120
4.10 Compressible mixing layer : RANS calculations : comparison of self-similar Reynolds stress profiles with the experiment.	121
4.11 Compressible mixing layer : RANS calculations : variation of pressure inside the test section.	122
4.12 Compressible mixing layer : LES calculations : mean streamwise velocity profile at the inflow.	125
4.13 Compressible mixing layer : LES calculations : mean cross-stream velocity profile at the inflow. $\langle v \rangle$ is positive near the upper wall at the secondary inflow, since it tapers upwards.	126
4.14 Compressible mixing layer : LES calculations : mean density profile at the inflow.	126
4.15 Compressible mixing layer : LES calculations : superblock topology (not drawn to scale).	127
4.16 Compressible mixing layer : LES calculations : grid structure: showing every 8 th grid point.	129
4.17 Compressible mixing layer : LES calculations : Reynolds stress profiles at the primary inflow.	133
4.18 Compressible mixing layer : LES calculations : Reynolds stress profiles at the secondary inflow.	134
4.19 Compressible mixing layer : LES : instantaneous u contours.	136
4.20 Compressible mixing layer : LES : instantaneous density contours.	137
4.21 Compressible mixing layer : LES : ω_z contours.	137
4.22 Compressible mixing layer : LES : iso-surface of $Q=0.03 \left(\frac{\Delta U}{\delta_{99_{ref}}}\right)^2$ colored by the non-dimensionalized streamwise velocity for the boundary layer on the splitter plate top.	139

Figure	Page
4.23 Compressible mixing layer : LES : iso-surface of $Q=0.001 \left(\frac{\Delta U}{\delta_{99_{ref}}}\right)^2$ colored by the non-dimensionalized streamwise velocity for the boundary layer on the splitter plate bottom.	139
4.24 Compressible mixing layer : LES : iso-surface of $Q=0.001 \left(\frac{\Delta U}{\delta_{99_{ref}}}\right)^2$ colored by the non-dimensionalized streamwise velocity for the boundary layer on the splitter top leading into the mixing section (high speed side). Only a short portion of the primary (boxed in black) and mixing sections (high speed side, boxed in red) in the cross-stream direction is shown for the sake of brevity.	140
4.25 Compressible mixing layer : LES : iso-surface of $Q=0.001 \left(\frac{\Delta U}{\delta_{99_{ref}}}\right)^2$ colored by the non-dimensionalized streamwise velocity for the boundary layer on the splitter plate bottom leading into the mixing section (low speed side). Only a short portion of the secondary (boxed in black) and mixing sections (low speed side, boxed in red) in the cross-stream direction is shown for the sake of brevity.	140
4.26 Compressible mixing layer : LES : instantaneous vorticity magnitude, and pressure contours shown for the plane of the splitter plate top and the adjoining plane in the mixing section.	141
4.27 Compressible mixing layer : LES : instantaneous vorticity magnitude contours shown for the plane of the splitter plate bottom and the adjoining plane in the mixing section at $y = -0.33$	142
4.28 Compressible mixing layer : LES : iso-surface of $Q=0.3 \left(\frac{\Delta U}{\delta_{99_{ref}}}\right)^2$ (colored by the non-dimensionalized streamwise velocity) shown for the plane of the splitter plate top and the adjoining plane in the mixing section. . . .	142
4.29 Compressible mixing layer : LES : iso-surface of $Q=0.001 \left(\frac{\Delta U}{\delta_{99_{ref}}}\right)^2$ (colored by the non-dimensionalized streamwise velocity) shown for the plane of the splitter plate bottom and the adjoining plane in the mixing section at $y = -0.33$	143
4.30 Compressible mixing layer : LES : velocity vectors close to the splitter plate face shown together with the iso-surface of $Q=0.1 \left(\frac{\Delta U}{\delta_{99_{ref}}}\right)^2$ (colored by the non-dimensionalized streamwise velocity) in regions where the streamwise velocity is negative.	144
4.31 Compressible mixing layer : LES calculations : $u - U_c$ contours with streamlines in the growing shear layer, shown at a given spanwise plane.	145
4.32 Compressible mixing layer : LES calculations : variation of δ_b inside the mixing section obtained using the three different sample sizes.	148

Figure	Page
4.33 Compressible mixing layer : LES calculations : Reynolds stresses at $\frac{x}{\delta_{99_{ref}}} \sim 80$ obtained using the three different sample sizes.	149
4.34 Compressible mixing layer : LES calculations : Reynolds stresses at $\frac{x}{\delta_{99_{ref}}} \sim 150$ obtained using the three different sample sizes.	150
4.35 Compressible mixing layer : LES calculations : contours of $\langle u \rangle$ with streamlines.	154
4.36 Compressible mixing layer : LES calculations : variation of pressure inside the mixing section.	154
4.37 Compressible mixing layer : LES calculations : mean streamwise velocity profiles of the LES (blue), $k - \epsilon$ (red) and RSM (green) simulations compared with the experiments (scatter) at several streamwise locations.	156
4.37 (cont.) Compressible mixing layer : LES calculations : mean streamwise velocity profiles of the LES (blue), $k - \epsilon$ (red) and RSM (green) simulations compared with the experiments (scatter) at several streamwise locations.	157
4.38 Compressible mixing layer : LES calculations : self-similar streamwise velocity profile compared with the reference experiment.	158
4.39 Compressible mixing layer : LES calculations : variation of δ_b inside the mixing section, compared against the results of RANS simulations and the reference experiment.	158
4.40 Compressible mixing layer : LES calculations : comparison of TKE with the experiment and the RANS.	161
4.41 Compressible mixing layer : LES calculations : Reynolds stresses at several streamwise stations.	162
4.42 Compressible mixing layer : LES calculations : Reynolds stresses compared with the experiment and the RANS (RSM).	163
4.43 Compressible mixing layer : LES calculations : anisotropy of the Reynolds stress tensor compared with the experiment and the RANS.	164
4.44 Compressible mixing layer : LES calculations : Reynolds stress correlation coefficient compared with the experiment and the RANS.	165

SYMBOLS

Roman Symbols

c	Speed of sound, Reynolds stress anisotropy coefficient
C_f	Skin friction coefficient
e_t	Total energy per unit volume
f	An arbitrary flow variable
$\mathbf{F}, \mathbf{G}, \mathbf{H}$	Flux vectors in curvilinear coordinates
h	Uniform grid spacing on the transformed computational grid
J	Determinant of Jacobian of the coordinate transformation
k	Turbulent kinetic energy
L	Integral length scale
L_r	Reference length
M	Mach number
M_c	Convective Mach number
N	Number of grid points
p	Static pressure
Pr	Prandtl number
q_i	Resolved heat flux
\mathbf{Q}	Vector of conservative flow variables
Q_i	SGS heat flux
Re	Reynolds number
S	Sutherland's constant
T	Static temperature or simulation reference time
U	Mean freestream velocity
u, v, w	Cartesian velocity components

u_τ	Friction velocity
x, y, z	Cartesian coordinates in streamwise, cross-stream and spanwise directions respectively

Greek Symbols

α_f	Spatial filtering parameter
γ	Ratio of specific heats for air
δ	Boundary layer thickness
δ_{99}	Boundary layer thickness based on a location where the streamwise velocity is 99% of the freestream velocity
δ_b	Shear layer thickness
δ_θ	Momentum thickness
δ_ω	Vorticity thickness
Δs	Grid spacing in direction s
Δt	Time-step size
ΔU	Mean freestream velocity difference between the primary and secondary streams
ϵ	Turbulent dissipation rate
μ	Dynamic molecular viscosity
ν	Kinematic molecular viscosity
ξ, η, ζ	Generalized curvilinear coordinates
ρ	Density
τ	Shear stress, retarded time, or reference time unit, L_r/U_r
τ_w	Wall shear stress
Ψ_{ij}	SGS stress tensor
ω	Specific turbulent dissipation rate, vorticity

Accent Marks

$\widetilde{(\quad)}$	Favre-filtered quantity
-----------------------	-------------------------

$\bar{()}$ Resolved scale component

Brackets

$\langle \rangle$ Mean quantity

Subscripts

$()_0$ Inflow quantity, stagnation quantity

$()_1$ Primary stream (or high speed stream) quantity

$()_2$ Secondary stream (or high speed stream) quantity

$()_\infty$ Freestream quantity

$()_{ref}$ Reference quantity

$()_{ts}$ Test section quantity

$()_v$ Viscous quantity

$()_w$ Quantity at the wall

Superscripts

$()'$ Differentiated quantity, perturbation quantity

$()^*$ Dimensional quantity

$()^+$ Quantity in inner (viscous) wall units

$()^T$ Transpose of the given vector or matrix

ABBREVIATIONS

CFD	Computational Fluid Dynamics
CFL	Courant-Friedrichs-Lewy
CPU	Central Processing Unit
DNS	Direct Numerical Simulation
FTC	Flow Through Cycle
I/O	Input/Output from Computer Code
ILES	Implicit Large Eddy Simulation
ILS	Integral Length Scale
LES	Large Eddy Simulation
RANS	Reynolds-Averaged-Navier-Stokes
rms	Root Mean Square
RSM	Reynolds Stress Model
SGS	Sub-Grid Scale
SWBLI	Shock Wave Boundary Layer Interaction
TACC	Texas Advanced Computing Center
TKE	Turbulent Kinetic Energy
TVD	Total Variation Diminishing
WENO	Weighted Essentially Non-Oscillatory

ABSTRACT

Balakrishnan, Sai Lakshminarayanan M.S., Purdue University, May 2020. Numerical Simulations of Spatially Developing Mixing Layers. Major Professor: Gregory A. Blaisdell.

Turbulent mixing layers have been researched for many years. Currently, research is focused on studying compressible mixing layers because of their widespread applications in high-speed flight systems. While the effect of compressibility on the shear layer growth rate is well established, there is a lack of consensus over its effect on the turbulent stresses and hence warrants additional research in this area. Computational studies on compressible shear layers could provide a deep cognizance of the dynamics of fluid structures present in these flow fields which in turn would be viable for understanding the effects of compressibility on such flows. However, performing a Direct Numerical Simulation (DNS) of a highly compressible shear layer with experimental flow conditions is extremely expensive, especially when resolving the boundary layers that lead into the mixing section. The attractive alternative is to use Large Eddy Simulation (LES), as it possesses the potential to resolve the flow physics at a reasonable computational cost. Therefore the current work deals with developing a methodology to perform LES of a compressible mixing layer with experimental flow conditions, with resolving the boundary layers that lead into the mixing section through a wall model. The wall model approach, as opposed to a wall resolved simulation, greatly reduces the computational cost associated with the boundary layer regions, especially when using an explicit time-stepping scheme. An in house LES solver which has been used previously for performing simulations of jets, has been chosen for this purpose. The solver is first verified and validated for mixing layer flows by performing simulations of laminar and incompressible turbulent mixing layer flows and comparing the results with the literature. Following this, LES of a

compressible mixing layer at a convective Mach number of 0.53 is performed. The inflow profiles for the LES are taken from a precursor RANS solution based on the $k - \epsilon$ and RSM turbulence models. The results of the LES present good agreement with the reference experiment for the upstream boundary layer properties, the mean velocity profile of the shear layer and the shear layer growth rate. The turbulent stresses, however, have been found to be underpredicted. The anisotropy of the normal Reynolds stresses have been found to be in good agreement with the literature. Based on the present results, suggestions for future work are also discussed.

1. INTRODUCTION

1.1 Motivation

Turbulent mixing layers have been the subject of research for many years. Besides providing an opportunity to study the fundamental and complex flow structures present in turbulent shear flows, it forms the core phenomenon in many entrainment applications in the aerospace industry such as in jets, fuel injectors etc. It is also the major cause of jet exhaust noise that results from the mixing of the hot exhaust gases with the atmosphere. It is highly desirable to promote the mixing rates in such cases to reduce the noise level. Because of the renewed interest in high-speed flight, the knowledge and understanding of compressible mixing layers become imperative as it finds application in the combustion systems of such aerospace vehicles, where the fuel and oxidizer streams must mix in a very short time interval. Knowledge of the characteristics and flow features of a planar compressible mixing layer could provide many insights that aid in the design and development of such systems aimed to enhance the mixing process.

A mixing layer is formed when two streams, typically of different velocities and initially separated by a splitter plate, are brought into contact with each other. The near field of a mixing layer evolving from laminar initial conditions is characterized by the presence of large two-dimensional rollers, formed by the roll-up of the initial vortex sheet due to the Kelvin-Helmholtz instability. Three-dimensional disturbances cause these spanwise rollers to bend, resulting in the formation of streamwise rib vortex structures in the braid regions between these rollers [1]. The pairing of these spanwise rollers is the primary mechanism contributing to the growth of the mixing layer (in a step-like fashion). Two pairing spanwise rollers undergo a cross-stream displacement (upward displacement of the upstream roller and downward displacement

of the downstream roller), rotate around a common center and eventually amalgamate into a single large vortex. The flow eventually transitions to a turbulent mixing layer that is characterized by the appearance of a large number of fine scales [2]. The seminal experiment of Brown and Roshko [3] showed the presence of large coherent quasi-two-dimensional structures in the post-transition mixing layers. These structures grow linearly with downstream distance, contributing to the growth of the mixing layer [4], entraining fluid from the two freestreams. These large scale structures subsequently interact with each other through two mechanisms: “pairing”, where two neighboring coherent structures merge with each other without any cross-stream displacement of either of them [4] (unlike their pre-transition counterparts); “tearing”, which occurs when a weaker structure becomes closely confined by two neighboring structures and gets torn apart by its neighbors and is amalgamated into them [4, 5]. After a sufficient distance from the splitter plate tip [6], turbulent mixing layers have known to become self-similar. This region is characterized by a linear growth of the mixing layer and the collapse of the mean streamwise velocity and the Reynolds stress profiles with downstream distance, when scaled by the local mixing thickness and the velocity difference between the two streams.

The evolution of the mixing layer is also found to be dependent on the freestream velocity ratio of the two mixing streams [7, 8], the splitter plate geometry [9], the state (laminar or turbulent) and thickness of the separating boundary layers at the splitter plate tip [6, 10] and compressibility effects. The level of compressibility [11] in a turbulent mixing layer is quantified with a parameter called the convective Mach number, M_c [12, 13].

The most important characteristic of compressible mixing layers that distinguish it from its incompressible counterpart is the reduction of growth rate that is observed at high convective Mach numbers (M_c). This has been observed in various experimental [12, 14–16] and numerical studies [17–19]. The reduction in growth rate is attributed due to the decrease in the pressure-strain term in the Reynolds stress equations, which ultimately reduces the turbulence production [18]. Though the effect of

compressibility on the growth rate is well established, the fluid dynamics community is divided over the compressibility effect on the anisotropy of the Reynolds stresses. For instance, the experimental results of Kim et al. [16] suggest that the streamwise Reynolds stress remains almost constant with increase in M_c whereas the other two normal stresses decrease monotonically. This leads to an increase in anisotropy values of the streamwise Reynolds stress and a reduction in the anisotropy values (i.e they become more negative) of the other two normal stresses. Contrary to this, the numerical results of Pantano and Sarkar [18] imply that all the three components of the normal Reynolds stresses decrease monotonically with M_c resulting in the anisotropy values being quasi-unaffected. Both of these works, however, agree that the anisotropy of the primary Reynolds shear stress remains almost a constant with varying M_c . Thus, further research needs to be done on this topic to gain more insight.

Numerical simulations could provide many insights on the flow structures and statistics of turbulence mixing layers, as they possess the potential to resolve and extract a great amount of flow field details. Computationally, mixing layers are investigated via two approaches, namely, temporally and spatially developing mixing layers. The latter gives a more realistic estimation of experimental flows, as the former cannot capture the asymmetry in entrainment from the two streams. Earlier numerical analyses on mixing layers was restricted to studying temporal shear layers to reduce the computational cost [17, 18] as it uses periodic boundary conditions in both the streamwise and spanwise directions. With the recent developments in supercomputing capabilities, studies of the spatially evolving mixing layer are becoming more prevalent [19, 20]. Even with the recent advances, performing a direct numerical simulation (where all relevant length scales of turbulence are resolved) of turbulent mixing layer flows with experimental conditions is very expensive, especially when resolving the turbulent boundary layers that lead into the mixing section. Alternatively, Large Eddy Simulation (LES) is an attractive tool to study high Reynolds number flows with reasonable physical accuracy and at a relatively cheap computational cost.

This is because in LES only the large scales of turbulent motion are resolved and the smaller scales not supported by the grid resolution are either implicitly or explicitly modeled. This approach is widely used currently to perform simulations of mixing layers with experimental flow conditions [21]. However, even with this approach, resolving the boundary layers on the splitter plate all the way to the wall could result in expensive computations for the boundary layer regions.

Therefore, the current work deals with developing and validating a methodology of performing large eddy simulation of a compressible mixing layer with experimental flow conditions, where the boundary layers that lead into the mixing section are resolved with a wall model approach. This would help reduce the computational cost in performing realistic compressible mixing layer simulations, especially when the focus of research is on understanding the compressibility effects on the shear layer.

1.2 Review

The following presents a brief review of some of the past experimental and computational research findings related to mixing layers.

1.2.1 Experimental Studies

Experimentally, mixing layers have been studied for more than half a century. Liepmann and Laufer [22] studied the mean velocity distribution and intensity of turbulent fluctuations of a planar turbulent mixing layer way back in 1947. Jones et al. [23] investigated the overall turbulent structure of a two-stream mixing layer and presented two-point space-time correlations of the streamwise component of the fluctuating velocity. Oster and Wygnanski [24] studied the development of a mixing layer subjected to periodic excitation at its origin. They found that the growth rate of the shear layer, turbulent intensity and the Reynolds stresses are all affected by the amplitude and frequency of the excitation.

Bell and Mehta [25] studied the evolution of incompressible mixing layers from tripped and untripped boundary layers. They found that the near field and far field growth rates of the untripped case are much higher compared to the former. They attributed the increased growth rate in the untripped case to the presence of streamwise vortex structures (rib vortices) that are present in the braid regions between the spanwise rollers which were absent in the former. The development distance to attain self-similarity is found to be higher for the untripped case. Though the near field evolution of the Reynolds stresses was different for the two cases, the final asymptotic peak Reynolds stresses were found to be comparable between the two cases. The role of the aforementioned streamwise vortices on the development of the shear layer is also established quantitatively in their subsequent study [25].

Huang and Ho [26] studied the generation of small scale structures from an initially laminar mixing layer. They found that the vortex pairing that occurs in the pre-transition region doubles the wavelength of the spanwise and streamwise structures with the ratio of these two length scales being constant. The generation of the fine-scale structures is found to be the consequence of the interaction between the merging spanwise vortices and the streamwise structures.

Mehta and Weshtpal [7] studied incompressible turbulent mixing layers at a series of velocity ratios from 0.5 to 0.9. They found that the splitter plate effects increase the near field turbulence levels of a mixing layer with this increase being proportional to the velocity ratio. Consequently, this causes the development distance to attain self-similarity decrease for moderate velocity ratios (0.5 to 0.7) and increase for higher velocity ratios (0.8 and 0.9).

Brown and Roshko [3] showed that the changes in growth rates of variable density incompressible mixing layers are much smaller compared to that observed in compressible shear layers, concluding that the strong reduction in growth rates observed in the latter is due to the effect of compressibility itself and not due to density effects. Following this, several experimental studies [12, 14–16] were performed to understand the effects of compressibility on turbulent shear layers. It is found that

at high convective Mach numbers, the spanwise roller structures observed by Brown and Roshko [3] for incompressible mixing layers become more three dimensional and disorganized [16, 27] and therefore become relatively less capable of entraining fluid from freestream and hence being partially responsible for the reduction in growth rate [11].

1.2.2 Numerical Studies

A brief review of the numerical simulations of temporally and spatially developing mixing layers are given next.

Rogers and Moser [1, 28] studied the temporal evolution of a three-dimensional incompressible mixing layer. They observed the rollup of the spanwise vorticity into spanwise rollers with streamwise (rib) vortices in the braid regions between these rollers. They also found that in cases with sufficiently strong initial three dimensional disturbances, these streamwise structures collapse into compact axisymmetric vortices. They also found that in weakly three-dimensional flows, the pairing of these spanwise rollers inhibit (or delay) the rapid growth of three-dimensionality. However, in flows with high three-dimensionality, these pairings have been found to trigger the transition to turbulence in some cases.

Wang et al. [29] performed a DNS of a spatially developing mixing layer at a Reynolds number based on initial vorticity thickness of 700. They studied the relationship between the coherent fine scale eddies and the laminar-turbulent transition in mixing layers. They observed that the maximum expected azimuthal velocity of these coherent eddies decreases from 2 to 1.2 times the Kolmogorov velocity during the transition with the latter being the asymptotic value in the fully developed turbulent state. Moreover, they found that rib vortices that are observed in the transition are still observed in the fully developed state, but are composed of a large number of coherent fine scale eddies instead of a single eddy as in the transition region.

McMullan [30, 31] studied the effect of the imposed boundary layer fluctuations and the spanwise domain length on the streamwise vortices of a mixing layer evolving from laminar initial conditions using large eddy simulations. It was found that artificial confinement of the flow occurs when the wavelength of the streamwise structure matches the spanwise domain length. High levels of fluctuations in the initial boundary layers were also found to weaken the streamwise vortex structure.

Zhou et al. [32] performed a direct numerical simulation of a spatially evolving compressible mixing layer at a convective Mach number of 0.7. They observed the presence of Λ vortices and hairpin vortices in the transition region. In addition to that, the hairpin vortices were found to evolve into newly shaped structures due to the hairpin head instability. These newly shaped structures resemble that of a flower bouquet, with several small slender vortices encircled by semi-ring vortices as tying ribbons. They called these structures as ‘flower’ structures. These were observed until the flow attained the self-similar state. They also reported the presence of shocklets in their simulation.

Zhang et al. [20] performed a direct numerical simulation of a highly compressible mixing layer at a convective Mach number of 1. They observe the presence of multiple ring-like vortices in the transition region that is associated with a huge transfer of energy and momentum between the two streams. The formation and evolution of these ring vortices were also found to cause a tremendous increase in the growth rate of the shear layer in the transition region that is higher than that found in moderately compressible shear layers. The momentum thickness growth rate of the shear layer in the transition region was found to be about 6 times of that in the self-similar region. As the growth rate in the self-similar region is suppressed due to the compressibility effects, they suggested extending the transition region as a possible technique for enhancing mixing in highly compressible shear layers.

Large eddy simulation of a compressible mixing layer at a convective Mach number of 0.5 was studied by Sharma et al [6] using three different inflow conditions. They found that the acoustic sound generation from the turbulent shear layer was strongly

affected by the state of the boundary layers at the splitter plate tip. Mankbadi et al. [21] examined the effect of spanwise domain width and the significance of inflow turbulence on the LES of a compressible shear layer. They considered two inflow boundary conditions: one with no inflow turbulence and the other with inflow turbulence modeled using the Synthetic Eddy Method (SEM). They found that the latter better captures the experimental trends in the turbulent stresses.

1.3 Thesis Objectives

The main objective of the present work is to develop a methodology to perform LES of a compressible mixing layer with experimental flow conditions, using a wall model approach to resolve the upstream boundary layers. An in-house LES solver that has been previously used to perform simulations of Jets, is slightly modified to allow it to simulate two-stream mixing layers. The solver is validated and verified by performing simulations of laminar and incompressible turbulent mixing layers and comparing the subsequent results with the analytical results and the data in the literature. The inflow profiles and initial conditions for the compressible mixing layer LES are taken from the RANS calculations performed with ANSYS Fluent.

1.4 Organization of the Thesis

The organization of the thesis is described as below:

- **Chapter 2:** This chapter describes the governing equations used in the LES, the numerical methods employed in the LES solver to solve these equations, boundary conditions housed in the solver along with modifications made to simulate mixing layers and the parallelization strategy used in the solver presented together with the parallel performance data of the solver on a current supercomputer. The RANS methodology is also described in this chapter, highlighting the various solver settings and boundary conditions used in Fluent for performing the RANS calculations.

- **Chapter 3:** This chapter presents the verification and validation cases performed for the LES solver as a part of this work. A laminar mixing layer case and a series of incompressible turbulent mixing layer cases matching the flow conditions of the DNS of Attili and Bisetti [33] are performed and the results are compared with the analytical solutions and the literature.
- **Chapter 4:** This chapter presents the RANS calculations and LES of a compressible mixing layer matching the flow conditions of the experiment of Kim et al [11]. The results are compared with the reference experiment and the literature.
- **Chapter 5 :** This chapter presents a summary of the present work together with suggestions for future work.

2. COMPUTATIONAL METHODOLOGY

This chapter presents a brief overview of the computational framework used in the current study. In the present work, an in-house LES solver, which has been used previously for jet noise calculations, has been used for performing LES of spatially developing mixing layers. The RANS calculations used for generating the inflow profiles and initial conditions for compressible LES have been performed with ANSYS Fluent.

The legacy version of the in-house LES solver was first developed by Uzun [34]. It was further extended by Lo [35] who implemented various shock-capturing schemes into the solver. A modular version of the LES solver with excellent parallel efficiency was built from the legacy version by Martha [36] and Situ [37]. Shock capturing methods, wall modeling strategies and additional boundary conditions were implemented in the modular LES solver by Aikens [38], Dhamankar [39,40] and Vankayala [41]. It is this modular version of the LES solver that is used in the current work.

First, the computational methodology used in the LES solver is described in section 2.1, with details given on the numerical methods employed, the various boundary conditions, the parallelization strategy used and some performance results of the LES solver on current supercomputers. The RANS methodology is described in section 2.2, highlighting the various solution methods, boundary conditions and other important solver settings used in Fluent.

2.1 LES Methodology

2.1.1 Governing Equations

In large eddy simulations, only the large scale turbulent structures are resolved and the impact of the small scale structures that are not supported by the grid resolution is modeled. Therefore, the Navier-Stokes equations can be filtered to decompose the flow field into a resolved scale component \bar{f} and a subgrid-scale component f_{SGS} such as

$$f = \bar{f} + f_{SGS}. \quad (2.1)$$

This filtering operation could be done using two approaches, explicit or implicit. In the explicit filtering strategy, a sub-grid scale model is used to model the SGS terms. In the implicit approach, however, these SGS terms are set to zero and the numerical dissipation provided by the grid and the numerical methods is assumed to mimic the physics of the unresolved small scale structures. This implicit approach, henceforth referred as ‘ILES’, is used in the current work.

For compressible LES, it is easier to express the resolved scale components in terms of the Favre-filtered variables written as

$$\tilde{f} = \frac{\overline{\rho f}}{\bar{\rho}}. \quad (2.2)$$

The resulting conservative form of the three dimensional Favre-filtered Navier-Stokes equations are non-dimensionalized in the following way:

$$\rho = \frac{\rho^*}{\rho_{ref}^*}, \quad u_i = \frac{u_i^*}{U_{ref}^*}, \quad x_i = \frac{x_i^*}{L_{ref}^*}, \quad p = \frac{p^*}{\rho_{ref}^* U_{ref}^{*2}}, \quad t = \frac{t^*}{\frac{L_{ref}^*}{U_{ref}^*}}. \quad (2.3)$$

Where a quantity with an asterisk(*) denotes a dimensional quantity. The reference variables denoted with the subscript ‘ref’ are chosen according to their relevance to the flow under study. The final non-dimensionalized governing equations which are to be solved numerically in generalized curvilinear coordinates are

$$\frac{1}{J} \frac{\partial \mathbf{Q}}{\partial t} + \frac{\partial}{\partial \xi} \left(\frac{\mathbf{F} - \mathbf{F}_v}{J} \right) + \frac{\partial}{\partial \eta} \left(\frac{\mathbf{G} - \mathbf{G}_v}{J} \right) + \frac{\partial}{\partial \zeta} \left(\frac{\mathbf{H} - \mathbf{H}_v}{J} \right) = 0. \quad (2.4)$$

Here \mathbf{Q} is the vector of conservative variables. $\mathbf{F}, \mathbf{G}, \mathbf{H}$ are the inviscid flux vectors and $\mathbf{F}_v, \mathbf{G}_v, \mathbf{H}_v$ are the viscous flux vectors. \mathbf{J} is the Jacobian determinant of the transformation of between physical (x, y, z) and computational coordinates (ξ, η, ζ) and t is time. These quantities are given as below:

$$\mathbf{Q} = [\bar{\rho} \quad \bar{\rho}\tilde{u} \quad \bar{\rho}\tilde{v} \quad \bar{\rho}\tilde{w} \quad \bar{\rho}\tilde{e}_t]^T, \quad (2.5)$$

$$\mathbf{F} = \begin{bmatrix} \bar{\rho}\tilde{U} \\ \bar{\rho}\tilde{u}\tilde{U} + \xi_x\bar{p} \\ \bar{\rho}\tilde{v}\tilde{U} + \xi_y\bar{p} \\ \bar{\rho}\tilde{w}\tilde{U} + \xi_z\bar{p} \\ (\bar{\rho}\tilde{e}_t + \bar{p})\tilde{U} \end{bmatrix}, \quad \mathbf{G} = \begin{bmatrix} \bar{\rho}\tilde{V} \\ \bar{\rho}\tilde{u}\tilde{V} + \eta_x\bar{p} \\ \bar{\rho}\tilde{v}\tilde{V} + \eta_y\bar{p} \\ \bar{\rho}\tilde{w}\tilde{V} + \eta_z\bar{p} \\ (\bar{\rho}\tilde{e}_t + \bar{p})\tilde{V} \end{bmatrix}, \quad \mathbf{H} = \begin{bmatrix} \bar{\rho}\tilde{W} \\ \bar{\rho}\tilde{u}\tilde{W} + \zeta_x\bar{p} \\ \bar{\rho}\tilde{v}\tilde{W} + \zeta_y\bar{p} \\ \bar{\rho}\tilde{w}\tilde{W} + \zeta_z\bar{p} \\ (\bar{\rho}\tilde{e}_t + \bar{p})\tilde{W} \end{bmatrix}, \quad (2.6)$$

$$\mathbf{F}_v = \begin{bmatrix} 0 \\ \xi_x(\tau_{xx} - \Psi_{xx}) + \xi_y(\tau_{xy} - \Psi_{xy}) + \xi_z(\tau_{xz} - \Psi_{xz}) \\ \xi_x(\tau_{yx} - \Psi_{yx}) + \xi_y(\tau_{yy} - \Psi_{yy}) + \xi_z(\tau_{yz} - \Psi_{yz}) \\ \xi_x(\tau_{zx} - \Psi_{zx}) + \xi_y(\tau_{zy} - \Psi_{zy}) + \xi_z(\tau_{zz} - \Psi_{zz}) \\ \tilde{u}F_{v2} + \tilde{v}F_{v3} + \tilde{w}F_{v4} - [\xi_x(q_x + Q_x) + \xi_y(q_y + Q_y) + \xi_z(q_z + Q_z)] \end{bmatrix}, \quad (2.7)$$

$$\mathbf{G}_v = \begin{bmatrix} 0 \\ \eta_x(\tau_{xx} - \Psi_{xx}) + \eta_y(\tau_{xy} - \Psi_{xy}) + \eta_z(\tau_{xz} - \Psi_{xz}) \\ \eta_x(\tau_{yx} - \Psi_{yx}) + \eta_y(\tau_{yy} - \Psi_{yy}) + \eta_z(\tau_{yz} - \Psi_{yz}) \\ \eta_x(\tau_{zx} - \Psi_{zx}) + \eta_y(\tau_{zy} - \Psi_{zy}) + \eta_z(\tau_{zz} - \Psi_{zz}) \\ \tilde{u}G_{v2} + \tilde{v}G_{v3} + \tilde{w}G_{v4} - [\eta_x(q_x + Q_x) + \eta_y(q_y + Q_y) + \eta_z(q_z + Q_z)] \end{bmatrix}, \quad (2.8)$$

$$\mathbf{H}_v = \begin{bmatrix} 0 \\ \zeta_x(\tau_{xx} - \Psi_{xx}) + \zeta_y(\tau_{xy} - \Psi_{xy}) + \zeta_z(\tau_{xz} - \Psi_{xz}) \\ \zeta_x(\tau_{yx} - \Psi_{yx}) + \zeta_y(\tau_{yy} - \Psi_{yy}) + \zeta_z(\tau_{yz} - \Psi_{yz}) \\ \zeta_x(\tau_{zx} - \Psi_{zx}) + \zeta_y(\tau_{zy} - \Psi_{zy}) + \zeta_z(\tau_{zz} - \Psi_{zz}) \\ \tilde{u}H_{v2} + \tilde{v}H_{v3} + \tilde{w}H_{v4} - [\zeta_x(q_x + Q_x) + \zeta_y(q_y + Q_y) + \zeta_z(q_z + Q_z)] \end{bmatrix}. \quad (2.9)$$

Now, each of the terms in the above vectors are defined. The contravariant velocities \tilde{U} , \tilde{V} and \tilde{W} are calculated as

$$\begin{bmatrix} \tilde{U} \\ \tilde{V} \\ \tilde{W} \end{bmatrix} = \begin{bmatrix} \xi_x & \xi_y & \xi_z \\ \eta_x & \eta_y & \eta_z \\ \zeta_x & \zeta_y & \zeta_z \end{bmatrix} \begin{bmatrix} \tilde{u} \\ \tilde{v} \\ \tilde{w} \end{bmatrix}. \quad (2.10)$$

The grid metrics (ξ_x, ξ_y, \dots) that arise from the transformation between physical and computational space can be computed as

$$\begin{bmatrix} \xi_x & \xi_y & \xi_z \\ \eta_x & \eta_y & \eta_z \\ \zeta_x & \zeta_y & \zeta_z \end{bmatrix} = \begin{bmatrix} x_\xi & x_\eta & x_\zeta \\ y_\xi & y_\eta & y_\zeta \\ z_\xi & z_\eta & z_\zeta \end{bmatrix}^{-1}. \quad (2.11)$$

However, the mesh metrics are evaluated in their conservative form,

$$\begin{bmatrix} \xi_x & \xi_y & \xi_z \\ \eta_x & \eta_y & \eta_z \\ \zeta_x & \zeta_y & \zeta_z \end{bmatrix} = J \begin{bmatrix} (y_\eta z)_\zeta - (y_\zeta z)_\eta & (z_\eta x)_\zeta - (z_\zeta x)_\eta & (x_\eta y)_\zeta - (x_\zeta y)_\eta \\ (y_\zeta z)_\xi - (y_\xi z)_\zeta & (z_\zeta x)_\xi - (z_\xi x)_\zeta & (x_\zeta y)_\xi - (x_\xi y)_\zeta \\ (y_\xi z)_\eta - (y_\eta z)_\xi & (z_\xi x)_\eta - (z_\eta x)_\xi & (x_\xi y)_\eta - (x_\eta y)_\xi \end{bmatrix}, \quad (2.12)$$

as it preserves accurate freestream properties [42]. The Jacobian J that results from the transformation between the physical and computational space is given by

$$J = \left| \frac{\partial(\xi, \eta, \zeta)}{\partial(x, y, z)} \right| = [x_\xi (y_\eta z_\zeta - y_\zeta z_\eta) - x_\eta (y_\xi z_\zeta - y_\zeta z_\xi) + x_\zeta (y_\xi z_\eta - y_\eta z_\xi)]^{-1}. \quad (2.13)$$

The total energy per unit volume is given as

$$\bar{\rho} \tilde{e}_t = \frac{1}{2} \bar{\rho} \tilde{u}_i \tilde{u}_i + \frac{\bar{p}}{\gamma - 1}, \quad (2.14)$$

in which the pressure \bar{p} is computed using the non-dimensionalized ideal gas equation of state

$$\bar{p} = \frac{\bar{\rho} \tilde{T}}{\gamma M_{ref}^2}. \quad (2.15)$$

The ratio of specific heats γ is taken as 1.4 (standard for air) and the reference mach number, M_{ref} , is computed as

$$M_{ref} = \frac{U_{ref}^*}{\gamma R T_{ref}^*}. \quad (2.16)$$

The value of the specific gas constant R is taken as $287 \frac{J}{kg.K}$ and the reference temperature T_{ref}^* is chosen according to the problem under study. The resolved scale stress tensor is given by

$$\tau_{ij} = \frac{\tilde{\mu}}{Re_{ref}} \left(2\tilde{S}_{ij} - \frac{2}{3}\tilde{S}_{kk}\delta_{ij} \right), \quad (2.17)$$

where the resolved scale strain rate tensor is given by

$$\tilde{S}_{ij} = \frac{1}{2} \left(\frac{\partial \tilde{u}_i}{\partial x_j} + \frac{\partial \tilde{u}_j}{\partial x_i} \right), \quad (2.18)$$

and the reference Reynolds number Re_{ref} is given as

$$Re_{ref} = \frac{\rho_{ref}^* U_{ref}^* L_{ref}^*}{\mu_{ref}^*}. \quad (2.19)$$

The resolved scale heat flux is given by

$$q_i = \frac{-\tilde{\mu}}{(\gamma - 1)M_{ref}^2 Re_{ref} Pr} \frac{\partial \tilde{T}}{\partial x_i}. \quad (2.20)$$

Here the Prandtl number, Pr , is set to 0.7. The molecular viscosity $\tilde{\mu}$ is computed using the Sutherland's law defined by

$$\tilde{\mu} = \frac{\tilde{\mu}^*}{\mu_{ref}^*} = \tilde{T}^{3/2} \frac{1 + S}{\tilde{T} + S}, \quad (2.21)$$

where S is the non-dimensional Sutherland constant given by $S = 110 \text{ K}/T_{ref}^*$. The subgrid scale stress tensor (ψ_{ij}) and heat flux (Q_i) are given by

$$\psi_{ij} = \bar{\rho}(\widetilde{u_i u_j} - \tilde{u}_i \tilde{u}_j), \quad (2.22)$$

and

$$Q_i = \bar{\rho}(\widetilde{u_i T} - \tilde{u}_i \tilde{T}). \quad (2.23)$$

As mentioned earlier, the ILES approach is used in the current work. Hence no subgrid scale modeling is employed and both the subgrid scale stress tensor (equation 2.22) and heat flux (equation 2.23) are set to zero.

2.1.2 Numerical Methods

The discretized governing equations are solved in the transformed computational space. The spatial derivatives are discretized through a 6th order compact scheme developed by Lele [43]. This scheme is preferred for its low dispersive and dissipative error. This is given as

$$\frac{1}{3}f'_{i-1} + f'_i + \frac{1}{3}f'_{i+1} = \frac{7}{9\Delta\xi}(f_{i+1} - f_{i-1}) + \frac{1}{36\Delta\xi}(f_{i+2} - f_{i-2}). \quad (2.24)$$

Here f' is the derivative of the quantity f with respect to ξ . Note that $\Delta\xi = 1$ as the computational coordinates are uniformly spaced. The spatial derivatives in the η and ζ are computed analogously. Equation 2.24 is used to compute the spatial derivatives in the interior points (i.e points $i=3$ to $i=N-2$, if there are N points in a given direction). For the points at and one point away from the boundaries, the above equation cannot be used as the stencil points will fall outside the computational domain. Hence at these points, the 3rd-order one-sided and 4th-order central compact schemes [43] are used, respectively. The fourth-order Runge-Kutta scheme is used to time advance the governing equations.

To improve the stability of the compact scheme, a spatial filter is applied after every time step to filter the conservative variables. The stability issue arises because of the numerical instabilities that could occur due to boundary conditions and non-uniform curvilinear meshes that are typically used here. Hence for this purpose, the 6th order tridiagonal filter of Gaitonde and Visbal [44] given by

$$\alpha_f \bar{f}_{i-1} + \bar{f}_i + \alpha_f \bar{f}_{i+1} = \sum_{n=0}^3 \frac{a_n}{2} (f_{i+n} + f_{i-n}), \quad (2.25)$$

where

$$|\alpha_f| < 0.5,$$

is used to damp out the spurious numerical instabilities. Here \bar{f} is the filtered conservative variable and f is the corresponding unfiltered variable. A higher value of the parameter α_f causes the filter to be less dissipative. In the present work, the

value of the parameter α_f is set to 0.47 as it has been found to work well in the past [34, 35, 38, 40, 41]. The values of the coefficients and other details can be found in [44]. The above equation can only be applied at the interior grid points away from the boundaries because of the stencil width. No filtering operation is performed for the points on the boundary. For the first and second points away from the boundary, the 6th order one-sided filter of Gaitonde and Visbal [44] is employed.

To improve the shock-capturing abilities, characteristic filters were implemented in the modular LES code [38]. Shock cells are identified with the help of the Ducros shock detector and a buffer of two points is added outside these shock regions. Inside the shock and the buffer regions, the spatial filter is completely turned off and a characteristic filter is applied. Details of the implementation can be found in [38].

Two types of characteristic filters are employed: the TVD and WENO characteristic filters. The filters can either be applied globally or locally. In the global application, the filters are applied everywhere in the flowfield. In the local application, the characteristics filters are applied only in the shock and buffer points. The Harten switch is also implemented in the current modular solver which can be turned on to limit the amount of dissipation in the non-shock regions of the flow field.

2.1.3 Boundary Conditions

Various boundary conditions have been implemented in the modular LES code for realistic simulations of turbulent flows. These were originally implemented to perform jet flows, flat plate boundary layers, and channel flows. A brief discussion of the boundary conditions implemented together with the changes made for performing a mixing layer type simulation will be discussed now.

A digital filter based turbulent inflow boundary condition was implemented in the modular LES solver by Dhamankar [39]. This allows us to specify unsteady correlated turbulent fluctuations at the inflow to result in physically realistic turbulent structures

in a short distance downstream. The digital filter based turbulent boundary condition requires the following input parameters:

1. Mean inflow profile of flow variables
2. Inflow Reynolds stresses
3. The integral length scales in the three directions
4. The cross-stream extent within which the fluctuations need to be applied

In the present work, all of these parameters are either taken from empirical relations, experiments, or from precursor RANS simulations. Details of the choice will be given when discussing particular cases. This inflow boundary condition could also be used to generate random white noise fluctuations at the inflow by not correlating the fluctuations at the inflow plane. This approach which is referred to as “white noise inflow” is also used in the present work when noted.

It should be noted that the DFGTI boundary condition was originally implemented to be used for a single fluid stream such as in a flat plate boundary layer or channel flow type of simulation. In the present work, this is extended to have an option to be applied to two streams, which is typical of a planar mixing layer evolving from two separate turbulent boundary layers downstream of a splitter plate. Hence two sets of the inputs are required as an input to the solver, if the number of fluid streams is chosen as two. Also, when simulating a channel flow type of simulation or mixing layer evolving from two separate channels, if the mean velocity profile is obtained using empirical relations as described in [39], one could specify separate boundary layer thicknesses for the top and bottom walls of the channel. This feature is added to the solver as a part of this work, since the boundary layers on the nozzle walls and splitter plate (typical of a mixing layer type simulation) will likely have different thicknesses.

It was observed in previous studies that the DGF'TI requires a short redevelopment length of about 11.5 times the boundary layer thickness at the inflow for wall resolved

flat plate boundary layer flows [39]. This is required for the synthetic turbulent fluctuations imposed at the inflow to evolve into realistic structures and for the turbulent boundary layer to exhibit the correct physical behavior.

Two types of outflow boundary conditions are used in the current work, namely the Tam and Dong outflow [45, 46] and the characteristic outflow boundary condition [47, 48] implemented by Dhamankar [39]. The Tam and Dong radiation boundary condition [45, 46] is also used in the cross-stream boundaries of the domain in some of the validation cases presented in the current work. The Tam and Dong radiation and outflow boundary conditions require mean flow variables and an assumed acoustic source position. It has been observed that it is sufficient to assume that this acoustic source is far away from the outflow boundary and that the results are weakly dependent on its location [49]. Therefore in the present work, the location of the acoustic source is taken close to the inflow plane. Details of the implementation of the Tam and Dong boundary conditions can be found in [34]. The characteristic outflow boundary condition requires the value of the static pressure at infinity [39]. This is set based on the physics of the problem/precursor RANS calculations in the present work.

It has been observed in the present work that numerical instabilities arise when strong vortices reach the outflow boundary. In order to damp out these vortices before they exit the domain, the sponge zone formulation given by Colonius et al. [50] that was implemented in the LES solver is used close to the outflow boundary. Following Aikens [38], details of the implementation will be given now. Inside the sponge zone, the turbulent flow field is forced to a smooth target solution by modifying the right-hand side of the governing equations (i.e equation 2.4) as

$$\frac{\partial \mathbf{Q}}{\partial t} = \mathbf{RHS} - \chi(x)(\mathbf{Q} - \mathbf{Q}_{\text{target}}), \quad (2.26)$$

Where $\chi(x)$ in the above equation is given by

$$\chi(x) = \chi_{max} \left(\frac{x - x_{phy}}{x_{max} - x_{phy}} \right)^3. \quad (2.27)$$

In the above set of equations, $\mathbf{Q}_{\text{target}}$ is the smooth target solution that the actual flow field is forced to and x_{phy} and x_{max} are the streamwise starting and ending locations of the sponge zone. The value of the parameter χ_{max} is set to 1. In the present work, the target solution is taken from the precursor RANS calculations, a feature that was added to the solver as part of this work. The RANS results are non-dimensionalized with respect to the reference variables used in the LES simulation and then written to a file which is then read by the LES solver. The grid is also highly stretched in the streamwise direction in the sponge zone to aid in damping the strong vortices. It should be noted that the above sponge zone approach is not used in all the simulation cases presented in this work. In some cases, a short buffer zone close to the outflow boundary with stretched grids is used without forcing the solution towards a target solution and is found to be efficient in avoiding numerical instabilities at the outflow plane.

The modular LES solver has several wall boundary conditions for performing both wall resolved ($\Delta y^+ \sim 1$) and wall modeled types of simulations. Dhamankar [39] implemented a characteristic based adiabatic viscous wall, isothermal hard wall and adiabatic hard-wall boundary conditions for wall resolved flows. The latter two were found to be much cheaper than the former [39]. Various wall models were also incorporated in the LES solver by Aikens [38] and Vankayala [41] to avoid resolving the wall in high Reynolds number simulations as it could be prohibitively expensive. These wall models take the information from the outer LES solution at some “Matching Point” and use it to compute the wall shear stress which in turn is used as the flux boundary condition for the LES at the wall. Details of the implementation can be found in the cited references. In the present work, the isothermal hard wall boundary condition and the generalized equilibrium wall model implemented by Vankayala [41] are used. The fourth grid point from the wall is chosen as the “Matching Point” for the wall model used in the present work. This choice is based on previous observations with wall models [38, 41] implemented in the LES solver.

In the present work, translational periodic boundary conditions have been used in the spanwise direction. Details of the implementation can be found in [39, 51]. Note that this is helpful to avoid including the sidewalls of the wind tunnels in the simulations since the flow can be assumed to be periodic in this direction. However, a proper domain size in the spanwise direction should be ensured so as to avoid inhibiting the turbulent structures/growth rate of the mixing layer. The domain size in the spanwise direction for all the cases simulated in the present work is based on *priori* knowledge of simulations from the literature. Further details will be provided when discussing the specific simulation cases.

Lastly, a series of edge boundary conditions have been incorporated in the modular LES solver, for the purpose of handling the edges formed between two faces in the fluid domain. Further details can be found in [38, 39].

2.1.4 Initial Conditions

The initial conditions for the LES calculations performed in the present work have either been obtained from empirical relations of the profiles of mean flow variables of boundary layers/mixing layers or from precursor RANS calculations. Appropriate changes were made to the solver as part of this work. Detailed information about the initial conditions used for each simulation is given when discussing the specific cases.

2.1.5 Solver Topology, Parallelization and Scaling

The Truncated SPIKE algorithm [52] is used in the modular LES solver to solve the large tridiagonal linear systems of equations resulting from the spatial differencing of the governing equations and the spatial filtering operations. The modular LES solver has demonstrated good parallel efficiency with this algorithm with up to 91,125 cores [36]. Details of the implementation can be found in [53, 54] .

A multi-block topology approach is used in the modular solver. At the highest level, the computational domain is partitioned into “superblocks” based on some

logical decomposition of the fluid domain under study. Each superblock either has a single boundary condition or a single neighboring superblock on each of its six faces. The superblocks are further subdivided into blocks by specifying the number of blocks in each computational direction (ξ, η and ζ). Each of these blocks is then assigned to a processor during runtime. Thus the number of computer processors used in running the simulation should be equal to the total number of blocks. The block to processor mapping has been done efficiently to help reduce network congestion when using a large number of processors [36]. One solution/grid file is written for each superblock as opposed to for each block resulting in efficient parallel I/O operations and it further reduces the simulation setup time when the number of processors is changed, as the connectivity information between superblocks will remain the same, requiring one to only change the number of blocks per superblock. Further details of this multi-block approach can be found in [36].

2.1.6 Solver Performance and Scaling

A scaling experiment is performed with the current LES solver as a part of the present work to determine the performance and scalability of the solver on current supercomputers. These tests also serve to determine the appropriate work per processor when performing the simulation runs. The petascale machine “Stampede 2” at the Texas Advanced Computing Center (TACC) is chosen as the platform for performing these tests. Stampede 2 houses two types of processors for computing purposes namely, the Intel Skylake processor (SKX) and the Intel Knights Landing processor (KNL).

The test case chosen for the current strong and weak scaling experiment on Stampede 2 is a nearly incompressible flow through a rectangular channel with a Mach number of 0.1 and at a Reynolds number (based on the channel half-height h) of 12,600. The channel dimensions are $(30 \times 2 \times \pi)h$ in the (x, y, z) directions. The scaling tests are performed on both the SKX and KNL nodes. Also, 5 grid configu-

rations (each of Cartesian topology) are considered for performing the scaling tests. The information about each configuration is shown in table 2.1

Table 2.1. Grid configurations considered for the scaling tests

Configuration	Number of Points			
	N_x	N_y	N_z	Total(in millions)
C1	768	192	576	85
C2	1536	192	576	170
C3	1536	192	1152	340
C4	1536	384	1152	680
C5	1536	768	1152	1359

Strong scaling

The Strong scaling tests are performed with configurations C1 and C5 on both the SKX and KNL nodes. Also, both wall resolved (with an adiabatic wall) and wall modeled (with an equilibrium wall model) LES are performed for C1. In reality, however, to match the high Reynolds number of the compressible mixing layer in the experiments, it is essential to run a wall modeled LES, since a wall resolved LES may be too expensive. Due to this fact and to save time, only wall-modeled LES simulations are performed for the rest of the other scaling tests.

The details of the cases considered for each of the strong scaling tests as well as the average time per time-step are shown in tables 2.2 to 2.4. Note that W.R. refers to wall resolved cases and W.M. to wall modeled.

It can be inferred from table 2.2 & 2.3 that the wall resolved case typically takes slightly less time per time step compared to the wall modeled case. Also evident from the timing results is that the code takes longer to run on the KNL nodes compared

Table 2.2. C1 - strong scaling test on SKX

Number of cores			Time per time step (seconds)				TFLOPS		
x	y	z	Total	Nodes	Pts/core	W.R.	W.M.	W.R.	W.M.
8	2	6	96	2	96^3	3.075	3.089	0.09	0.09
12	3	9	324	6.75	64^3	1.016	1.041	0.27	0.27
16	4	12	768	16	48^3	0.399	0.409	0.70	0.69
24	6	18	2592	54	32^3	0.094	0.101	3.02	2.82
32	8	24	6144	128	24^3	0.044	0.044	6.56	6.56
48	12	36	20736	432	16^3	0.037	0.042	7.82	6.93

Table 2.3. C1 - strong scaling test on KNL

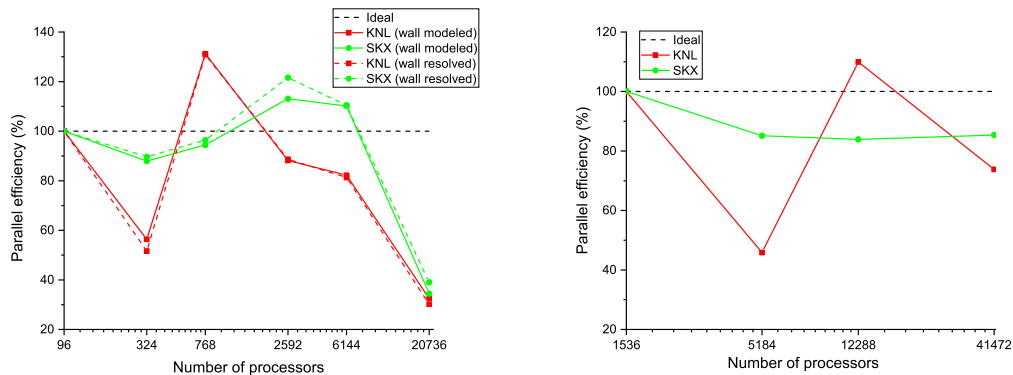
Number of cores			Time per time step (seconds)				TFLOPS		
x	y	z	Total	Nodes	Pts/core	W.R.	W.M.	W.R.	W.M.
8	2	6	96	1.41	96 ³	5.517	5.777	0.05	0.05
12	3	9	324	4.76	64 ³	3.164	3.036	0.09	0.09
16	4	12	768	11.29	48 ³	0.527	0.550	0.53	0.51
24	6	18	2592	38.12	32 ³	0.231	0.243	1.23	1.17
32	8	24	6144	90.35	24 ³	0.106	0.110	2.69	2.62
48	12	36	20736	304.94	16 ³	0.085	0.082	3.37	3.49

Table 2.4. C5 - strong scaling test on SKX and KNL (W.M.)

Number of cores			Time per time step (seconds)				TFLOPS			
x	y	z	Total	Nodes	Pts/core	SKX	KNL	SKX	KNL	
16	8	12	1536	32	22.59	96 ³	3.005	5.744	1.48	0.77
24	12	18	5184	108	76.24	64 ³	1.046	3.712	4.26	1.20
32	16	24	12288	256	180.71	48 ³	0.448	0.653	9.96	6.83
48	24	36	41472	864	609.88	32 ³	0.130	0.288	34.21	15.47

to the SKX nodes. Thus it might be more expensive to run the code on the KNL nodes than on the SKX nodes.

The parallel efficiency for the present strong scaling results with respect to the baseline case (96 cores for case 1 and 1536 cores for case 5) is plotted and is shown in figure 2.1. For C1, the code achieves superlinear speed up at 32^3 and 24^3 pts/core on the SKX nodes, with the peak efficiency occurring at 32^3 pts/core. On the KNL nodes, peak efficiency and superlinear speed up occur at 48^3 pts/core. Also, the efficiency drops significantly lower (below 40%) at 16^3 pts/core on both the SKX and KNL nodes. Moreover, it can be seen that on the SKX nodes, the wall resolved case is slightly more efficient than the wall modeled case whereas it is the other way around on the KNL nodes. For C5, no superlinear speedup is seen on the SKX nodes and the efficiency remains almost constant at around 85 %. On the KNL nodes, however, a similar trend as for C1 is seen with the code achieving superlinear speed up and peak efficiency at 48^3 pts/core. Therefore, based on the results, we see that it is more efficient for us to use around 32^3 pts/core on the SKX nodes and around 48^3 pts/core on the KNL nodes for future runs.



(a) Parallel efficiency (case 1)

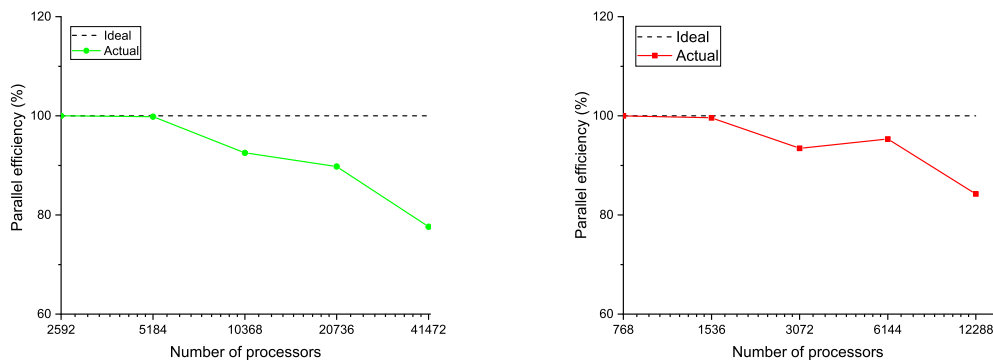
(b) Parallel efficiency (case 5)

Figure 2.1. Strong scaling tests.

Weak scaling

As noted previously, the maximum strong scaling parallel efficiency occurs at 32^3 pts/core on the SKX nodes and at 48^3 pts/core on the KNL nodes. Therefore, the weak scaling is performed for configurations C1-C5 with 32^3 pts/core on the SKX nodes and with 48^3 pts/core on the KNL nodes. The timing results are shown in tables 2.5 and 2.6. The parallel efficiency with respect to the baseline case (2592 cores for SKX and 768 cores for KNL) is plotted for the weak scaling tests and is shown in figure 2.2.

It is evident from figure 2.2 that on the SKX nodes, the parallel efficiency remains fairly close to the ideal value until about 5184 cores and then drops continuously as the number of processors are increased. Similar behavior is also seen in the weak scaling results on the KNL nodes where the efficiency remains close to the ideal till about 1538 cores. Hence it will be desirable to use around 2592-5184 cores on the SKX nodes and around 768-1538 cores on the KNL nodes when maintaining the respective problem size per core recommended earlier. However, using higher number of cores (up to 20736 cores for SKX and 6144 cores for KNL) than that mentioned above should still result in a good performance, as the efficiency values are still reasonably good in this range, as observed through figure 2.2.



(a) Weak scaling: SKX (32^3 pts/core)

(b) Weak scaling: KNL (48^3 pts/core)

Figure 2.2. Weak scaling tests.

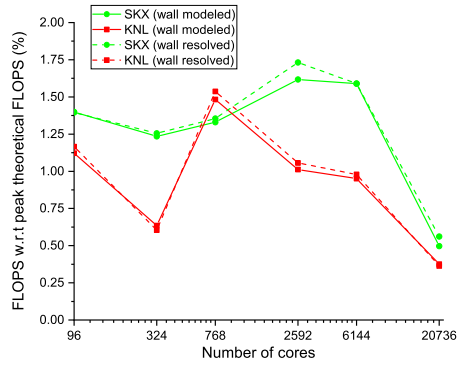
Floating point performance

The last column of tables 2.2 - 2.6 contains information on the floating point operations per second (FLOPS) for the different cases considered above. Due to the difficulty in measuring the FLOPS on the KNL nodes, the FLOPS for all cases running on KNL are estimated by using its timing information and the measured floating point operations (FLOPs) from the respective cases running on SKX nodes. For instance, for estimating the FLOPS in the strong scaling test on KNL for configuration C1 (table 2.3), the timing information from table 2.3 and the measured floating point operations (FLOPs) from corresponding cases in table 2.2 are used. Also, since it was difficult to measure the FLOPS for cases using a large number of cores (more than 10368 cores), the FLOPS for such cases are estimated in a similar procedure by using their timing information and the measured FLOPs from the cases using a lower number of cores within the same grid configuration. The estimated FLOPS are indicated in red. It can be noted that no FLOPS data is reported for case C4 in table 2.5 and 2.6. This is because no scaling tests with a lower number of cores were performed for C4 and hence the FLOPS count for this case could not be estimated.

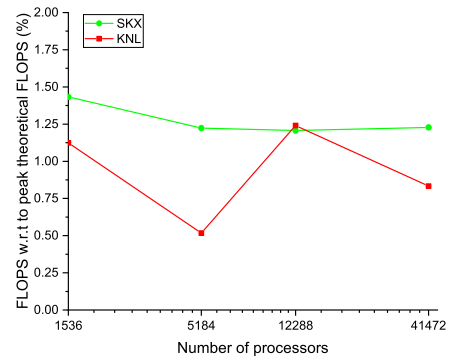
The ratio of the FLOPS obtained with different numbers of cores with respect to the peak theoretical FLOPS on that many cores is expressed as a percentage and is plotted for all of the above cases. This is shown in figures 2.3 and 2.4. It can be seen that this ratio is less 2 % for all the cases. Though these values are low, these are typical of a turbulent CFD code running on current supercomputers.

2.2 RANS Methodology

As mentioned earlier, a set of RANS calculations have been performed as a part of this work. The results of these calculations have been used to serve as an initial condition and for generating the necessary inflow profiles (for the mean flow/Reynolds stresses) for the LES calculations. These RANS calculations have been performed with ANSYS Fluent, which is a commercial CFD tool for solving a wide variety of



(a) C1



(b) C5

Figure 2.3. Floating point Performance - strong scaling tests.

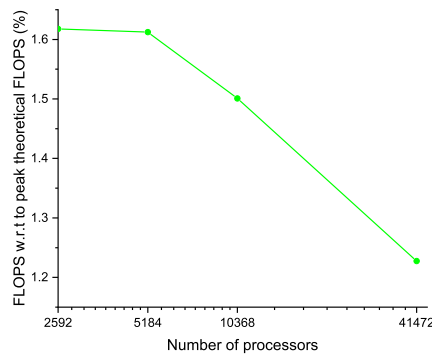
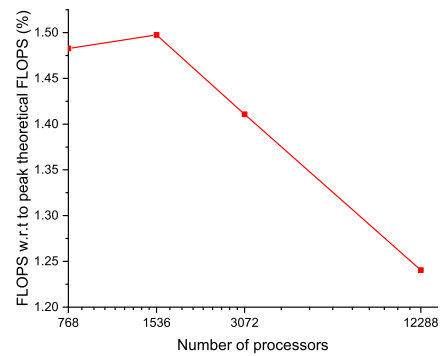
(a) SKX (32^3 pts/core)(b) KNL (48^3 pts/core)

Figure 2.4. Floating point performance - weak scaling tests.

fluid flow problems of laminar/turbulent flows in incompressible/compressible regimes with and without heat transfer. ANSYS Fluent uses a cell-centered finite-volume based approach. Detailed information about the solver can be found in [55].

In the present work, RANS simulations of only compressible mixing layers have been performed. Information regarding the type of solver used, the choice of various solver settings, the different boundary conditions and turbulence models used are discussed next.

Fluent houses two types of solvers: the pressure-based solver and the density-based solver. The density-based solver is used in the present work as it works well for flows in the highly compressible regime. Only steady-state simulations have been performed in the present work. The ideal gas assumption is used and Sutherland's law is used for determining the viscosity.

The second-order upwind scheme is used for the spatial discretization of the flow equations (continuity, momentum and energy equations). The other equations which may arise because of the choice of the turbulence model used are spatially discretized using the first-order upwind scheme. The Roe flux difference splitting (Roe-FDS) scheme is used for the convective fluxes. The gradients are evaluated using the "Least Squares Cell Based" method available in Fluent. The implicit scheme available in Fluent for the steady-state solver is used for the temporal discretization of the governing equations. The Courant number is varied slightly for each of the simulations performed and specific values will be given when discussing the particular cases. The default under-relaxation factors available in fluent have been used in the present work.

Various turbulence models have been incorporated in Fluent for modeling the terms that result from the Reynolds averaging process. Two such turbulence models, namely the realizable $k - \epsilon$ and the Stress- ω based Reynolds Stress Model (RSM) are used in the present work. The compressibility effects option that is available in Fluent is turned on, which allows one to take into account of the effects of compressibility on turbulence through the dilatational dissipation term that is modeled using the method proposed by Sarkar [56]. This is important to model the decreased spreading rate that is observed in high speed compressible mixing layers. The shear flow corrections option is also enabled for the RSM to improve the accuracy of predicting free shear flows [55].

The pressure inlet and pressure outlet boundary conditions available in fluent have been used as the inflow and outflow boundary conditions in the present work. The enhanced wall treatment is used when using the $k - \epsilon$ turbulence model that allows for the placement of the first grid point away from the wall in any of the viscous

sub-layer, buffer layer or the fully turbulent outer regions. For the Stress- ω based RSM, Fluent incorporates a default near-wall treatment to perform blending between the viscous sublayer and the logarithmic region and it is recommended to use a low Reynolds number mesh ($y^+ \sim 1$) when using this turbulence model [57].

Table 2.5. Weak scaling with 32^3 pts/core - SKX

Number of cores							
Configuration	x	y	z	Total	Nodes	Time per time step (seconds)	TFLOPS
C1	24	6	18	2592	54	0.1012	2.82
C2	48	6	18	5184	108	0.1013	5.62
C3	48	6	36	10368	216	0.1093	10.46
C4	48	12	36	20736	432	0.1127	-
C5	48	24	36	41472	864	0.1303	34.21

Table 2.6. Weak scaling with 48^3 pts/core - KNL

Number of cores							
Configuration	x	y	z	Total	Nodes	Time per time step (seconds)	TFLOPS
C1	16	4	12	768	11.29	0.5502	0.51
C2	32	4	12	1536	22.59	0.5523	1.03
C3	32	4	24	3072	45.18	0.5888	1.94
C4	32	8	24	6144	90.35	0.5772	-
C5	32	16	24	12288	180.71	0.6530	6.83

3. CODE VERIFICATION AND VALIDATION

This chapter presents some of the validation cases performed as a part of this work. Though the code has been successfully used in the past to perform simulations of turbulent jets, it is essential to validate it for mixing layers with non-zero velocity ratios. To this end, simulations of a laminar mixing layer and incompressible turbulent mixing layers have been performed and the data is compared with the literature. These cases have been chosen for validation considering the fact that there is an abundance of data in the literature regarding these two types of flows that could serve as a benchmark for validation.

3.1 Laminar Mixing Layer : Case 1

One of the classical mixing layer problems for which one can obtain asymptotic solutions (self-similar solutions) is a laminar mixing layer. Hence it will be interesting to validate the code against the widely agreed upon self-similar solutions for a laminar mixing layer. A simulation of an incompressible laminar mixing layer with a velocity ratio of 0.5 and with uniform density and viscosity is performed for this purpose. The results are compared with the analytical solutions obtained by solving the self-similar equations (with BC's appropriate for a mixing layer), taking into consideration the displacement effects, following Casarella and Choo [58]. Details of the solution procedure are given in the appendix.

3.1.1 Simulation Details

The inflow streamwise (U) and cross-stream (v) velocity profiles are taken from an instance of the analytical self-similar solution at

$$\frac{U_1 x_{vo}}{\nu} \sim 100, \quad (3.1)$$

where x_{vo} refers to the distance from the virtual origin. These velocity profiles are shown in figures 3.11(a) and 3.11(b) respectively. The streamwise velocity ratio of the two streams is given by

$$\frac{U_2}{U_1} = 0.5. \quad (3.2)$$

Two types of mixing layer thickness definitions are used in this section, namely the shear layer thickness δ_b and the vorticity thickness δ_ω . The shear layer thickness δ_b is defined as the vertical distance between the locations where the non-dimensional streamwise velocity U^* is 0.1 and 0.9. This non-dimensional velocity is given by

$$U^* = \frac{U(y) - U_2}{U_1 - U_2}. \quad (3.3)$$

The vorticity thickness is defined as

$$\delta_\omega = \frac{\frac{dU}{dy} \max}{U_1 - U_2}. \quad (3.4)$$

The density is set to be uniform at the inflow. For this case, ρ , U_1 and shear layer thickness at the inflow (δ_{b0}) are taken as the reference variables. The reference temperature is taken as 286 K. The reference Mach number is $M_{ref} = 0.1$, which is small enough for the flow to be assumed incompressible. The reference Reynolds number is

$$Re_{ref} = \frac{\rho U_1 \delta_{b0}}{\mu} = 42. \quad (3.5)$$

It should be noted that the viscosity is set to a constant value everywhere in the flowfield for this case and Sutherland's law is not applied. This is done to achieve a very low Reynolds number, which is required for the flow to remain laminar. The

pressure at the inflow is set by numerically solving the incompressible y-momentum equations at the inflow, using the velocity profiles from the analytical solutions and using the values of viscosity and density given above. This is shown in figure 3.1(c). It can be seen that there is a pressure gradient across the mixing layer. This is because the analytical solutions for v exhibit a streamwise gradient even in the freestream, with the absolute value of v being inversely proportional to the square root of the distance from the virtual origin. Refer to the appendix for more details.

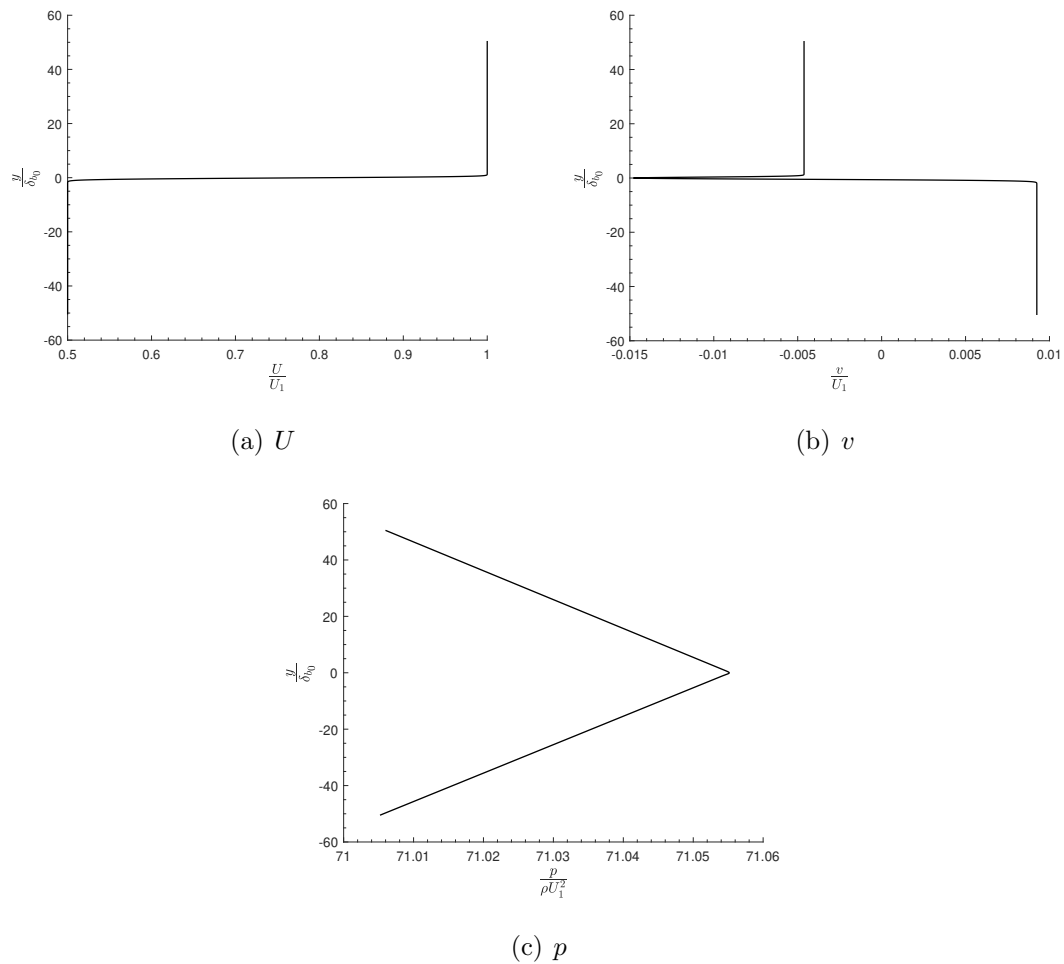


Figure 3.1. Laminar mixing layer : case 1 : inflow profiles.

The fluid domain used for this case is shown in figure 3.2. The total length in the streamwise direction is $300 \delta_{b0}$ with the physical domain extending from 0 to

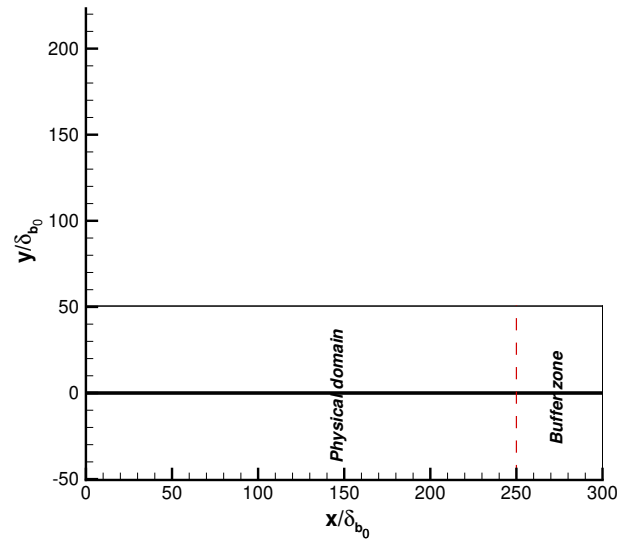


Figure 3.2. Laminar mixing fluid domain: case 1 : 2D view.

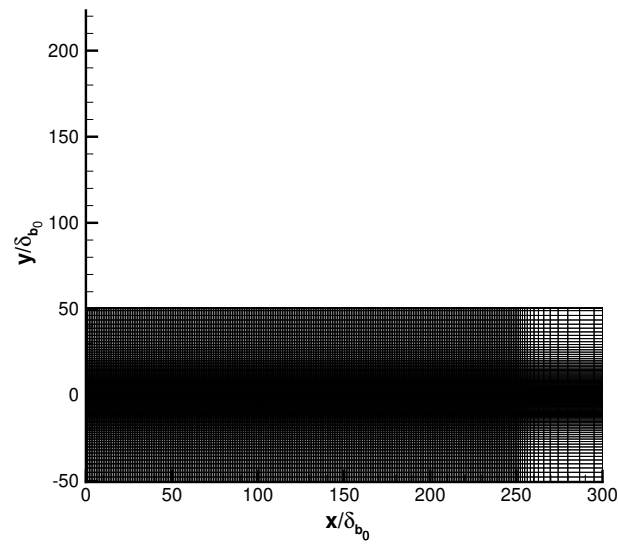


Figure 3.3. Laminar mixing layer : case 1 : grid distribution: showing every 4th grid point.

$250 \delta_{b_0}$ and a buffer zone is added at the end from $250 \delta_{b_0}$ to $300 \delta_{b_0}$. The buffer is added at the end to damp out any vortices (if present) before they reach the outflow boundary. This is done through extensive grid stretching in this region. In the cross-stream direction, the domain extends from $-50.5 \delta_{b_0}$ to $50.5 \delta_{b_0}$. Since the laminar mixing layer is nominally two-dimensional, a short domain length of $1 \delta_{b_0}$ is used in the spanwise direction.

A three superblock topology is used. The extents of and the number of grid points in each of the three superblocks are given in the table 3.1. The grid resolution details will be explained now. In the streamwise direction, a constant spacing of $\Delta x = 0.25 \delta_{b_0}$ is used throughout the physical domain. In the buffer zone, the grid is highly stretched, for the reasons mentioned earlier, with a maximum stretching ratio of $\sim 5\%$. In the cross-stream direction, the grid is symmetric about $y=0$ and is tailored to refine the regions of the shear layer (figure 3.3). The grid spacings in the upper half of the plane will be explained now. From $y=0$ to $1.5 \delta_{b_0}$, a constant spacing of $\Delta y = 0.05 \delta_{b_0}$ is used. The grid is then stretched smoothly from $\Delta y = 0.05 \delta_{b_0}$ at $y = 1.5 \delta_{b_0}$ to $\Delta y = 0.12 \delta_{b_0}$ at $y = 6.5 \delta_{b_0}$ with a maximum stretching ratio of $\sim 2\%$. Outside $y = 6.5 \delta_{b_0}$, the grid is smoothly stretched with a maximum stretching ratio of $\sim 1.7\%$. In the spanwise direction, a constant spacing of $\Delta z = 0.05 \delta_{b_0}$ is used. The boundary conditions on each of the six faces of the three superblocks are given in table 3.2. In the table 3.2, TD refers to ‘‘Tam and Dong’’. Additional simulation details are given in table 3.3. Since the flow is nominally laminar, our goal here is to obtain a steady-state solution. The total duration of the simulation is such that a particle in the low-speed stream will travel the fluid domain thrice during this time window. The statistics are collected during the final one-third of the simulation to ensure that the fluctuations are small enough to indicate a laminar flow field.

The initial conditions of the streamwise velocity U is taken as an hyperbolic tangent velocity profile given by

$$U = \frac{U_1 + U_2}{2} + \frac{U_1 - U_2}{2} \tanh \left(\frac{\sigma_0 y}{\lambda_s (x - x_0)} \right) \quad (3.6)$$

where

$$\lambda_s = \frac{(U_1 - U_2)}{(U_1 + U_2)} \quad (3.7)$$

The parameter σ_0 is taken as 11 and the value of x_0 is chosen such that the shear layer thickness at the location of the inflow matches δ_{b_0} . It should be noted that the above empirical relation for the velocity profile is for an incompressible turbulent mixing layer. The reason for the choice of the above over the solution for the laminar mixing layer as an initial condition is to allow for the simulation to go through a transient and reach the steady-state solution naturally, as using the latter may directly force the solution to reach the steady-state quickly. The other two velocity components are initialized to zero and the values of density and pressure are taken as uniform throughout the fluid domain. Next, the results of the simulation are discussed.

3.1.2 Results and Discussions

First, the results are analyzed to ensure that the solution has reached a steady state. The mixing layer velocity profiles are shown at two different locations plotted at three different times in figure 3.4. The velocity profiles match well at all the three times at both the locations, implying that the solution has reached a steady-state even around $T = 600 \frac{\delta_{b_0}}{U_1}$. To further ascertain this, the shear layer thickness (δ_b) of the mixing layer in the physical domain is plotted at these three different simulation times and is shown in figure 3.5. The profiles stack on top of each other, further bolstering that the solution has reached a steady state. Hence, the current simulation time of $1800 \frac{\delta_{b_0}}{U_1}$ is considered adequate for further analysis and comparisons of the results with the analytical solutions.

The collected statistics are now analyzed to ensure that the velocity fluctuations are negligible. The statistics are averaged both temporally and spatially in the span-wise direction. The contours of the non-dimensional velocity fluctuations in the physical domain are shown in 3.6. It can be seen from the contour values that the velocity fluctuations are extremely small with respect to the mean flow. The maximum

Table 3.1. Laminar mixing layer : case 1 : superblock extents and grid distribution (total number of grid points ~ 11 million)

Superblock #	Extents			Number of grid points		
	x	y	z	N_x	N_y	N_z
1	0 to $300 \delta_{b_0}$	$-50.50 \delta_{b_0}$ to $-0.50 \delta_{b_0}$	0 to $1 \delta_{b_0}$	1059	239	21
2	0 to $300 \delta_{b_0}$	$-0.45 \delta_{b_0}$ to $0.45 \delta_{b_0}$	0 to $1 \delta_{b_0}$	1059	19	21
3	0 to $300 \delta_{b_0}$	$-0.50 \delta_{b_0}$ to $50.50 \delta_{b_0}$	0 to $1 \delta_{b_0}$	1059	239	21

Table 3.2. Laminar mixing layer : case 1 : superblock boundary conditions

Superblock #	ξ_{min}	ξ_{max}	η_{min}	η_{max}	ζ_{min}	ζ_{max}
1	Inflow	TD Outflow	TD Radiation	Superblock 2	Periodic	Periodic
2	Inflow	TD Outflow	Superblock 1	Superblock 3	Periodic	Periodic
3	Inflow	TD Outflow	Superblock 2	TD Radiation	Periodic	Periodic

Table 3.3. Laminar mixing layer : case 1 : additional simulation settings

Parameter	Value
Timestep (Δt)	$4 \times 10^{-3} \frac{\delta_{b0}}{U_1}$
(CFL_x, CFL_y, CFL_z)	(0.18, 0.80, 0.80)
Initial Transients (T)	$1200 \frac{\delta_{b0}}{U_1}$
Statistics (T)	$600 \frac{\delta_{b0}}{U_1}$
# of CPU cores used	920
Cost (in core hours)	2687

streamwise velocity fluctuation is less than 0.0015 % of the reference velocity, with the other two fluctuating velocity components being smaller than this. Thus, the flow field is considered adequately laminar.

It is essential to plot the non-dimensional velocity U^* against the non-dimensional coordinate η to infer the self-similarity of the solution, where η is given by

$$\eta = \frac{y}{\sqrt{\frac{\nu x}{U_1}}}. \quad (3.8)$$

Here ν is the kinematic viscosity. This is done at various streamwise locations starting from the inflow till the end of the physical domain and is shown in figure 3.7 together with the analytical solution. It should be noted that the freestream velocity varies continuously throughout the physical domain. Hence at each streamwise location, the local freestream velocities close to the cross-stream boundaries are used when evaluating U^* . Only a small region close to the shear layer ($-10 \leq \eta \leq 10$) is shown in the figure. It can be seen from the figure that the profiles of the numerical solution stack on top of each other really well close to the center of the shear layer but slightly deviate from this self-similar behavior at the edges of the shear layer and in the free stream. Agreement with the analytical solution is also excellent near the center of the shear layer and the agreement deteriorates away from this region. This behavior follows from the shape of the velocity profile as shown in figure 3.4. The velocity profile has a slight velocity gradient in the cross-stream direction. This is because of the variation of pressure in the fluid domain, especially close to the inflow plane, as shown in figure 3.8. There is a step decrease of pressure near the center of the shear layer and the pressure increases close to the boundaries near the inflow plane which in turn becomes responsible for the cross-stream velocity gradient found in the freestreams of the two flows. Further downstream, the pressure becomes more uniform in the cross-stream direction and increases in the streamwise direction. The cross-stream gradient of the freestream velocity, however, still persists and it may take a much larger domain in the streamwise direction for the velocity to become uniform in the freestream. It should be noted that this cross-stream pressure gradient is not

just because of the way pressure is set at the inflow. Limited studies with having a uniform pressure at the inflow were found to have a cross-stream pressure gradient immediately downstream of the inflow as well.

The mixing layer thickness is plotted together with the analytical solution and is shown in figure 3.9. The maximum difference between the two solutions is expressed as a percentage error for each of the two types of thicknesses and is shown in table 3.4. It can be seen there is an excellent agreement with the vorticity thickness but the shear layer thickness is slightly off with respect to the analytical solution. This follows from the differences between the velocity profiles of the analytical and numerical solutions discussed earlier. The linear fit to the square of the mixing layer thicknesses (figure 3.10) gives a R^2 value of ~ 1 , agreeing with the widely accepted fact that the thickness of the laminar mixing layer is proportional to the square root of the distance from the virtual origin.

Table 3.4. Laminar mixing layer : case 1 : mixing layer thickness: error

Thickness type	Percentage error
δ_b	3.00 %
δ_ω	0.29 %

3.2 Laminar Mixing Layer : Case 2

As mentioned earlier, the analytical self-similar solution for the cross-stream velocity of a laminar mixing layer exhibits a streamwise gradient in the freestream which in turn results in a pressure gradient in the cross-stream direction. This velocity gradient (and hence the pressure gradient) however becomes negligible further downstream. This was also observed in the numerical results in the previous section, where the cross-stream pressure gradient in the freestream dropped with distance and became negligible far downstream. This streamwise variation, however, resulted in a

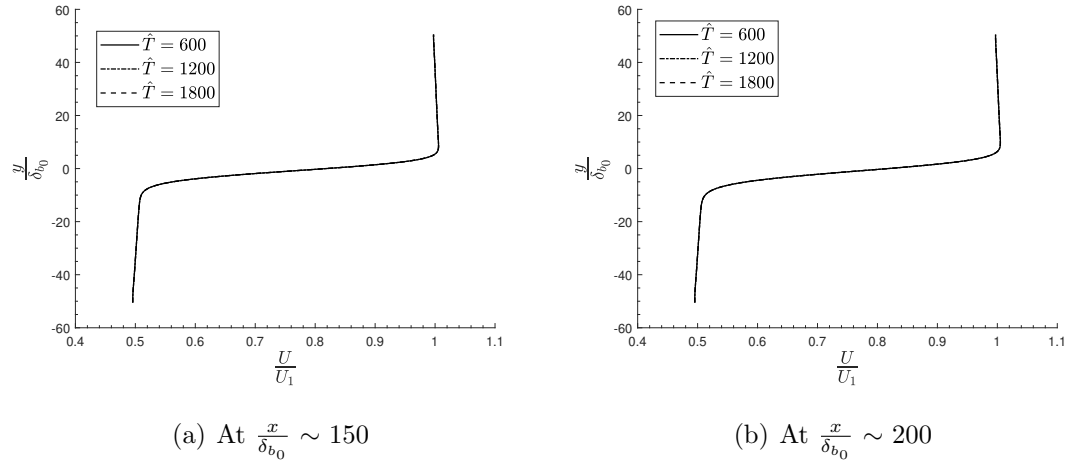


Figure 3.4. Laminar mixing layer : case 1 : velocity profiles. Here $\hat{T} = T \frac{U_1}{\delta_{b_0}}$.

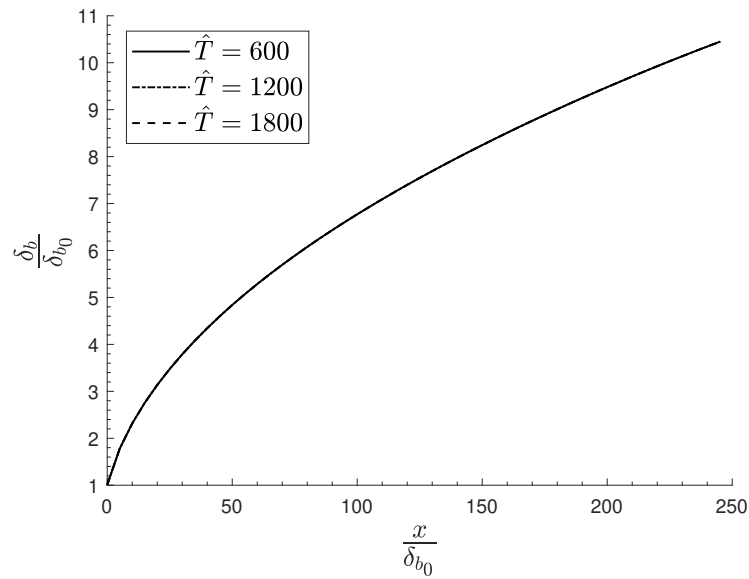


Figure 3.5. Laminar mixing layer : case 1 : shear layer thickness δ_b . Here $\hat{T} = T \frac{U_1}{\delta_{b_0}}$.

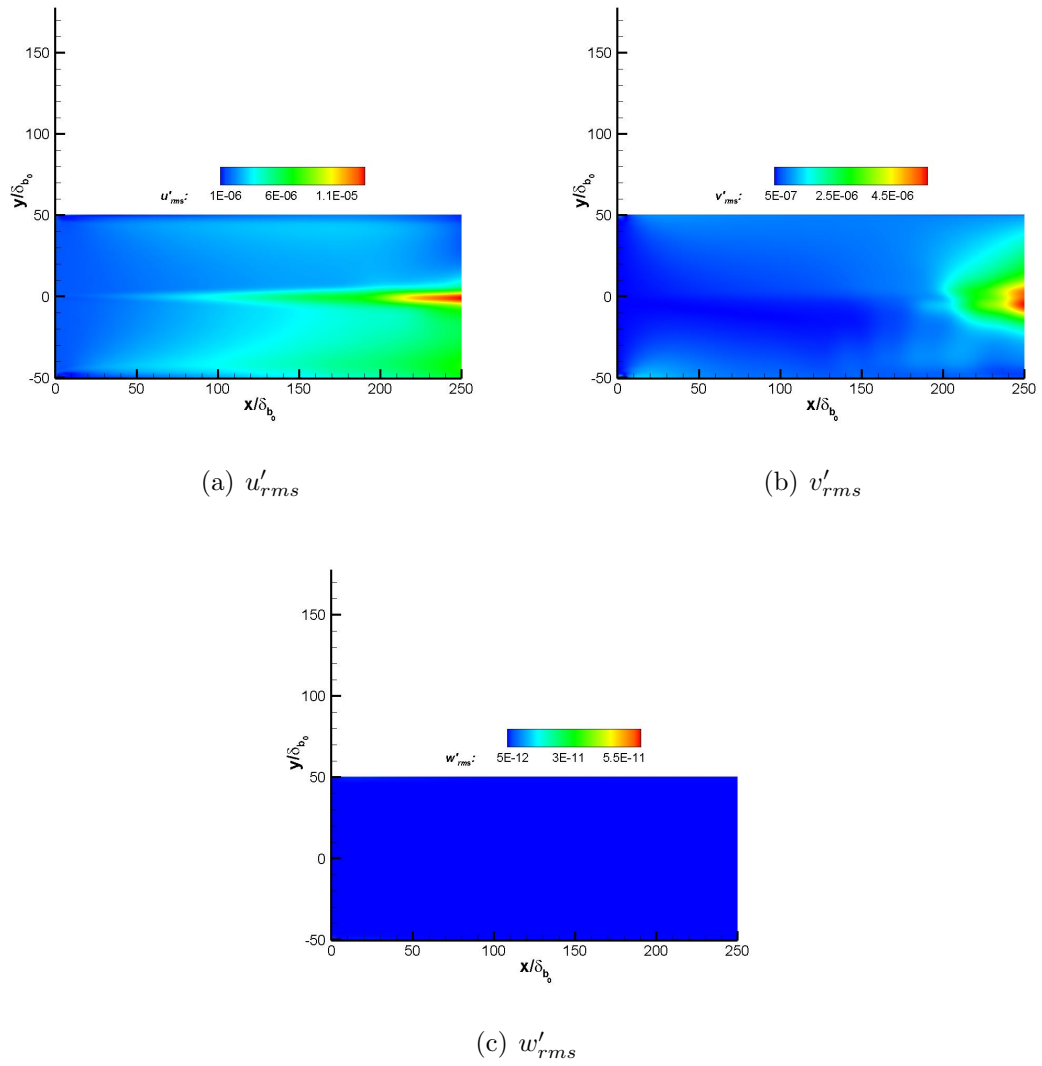


Figure 3.6. Laminar mixing layer : case 1 : contours of the mean of the velocity fluctuations.

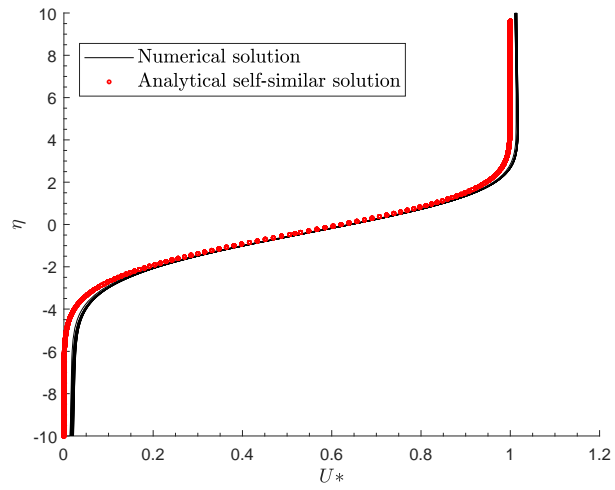


Figure 3.7. Laminar mixing layer : case 1 : self-similar velocity profile.

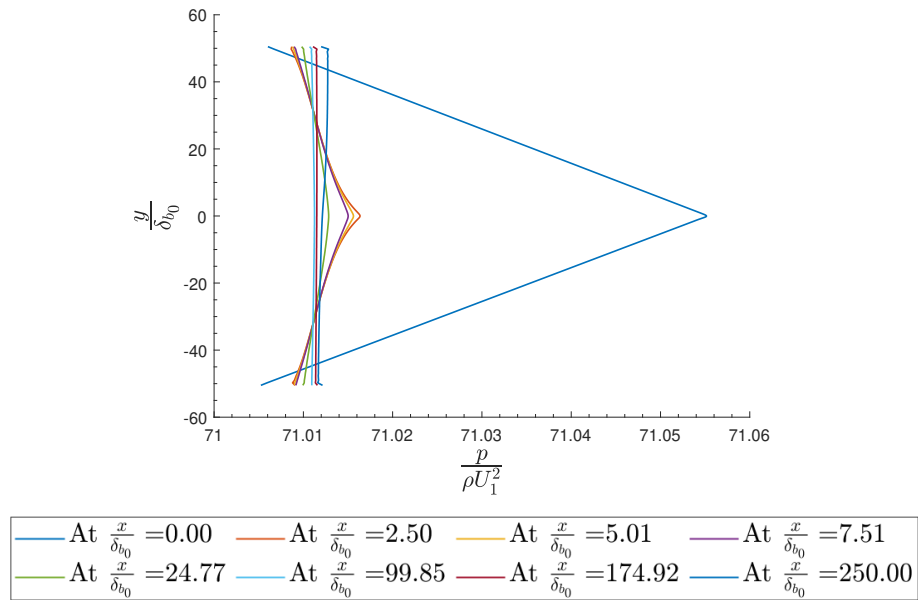


Figure 3.8. Laminar mixing layer : case 1 : static pressure variation.

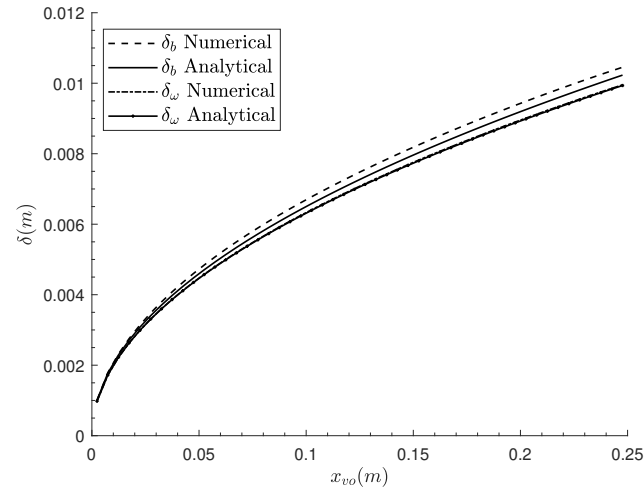


Figure 3.9. Laminar mixing layer : case 1 : mixing layer thickness: comparison with the analytical solution. ‘ x_{vo} ’ indicates that the solution is plotted with respect to the virtual origin.

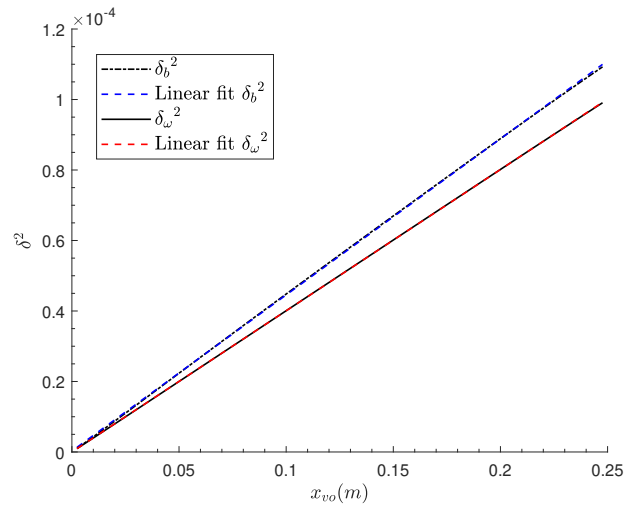


Figure 3.10. Laminar mixing layer : case 1 : linear fit to the square of the mixing layer thicknesses. ‘ x_{vo} ’ indicates that the solution is plotted with respect to the virtual origin.

strange velocity profile as discussed earlier. Hence to avoid this, it will be interesting to start the numerical simulation with the inflow profiles taken from a downstream instance of the analytical solution where the pressure gradient in the cross-stream direction is negligible. This is performed in the current section and is referred to as case 2 of the laminar mixing layer simulations.

3.2.1 Simulation Details

The inflow velocity profiles for the current simulation are shown in figure 3.11. Uniform pressure is set at the inflow, since the pressure variation obtained by numerically solving the incompressible y-momentum equations was negligible. The shear layer thickness at the inflow is approximately 6.5 times the shear layer thickness at the inflow in the previous simulation. All other quantities, including the reference variables and the associated values, are the same as in the previous case. Since the reference length scale in the previous section was the shear layer thickness at the inflow and the same value for the reference length scale (i.e reference length scale is not the shear layer thickness at the inflow for the current simulation) is used in the current simulation, the reference length scale will be referred as l_{ref} to avoid any confusion.

A shorter domain is used in the streamwise direction compared to the previous case. The physical domain extends from 0 to $150 l_{ref}$ followed by a buffer region of length $50 l_{ref}$. The cross-stream and spanwise domain dimensions are the same as the previous case. The grid spacings in all the three directions in the physical and buffer zone are identical to the previous simulation. This implies that the total number of grid points in the streamwise direction is reduced to 659, since the domain here is shorter along this direction compared to the previous simulation. The superblock topology and the boundary conditions are the same as the previous case. The total simulation time is $1200 \frac{l_{ref}}{U_1}$ to reach the steady-state with the statistics being collected for the last $400 \frac{l_{ref}}{U_1}$. This is based on the observations made in the previous section.

The remaining simulation settings were the same as in the previous case. The flow is initialized in a similar way as the previous case. Next, the results of the simulation are discussed.

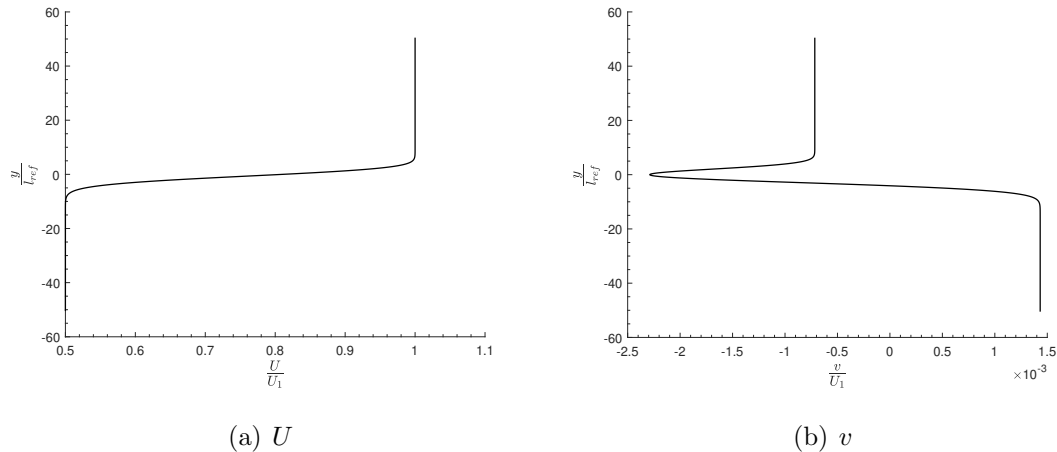


Figure 3.11. Laminar mixing layer : case 2 : inflow profiles.

3.2.2 Results and Discussion

The collected statistics are averaged temporally and spatially in the spanwise direction as before and the contours of the root mean square of the fluctuating velocity components (non-dimensionalized) in the physical domain are shown in the figure 3.12. As before, the fluctuations are very small compared to the mean and hence the flow field could be considered laminar.

The non-dimensional velocity U^* together with the analytical self-similar solution at various streamwise locations (starting from the inflow) as before, are shown in the figure 3.13. The profiles exactly stack on top of each other indicating self-similarity and the self-similar solution matches well with the analytical result. Figure 3.14 shows the two types of mixing layer thicknesses plotted together with its analytical counterpart. The current results match extremely well with the analytical solution. The maximum percentage error in the numerical solution is shown in table 3.5. The

variation of static pressure in the physical domain is shown in figure 3.15. It could be observed that the variation of pressure along the cross-stream direction close to the inflow is minimised compared to the previous case, as expected. This in turn is attributed to the excellent agreement between the numerical and analytical solutions of the velocity profiles. The pressure, however, sharply increases in the streamwise direction close to the inflow. This is because the specified pressure at the inflow may not be the actual pressure obtained from numerically solving the governing equations. Specifying the exact pressure at the inflow, however, is difficult.

Thus, starting with an inflow profile that is taken from a downstream instance of the analytical solution is found to result in excellent agreement of the numerical solution with analytical self-similar profile and mixing layer thicknesses, for the reasons mentioned above. The validation of the solver with a laminar mixing layer is now considered complete.

Table 3.5. Laminar mixing layer : case 2 : mixing layer thickness: error computed against the analytical result

Thickness type	Percentage error
δ_b	0.11 %
δ_ω	0.07 %

3.3 LES of an Incompressible Turbulent Mixing Layer

Incompressible turbulent mixing layers have been studied for many decades both computationally and experimentally. Many characteristics of incompressible turbulent mixing layers are well established. It is therefore important to validate the solver against the data in the literature for an incompressible turbulent mixing layer. The flow conditions chosen here are that of Attili and Bisetti [33], which is a DNS of a spatially developing mixing layer at a velocity ratio of 1/3 and at a Reynolds number

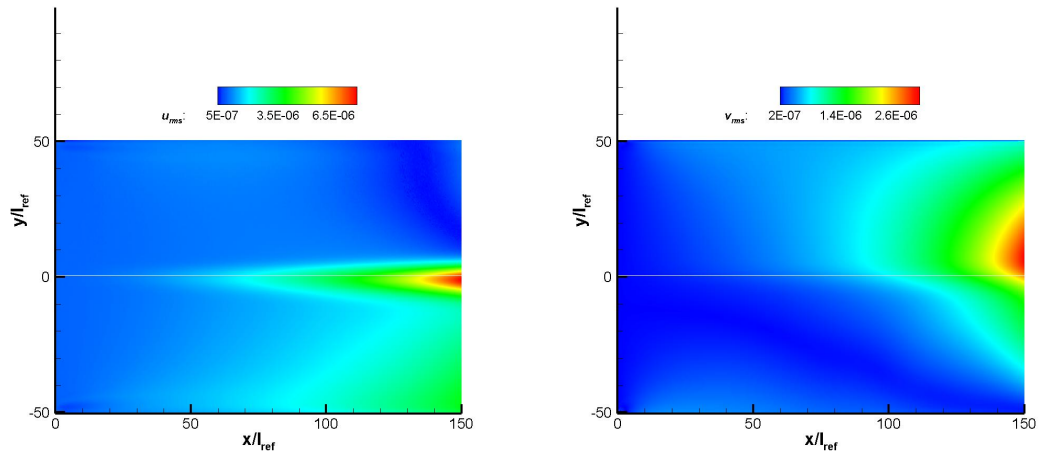
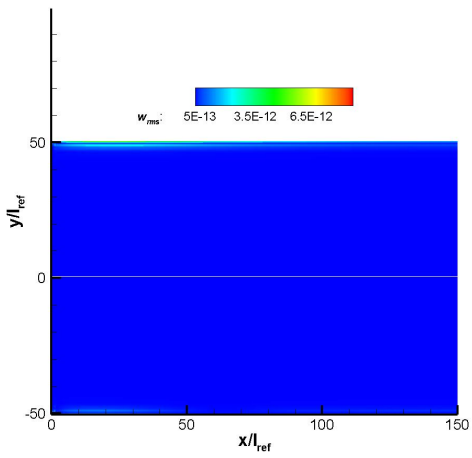
(a) u'_{rms} (b) v'_{rms} (c) w'_{rms}

Figure 3.12. Laminar mixing layer : case 2 : contours of the mean of the velocity fluctuations.

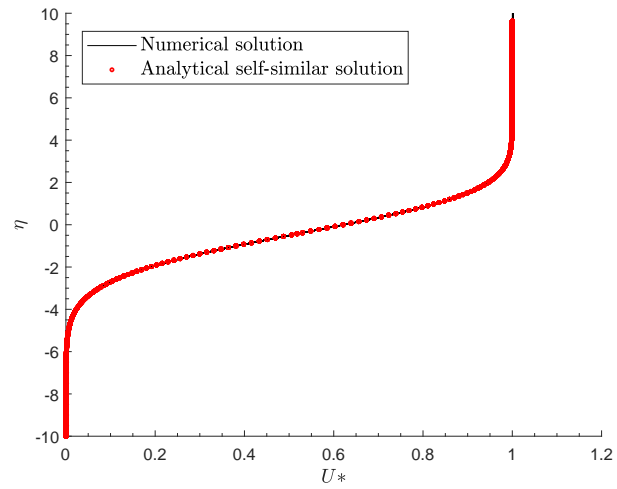


Figure 3.13. Laminar mixing layer : case 2 : self-similar velocity profile.

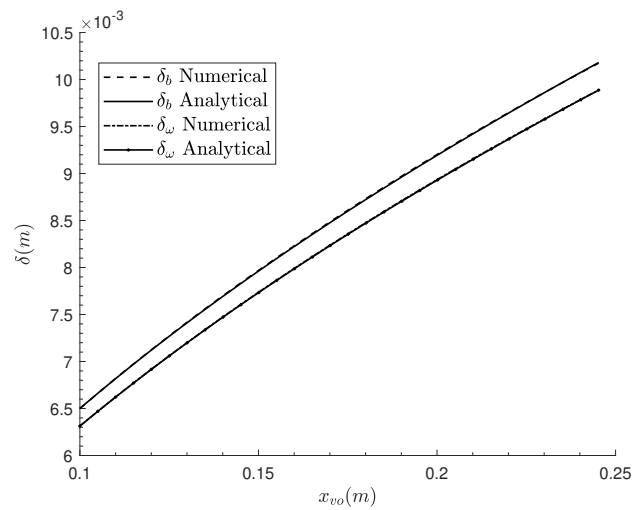


Figure 3.14. Laminar mixing layer : case 2 : mixing layer thickness.

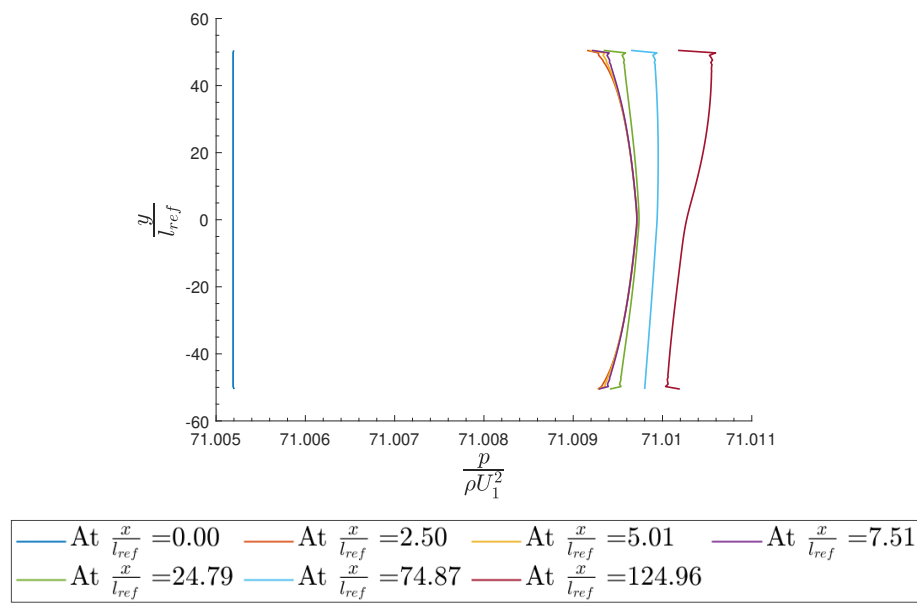


Figure 3.15. Laminar mixing layer : case 2 : static pressure variation.

based on initial vorticity thickness of 600. Three different cases with the above flow conditions have been performed as below

- Case 1: white noise inflow with Tam and Dong outflow boundary condition
- Case 2: white noise inflow with subsonic characteristic outflow boundary condition
- Case 3: correlated inflow with subsonic characteristic outflow boundary condition

Identical grid distributions and domain sizes have been used for all the three cases. The simulation details are given next followed by results compared against the reference simulation and data in the literature.

3.3.1 Simulation Details

As mentioned before, the flow conditions are taken from Attili and Bisetti [33] and are given as follows. The mean streamwise velocity profile at the inflow is a hyperbolic tangent given by

$$U = \frac{U_1 + U_2}{2} + \frac{U_1 - U_2}{2} \tanh\left(\frac{2y}{\delta_{\omega_0}}\right), \quad (3.9)$$

where δ_{ω_0} is the mixing layer vorticity thickness at the inflow and is chosen as the reference length scale. U_1 and U_2 are the velocity of the primary and secondary streams respectively, with the velocity ratio $\frac{U_2}{U_1}$ being 1/3. The other two components of the mean velocity are set to 0 at the inflow. The $\Delta U = U_1 - U_2$ is chosen as the reference velocity and the reference temperature is taken as 286 K. The reference Mach number, M_{ref} is 0.13 which is small enough for the flow to be considered incompressible. Mean density and pressure are set to be uniform at the inflow. The reference Reynolds number is

$$Re_{ref} = Re_{\delta_{\omega_0}} = 600. \quad (3.10)$$

The fluid domain used in the study is shown in figure 3.16. A single superblock topology is used. In the streamwise direction, the domain extends from $x = 0$ to $474 \delta_{\omega_0}$ followed by a short buffer region of length $100 \delta_{\omega_0}$. In the buffer zone, the grid is extensively stretched to damp out the strong vortices from reaching the outflow plane. In the cross-stream direction, the domain extends from $y = -145 \delta_{\omega_0}$ to $145 \delta_{\omega_0}$. The length of the physical domain in the streamwise and cross-stream directions are similar to the one used in the reference simulation ($473 \delta_{\omega_0} \times 290 \delta_{\omega_0}$). In the spanwise direction, however, a shorter domain length (compared to the reference simulation) of $102 \delta_{\omega_0}$ is used to reduce the simulation costs. The domain length in the spanwise direction is chosen based on the recommendations in the literature [30]. The criteria used is that the spanwise width of the physical domain used in the simulations should be at least 10 times the maximum value of the mixing layer momentum thickness (δ_θ) observed in the physical domain [30]. This maximum δ_θ is taken from the reference simulation (as its value in the present case is unknown prior to running the simulation) and a conservative length of ~ 14 times this value is used as the spanwise width.

The grid distribution showing every 4th grid point is shown in the figure 3.17. The grid spacings chosen here are about 4 times coarser in every direction (except the cross-stream grid spacings near $y=0$) compared to the reference DNS, as the goal here is to perform an LES. The factor of 4 is chosen because the reference simulation mentions precursor LES simulations of this resolution having been performed to decide the domain dimensions for their DNS. Now the grid resolution details are explained. In the streamwise direction, a constant spacing of $\Delta x = 0.6 \delta_{\omega_0}$ is used in the physical domain. The grid is highly stretched in the buffer zone with a maximum stretching ratio of $\sim 4.9 \%$. In the spanwise direction a constant spacing of $\Delta z = 0.6 \delta_{\omega_0}$ is used. The cross-stream grid spacings are symmetric about $y=0$ and are tailored to refine the regions of the shear layer ($-45 \delta_{\omega_0} \leq y \leq 45 \delta_{\omega_0}$, following the reference simulation). From $y=0$ to $4 \delta_{\omega_0}$, the grid is smoothly stretched from $\Delta y = 0.15 \delta_{\omega_0}$ to $\sim 0.16 \delta_{\omega_0}$. It should be noted that the grid spacings in this region are comparable to the grid spacings in the reference DNS. This is done to highly resolve the initial shear

layer and the portion of the inflow profile where the fluctuations are applied (more on this later). From $y = 4 \delta_{\omega_0}$ to $45 \delta_{\omega_0}$, the grid is smoothly stretched from $\Delta y = 0.16 \delta_{\omega_0}$ to $0.6 \delta_{\omega_0}$ with a maximum stretching ratio of 1.3 %. Outside these regions, the grid is stretched smoothly to the cross-stream boundaries with a maximum stretching ratio of ~ 2.9 %. The the total number of grid points used is $N_x \times N_y \times N_z = 849 \times 449 \times 171 \sim 65$ million.

The digital filter based turbulent inflow boundary condition is used at the inflow to add fluctuating velocity components to the mean laminar inflow to allow for a quicker transition to turbulence. These fluctuations are imposed only between the cross-stream regions of $-4 \leq \frac{y}{\delta_{\omega_0}} \leq 4$, following the reference DNS. The profiles of the Reynolds stresses are to required to be specified at the inflow for this boundary condition. The profiles of the normal Reynolds stresses imposed at the inflow are the self-similar Reynolds stress profiles taken from the reference simulation and scaled to result in a maximum turbulent kinetic energy of $\frac{k}{\Delta U^2} = 2 \times 10^{-6}$. This peak value of the T.K.E at the inflow is in accordance with the reference simulation. Since the profiles of the primary Reynolds shear stress is not available from the reference simulation, following Rogers [59], at the inflow, it is set as

$$Re_{uv} = -0.30k. \quad (3.11)$$

It should be noted that the fluctuations imposed at the inflow are not correlated in the inflow plane for cases 1 and 2 and are referred to as white noises. The streamwise length scale is set to be the local grid spacing for these cases. A correlated inflow, however, is used for case 3 to determine the effects of such an inflow. The integral length scales in each of the three directions at the inflow for this case are chosen based on the experimental results of Jones et al. [23]. Based on the current inflow method [39], the value of the two-point correlation at the integral length scale is 0.2078. Using this information, the required integral length scale is extracted from the figures of spatial two-point correlations presented by Jones [23] for a mixing layer with a velocity ratio of 0.3. These integral length scales are found to be $(ILS_x, ILS_y, ILS_z) \sim (0.74, 0.42, 0.20) \delta_{\omega_0}$. It should be noted that these values are taken at the centerline

of the mixing layer. In the current inflow method, the integral length scales in the y and z directions are imposed in terms of the grid intervals. Hence with the present grid distribution, it will not be possible to impose the obtained length scales exactly especially in the z -direction. However, it should be noted that the length scales are only imposed approximately in the current inflow method [39]. Hence the ILS_x is taken as 0.8 and the number of grid intervals is taken as 2 for ILS_y and ILS_z . The Tam and Dong outflow boundary condition is used in case 1 whereas the subsonic characteristic outflow condition is used for the other two cases. The Tam and Dong radiation boundary condition is used at the cross-stream boundaries for all the three cases. Periodic boundary condition is used in the spanwise direction.

The streamwise velocity is initialized with a hyperbolic tangent velocity profile as in equation 3.6 and the other two velocity components are initialized to zero. The pressure and density are set to be uniform throughout the fluid domain.

The timestep Δt chosen here is $1.63 \times 10^{-2} \frac{\delta_{\omega_0}}{\Delta U}$ for all the three cases discussed here. The maximum CFL number in x, y and z directions are $\sim (0.25, 0.90, 0.23)$ respectively. The concept of a Flow Through Cycle (FTC) is used as a measure of simulation time in the present case. 1 FTC is defined as the time a particle in the low-speed stream takes to traverse the entire fluid domain and it roughly corresponds to $\sim 70,000$ timesteps. In all of the present cases, the initial conditions are flushed out during the 1st FTC and the statistics are collected thereafter. The statistics are collected every time step. The results of the simulations are discussed next.

3.3.2 Results and Discussion

Effect of statistical sample size

It is important to ensure that the collected statistics have converged to make comparisons with the reference DNS. For this purpose, the collected samples are averaged both temporally and spatially in the spanwise direction for three different averaging sample sizes, namely 6, 8 and 10 FTCs and have been analyzed for statistical

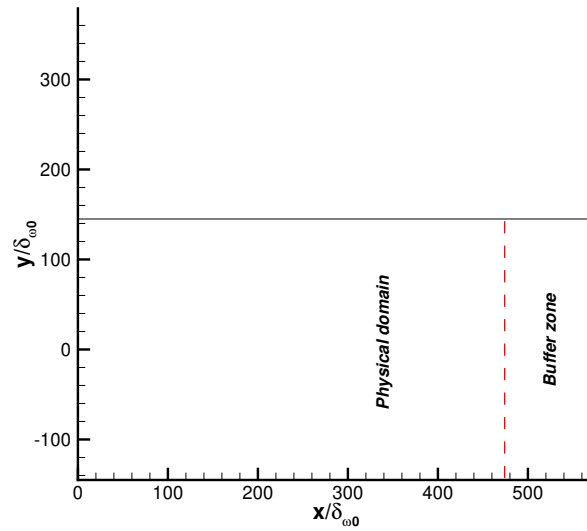


Figure 3.16. Incompressible turbulent mixing layer : fluid domain: 2D view.

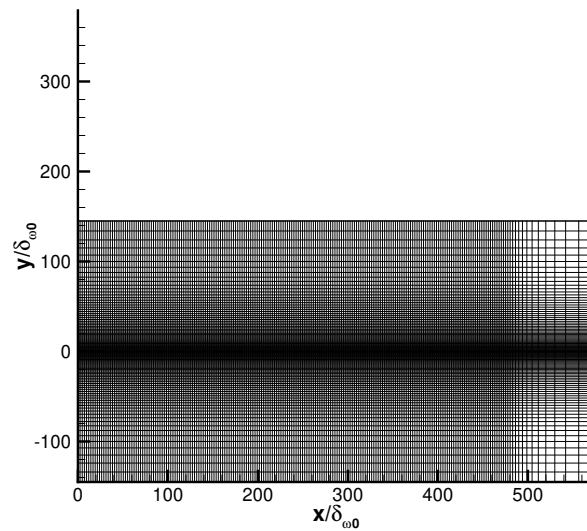


Figure 3.17. Incompressible turbulent mixing layer : grid distribution : showing every 4th grid point.

convergence. This study is performed for case 2 of the incompressible turbulent mixing layer simulations. The inference from this study is then used to decide the simulation times for the other two cases.

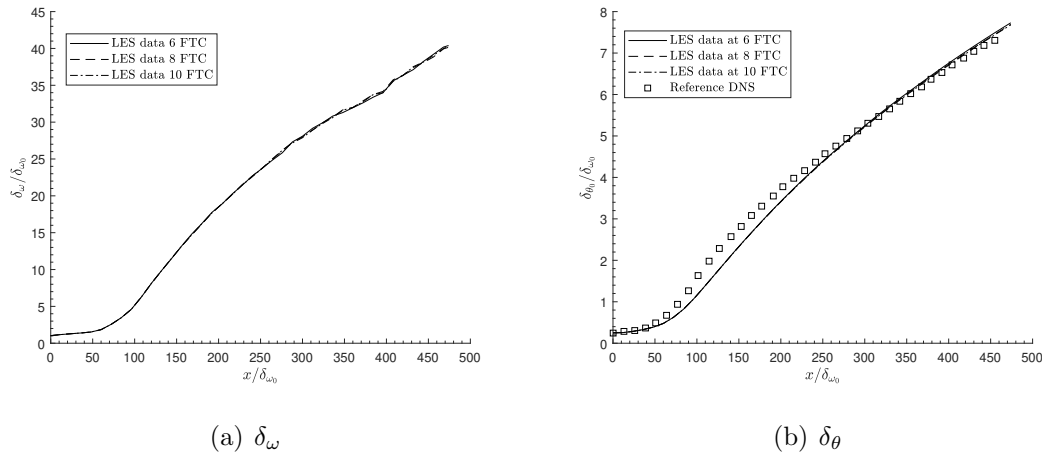


Figure 3.18. Incompressible turbulent mixing layer : case 2 : vorticity and momentum thickness for three different sample sizes.

From the figure 3.18 it could be seen that mixing layer thicknesses that have been measured at the three averaging periods are very similar, especially the thicknesses measured from the last two sample sizes are almost indistinguishable. This indicates that the first-order statistics are well converged at 8 FTC of statistics collection. In order to ensure that the second-order statistics are also statistically stationary with this averaging window, the Reynolds normal and primary shear stresses are plotted with respect to the non-dimensionalized cross-stream coordinate $\frac{y}{\delta_\theta} = y^+$ at two different locations, one at the beginning of the self-similar zone (more on this later) and one close to the end of the fluid domain. This is shown in the figures 3.19 and 3.20. The Reynolds stresses measured at $\frac{x}{\delta_{\omega_0}} = 300$ is well converged for all the three sample sizes under consideration. Observing the peak value of the Reynolds stresses at $\frac{x}{\delta_{\omega_0}} = 456$ (close to the end of the physical zone) seems to indicate that Reynolds stresses are well converged for the last two averaging periods at this location. This is reasonable since the statistics of the turbulent flow field towards the end of

the domain take a longer time to converge as the size of the large scale turbulent structures become bigger. Thus it follows to have the statistics collection period be 8 FTC to result in statistically stationary results. This is followed for the other two cases i.e case 1 and case 3. All subsequent turbulent statistics that are discussed are obtained from this chosen sample size. Also, unless otherwise specified, the samples collected are both temporally and spatially averaged (in the spanwise direction) when presenting the appropriate results of the mean turbulent quantities.

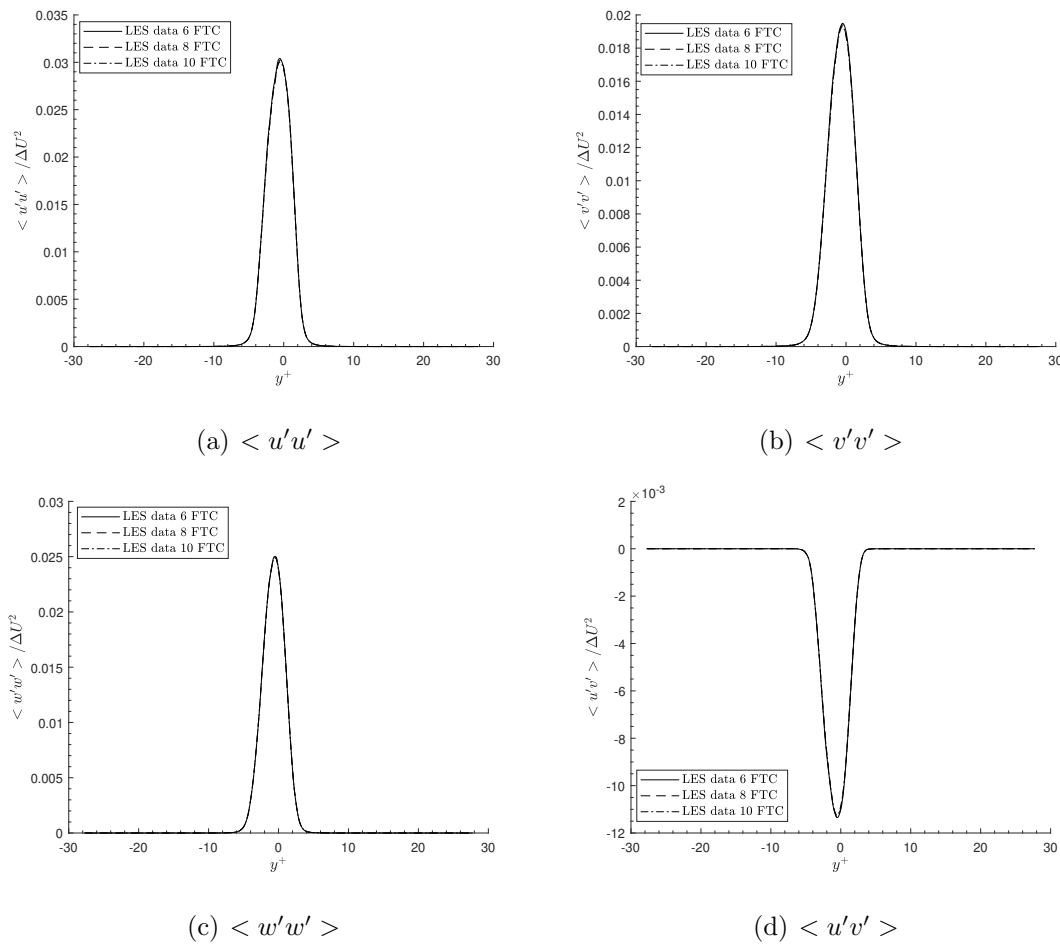


Figure 3.19. Incompressible turbulent mixing layer : case 2 : Reynolds stresses at $\frac{x}{\delta_{\omega_0}} = 300$ at 6,8,10 FTC's of statistics collection.

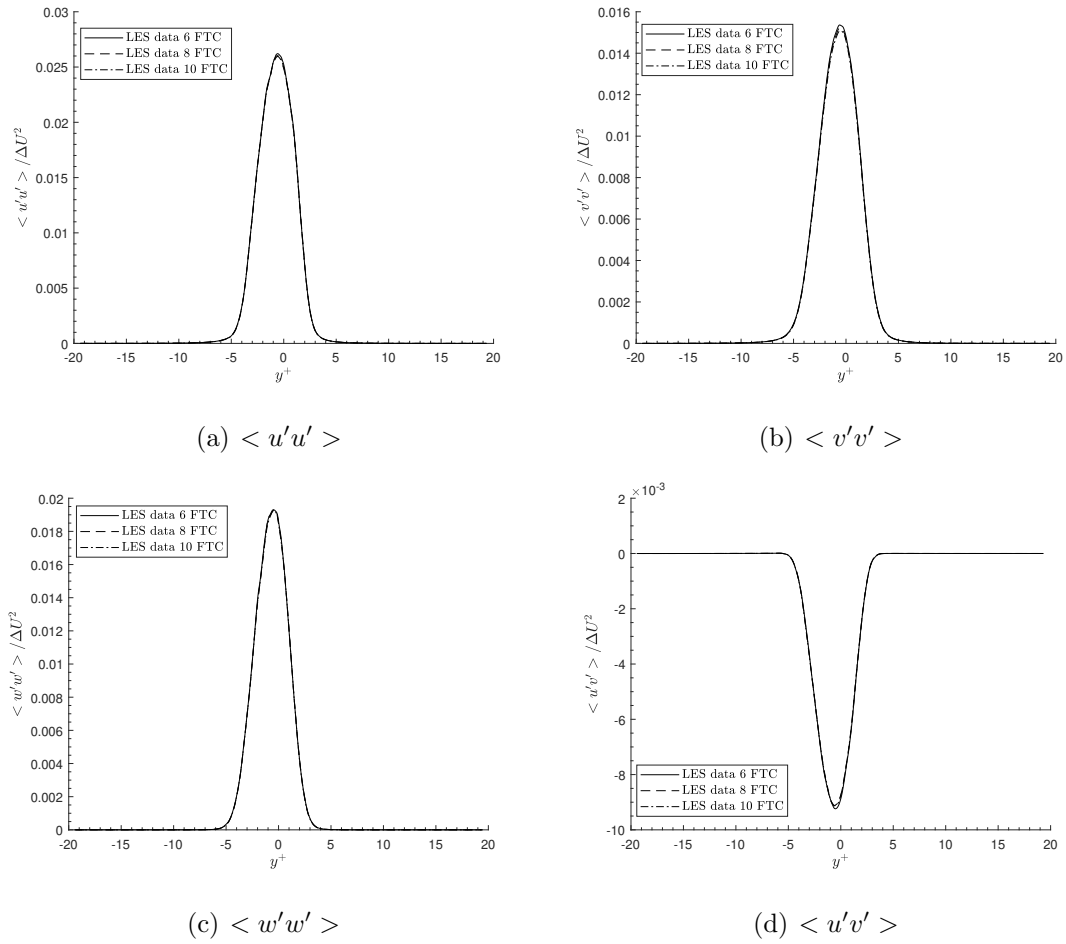


Figure 3.20. Incompressible turbulent mixing layer : case 2 : Reynolds stresses at $\frac{x}{\delta_{\omega_0}} = 456$ at 6,8,10 FTC's of statistics collection.

Case 2 : results and comparison with the reference DNS

In this part, the results of the case 2 simulation is compared against the reference DNS. A turbulent mixing layer develops self-similarity in the mean velocity profile and Reynolds stresses after a short distance downstream from the inlet, when scaled by the appropriate velocity and length scales. The velocity and length scales are chosen to be the same as the reference DNS [33] for direct comparison and are the velocity difference across the mixing layer and the mixing layer momentum thickness.

The streamwise variation of the mixing layer momentum thickness is shown in figure 3.21 and is compared against the reference DNS. The mixing layer evolving from laminar inflow conditions exhibits an initial exponential growth [33] due to the pairing of the vortices that result from the KH instability which then breaks down to fully developed turbulence. Further downstream, the mixing layer develops self-similarity in the mean streamwise velocity that is characterized by a linear growth of the mixing layer. In the present case, this self-similar zone is observed to start from $\frac{x}{\delta_{\omega_0}} = 300$ which is in agreement with the reference DNS. Overall, a good agreement with the reference DNS is observed for the mixing layer thickness, especially in the fully developed zone. The mixing layer thickness in the pairing region is found to be slightly underpredicted. A linear fit to the mixing layer thickness between $\frac{x}{\delta_{\omega_0}} = 300$ and $\frac{x}{\delta_{\omega_0}} = 400$ gives a value of the growth rate $\frac{d\delta_{\theta}}{dx} = 0.01488$ while a similar fit to the reference DNS gives a value of $\frac{d\delta_{\theta}}{dx} = 0.01404$, which is reasonably close. The reference DNS, however, reports a value of $\frac{d\delta_{\theta}}{dx} = 0.0168$ using a linear fit within the region mentioned before. The reason for this discrepancy is unknown.

The non-dimensionalized mean velocity profile is plotted against the non-dimensional cross-stream coordinate for downstream locations $\frac{x}{\delta_{\omega_0}} > 300$ and is shown in the figure 3.22. The profiles exactly stack on top of each other further bolstering that self-similarity is achieved in the mean streamwise velocity. Furthermore, excellent agreement with the reference DNS is achieved. The mixing layer vorticity thickness is shown in figure 3.23. The vorticity thickness shows some slight wiggles in the self-

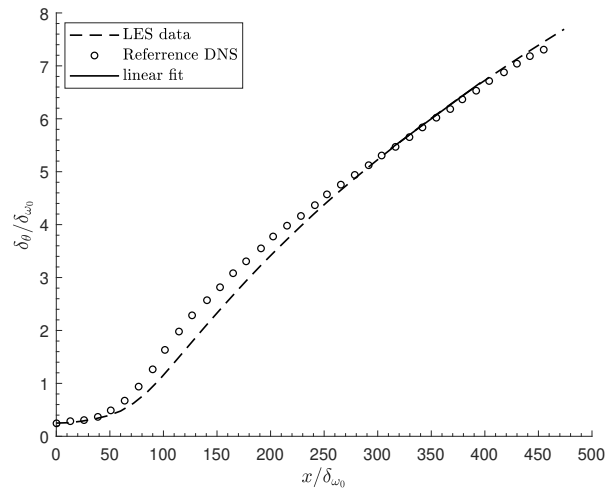


Figure 3.21. Incompressible turbulent mixing layer : case 2 : momentum thickness δ_θ .

similar region. This is because the vorticity thickness is more sensitive to statistical noise as it is obtained from the derivative of mean velocity [60] and may take much longer averaging periods to smooth out. The vorticity thickness growth rate is obtained using a linear fit to the vorticity thickness in the self-similar region ($\frac{x}{\delta_{\omega_0}} > 300$). This is compared with the relation for vorticity growth rate of an incompressible turbulent mixing layer [3,25] obtained using the best fit to the scatter of experimental data, given by

$$\frac{d\delta_{\omega}}{dx} = C_{\omega} \frac{U_1 - U_2}{U_1 + U_2}, \quad (3.12)$$

where $C_{\omega}=0.16$. It could be seen from table 3.6 that the current results seem to underpredict the growth rate. This will be discussed in detail later.

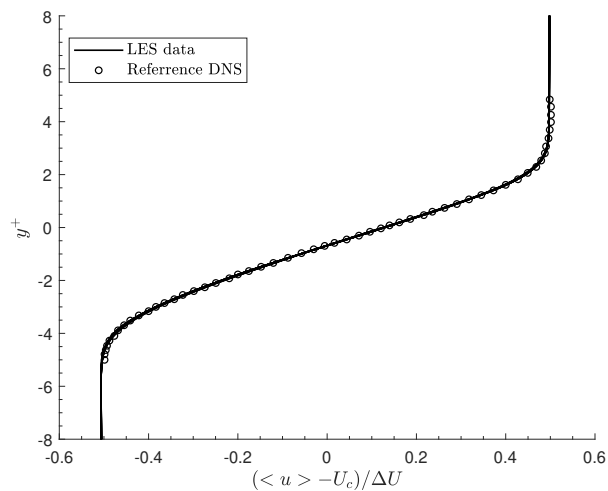


Figure 3.22. Incompressible turbulent mixing layer : case 2 : self-similar profile. $U_c = \frac{U_1+U_2}{2}$.

Table 3.6. Incompressible turbulent mixing layer : case 2 : $\frac{d\delta_{\omega}}{dx}$ comparison

Case	$\frac{d\delta_{\omega}}{dx}$
Current results	0.0695
Experimental fit	0.0800

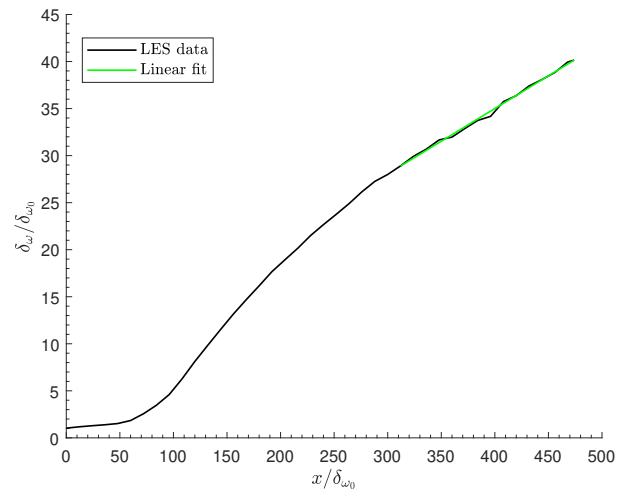


Figure 3.23. Incompressible turbulent mixing layer : case 2 : vorticity thickness δ_{ω} .

The integral normalized crosswise component of the turbulent kinetic energy defined as [33]

$$\nu(x) = \frac{1}{\Delta U^2 \delta_\theta} \int_{-\infty}^{\infty} \langle v'v' \rangle dy , \quad (3.13)$$

is plotted against the reference DNS and is shown in the figure 3.24. The trend is in good agreement with the DNS. The large overshoot that occurs because of the pairing of the vortices that result from KH instability is found to be slightly overpredicted and is found to occur slightly downstream than that compared to the reference DNS. These differences could be because of the differences in the inflow method (for seeding the random white noise fluctuations) used between the current work and the reference DNS. The decay towards an asymptotic value in the self-similar region is clearly observed in the latter whereas in the current case it is observed to reach the asymptotic value very close to the end of the physical domain, which could be a consequence of the overprediction of the overshoot and its downstream location compared to the reference DNS. This asymptotic value is also slightly underpredicted compared to the reference DNS.

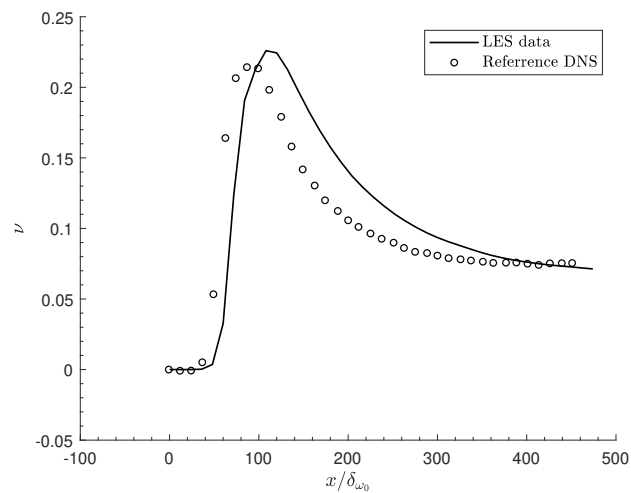


Figure 3.24. Incompressible turbulent mixing layer : case 2 : integral normalized crosswise component of the turbulent kinetic energy.

The Reynolds stresses are shown in the figure 3.25. The self-similarity of the Reynolds stresses could be observed towards the end of the physical domain. This indicates that the Reynolds stresses attain self-similarity much farther downstream than the mean velocity, an observation that is made in the reference DNS as well. The normal Reynolds stresses at a specific location is compared against the reference DNS and is shown in the figure 3.26 (no data for the primary Reynolds shear stress $\langle u'v' \rangle$ is available from the reference simulation). This location is chosen as it was the farthest location for which data was available in the reference DNS, as the motivation is to compare the Reynolds stresses in the self-similar region. Overall, excellent agreement with the reference DNS is observed for the Reynolds stresses, though a slight underprediction is observed in the peak values of the streamwise Reynolds stress whereas the peak cross-stream Reynolds stress is slightly overpredicted.

The contours of instantaneous non-dimensionalized vorticity magnitude (non-dimensionalized by the reference velocity and length scales) is shown in the figure 3.27. It should be noted that only a smaller cross-stream extent of the fluid domain is shown for brevity. Small scales of motion, characteristic of a turbulent flow field, could be seen in the self-similar region bolstering the fact that transition to turbulence has occurred in the fluid domain starting from a laminar inflow. The flow evolution close to the inflow could be observed from the contours shown in figure 3.28. The roll-up of the initial vortex sheet due to the KH instability could be observed around $\frac{x}{\delta_{\omega_0}} = 60$ leading to the formation of coherent vortices downstream. These vortices pair-up leading to the formation of larger vortices. This could be seen around $\frac{x}{\delta_{\omega_0}} = 95$, where two rolled-up vortices interact between them, with an apparent increase in vorticity magnitude, and merge shortly downstream of $\frac{x}{\delta_{\omega_0}} = 100$. It is well known from literature [2,26] that transition to fine-scale turbulence occurs when these paired up vortices undergo a second set of pairing. This could be observed in the present case as well, where the interaction between these paired up vortices coincides with the formation of fine scales of turbulence around $\frac{x}{\delta_{\omega_0}} = 150$. This is evident by the change in vorticity magnitude from being concentrated in laminar cores to being more uni-

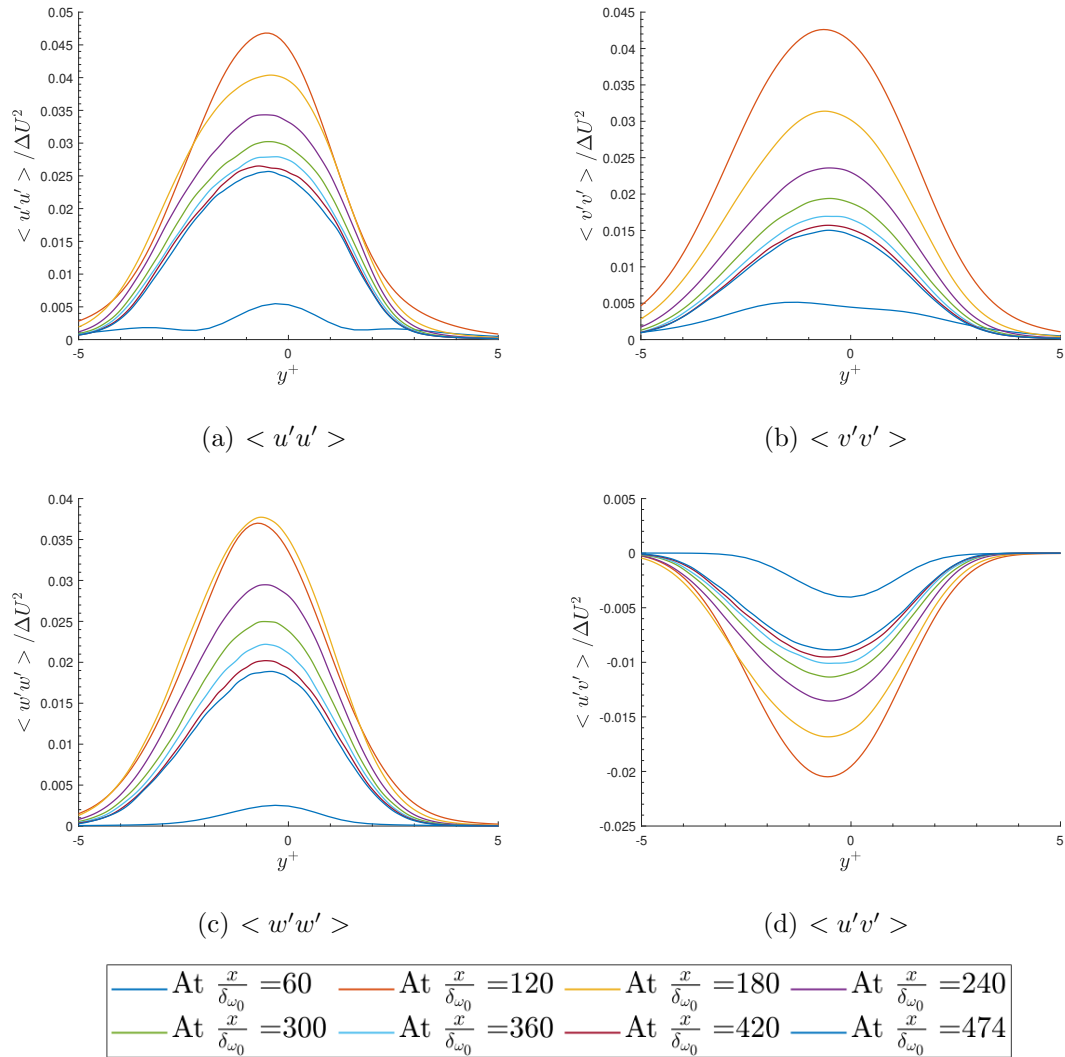


Figure 3.25. Incompressible turbulent mixing layer : case 2 : Reynolds stresses.

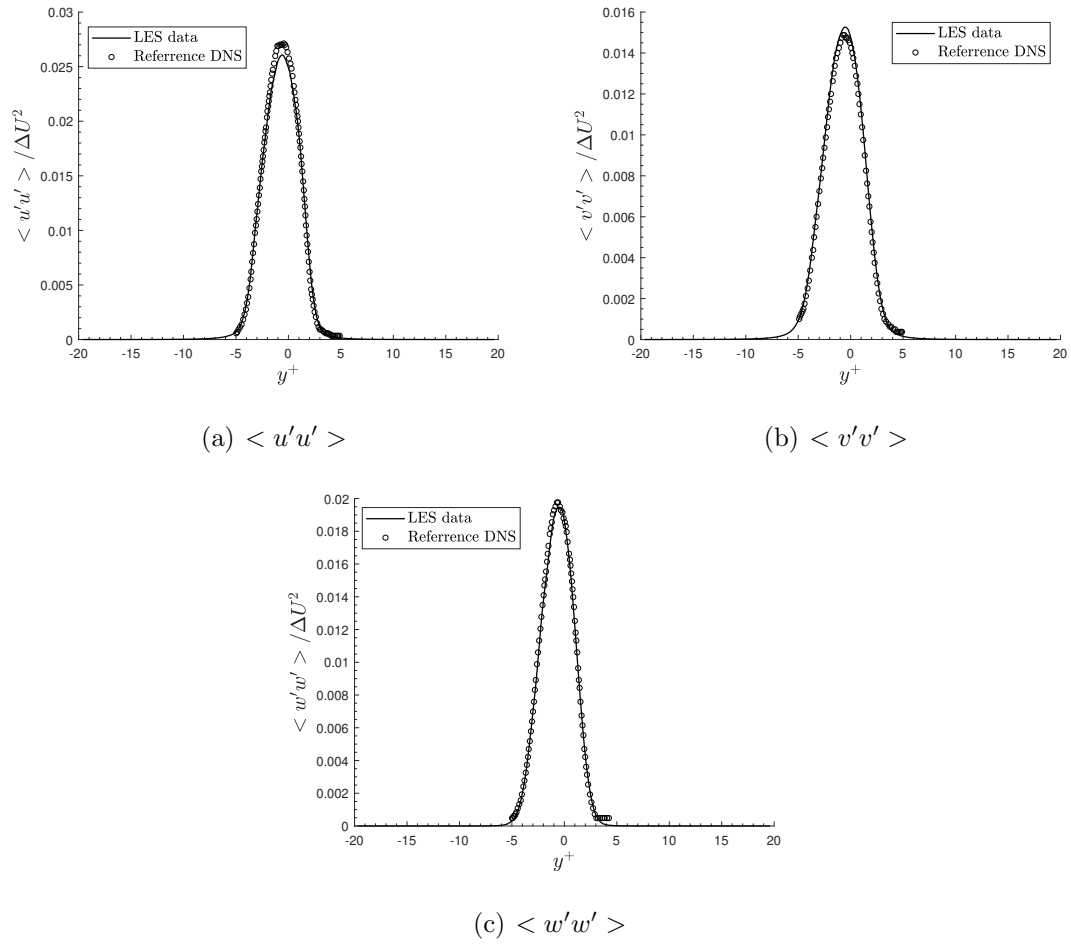


Figure 3.26. Incompressible turbulent mixing layer : case 2 : Reynolds stresses at $\frac{x}{\delta_{\omega_0}} = 450$ compared against the reference DNS.

formly distributed across the small scales of turbulence [2]. In the buffer zone, it could be easily observed that these small scale vortices are smeared out from reaching the outflow, which aids in numerical stability. The iso-surface of the vorticity magnitude is shown in the figure 3.29. The occurrence of spanwise rollers with interconnecting braid vortices (streamwise vortices) could be seen in the transition region leading to the formation of 3D small scale structures further downstream in the fully turbulent region. Such a flow field is very typical of a mixing layer evolving from laminar initial conditions as observed in [2]. The iso-surface of the vorticity magnitude close to the inflow is shown in plan view in figure 3.30. The location of the peak of the integral normalized crosswise component of the turbulent kinetic energy (see figure 3.24) is found to occur around $\frac{x}{\delta_{\omega_0}} \sim 110$. From figure 3.30, it could be seen that the upstream region of this location is characterized by the presence of spanwise rollers with interconnecting streamwise vortices while the downstream region is more 3D, with the appearance of a large number of small scale structures [33]. This observation is in direct agreement with the observation made in the reference DNS.

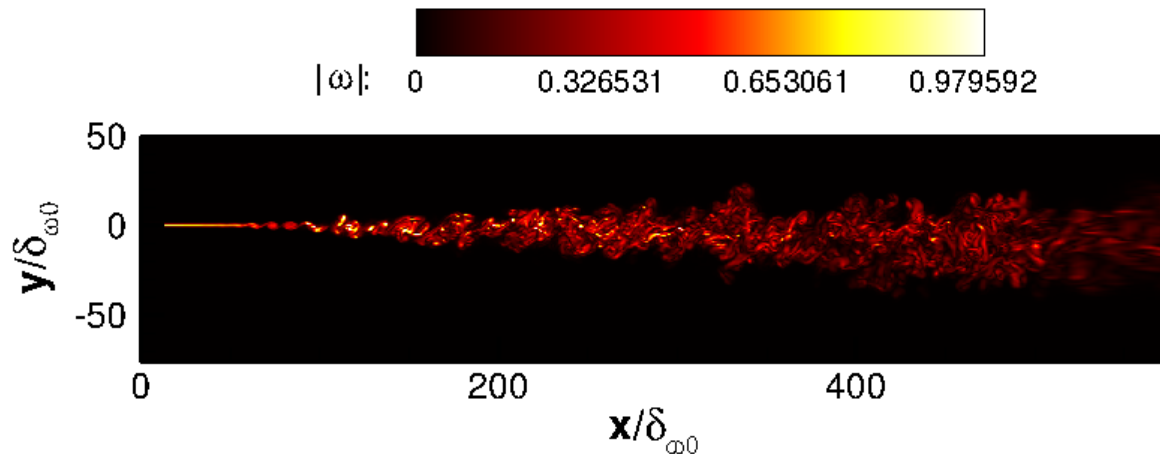


Figure 3.27. Incompressible turbulent mixing layer : case 2 : contours of vorticity magnitude.

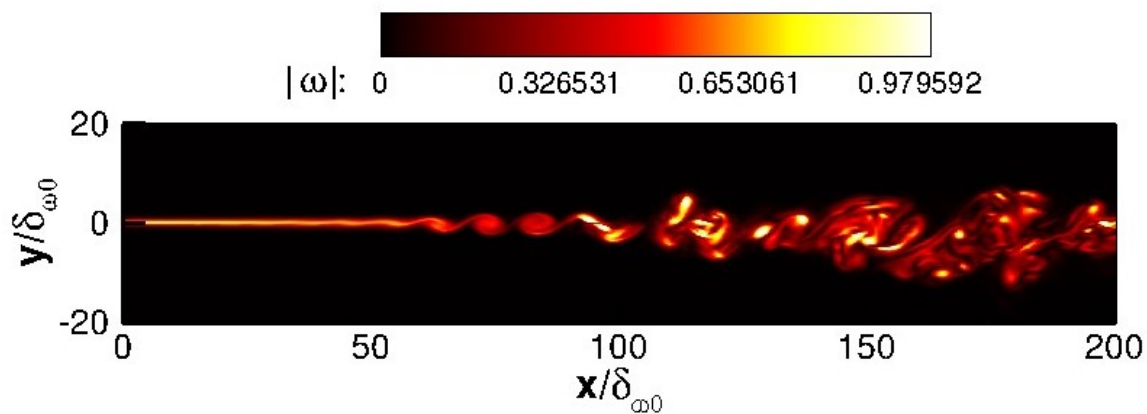


Figure 3.28. Incompressible turbulent mixing layer : case 2 : contours of vorticity magnitude close to the inflow.

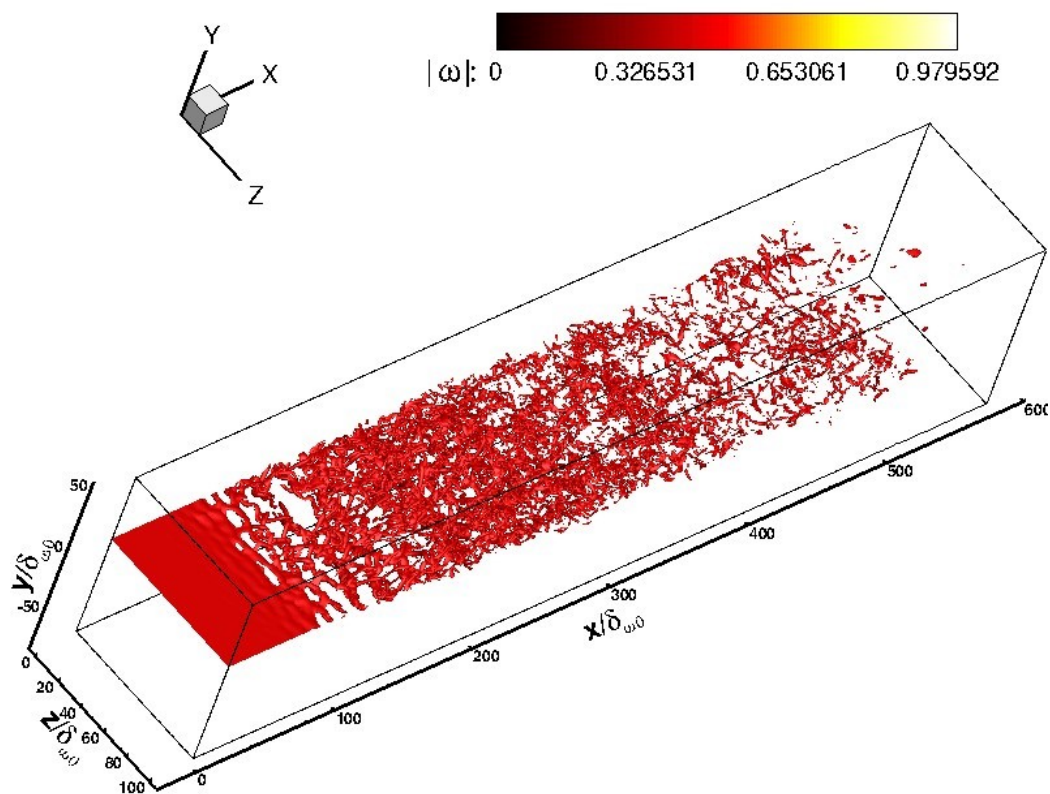


Figure 3.29. Incompressible turbulent mixing layer : case 2 : iso-surface of vorticity magnitude at $|\omega| = 0.45 \frac{\Delta U}{\delta_{\omega_0}}$.

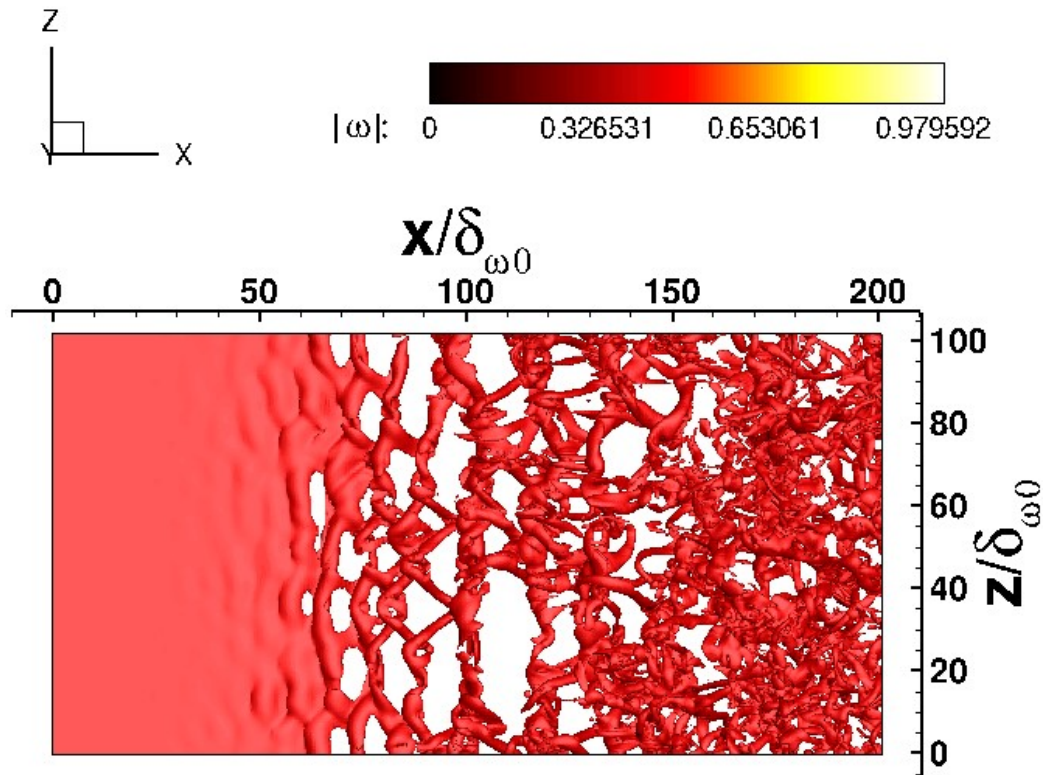


Figure 3.30. Incompressible turbulent mixing layer : case 2 : iso-surface of vorticity magnitude at $|\omega| = 0.45 \frac{\Delta U}{\delta_{\omega_0}}$: plan view close to the inflow.

Thus, the results of the present case exhibit a very good agreement with the reference DNS simulation and the literature. All the statistics except the vorticity thickness match very well with the reference DNS and the data in the literature. The instantaneous flow field images seem to match a typical turbulent mixing layer evolving from a laminar inflow superimposed with white noise fluctuations, that is observed in the literature.

Case 1 results and comparison against case 2 and reference DNS

The LES solver houses two outflow boundary conditions, namely the Tam and Dong outflow boundary condition and the subsonic characteristic outflow boundary condition. It will be worthwhile to make a comparison of the results from simulations using these two outflow boundary conditions (i.e case 1 vs case 2) as it will provide some insight to make a decision on the type of outflow boundary condition to be used for future simulations involving subsonic flows. With this motivation, the results of case 1 are presented and compared against the results of case 2 and the reference DNS.

Comparisons of momentum thickness, δ_θ , and vorticity thickness, δ_ω , for case 1 and case 2 is shown in figures 3.31 and 3.32. The results of case 1 are labelled as “TD outflow” whereas the results of case 2 are labelled as “Characteristic outflow” and this is followed for the remainder of the comparisons as well. It could be seen that case 1 overpredicts δ_θ compared to case 2 with the latter being in better agreement with the reference DNS. Self-similarity in mean velocity is achieved around $\frac{x}{\delta_{\omega_0}} = 300$ for case 1, as the velocity profiles, shown in 3.33, stack on top of each other starting from this location. A linear fit to δ_θ between $\frac{x}{\delta_{\omega_0}} = 300$ and $\frac{x}{\delta_{\omega_0}} = 400$ for this case gives a growth rate of $\frac{d\delta_\theta}{dx} = 0.01525$ which is slightly more than that obtained from case 2. A similar observation could be made about δ_ω from figure 3.32. A linear fit to determine to $\frac{d\delta_\omega}{dx}$ as before for case 1 gives a value of 0.07001 which is still lower than the growth rate given by the experimental fit as in table 3.6.

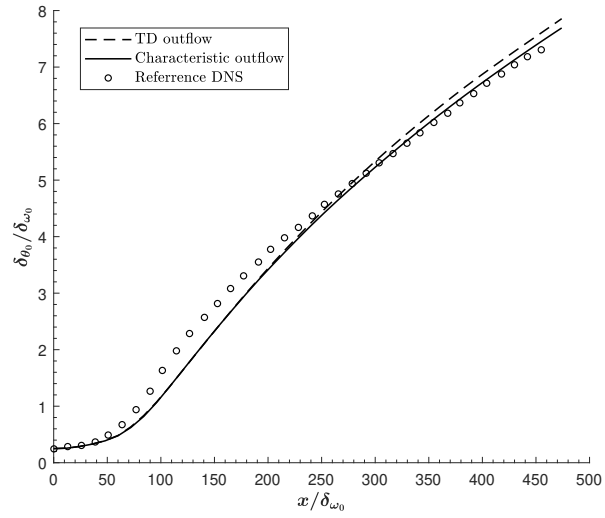


Figure 3.31. Incompressible turbulent mixing layer : comparison of δ_{θ} for case 1 (TD outflow) and case 2 (Characteristic outflow).

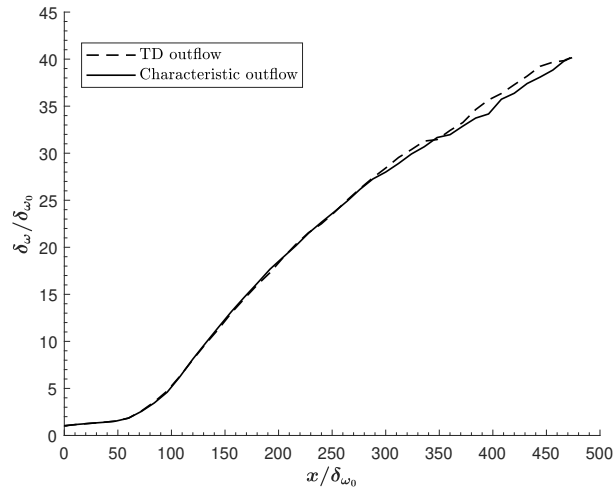


Figure 3.32. Incompressible turbulent mixing layer : comparison of δ_{ω} for case 1 (TD outflow) and case 2 (Characteristic outflow).

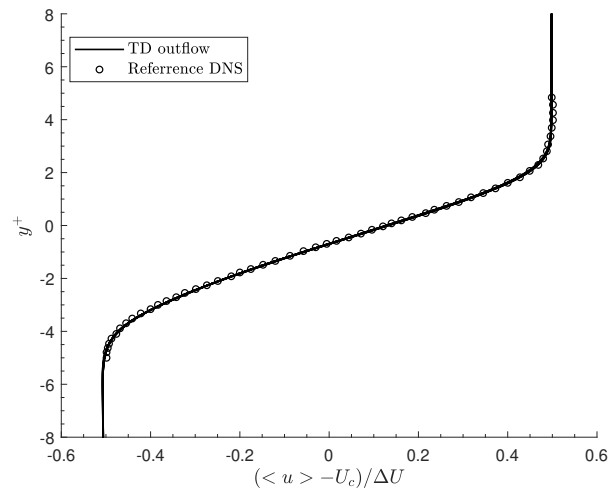


Figure 3.33. Incompressible turbulent mixing layer : case 1 : self-similar profile. $U_c = \frac{U_1+U_2}{2}$.

The Reynolds stresses for case 1 are plotted at several streamwise locations and are shown in 3.34. The Reynolds stresses approach self-similarity towards the end of the physical domain similar to case 2. The streamwise evolution of the peak value of the Reynolds stresses is shown in figure 3.35 for case 1 and case 2. Case 1 clearly exhibits higher turbulence levels in the transition and fully turbulent regions of the flow field. This is especially more pronounced for the cross-stream Reynolds stresses. The peak value in figure 3.35(b) (which is due to the high energy resulting from the pairing of the vortices) is higher for case 1. It is reiterated that except for the use of a different outflow boundary condition, all other simulation settings are the same for case 1 and case 2. Hence any difference observed between the two cases is likely due to the choice of a different outflow boundary condition. From figure 3.36, it could be seen that case 1 clearly overpredicts the Reynolds stresses compared to the reference DNS. The agreement with reference DNS is poor for case 1 compared to case 2. This overprediction is also reflected in the integral normalized crosswise component of the turbulent kinetic energy for case 1 as shown in figure 3.37 with the peak value being much further off from the reference DNS when compared with that from case 2. The location of the peak, however, seems to be similar for case 1 and case 2.

Figure 3.38 shows the non-dimensionalized mean pressure contours. Pressure is fairly uniform inside the fluid domain for case 2 except a small region of low pressure in the center of the domain in the transition region that arises because of the low pressure inside the vortex cores. Case 1, however, exhibits an unphysical pressure rise close to the end of the domain in the buffer zone. The reason for this behavior is unknown. It could be that case 1 requires a longer buffer zone or a sponge zone where the solution is forced to a target solution so that the vortices are completely damped out to avoid this unphysical pressure rise. Note that the former suggestion further increases the computational cost. The latter, however, is a viable subject for future research. The variation of the mean pressure along the centreline $y = 0$ is shown in the figure 3.39. It could be seen that though the unphysical pressure rise is observed only in the buffer zone, this still causes a slight change in the pressure distribution all

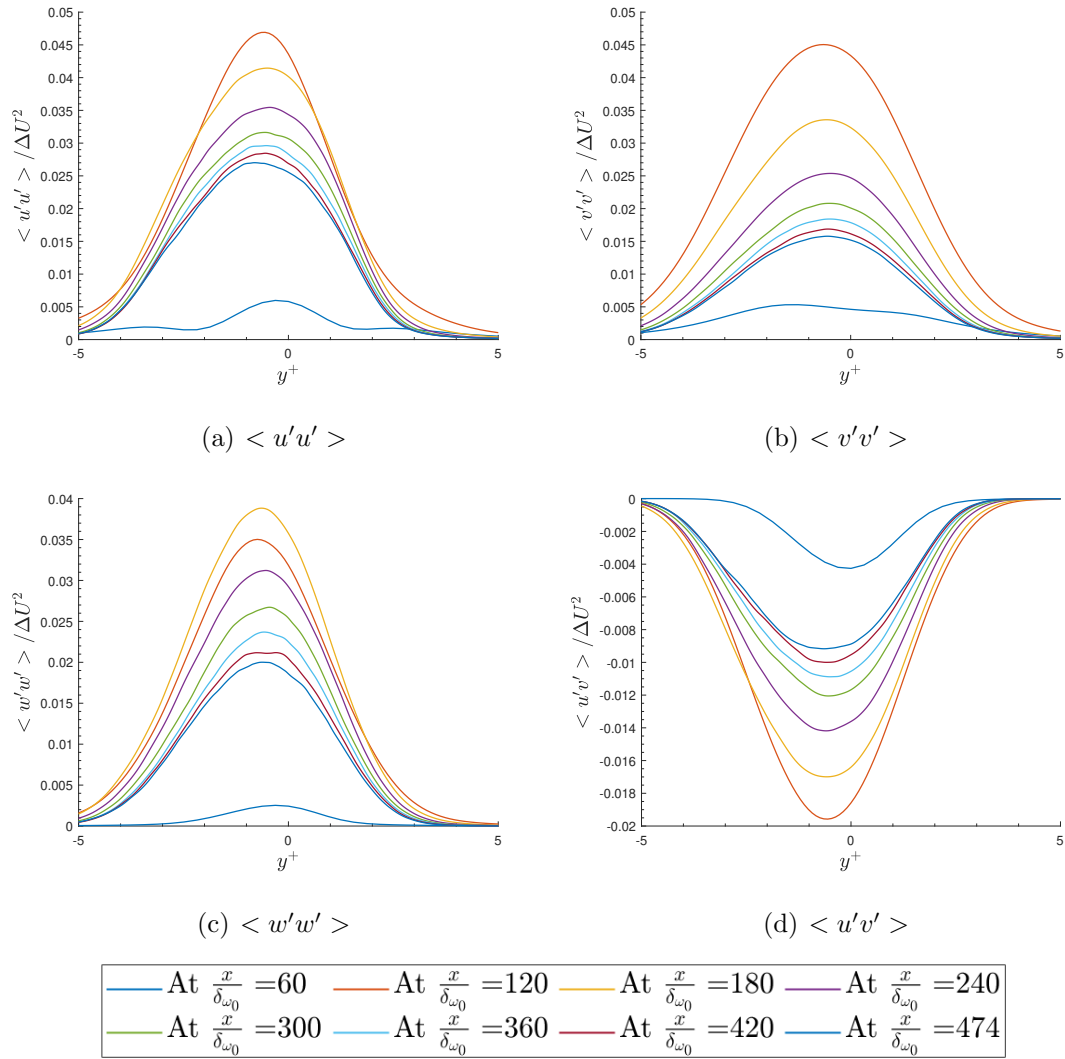


Figure 3.34. Incompressible turbulent mixing layer : case 1 : Reynolds stresses.

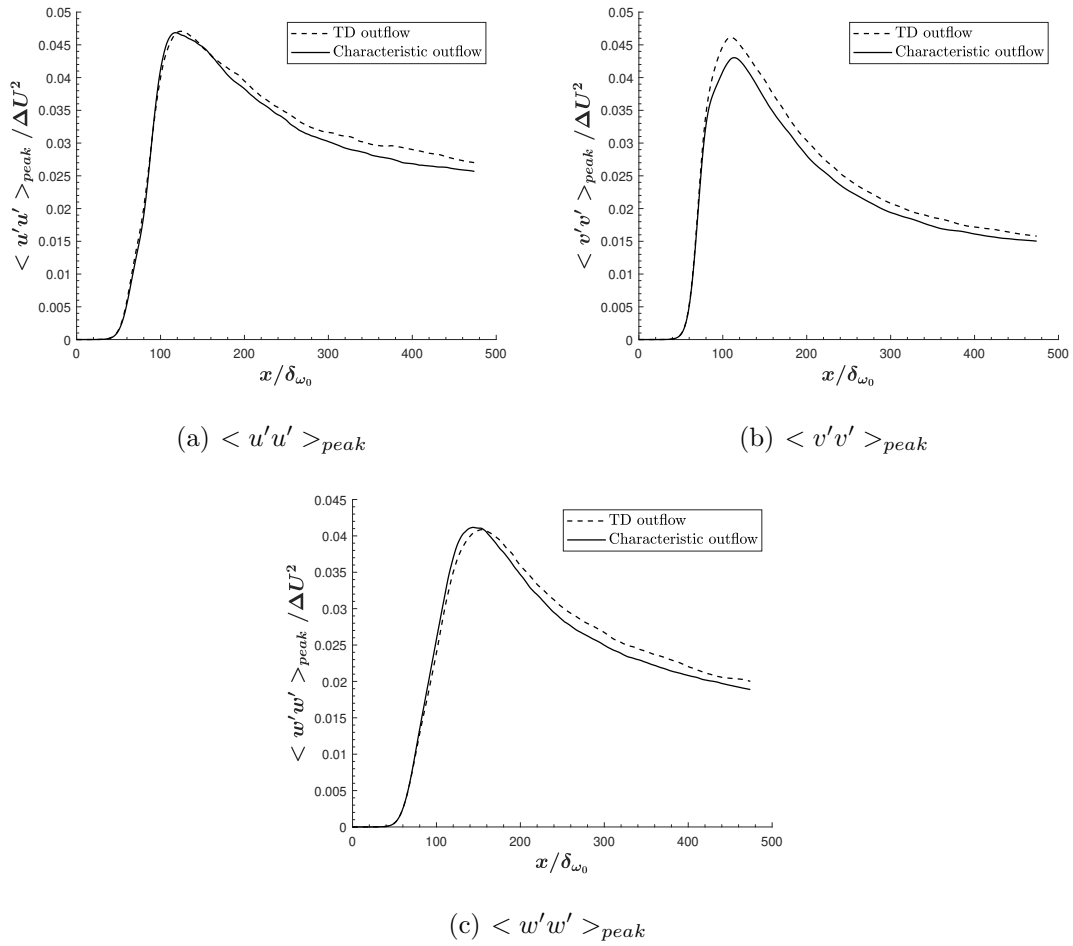


Figure 3.35. Incompressible turbulent mixing layer : streamwise variation of the peak Reynolds stresses : case 1 (TD outflow) vs case 2 (Characteristic outflow).

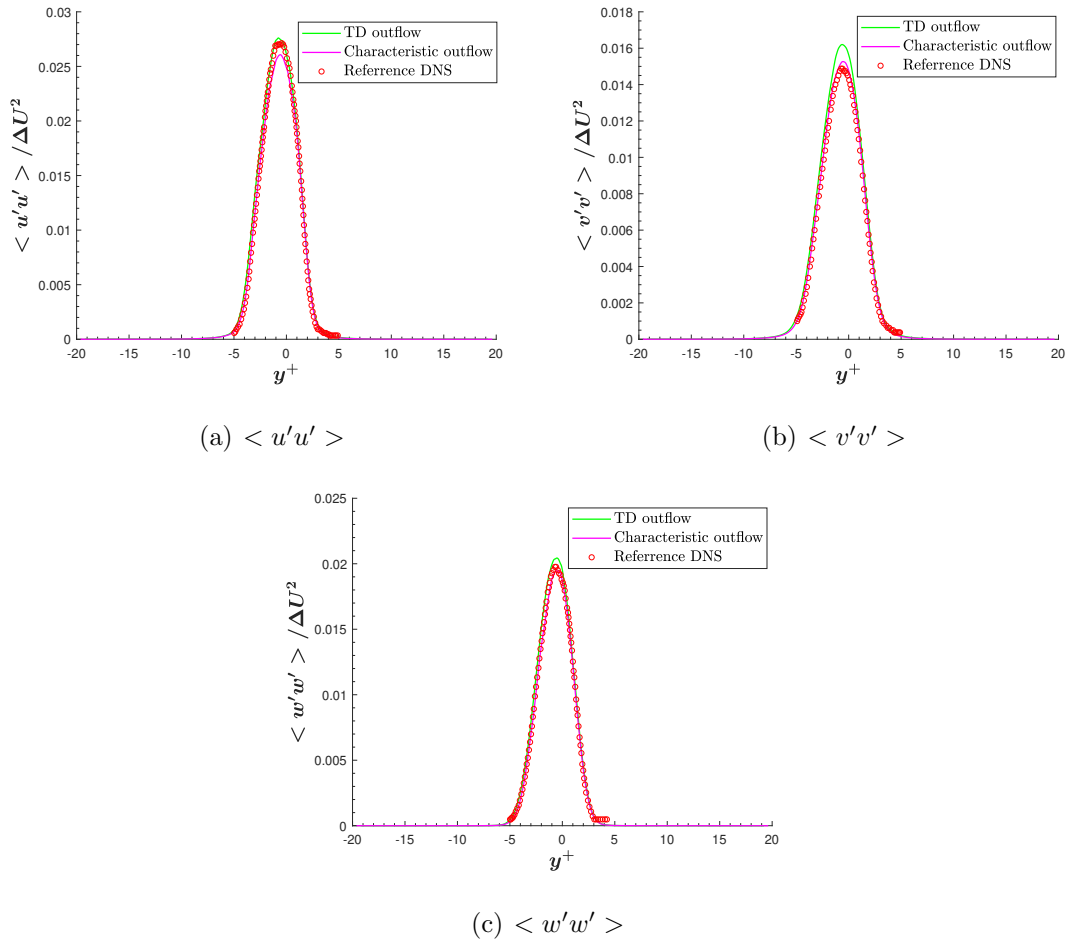


Figure 3.36. Incompressible turbulent mixing layer : Reynolds stresses at $\frac{x}{\delta_{\omega_0}} = 450$: case 1 (TD outflow) compared against case 2 (Characteristic outflow) and the reference DNS.

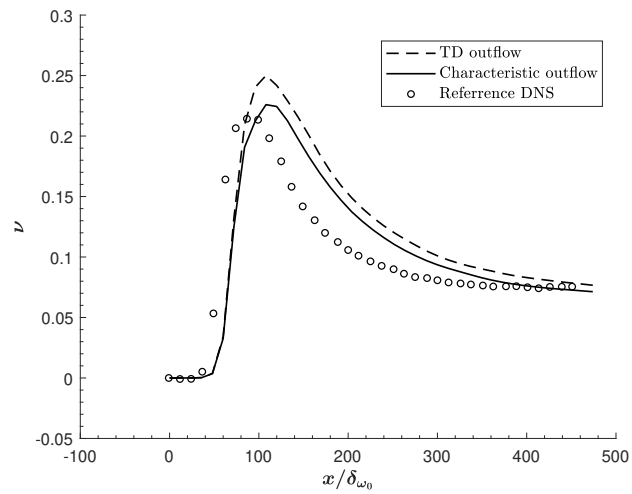
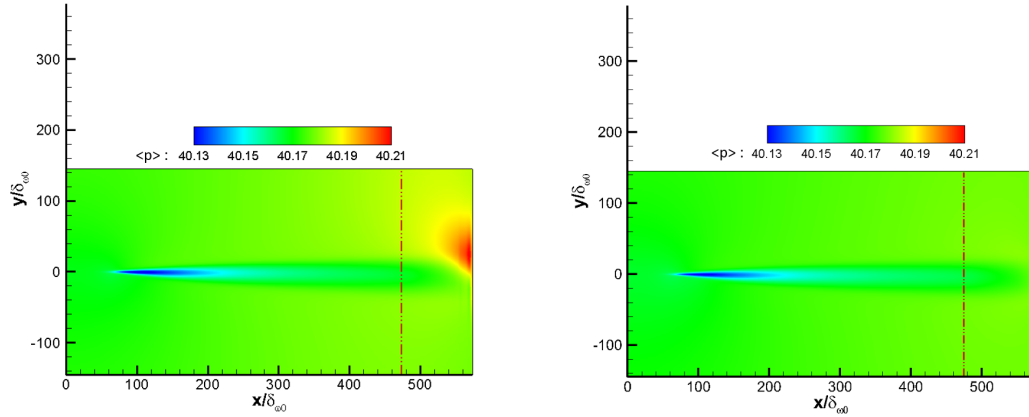


Figure 3.37. Incompressible turbulent mixing layer : integral normalized crosswise component of the turbulent kinetic energy : case 1 (TD outflow) and case 2 (Characteristic outflow).

the way close to the inflow. This could likely be the reason for the slight differences observed in the mean profile and in Reynolds stresses that was mentioned before.



(a) Mean pressure (TD outflow)

(b) Mean pressure (Characteristic outflow)

Figure 3.38. Incompressible turbulent mixing layer : Mean pressure contours : case 1 (TD outflow) vs case 2 (Characteristic outflow). The dash dotted red line indicates the end of the physical zone.

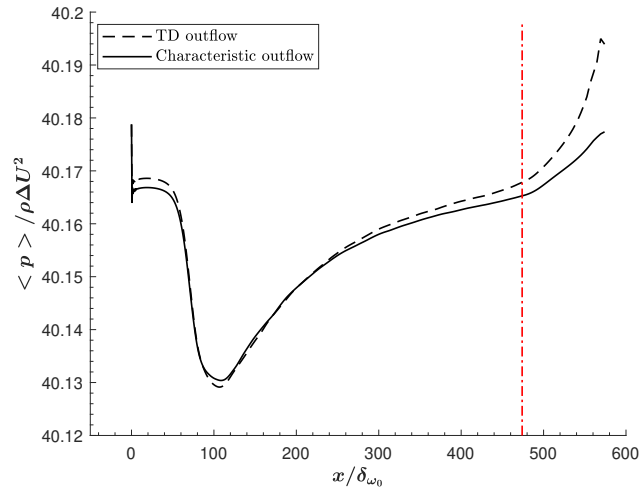


Figure 3.39. Incompressible turbulent mixing layer : Pressure variation along the centreline $y = 0$: case 1 (TD outflow) vs case 2 (Characteristic outflow).

Thus it is concluded that, though overall, case 1 presents a reasonable agreement with the reference DNS, the simulation with subsonic characteristic outflow boundary condition is found to provide a much better agreement with the reference DNS and hence this outflow boundary condition is chosen for the physically correlated inflow simulation (case 3).

Case 3: results and discussion

In numerical studies of mixing layers, the nature of the imposed fluctuations on the initially laminar inflow profile has a profound effect on the mixing layer characteristics [61]. Most numerical studies on mixing layers, especially ones starting with a laminar type profile, seed random white noise fluctuations to the inflow profile to instigate the roll-up instability in a short distance downstream. However, numerical studies of McMullan and Garrett [61] showed that in order to match the experimental trends observed in the characteristics of mixing layers, it is essential to use physically correlated fluctuations at the inflow, even if the mean profile is laminar, as this is likely to be the nature of the fluctuations in experiments. They found that such a correlated inflow condition is necessary for the development of statistically stationary streamwise vortices in the near field region that further persist downstream in the fully turbulent region. These secondary vortices were also found in the experimental studies of Bell and Mehta [25]. These streamwise vortices were found to be necessary to provide the additional entrainment [10] in mixing layers that further improve the growth rate that matches well with the experimental data [61]. This served as the motivation to perform a mixing layer simulation with a physically correlated inflow in the present work. To the author's knowledge, this is the first time that a physically correlated inflow has been used for a mixing layer evolving from a hyperbolic tangent type inflow profile, though studies have been performed with physically correlated laminar boundary layer type inflows [31, 61]. The results are compared against the simulation using white noise type inflow (case 2).

The non-dimensionalized mean streamwise velocity profiles are shown in figure 3.40 for $\frac{x}{\delta_{\omega_0}} > 300$, that indicates self-similarity in the mean streamwise velocity. The Reynolds stresses are shown in figure 3.41. The Reynolds stresses approach self-similarity towards the end of the domain but relatively quickly compared to the other two cases discussed earlier. This is especially clearly evident for the streamwise Reynolds stresses as the profiles at the last two stations almost stack on top of each other. The comparison of δ_θ and δ_ω for case 2 and case 3 is shown in figures 3.42 and 3.43 respectively. The results of case 2 are labeled as “White noise Inflow” and that of case 3 are noted as “Correlated Inflow” and as so for the remainder of the comparisons. It could be seen that case 3 exhibits slightly higher values of δ_θ compared to case 2 in the near field region whereas the trend gets reversed further downstream in the self-similar region. A similar observation is made for the vorticity thickness in figure 3.43. The growth rates measured using a linear fit in the same regions as before for the previous cases gives $\frac{d\delta_\theta}{dx} = 0.013874$ and $\frac{d\delta_\omega}{dx} = 0.06284$ which is lower than measured in case 2.

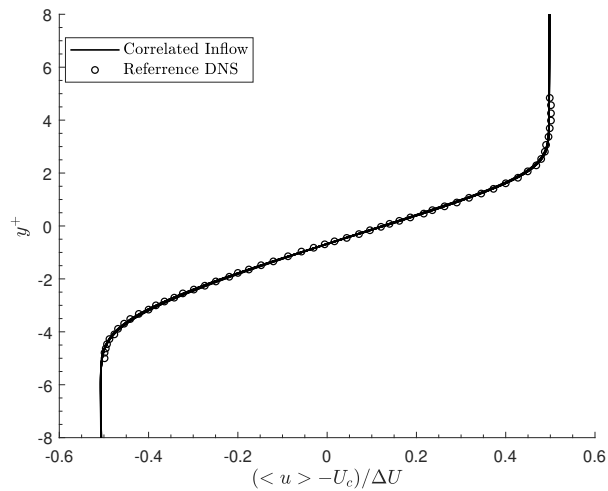


Figure 3.40. Incompressible turbulent mixing layer : case 3 : self-similar profile. $U_c = \frac{U_1+U_2}{2}$.

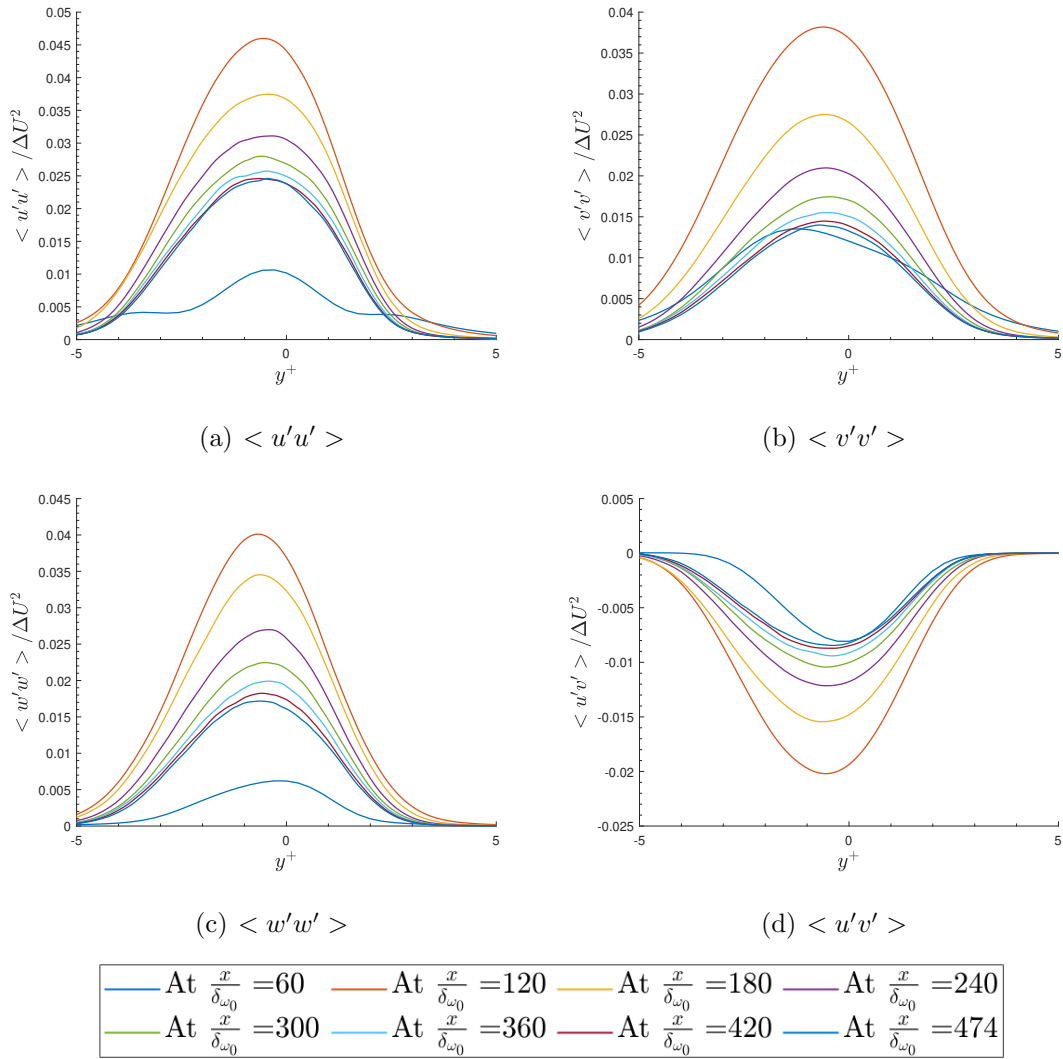


Figure 3.41. Incompressible turbulent mixing layer : case 3 : Reynolds stresses.

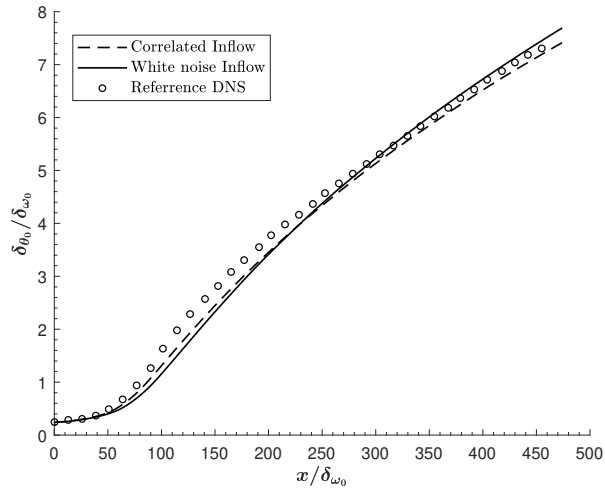


Figure 3.42. Incompressible turbulent mixing layer : momentum thickness : case 2 (White noise Inflow) vs case 3 (Correlated Inflow).

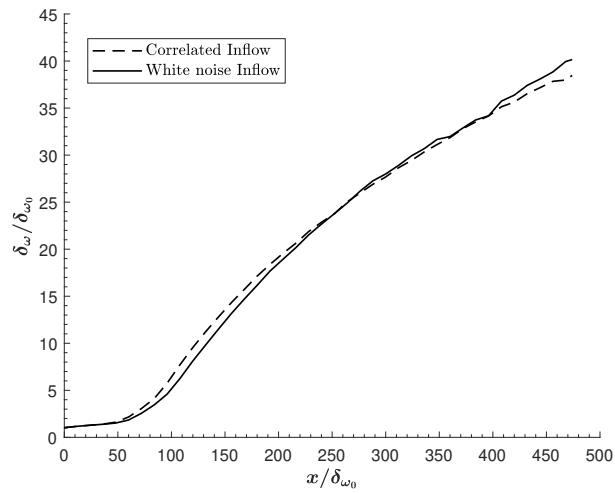


Figure 3.43. Incompressible turbulent mixing layer : vorticity thickness : case 2 (White noise Inflow) vs case 3 (Correlated Inflow).

The streamwise evolution of the peak Reynolds stresses is shown in figure 3.44. Case 3 exhibits slightly higher turbulence levels in the near field region (close to the inflow) compared to case 2 but drops down to a lower value in the self-similar region. This is consistent with what is observed in the mixing layer thickness data. The higher initial growth rate exhibited by case 3 in the near field region is likely due to the increased turbulence levels and the subsequent lower growth rate in the self-similar region compared to case 2 is caused by this reduction in turbulence levels in this region. However, it could be seen that the peak values of case 2 are found to approach that of case 3 towards the end of the fluid domain, especially for the streamwise and cross-stream Reynolds stresses. The reason that this is not apparent for the spanwise Reynolds stresses maybe because of the fact that the spanwise Reynolds stress approaches the self-similar state rather slowly compared to the other two stresses as observed in figure 3.41 and 3.25. The maximum value of the peak Reynolds stresses in the fluid domain is comparable between case 2 and case 3 for the streamwise and spanwise Reynolds stresses. The maximum value of the peak cross-stream Reynolds stress is, however, lower for case 3 when compared to case 2. These maximum values are also found to occur slightly upstream for case 3. Note that such a shift between the correlated and white noise inflow is also observed in [61]. The Reynolds stress profiles (figure 3.45), however, are reasonably close between case 2 and case 3 except the peak value which is lower for case 3 as mentioned before.

In the following discussions, it is attempted to understand some of the observed differences between the two cases under consideration using instantaneous and time-averaged flow field data. An iso-surface of instantaneous vorticity is shown in figure 3.46. Large spanwise rollers could be seen in both the figures with the presence of small positive and negative streamwise vortices in the braid regions between them. For instance, a pair of streamwise vortices of opposite sign could be clearly seen interconnecting two spanwise rollers, wound around the bottom of the first roller to the top of the second and back, in figure 3.46(c) (marked by a black circle for identification). A clear difference in the near field structures could be seen between the two

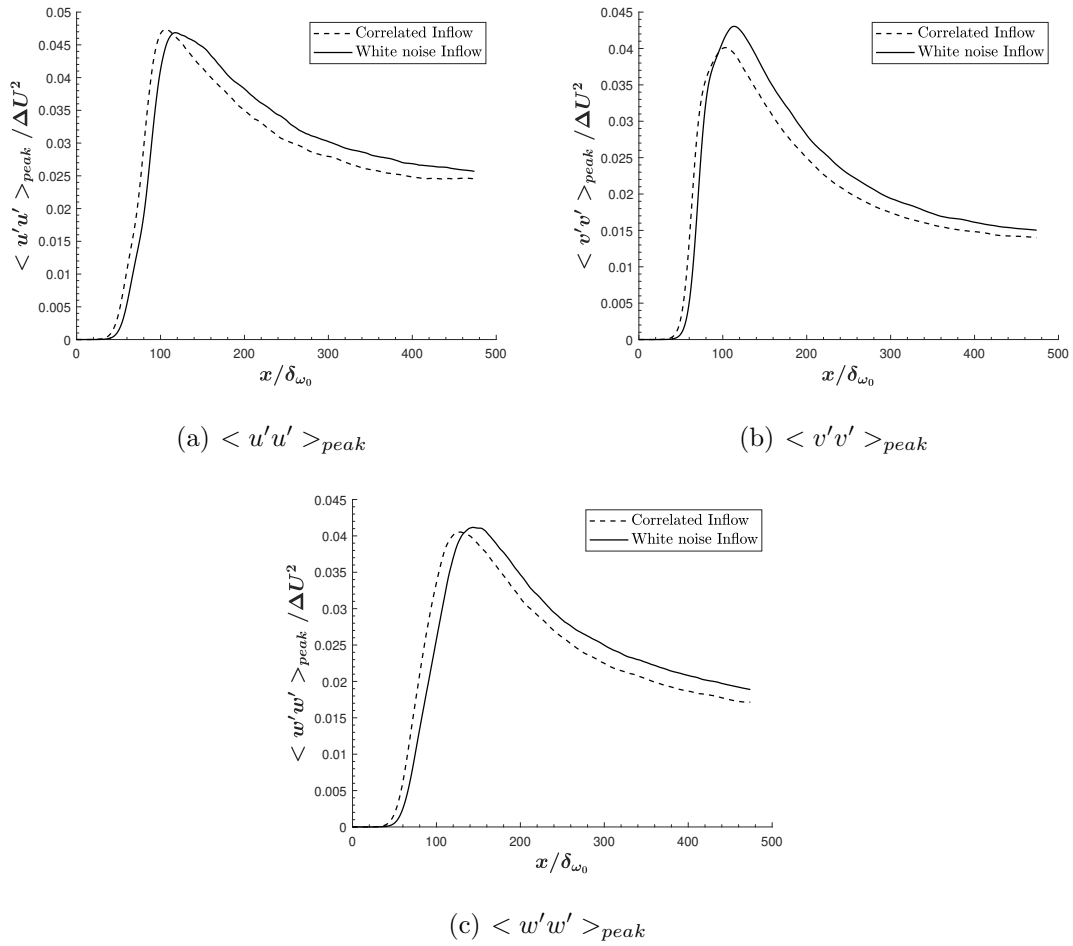


Figure 3.44. Incompressible turbulent mixing layer : streamwise variation of the peak Reynolds stresses : case 2 (White noise Inflow) vs case 3 (Correlated Inflow).

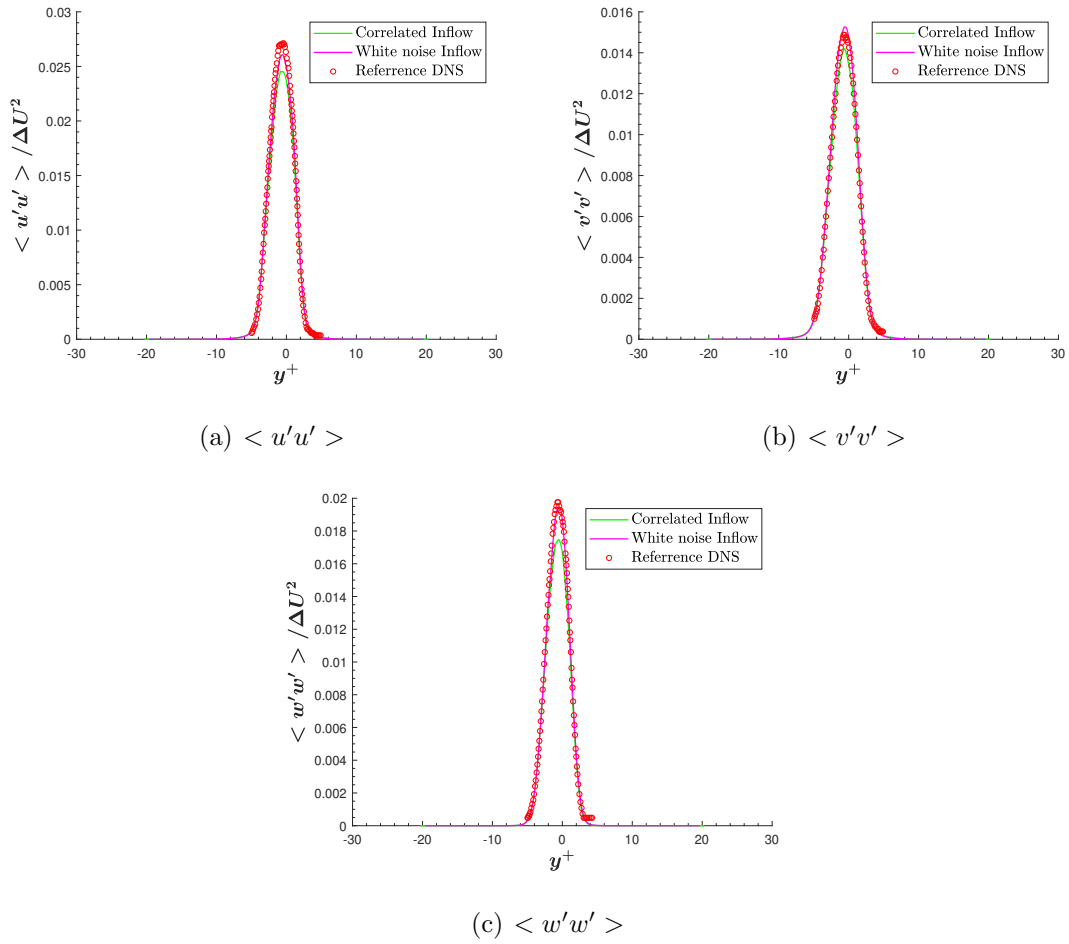


Figure 3.45. Incompressible turbulent mixing layer : Reynolds stresses at $\frac{x}{\delta_{\omega_0}} = 450$: case 3 (Correlated Inflow) compared against case 2 (White noise Inflow) and the reference DNS.

cases. Case 3 is clearly more three dimensional in the near field consisting of a large number of small scale structures. This is also clearly seen in figure 3.47, where case 3 clearly has a large number of small scale streamwise vortex structures compared to case 2. The increased presence of these small scale structures is likely the cause for the higher turbulence levels in the near field that is observed for this case. The higher initial growth rate that is found in figures 3.42 and 3.43 is probably due to the additional entrainment caused by these structures. It is possible that the increased three-dimensionality of case 3 in the near field is because of the earlier establishment of these small scale structures by the correlated inflow. The subsequent reduction in two-dimensionality of the spanwise rollers is probably responsible for the slight reduction in the maximum value of the peak cross-stream Reynolds stress observed in figure 3.44(b), as it is caused by the pairing interactions of these spanwise vortices. Consequently, this increased presence of small scale structures in the near field region could be the reason for the relatively quick convergence in the self-similar Reynolds stresses profiles observed in figure 3.41. This faster approach to self-similarity observed in case 3 could in turn be the reason for the apparent reduction in peak Reynolds stresses observed in figure 3.44 for case 3 in the fully turbulent region. This is further supported by the observation that the peak Reynolds stresses for case 2 is found to approach that of case 3 towards the end of the domain. Thus it is possible that, if the flow in both cases was allowed to continue further downstream (with a longer streamwise extent for the physical domain), the peak Reynolds stresses of both cases would asymptote to the same value and in turn, would result in identical growth rates for the two cases.

Next, the results of the present simulation are analyzed for the presence of statistically stationary streamwise vortex structures found in the numerical simulations of McMullan and Garrett [61] and in the experimental studies of Bell and Mehta [25]. This is done by first looking at the contours of time-averaged non-dimensionalized secondary shear stress $\langle u'w' \rangle$ (non-dimensionalized by ΔU^2). This is because, the presence of organized positive and negative streamwise vortices results in additional

gradients of the velocity components (spanwise and cross-stream gradients in w and spanwise gradient in u) that aid in the production of this shear stress [25]. Individual bands of $\langle u'w' \rangle$ with peaks, alternating in sign along the span, was found to be the indication of the presence of these statistically stationary streamwise vortices [10, 31, 61]. This is shown in figure 3.48, adapted from Bell and Mehta [25]. In the present work, the time-averaged contours of this non-dimensionalized secondary shear stress on a cross-stream plane (y - z plane) is observed at different streamwise locations and is shown in figures 3.49 - 3.57 for both case 2 and case 3. In the initial region of the flow field (figures 3.49 - 3.51), elongated clusters of $\langle u'w' \rangle$ could be seen. At a given spanwise location, the signs of these clusters were found to alternate along the cross-stream direction with a cluster of a given sign being sandwiched between two clusters of opposite sign. These clusters were also found in the experimental observations of Bell and Mehta [25] and in the correlated inflow measurements of McMullan and Garrett [61]. They attributed the presence of these clusters in the initial region to the weak residual streamwise vortices shed from the boundary layers separating at the splitter plate tip into the mixing region. In the present case, these clusters could have been a consequence of the imposed fluctuations at the inflow. Comparing case 2 and case 3 in this near field region, it could be seen clearly that these clusters are more distinct and of higher magnitude in the latter. It should be noted that the magnitude of the inflow fluctuations is the same for both cases (case 2 and case 3) and hence the observed difference should be a result of correlating the inflow fluctuations. The magnitude clearly increases as the flow evolves downstream in both the cases. It was observed in the above two references that these clusters get amplified by the KH instability and re-organize themselves into alternating bands of positive and negative clusters along the spanwise direction. In the present case, this reorganisation could be seen in figure 3.52. Downstream of this location, in figure 3.53 and 3.54, some banding of $\langle u'w' \rangle$ of positive and negative sign could be seen. However, they are irregular for both the cases and do not appear as clear individual bands alternating in sign that is indicative of the presence of organized statistically

stationary streamwise vortices. These bands grow in size with downstream location and their number density reduces (3.55 - 3.57). Though these bands are irregular unlike in 3.48, the bands in case 3 are more organized than in case 2. This is especially observed in figure 3.57. Still, no clear evidence for the presence of statistically stationary streamwise vortices could be obtained from the contours of $\langle u'w' \rangle$ for both of the cases under consideration.

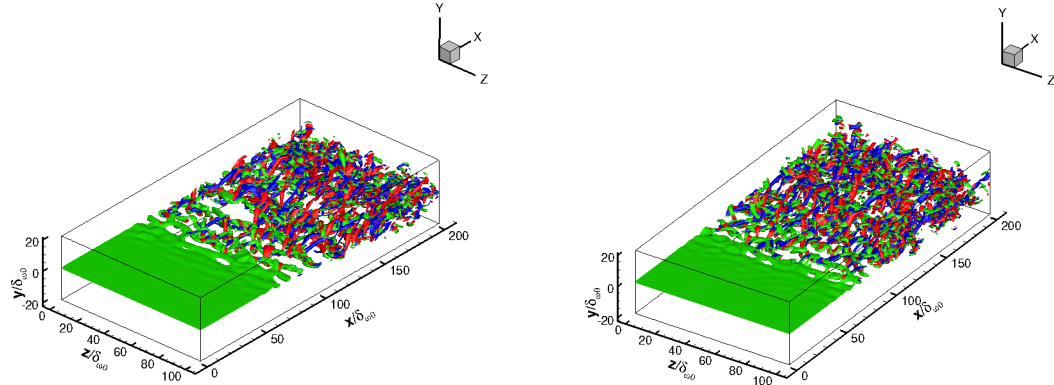
A quantitative indication of the presence of statistically stationary streamwise vortices is the wrinkling of the mean streamwise velocity along the span with the presence of periodic crests and troughs. A crest is caused by a cross-stream transfer of axial momentum by a streamwise vortex pair with common flow upwards and a trough is caused by such a transfer of axial momentum by a streamwise vortex pair with common flow downwards. Figure 3.58 shows the spanwise variation of the time-averaged streamwise velocity at several streamwise locations. At the first two streamwise stations, the mean velocity is fairly uniform in the spanwise direction. This is consistent with what is observed in the $\langle u'w' \rangle$ contours as no banding is observed in these locations. Starting from $\frac{x}{\delta_{\omega_0}} = 120$, small wrinkles could be seen to appear. Comparing case 2 and case 3, it could be seen that case 3 exhibits wrinkles that are more regular in appearance compared to the wrinkles observed in case 2 at these downstream locations (except at $\frac{x}{\delta_{\omega_0}} = 300$, the reason for this anomaly is unknown). This is consistent with the observation made in the appearance bands in the $\langle u'w' \rangle$ contour of case 2 and case 3. The wavelength of these wrinkles in case 3 seems to increase with downstream location which is consistent with the observation made in the literature [25,61]. The maximum peak to peak amplitude of these variations is less than 3 % for case 3. Bell and Mehta [25] reported this peak to peak amplitude to be ~ 10 % in their case whereas this value was found to be ~ 20 % in the numerical studies of McMullan and Garrett [61] for a correlated inflow. Thus, the magnitude of the variation of the mean streamwise velocity along the span is much lower in the present case compared to what is found in the literature. Thus

it could be concluded that strong organized streamwise vortices that are statistically stationary are absent in the present simulations.

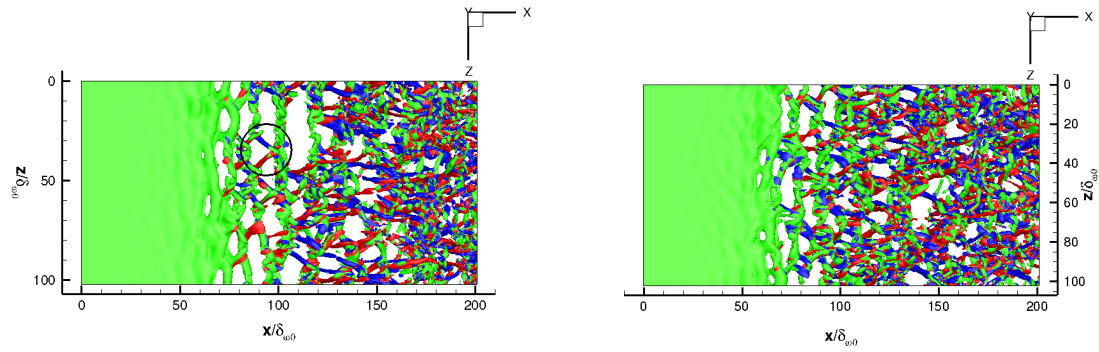
The exact reason for the absence of strong streamwise vortices in case 3 is unknown. However, the strength and appearance of these streamwise vortices are very sensitive to the inflow conditions used [8, 25, 31] in both numerical and experimental studies. The hyperbolic tangent inflow used in the present case could be the reason for this absence, as the references compared against the present simulation consist of a mixing layer evolving from two laminar boundary layers (typical of experiments). Furthermore, McMullan et al. [2] observed that there are marked differences in numerical studies of mixing layers evolving from hyperbolic type and boundary layer type inflows, with the latter being in better agreement with the experimental results. The former is also found to underpredict the growth rate of the mixing layer compared to the experiments. These observations are in support of the reasoning made earlier. The underprediction of vorticity growth rate in the present simulations compared to the experimental fit in equation 3.12 is likely due to the absence of these strong streamwise vortices. However, in lieu of the arguments made above, this is rather viewed as an artifact of the inflow conditions used.

3.4 Summary

The validation cases presented here show that the numerical results produced by the solver match reasonably well with the qualitative and quantitative trends observed in the literature for a mixing layer flow. This serves as a proof that the numerical methods used are of good accuracy to study mixing layer flows. Thus with this confidence, a numerical simulation of a compressible mixing layer is performed with the present code and is presented in the next chapter.

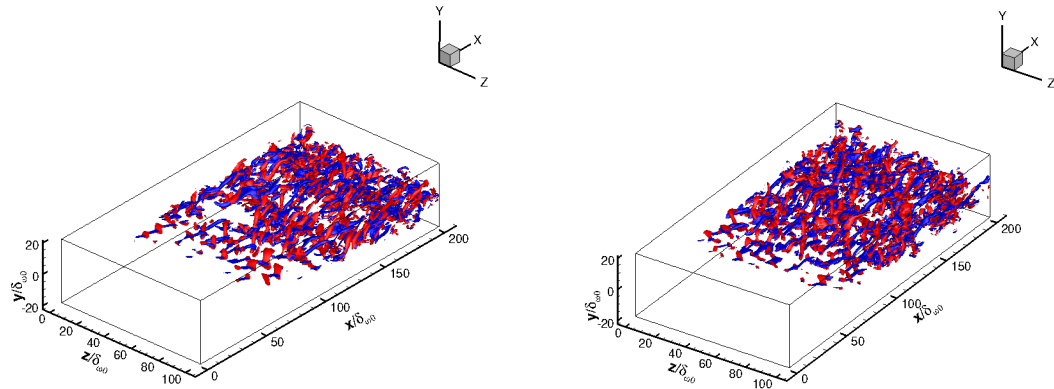


(a) Case 2 (White noise Inflow), isometric view (b) Case 3 (Correlated Inflow), isometric view

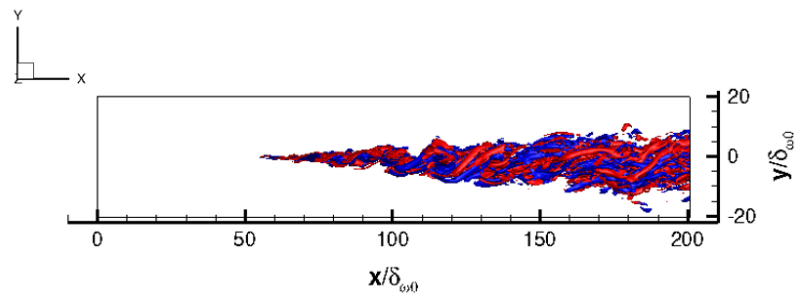


(c) Case 2 (White noise Inflow), plan view (d) Case 3 (Correlated Inflow), plan view

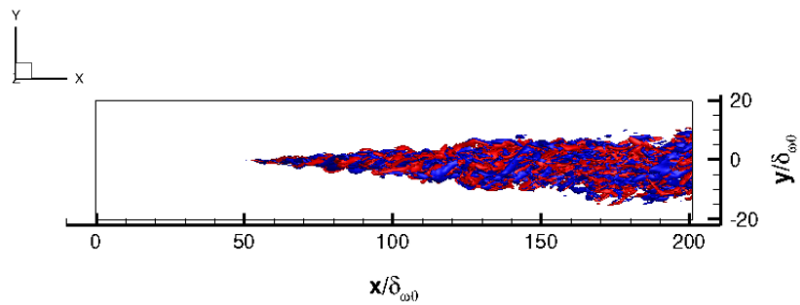
Figure 3.46. Incompressible turbulent mixing layer : iso-surface of instantaneous vorticity : $\omega_z = -0.4 \frac{\Delta U}{\delta_{\omega_0}}$ (green), $\omega_x = -0.3 \frac{\Delta U}{\delta_{\omega_0}}$ (blue), $\omega_x = 0.3 \frac{\Delta U}{\delta_{\omega_0}}$ (red).



(a) Case 2 (White noise Inflow), isometric view (b) Case 3 (Correlated Inflow), isometric view



(c) Case 2 (White noise Inflow), side view



(d) Case 3 (Correlated Inflow), side view

Figure 3.47. Incompressible turbulent mixing layer : iso-surface of streamwise vorticity : $\omega_x = -0.3 \frac{\Delta U}{\delta_{\omega_0}}$ (blue) & $\omega_x = 0.3 \frac{\Delta U}{\delta_{\omega_0}}$ (red).

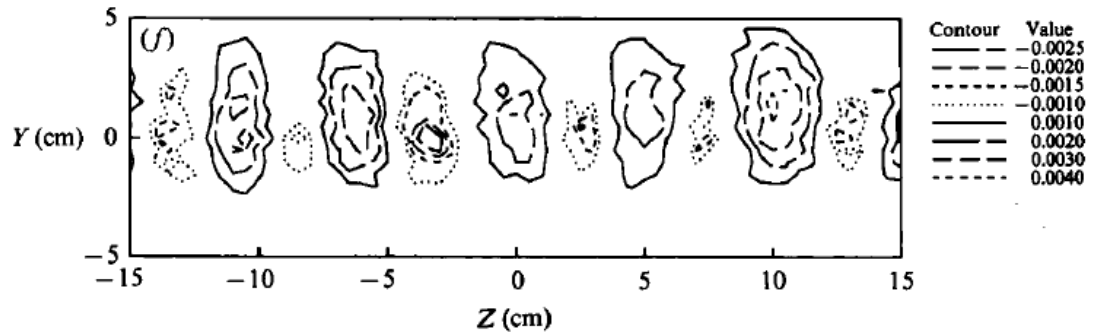


Figure 3.48. Contours of secondary shear stress $\langle u'w' \rangle$ (taken from [25], used with permission).

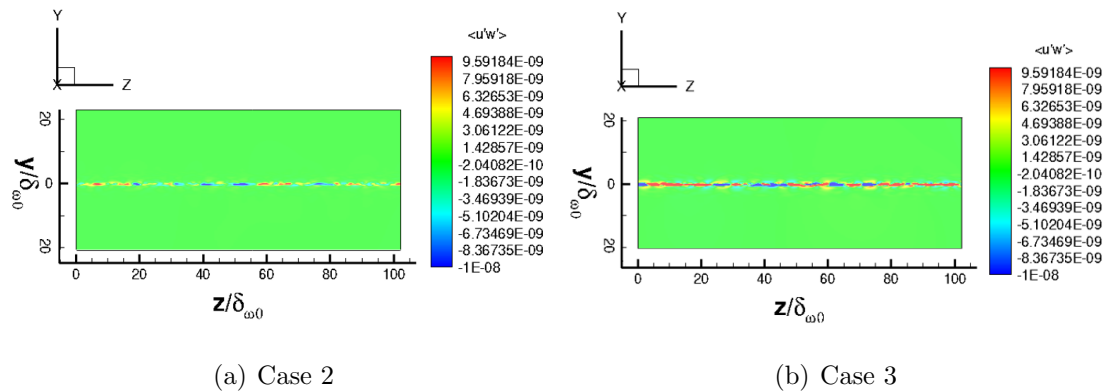


Figure 3.49. Incompressible turbulent mixing layer : secondary shear stress $\langle u'w' \rangle$ at $\frac{x}{\delta_{\omega_0}} = 11$: case 2 (White noise Inflow) vs case 3 (Correlated Inflow).

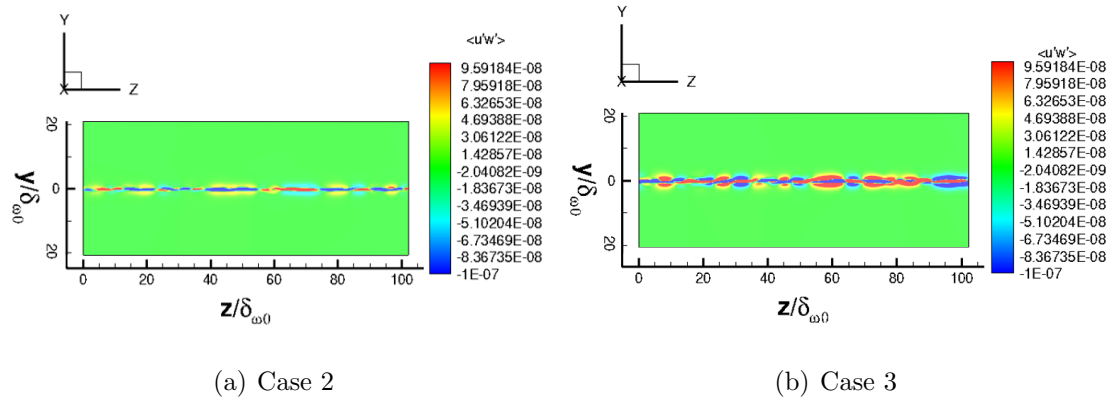


Figure 3.50. Incompressible turbulent mixing layer : secondary shear stress $\langle u'w' \rangle$ at $\frac{x}{\delta_{\omega_0}} = 30$: case 2 (White noise Inflow) vs case 3 (Correlated Inflow).

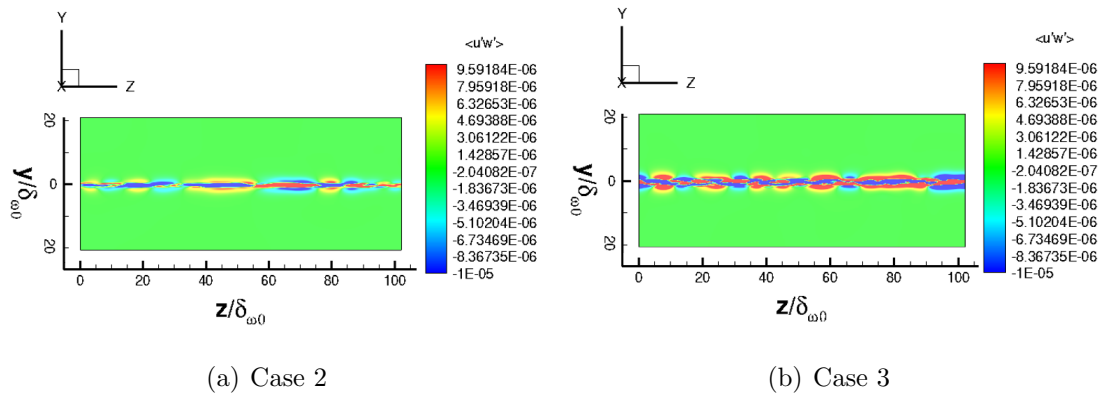


Figure 3.51. Incompressible turbulent mixing layer : secondary shear stress $\langle u'w' \rangle$ at $\frac{x}{\delta_{\omega_0}} = 54$: case 2 (White noise Inflow) vs case 3 (Correlated Inflow).

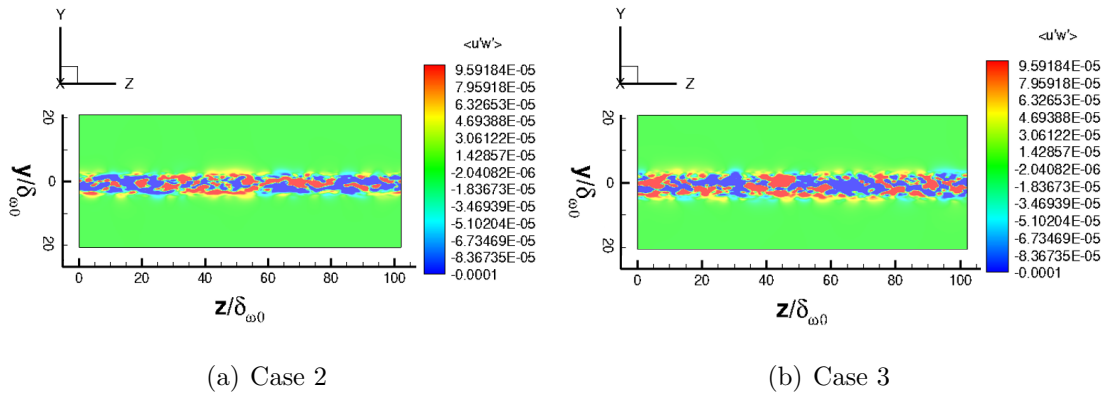


Figure 3.52. Incompressible turbulent mixing layer : secondary shear stress $\langle u'w' \rangle$ at $\frac{x}{\delta_{\omega_0}} = 84$: case 2 (White noise Inflow) vs case 3 (Correlated Inflow).

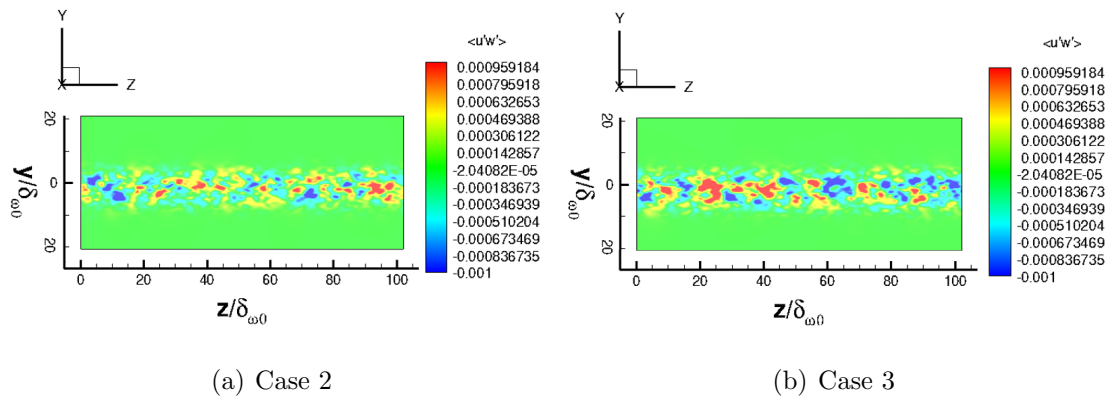


Figure 3.53. Incompressible turbulent mixing layer : secondary shear stress $\langle u'w' \rangle$ at $\frac{x}{\delta_{\omega_0}} = 120$: case 2 (White noise Inflow) vs case 3 (Correlated Inflow).

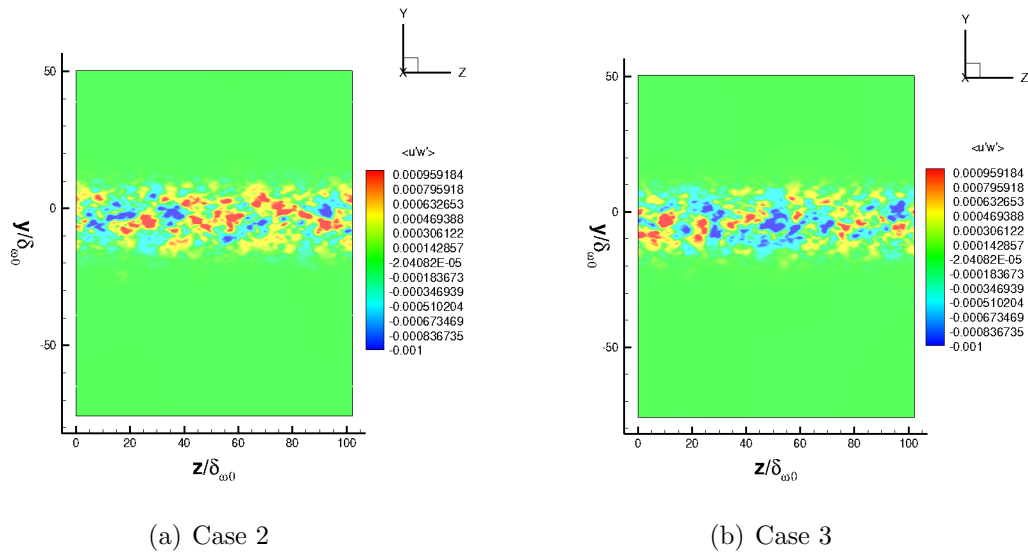


Figure 3.54. Incompressible turbulent mixing layer : secondary shear stress $\langle u'w' \rangle$ at $\frac{x}{\delta_{\omega_0}} = 200$: case 2 (White noise Inflow) vs case 3 (Correlated Inflow).

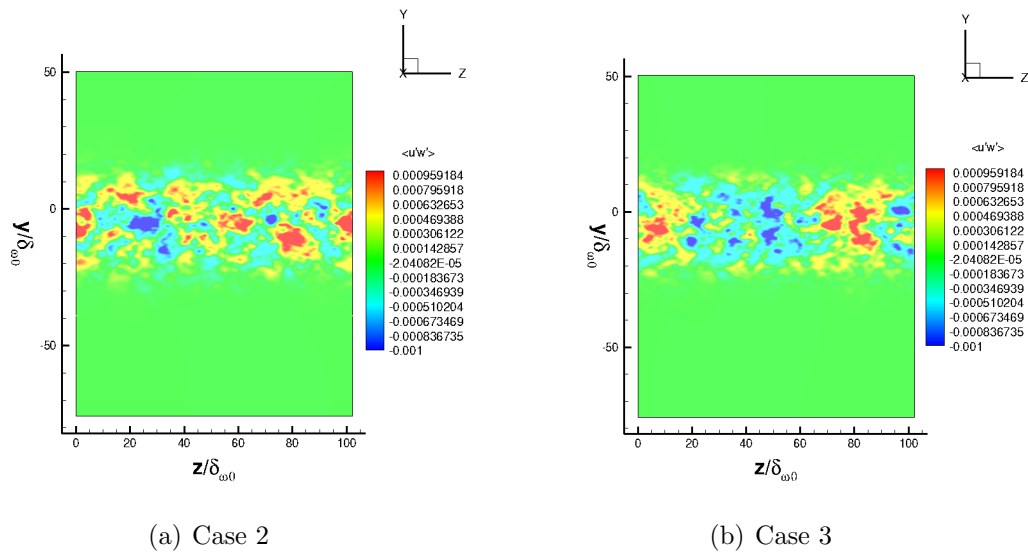


Figure 3.55. Incompressible turbulent mixing layer : secondary shear stress $\langle u'w' \rangle$ at $\frac{x}{\delta_{\omega_0}} = 300$: case 2 (White noise Inflow) vs case 3 (Correlated Inflow).

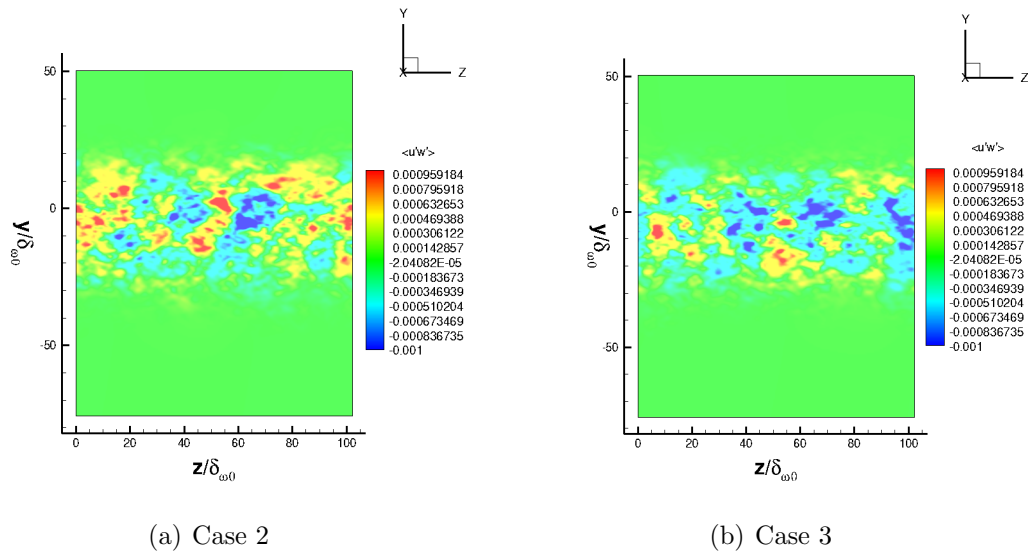


Figure 3.56. Incompressible turbulent mixing layer : secondary shear stress $\langle u'w' \rangle$ at $\frac{x}{\delta_{\omega_0}} = 400$: case 2 (White noise Inflow) vs case 3 (Correlated Inflow).

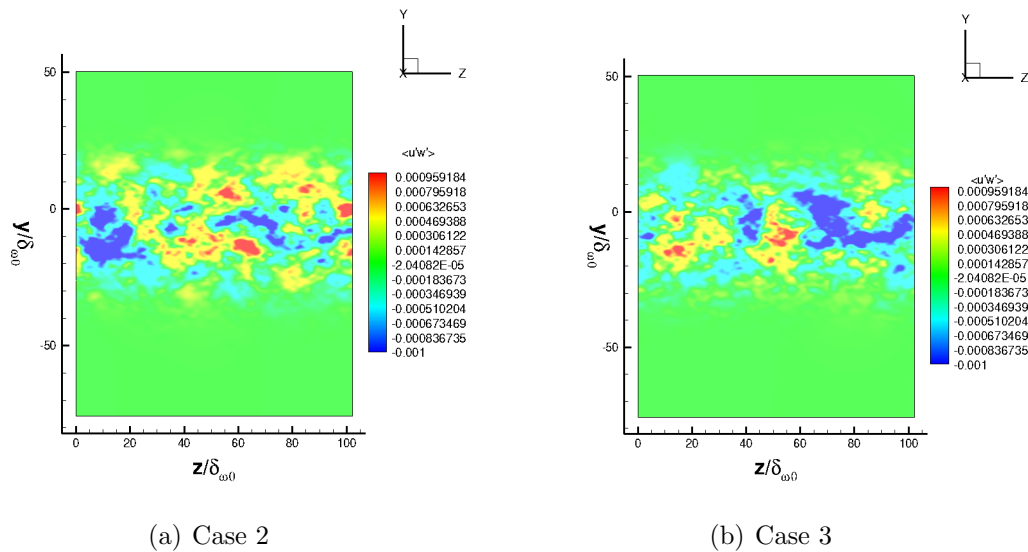


Figure 3.57. Incompressible turbulent mixing layer : secondary shear stress $\langle u'w' \rangle$ at $\frac{x}{\delta_{\omega_0}} = 440$: case 2 (White noise Inflow) vs case 3 (Correlated Inflow).

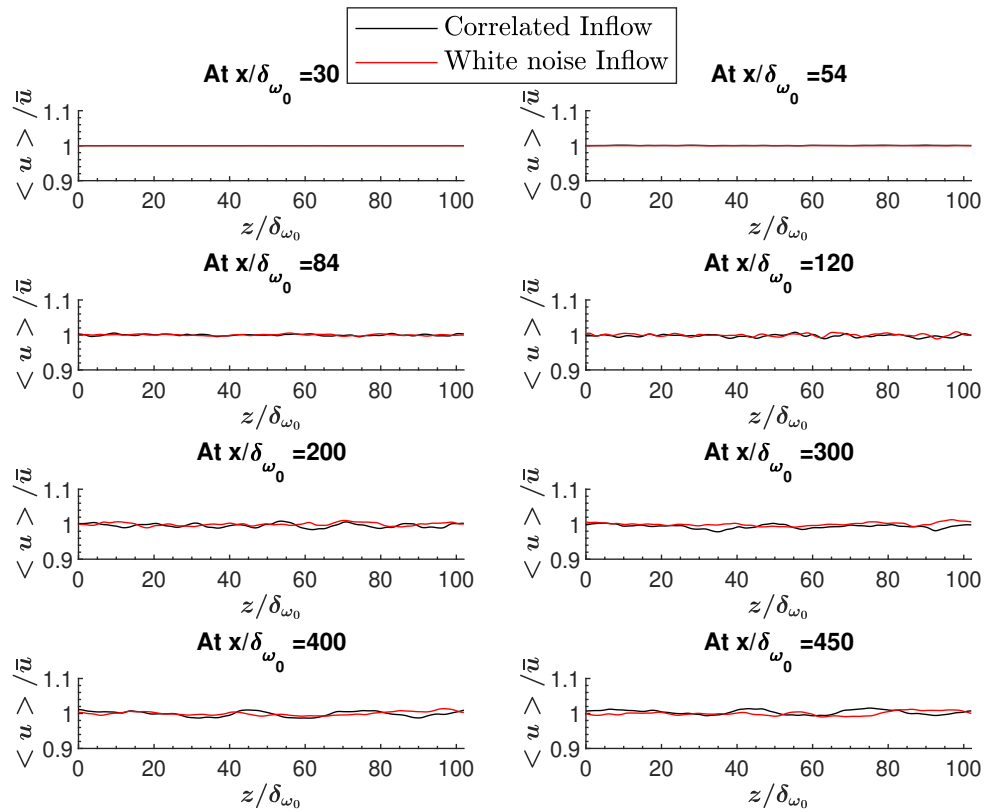


Figure 3.58. Incompressible turbulent mixing layer : spanwise wrinkling of $\langle u \rangle$ normalised by its spanwise-averaged value. Here the spanwise averaged value is represented by \bar{u} : case 2 (White noise Inflow) vs case 3 (Correlated Inflow).

4. COMPRESSIBLE MIXING LAYER

In this chapter, RANS and LES calculations of a compressible mixing layer are presented. First, the case details of the problem under study are given in section 4.1. The RANS simulations performed as a part of the current work, for the purpose of obtaining the initial conditions and inflow profiles for the LES, are described in section 4.2. Finally, the simulation details and the results of the LES are discussed in section 4.3.

4.1 Case Details

In the present work, case 3 of the compressible mixing layer experiments of Kim et al. [11] is chosen for the numerical study. The flow conditions reported for this test case are mentioned in table 4.1 (more precise values than found in [11] were obtained through private communication). This test case is chosen because the reference experiment is specifically performed for CFD validation with the properties of the boundary layers that lead into the mixing section and that of the growing shear layer downstream being clearly documented. Moreover, following [11], a wide range of mixing layer cases at different convective Mach numbers have also been performed and published as a part of this experimental project [16], which could serve as test cases for future numerical studies with the current LES solver, aimed at understanding the effect of compressibility on shear layers.

4.2 Precursor RANS Simulations

As mentioned earlier, a precursor RANS simulation is performed with ANSYS Fluent (with $k - \epsilon$ and RSM turbulence models) to obtain the initial conditions and

Table 4.1. Compressible mixing layer : case details

Parameters	Values
M_1	0.285
M_2	1.541
p_{ts} (kPa)	68.698
p_{01} (kPa)	267.360
p_{02} (kPa)	72.670
T_{01} (kPa)	286.570
T_{02} (kPa)	295.930
U_1 (m/s)	430.660
U_2 (m/s)	97.650
M_c	0.536

the inflow profiles (mean flow variables and Reynolds stresses) for the LES. The specific type of the $k - \epsilon$ and RSM models selected for this purpose together with the chosen flow corrections/wall treatment options available with these models were mentioned in section 2.2. Several initial RANS simulations (with the $k - \epsilon$ turbulence model) were performed to decide the inflow parameters of the RANS calculations to result in the desired flow properties as mentioned in table 4.1 and also to decide the appropriate domain size. All RANS calculations are performed in 2D in the present work. The details of the simulations are given next followed by the results and discussions.

4.2.1 Simulation Details

The fluid domain used in the RANS studies is shown in figure 4.1. The primary and secondary flow evolve in the respective sections and mix downstream of the splitter plate in the test section. The primary section includes a convergent-divergent nozzle

and the secondary portion includes a convergent nozzle to accelerate their respective flows to the desired velocities. These two sections are separated by a splitter plate. The splitter plate is tapered on its bottom wall (i.e the secondary section top wall) to bring the two flows at an angle. The fluid domain used here corresponds to a portion of the experimental domain [11] i.e from ~ 0.103 m upstream of the nozzles to a certain extent in the test section. The dimensions of the experimental domain are obtained for this purpose from [62]. Thus, the test section used in the RANS studies is shorter (~ 0.4 m) in the streamwise direction compared to the experiments (0.762 m). This is because, during the initial studies, using such a large test section is found to cause flow reversal at the test section bottom wall towards the end of the domain, which caused issues with the convergence of the solution. Nevertheless, the current streamwise extent of the test section is much longer than the regions of interest mentioned in the experiment. The farthest location at which data is reported in the experiments is at 0.24 m from the splitter plate tip. Hence the current length of the test section is deemed adequate.

The grid is formed with the help of the commercial software Pointwise. Three different grids named as coarse, medium and fine are used in the present RANS studies, obtained by successively refining the number of grid points in each direction by a factor of $\sim \sqrt{2}$. These three grids of different resolutions are used in the grid convergence study performed as a part of this work. The number of nodes in each of the grids is shown in table 4.2 together with the other mesh metrics that indicate the quality of the grids. The aspect ratio of a cell is defined as the ratio of its longest edge length to the shortest edge length. In the present case, the maximum aspect ratio of all three grids is around 300. Though this may seem high, this is very typical of RANS simulations involving boundary layers. This is because of the clustering of the mesh points in the cross-stream direction, close to the wall, to capture the high gradients present in boundary layers. Orthogonal quality is a mesh metric that is a measure of the orthogonality of the cell. This metric ranges from values of 0 (unacceptable) to 1 (perfect mesh). The minimum orthogonal quality in all of the three grids in the

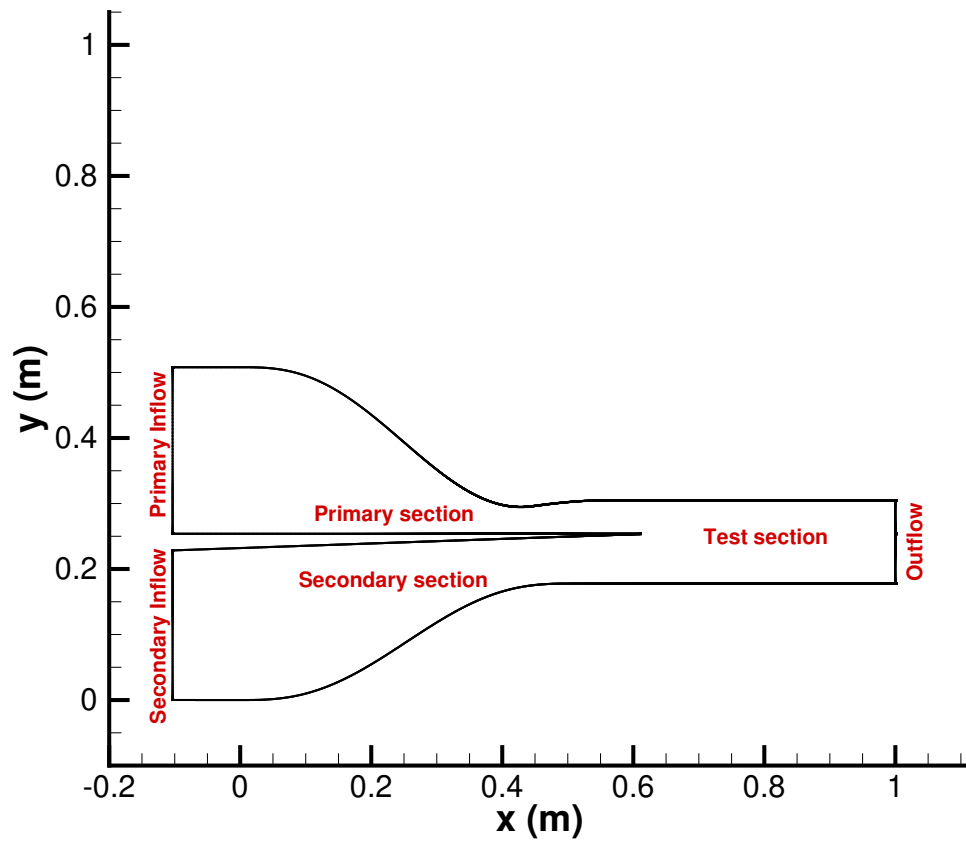


Figure 4.1. Compressible mixing layer : RANS calculations : fluid domain.

present case is well above 0 and suggests a good mesh. The equiangle skewness is a measure of skewness of the cell based on its deviation from an equilateral angle (90° for quad cells). This metric ranges from 0 (perfect or equilateral cell) to 1 (degenerate). The maximum equiangle skewness in all the three grids in the present case are in the range that is indicative of a good mesh. Further details on the evaluation of these mesh metrics and their recommended values for a good quality mesh can be found in [55].

Table 4.2. Compressible mixing layer : RANS calculations : mesh details

Mesh metrics	Coarse mesh	Medium mesh	Fine mesh
Total number of nodes	340779	693016	1393876
Maximum aspect ratio	300.621	298.878	298.352
Minimum orthogonal quality	0.625	0.660	0.685
Maximum equiangle skewness	0.461	0.462	0.463

Some qualitative and quantitative aspects of the mesh employed in the primary, secondary and the test section will be given now (figure 4.2). In the primary section, the grid is smoothly refined in the streamwise direction from the inflow to the nozzle throat area and then again stretched out smoothly to the test section entrance. This is done to resolve the high gradients that occur near the throat area. In the secondary section, the grid is uniformly refined from the inflow to the splitter plate tip along the streamwise direction. The streamwise spacing of the grid points at the splitter plate tip is the same in both sections and remains constant throughout the test section. In the cross-stream direction, grid points are clustered near the walls and in the regions of the shear layer. The edges of the shear layer at the end of the domain are identified from the initial simulations and the grid is refined within this region. The maximum and minimum cross-stream grid spacings and the streamwise grid spacing inside this region of refinement are given in table 4.3 for all three grids considered here. The cross-stream spacing of the grid points in the test section are the same at

all streamwise locations of the test section. The maximum stretching ratios employed in the streamwise and cross-stream directions for the three grids used here are shown in tables 4.4 and 4.5 respectively.

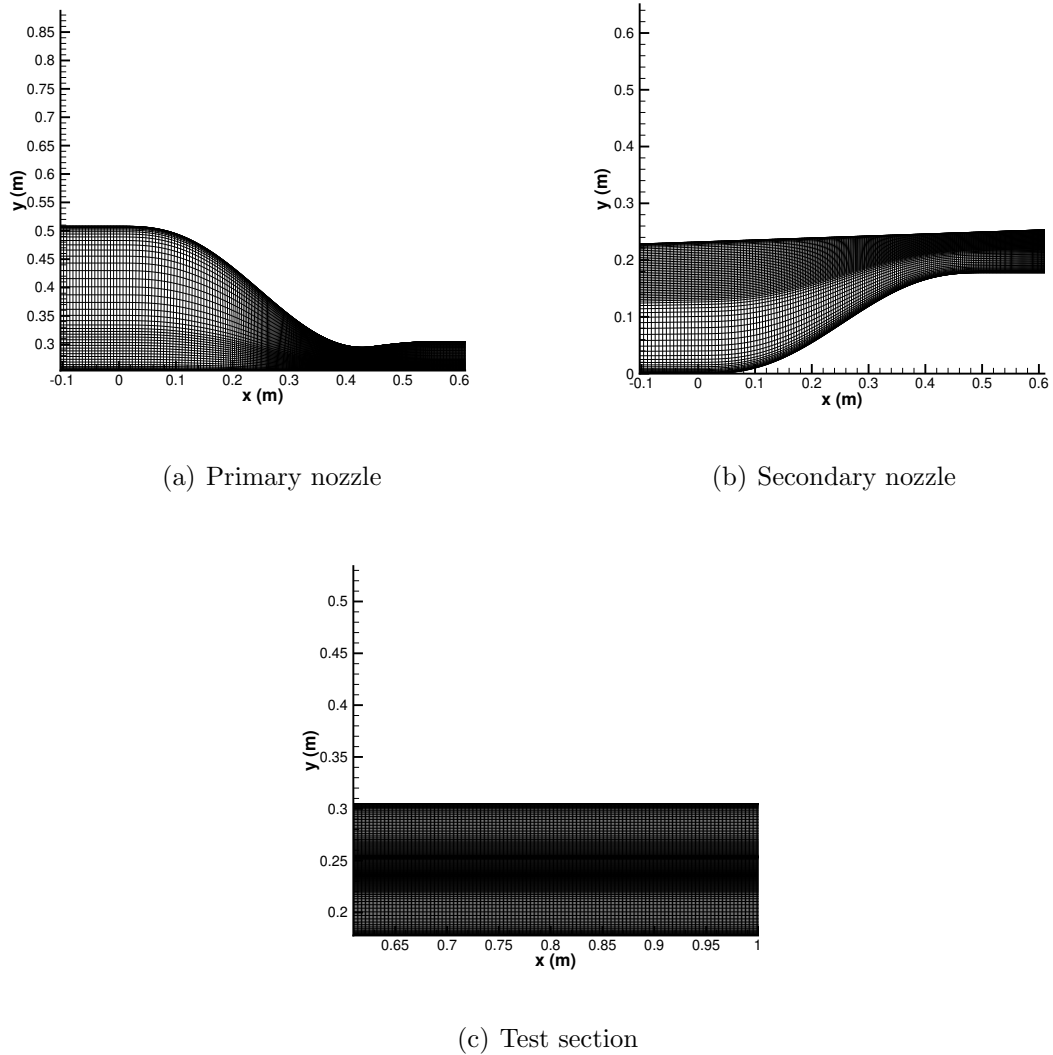


Figure 4.2. Compressible mixing layer : RANS calculations : fine grid (showing every 4th grid point).

A pressure inflow boundary condition is used at the primary and secondary inflows and the pressure outflow boundary condition is used at the outflow. The values of the pressures and total temperatures that are set at these locations are shown in table

Table 4.3. Compressible mixing layer : RANS calculations : grid spacings inside the shear layer

Mesh	Δx (m)	Δy_{\min} (m)	Δy_{\max} (m)
Coarse mesh	6.53×10^{-4}	2.83×10^{-6}	5.37×10^{-4}
Medium mesh	4.62×10^{-4}	2.00×10^{-6}	3.51×10^{-4}
Fine mesh	3.26×10^{-4}	1.41×10^{-6}	2.46×10^{-4}

Table 4.4. Compressible mixing layer : RANS calculations : maximum streamwise grid stretching ratios

Region	Coarse mesh	Medium mesh	Fine mesh
Primary nozzle	3.59 %	4.79 %	4.44 %
Secondary nozzle	1.27 %	0.65 %	0.81 %
Test section	uniformly spaced	uniformly spaced	uniformly spaced

Table 4.5. Compressible mixing layer : RANS calculations : maximum cross-stream grid stretching ratios

Region	Coarse mesh	Medium mesh	Fine mesh
Primary nozzle	23.63 %	15.56 %	10.44 %
Secondary nozzle	22.27 %	19.21 %	9.94 %
Test section	23.63 %	26.91 %	10.43 %

4.6. These are obtained from the initial simulations using a trial and error approach to result in the desired parameters shown in table 4.1. All other boundaries are taken as adiabatic walls. The primary section bottom wall, secondary section top wall and the secondary section bottom wall are comprised of a region of inviscid wall from the inflow followed by a no-slip wall. The location at which the inviscid wall turns into a viscous wall is different for each of the three walls mentioned above and is given in the table 4.7. This location is obtained through a trial and error approach to result in boundary layer properties on these walls at the test section entrance to be reasonably close to the experimental values. The other four walls (primary section top wall, test section top and bottom walls, and the splitter plate face) are simply taken as viscous walls. At the inflows, the turbulent intensity is taken as 1 % and the turbulent to molecular viscosity ratio is set to 1. These are very typical values found in high-quality wind tunnels.

Table 4.6. Compressible mixing layer : RANS calculations : pressure values at the inlet and outlet

Location	Pressure (Pa)	Total temperature (K)
Primary inlet	267360	286.57
Secondary inlet	70670	295.93
Outlet	67661.3	-

The Courant number is set to 5 for the simulations involving the $k - \epsilon$ turbulence model and also for simulations using the RSM with the coarse and medium grids. The Courant number is changed to 8 for the simulation using the RSM with the fine grid. This is done to accelerate convergence as the RSM is very slow in convergence. The hybrid initialization option available in Fluent is used for initializing the flow field for simulations using the $k - \epsilon$ model. The results of the simulations using the $k - \epsilon$ model were used as initial conditions for the simulations using the RSM to aid in numerical stability. The simulations are run in parallel with a total of 16 cores. The scaled continuity and energy residuals in each of the simulations have dropped

at least to the order of 10^{-3} with the other residuals of momentum and turbulent quantities dropping to much lower values at the end of the simulation. Moreover, the skin friction coefficient has been monitored at different locations to ensure that the solution has converged. Next, the results of the simulations are discussed.

Table 4.7. Compressible mixing layer : RANS calculations : location of transition from inviscid to viscous wall given as streamwise distance from inflow

Wall	Distance from the inflow (m)
Primary section bottom wall	0.549
Secondary section top wall	0.564
Secondary section bottom wall	0.552

4.2.2 Results and Discussion

Grid independence study

In this part, some of the results from the three grids that are employed are compared to establish that mesh independence is achieved in the present work. The boundary layer thickness (δ) and the skin friction coefficient (C_f) of the two streams on the splitter plate at a specific location upstream of the splitter plate tip are shown in tables 4.8 and 4.9. The boundary layer thickness presented in this section is measured using the following approach. An effective velocity is defined based on the z -component of vorticity as

$$U^* = \int_0^\infty \omega_z dy = \int_0^\infty \left(\frac{\partial \langle u \rangle}{\partial y} - \frac{\partial \langle v \rangle}{\partial x} \right) dy. \quad (4.1)$$

The location where this effective velocity reaches 99 % of its freestream value is taken as the edge of the boundary layer. The reason for using the effective velocity instead of the mean streamwise velocity ($\langle u \rangle$) to measure the boundary layer thickness is

explained by observing the profiles of $\langle u \rangle$ and U^* on the secondary section top wall at the splitter plate tip shown in the figure 4.3. The flow accelerates close to the splitter tip near the wall. This causes a small overshoot in the $\langle u \rangle$ profile which makes it difficult to locate the edge of the boundary layer. U^* on the other hand monotonically increases to a constant freestream value in the outer irrotational stream and hence provides a clean way to measure the boundary layer thickness using the procedure described above. The skin friction coefficient is computed using,

$$C_f = \frac{\tau_w}{\frac{1}{2} \langle \rho_e \rangle \langle u_e \rangle^2}, \quad (4.2)$$

where the subscript ‘e’ indicates that the values are taken from the edge of the boundary layer. From tables 4.8 and 4.9, it could be seen that the values obtained using the three meshes are very close to each other for both the $k - \epsilon$ and RSM type simulations. The maximum percentage difference in the boundary layer thickness and in the skin friction coefficient between the medium and the fine mesh is less than 2 % in both cases.

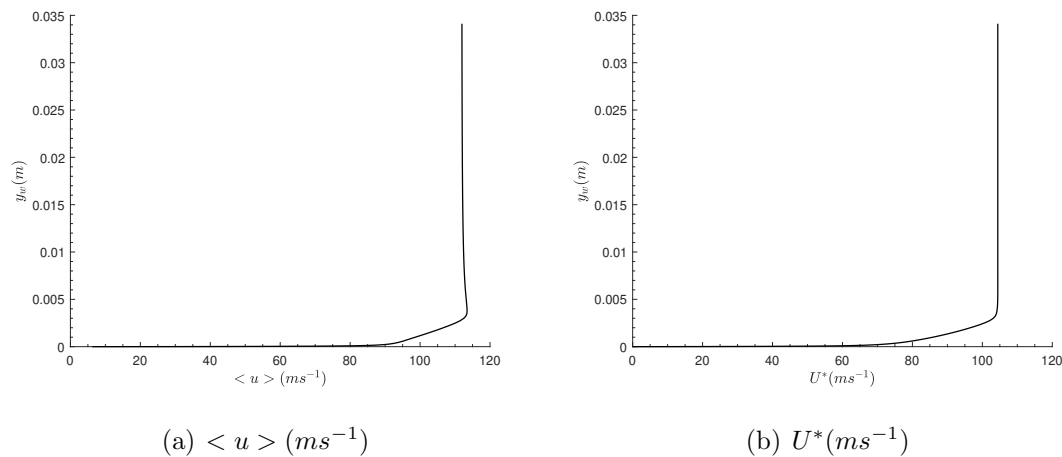


Figure 4.3. Compressible turbulent mixing layer : RANS studies: velocity profiles at the splitter tip on the secondary section top wall. Here y_w is the distance from the secondary section top wall.

Table 4.8. Compressible mixing layer : RANS calculations : $k - \epsilon$ model : δ and C_f at 5 mm upstream of the splitter plate tip

Location	Coarse mesh		Medium mesh		Fine mesh	
	$\delta(\text{mm})$	C_f	$\delta(\text{mm})$	C_f	$\delta(\text{mm})$	C_f
Splitter plate top	1.96	0.00225	1.98	0.00224	2.01	0.00223
Splitter plate bottom	2.98	0.00412	3.07	0.00411	3.12	0.00409

Table 4.9. Compressible mixing layer : RANS calculations : RSM : δ and C_f at 5 mm upstream of the splitter plate tip

Location	Coarse mesh		Medium mesh		Fine mesh	
	$\delta(\text{mm})$	C_f	$\delta(\text{mm})$	C_f	$\delta(\text{mm})$	C_f
Splitter plate top	1.79	0.00230	1.80	0.00228	1.82	0.00227
Splitter plate bottom	2.49	0.00426	2.57	0.00424	2.61	0.00419

Table 4.10. Compressible mixing layer : RANS calculations : $\frac{d\delta_b}{dx}$ for the three meshes

Simulation type	$\frac{d\delta_b}{dx}$		
	Coarse mesh	Medium mesh	Fine mesh
$k - \epsilon$	0.070042	0.070020	0.069997
<i>RSM</i>	0.054902	0.054684	0.054546

Next, the variation of the shear layer thickness δ_b is shown in figure 4.4 at several streamwise locations downstream of the splitter plate tip. In all of the subsequent discussions, x_{spt} is used to denote the distance downstream of the splitter plate tip. The mixing layer thickness at several streamwise locations is found to almost stack on top of each other for the three meshes in the $k - \epsilon$ case and are found to be pretty close to each other for the RSM case. A linear fit to δ_b is done to measure the mixing layer growth rate and is shown in the table 4.10. All the three meshes give growth rates that are very close to each other. The percentage difference in the growth rate between the medium and fine mesh is $\sim 0.008 \%$ and $\sim 0.06 \%$ for the $k - \epsilon$ and RSM cases respectively.

Thus, from the above discussions, it is concluded that the solution is well converged with grid resolution in both the upstream and mixing sections, for both the RSM and $k - \epsilon$ simulations. Hence, in all subsequent discussions, the results of the fine mesh are used.

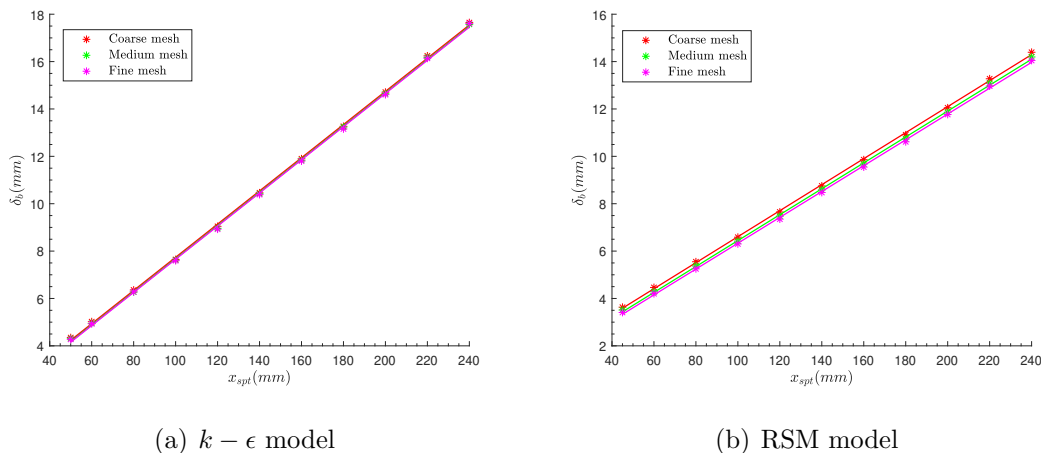


Figure 4.4. Compressible turbulent mixing layer : RANS studies: shear layer thickness δ_b .

Comparison with the reference experiment

In this part, the results of the RANS simulations are compared with the experiment. Firstly, the boundary layer properties of the two streams upstream of the splitter plate tip are compared with the data reported in the experiments [11]. The properties reported in the experiments are taken from the location in the range of 0-20 mm upstream of the splitter plate tip with the exact location unspecified. Hence in the present work, the boundary layer thickness and skin friction coefficient at four locations chosen in the above range are compared against the experimental data and are shown in tables 4.11 and 4.12 respectively for the $k - \epsilon$ and in tables 4.13 and 4.14 for the RSM type simulations.

From table 4.11, it could be seen the boundary layer thickness presented in the range of locations on the four walls are reasonably close to the experimental data, for the $k - \epsilon$ simulation. Out of the boundary layers on these four walls, the ones on the splitter plate are the most important as they directly affect the growing shear layer downstream. The boundary layer thicknesses on the splitter plate top are in good agreement with the experimental data whereas the δ on the splitter plate bottom are lower compared to the experiments. However, it should be noted that the way the boundary layer thickness is measured is different between the experiment and in the present case, where in the former, the typical 99 % thickness based on the mean freestream velocity is used. So this could be an additional cause for the difference observed in the boundary layer thicknesses. The skin friction coefficient, which allows for a direct comparison with the experiment, is shown in the table 4.12 for the $k - \epsilon$ simulation. The results are in good agreement with the experiment, especially for boundary layers on the splitter plate walls. These results serve as an indication that the upstream boundary layer properties are in reasonable agreement with that reported in the experiment. A similar conclusion can be made about the results of the RSM simulation from tables 4.13 and 4.14. However, the boundary layer thicknesses observed in the RSM simulation are lower compared to the $k - \epsilon$ simulation and is

further off from the experimental data. In both the simulations, the flow close to the splitter plate is found to accelerate near the splitter plate tip, as evident by the increase in skin friction coefficient. This effect is also observed in δ for the boundary layers on the splitter plate bottom, as it reduces towards the splitter plate tip. The reason for this behavior is unknown.

Table 4.11. Compressible mixing layer : RANS calculations : $k - \epsilon$ simulation : δ compared with the experiment. Here 'l' denotes distance upstream of the splitter plate tip in mm

Wall	δ (mm)				
	RANS				Experiment
	l = 0	l = 5	l = 10	l = 15	0<l<20
Primary section top wall	2.43	2.39	2.33	2.28	2.98
Splitter plate top wall	2.07	2.01	1.94	1.89	2.24
Secondary section bottom wall	3.71	3.63	3.54	3.45	4.10
Splitter plate bottom wall	3.09	3.12	3.09	3.02	4.05

Table 4.12. Compressible mixing layer : RANS calculations : $k - \epsilon$ simulation : C_f compared with the experiment. Here 'l' denotes distance upstream of the splitter plate tip in mm

Wall	C_f				
	RANS				Experiment
	l = 0	l = 5	l = 10	l = 15	0<l<20
Primary section top wall	0.0022	0.0022	0.0022	0.0022	0.0017
Splitter plate top wall	0.0028	0.0022	0.0023	0.0023	0.0021
Secondary section bottom wall	0.0034	0.0034	0.0035	0.0035	0.0034
Splitter plate bottom wall	0.0145	0.0041	0.0039	0.0038	0.0036

The velocity profiles at several locations downstream of the splitter plate tip are shown in the figure 4.5. At the first two locations (at $x_{spt} = 10$ and 35 mm), a velocity

Table 4.13. Compressible mixing layer : RANS calculations : RSM simulation : δ compared with the experiment. Here 'l' denotes distance upstream of the splitter plate tip in mm

Wall	δ (mm)				
	RANS				Experiment
	l = 0	l = 5	l = 10	l = 15	0<l<20
Primary section top wall	2.18	2.12	2.08	2.04	2.98
Splitter plate top wall	1.89	1.82	1.76	1.71	2.24
Secondary section bottom wall	3.28	3.19	3.08	2.99	4.10
Splitter plate bottom wall	2.59	2.61	2.56	2.49	4.05

Table 4.14. Compressible mixing layer : RANS calculations : RSM simulation : C_f compared with the experiment. Here 'l' denotes distance upstream of the splitter plate tip in mm

Wall	C_f				
	RANS				Experiment
	l = 0	l = 5	l = 10	l = 15	0<l<20
Primary section top wall	0.0022	0.0022	0.0022	0.0022	0.0017
Splitter plate top wall	0.0022	0.0023	0.0023	0.0023	0.0021
Secondary section bottom wall	0.0035	0.0035	0.0036	0.0036	0.0034
Splitter plate bottom wall	0.0172	0.0042	0.0039	0.0039	0.0036

deficit exists in the secondary stream in both cases which is in agreement with that reported in the experiment [11]. This is due to the momentum deficit present in the upstream boundary layers. Reasonable agreement with the experiments is observed for both cases at these two streamwise stations. However, further downstream, as the mixing layer grows, this velocity deficit becomes absent. It could be observed that at the these downstream stations, the agreement with the experiment deteriorates for the simulation with the RSM, whereas the one with the $k - \epsilon$ model matches the experimental results reasonably well. It could be inferred from these figures that the mixing layer is thinner in the simulation with the RSM compared to the one with the $k - \epsilon$ model and the experiment. The velocity deficit region, mentioned earlier, dies off around $x_{spt} \sim 43$ mm in the RSM case and around $x_{spt} \sim 49$ mm for the $k - \epsilon$ case. This behavior of earlier termination of the velocity deficit region in the RSM case is consistent with the relatively thin boundary layers observed in this case. The end of this region marks the approach to self-similarity in the mean stream-wise velocity [11], as the normalized $\langle u \rangle$ profiles plotted against the non-dimensional cross-stream coordinate $(y-y_0)/\delta_b$ start to collapse on top of each other shortly downstream. Here y_0 is the center of the mixing layer defined as in [11]. Self-similarity in the streamwise velocity is reported to occur around $x_{spt} \sim 40$ mm in the experiment, which is slightly upstream of what is observed in the present work. Comparing the self-similar velocity profile with the experiment (see figure 4.6), it could be seen that the results of the $k - \epsilon$ model are in better agreement with the experiment compared to the RSM. The start of the self-similar region is also observed through linear growth of the mixing layer as shown in the figure 4.7. It could be observed that δ_b from the simulation with the $k - \epsilon$ model is in good agreement with the experiment whereas the one with the RSM is found to significantly underpredict the mixing layer thickness, as observed earlier through the velocity profiles in figure 4.5. A linear fit to δ_b is performed in the range : $45 \text{ mm} \leq x_{spt} \leq 240 \text{ mm}$ for the RSM case and $50 \text{ mm} \leq x_{spt} \leq 240 \text{ mm}$ for the $k - \epsilon$ case to measure the mixing layer growth rate. This is given in table 4.15, together with the experimental growth rate (reported to be measured in the range

: $40 \text{ mm} < x_{spt} < 240 \text{ mm}$). The growth rate obtained with the $k - \epsilon$ model is in good agreement with the experimental result whereas the RSM is found to largely underpredict the growth rate.

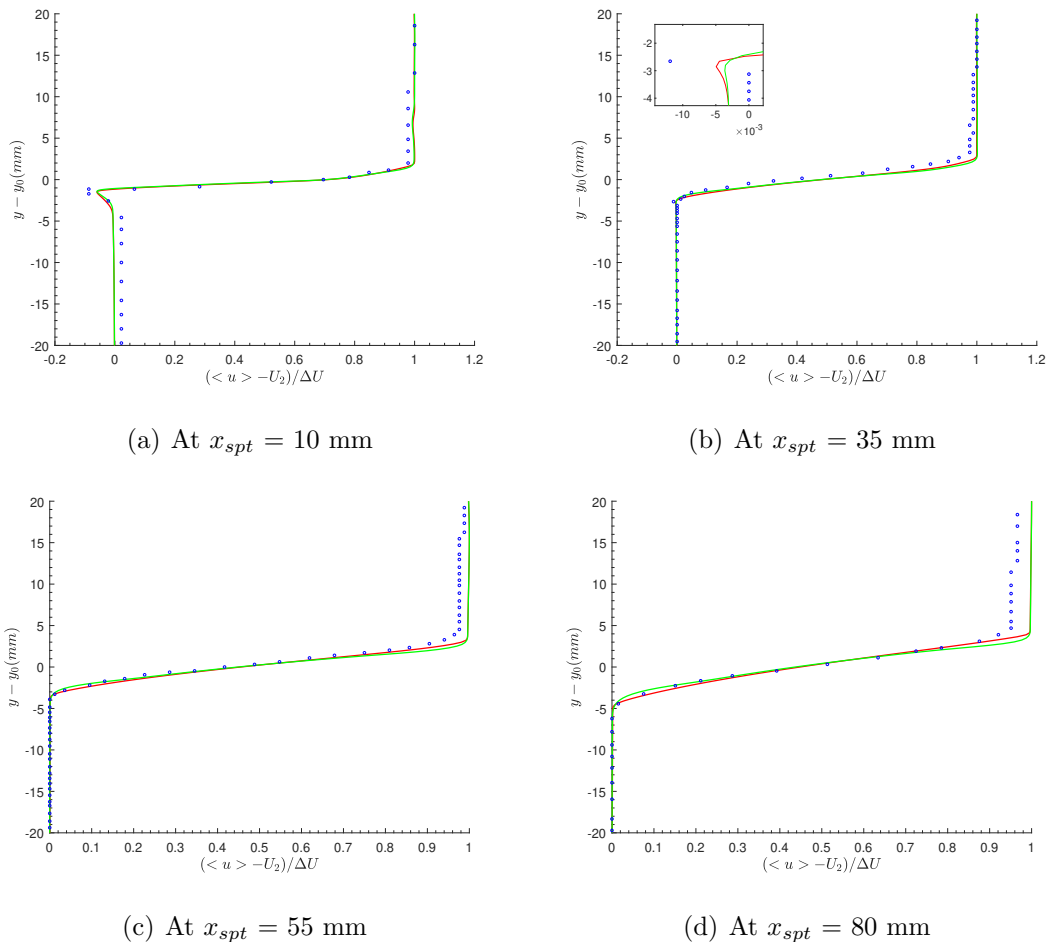


Figure 4.5. Compressible mixing layer : RANS calculations : mean streamwise velocity profiles of the $k - \epsilon$ (red) and RSM (green) simulations compared with the experiments (scatter) at several streamwise locations.

Figure 4.8 shows the profiles of the non-dimensionalized turbulent kinetic energy at several locations downstream of the splitter plate together with the experimental data. Both of the turbulence models underpredict the peak TKE at all locations downstream of the splitter plate tip, with the RSM resulting in the lowest value of

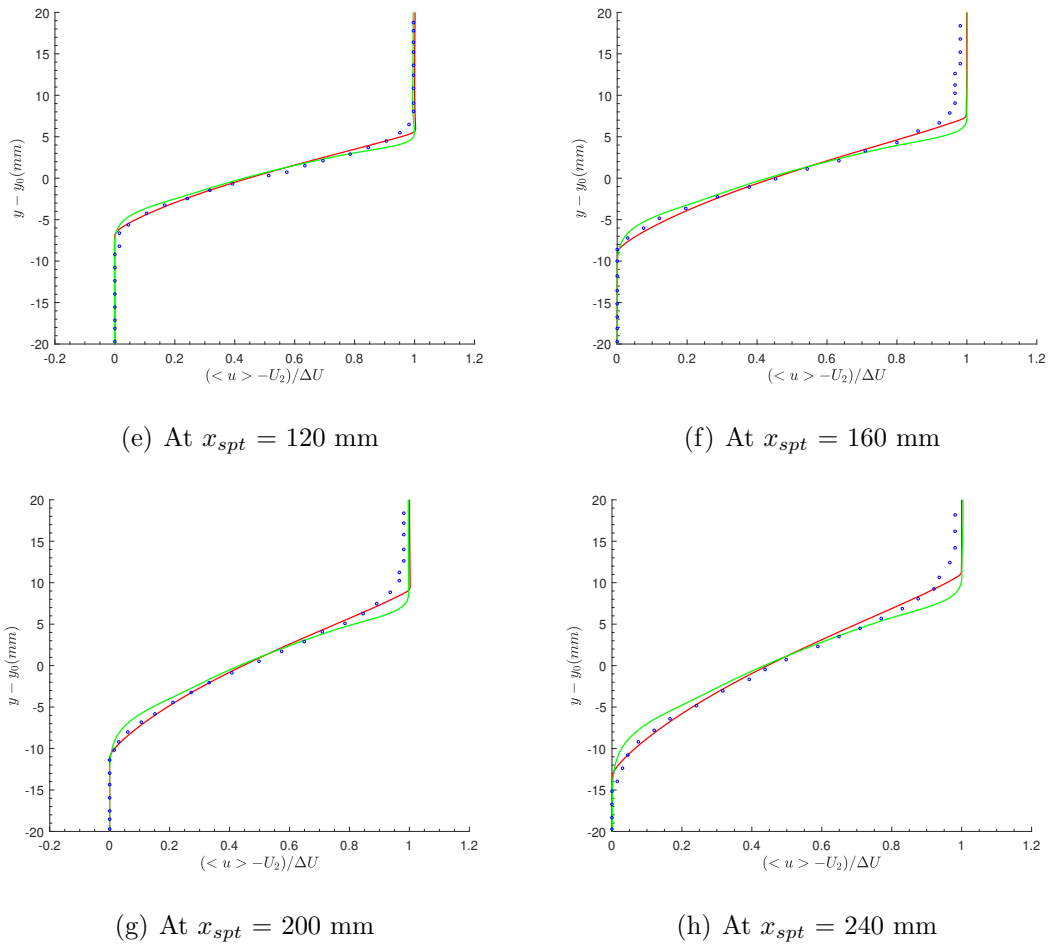


Figure 4.5 (cont.). Compressible mixing layer : RANS calculations : mean streamwise velocity profiles of the $k - \epsilon$ (red) and RSM (green) simulations compared with the experiments (scatter) at several streamwise locations.

Table 4.15. Compressible mixing layer : RANS calculations : comparison of $\frac{d\delta_b}{dx}$ with the experiment

Case	$\frac{d\delta_b}{dx}$	Percentage error w.r.t the experiment
$k - \epsilon$ model	0.07000	4.74 %
<i>RSM</i>	0.05455	18.37 %
Experimental	0.06683	-

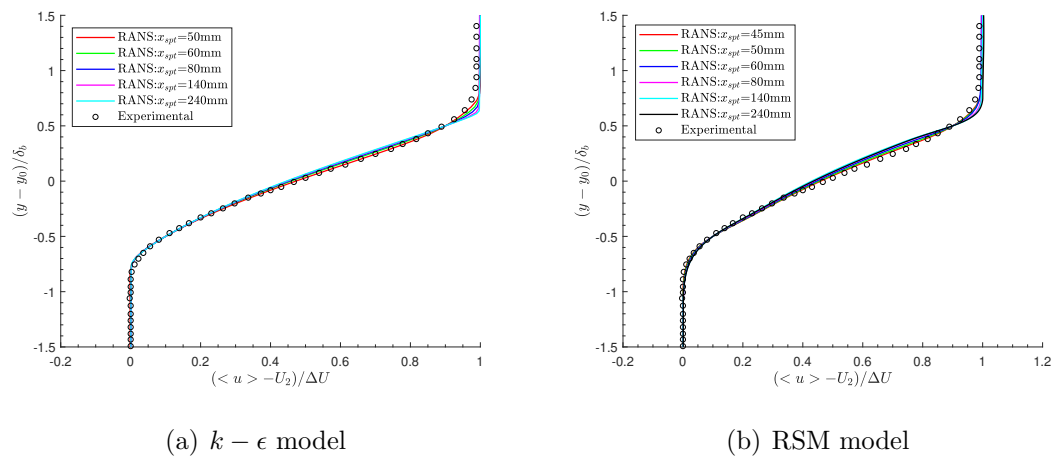


Figure 4.6. Compressible turbulent mixing layer : RANS studies: self-similar velocity profile.

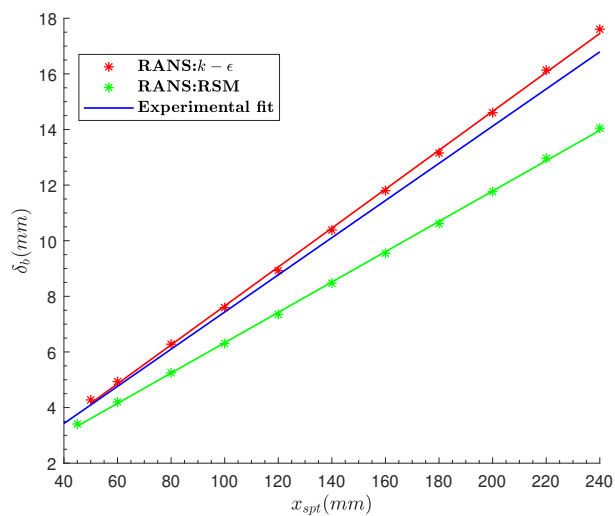


Figure 4.7. Compressible mixing layer : RANS calculations : δ_b comparison with the experiment.

peak TKE at all the locations. However, the TKE profiles of the $k - \epsilon$ model are in good agreement with the experimental profiles outside the location of the peak, whereas this is not the case with the RSM, as the value of the TKE is underpredicted throughout the shear layer. This discrepancy between these models is especially pronounced in the self-similar region of the mixing layer. This in turn could be the reason for the observed behavior of these two models with respect to the mixing layer growth rate.

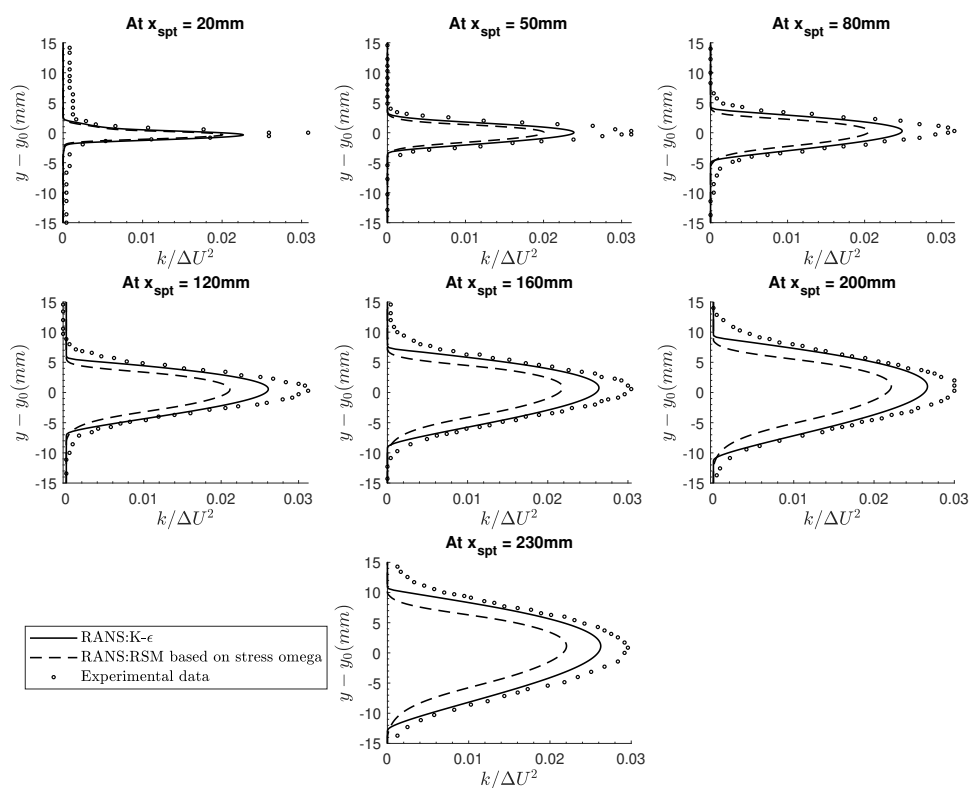


Figure 4.8. Compressible mixing layer : RANS calculations : comparison of TKE with the experiment.

The Reynolds stresses achieve self-similarity farther downstream than the mean streamwise velocity. The experiment reports that the Reynolds stresses are self-similar

in the region $200 \text{ mm} \leq x_{spt} \leq 230 \text{ mm}$. This is also observed in the present case with the RSM, as the non-dimensional Reynolds stresses (non-dimensionalized by ΔU^2) plotted against the self-similar scale $\frac{y-y_0}{\delta_b}$ stack on top of each other in this region as shown in figure 4.9. It should be noted that the information about the individual Reynolds stresses is available only in the simulation with the RSM as the $k - \epsilon$ turbulence model does not solve for the Reynolds stresses. The self-similar Reynolds stress profiles (obtained by averaging the profiles in figure 4.9) is plotted against its experimental counterpart and is shown in figure 4.10. The Reynolds stresses are underpredicted compared to the experiment, which is expected since the TKE was underpredicted. The magnitude of underprediction is the highest for the streamwise Reynolds stresses and is the least for the transverse Reynolds stress.

The variation of the pressure inside the test section at around $\sim 25 \text{ mm}$ below the splitter plate tip is shown in figure 4.11. Considering the information that there is a 1 kPa uncertainty in the experimental measurement of the test section pressure (obtained through private communication), the present RANS simulations are in reasonable agreement with the experiment, with the $k - \epsilon$ simulation again being better in agreement with the experiment compared to the RSM. The pressure at the test section entrance is higher in the RSM case which is consistent with the thinner boundary layer that is observed with this case. The mean freestream velocity of the primary and secondary streams and the convective Mach number M_c in the experiment given in 4.1 are reported to be measured in the region where the Reynolds stresses are fully developed ($200 \text{ mm} \leq x_{spt} \leq 230 \text{ mm}$). The freestream velocities and M_c in this range are given in tables 4.16 and 4.17 for the present RANS calculations. It could be seen that velocities and M_c in the present RANS calculations are in good agreement with the experimental results, with the $k - \epsilon$ model again performing superior compared to the RSM. It could be noted that the secondary stream velocity monotonically drops with distance downstream of the splitter plate tip, which is consistent with the pressure variation shown earlier. This monotonic decrease in U_2 was also observed in the experiment (obtained through private communication). The

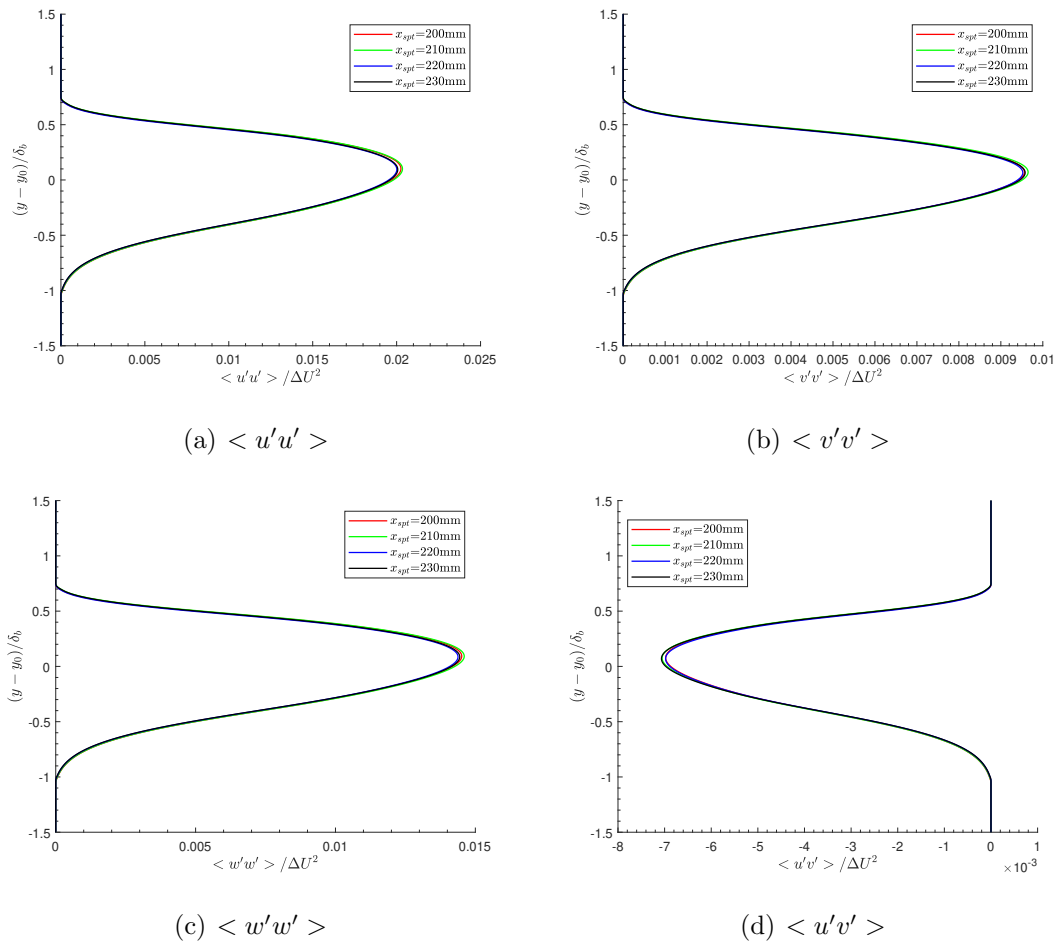


Figure 4.9. Compressible mixing layer : RANS calculations : Reynolds stresses.

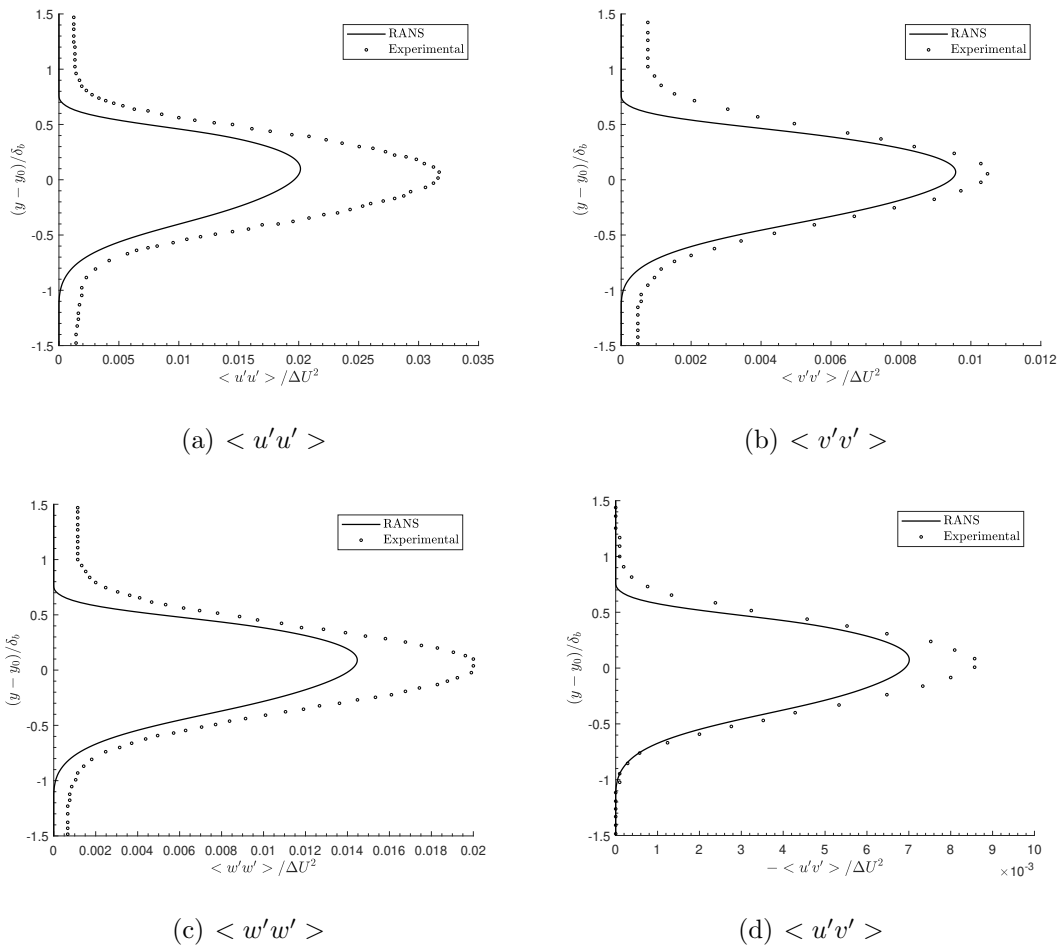


Figure 4.10. Compressible mixing layer : RANS calculations : comparison of self-similar Reynolds stress profiles with the experiment.

presence of weak shock waves in the primary stream could be the reason for variation in U_1 . The variation in M_c in table 4.17 is also attributed to the aforementioned reasons.

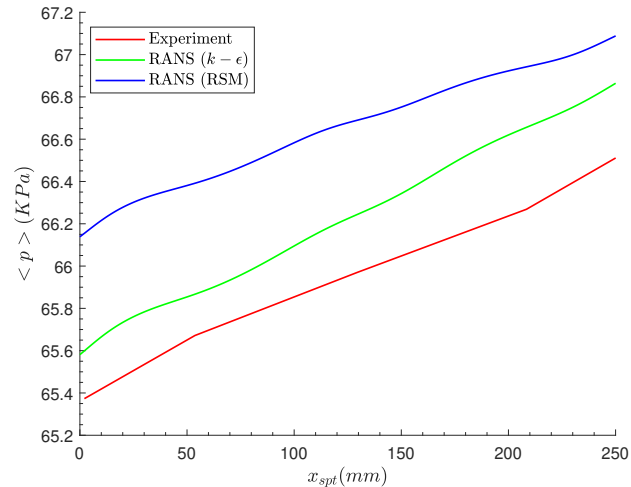


Figure 4.11. Compressible mixing layer : RANS calculations : variation of pressure inside the test section.

Thus, it could be concluded that the simulation with the $k - \epsilon$ model is in much better agreement with the experiment than the one with the RSM model. It could be tempting to conclude that this is a consequence of the fact that the initial simulations performed to tune the length of the inviscid wall and the boundary values of pressure for favorable boundary layer properties and the free stream velocities respectively, made use of the $k - \epsilon$ model. Though this could partially be the reason for the difference observed in the values of δ and the freestream velocities, it is debatable to conclude the same for the huge under prediction observed in the mixing layer thickness properties and the TKE/Reynolds stresses and other discrepancies observed in the simulation with the RSM. Further research needs to be done on this topic. Nevertheless, the only purpose of the current RANS calculations is to generate the inflow profiles and initial conditions for the LES calculations. Thus, in that perspective, the results presented here seem adequate.

Table 4.16. Compressible mixing layer : RANS calculations : mean freestream velocities U_1 and U_2

Case	At $x_{spt} =$							
	200 mm		210 mm		220 mm		230 mm	
	U_1	U_2	U_1	U_2	U_1	U_2	U_1	U_2
	$(m.s^{-1})$		$(m.s^{-1})$		$(m.s^{-1})$		$(m.s^{-1})$	
$k - \epsilon$ model	432.67	99.68	433.81	99.06	435.08	98.41	435.74	97.76
<i>RSM</i>	433.84	95.81	433.35	95.58	436.21	94.86	436.58	94.39

Table 4.17. Compressible mixing layer : RANS calculations : convective Mach number M_c

Case	M_c at $x_{spt} =$			
	200 mm	210 mm	220 mm	230 mm
$k - \epsilon$ model	0.537	0.540	0.543	0.545
<i>RSM</i>	0.545	0.544	0.551	0.552

4.3 LES of the Compressible Mixing Layer

In this section, an LES of the compressible mixing layer discussed in the previous sections is performed. It should be noted that the domain used for the LES study is shorter in the streamwise and spanwise directions compared to that from the experiments and the RANS calculations (in the streamwise direction, as RANS was performed in 2D), to reduce the simulation costs. The start of the physical domain in the streamwise direction in the LES study coincides with the primary and secondary stream nozzle exits. The end of the physical domain in the LES study is chosen around $x_{spt} \sim 250$ mm since the Reynolds stresses in the test section have become self-similar before this streamwise location in the experiments and in the RANS calculations and beyond which no turbulent statistical data is reported in the experiments. The spanwise extent is chosen based on considerations mentioned in the literature and will be discussed shortly. Next, the details regarding the simulation setup are presented followed by the results and discussions.

4.3.1 Flow Parameters

As mentioned earlier, the LES inflow planes (for the two streams) are the primary and secondary nozzle exits in the experiments and in the RANS calculations. The mean inflow profiles of the streamwise and cross-stream velocities, density and pressure are taken from the RANS calculations based on the $k - \epsilon$ turbulence model as it was observed in the previous section that the results of the RANS simulation with the $k - \epsilon$ model are in much better agreement with the experiment compared to the one with the RSM. The mean spanwise velocity is set to zero at the inflow. The inflow profiles of the mean streamwise velocity, cross-stream velocity and the mean density are shown in figures 4.12-4.14 respectively. The mean pressure profile (non-dimensionalized) set at the inflow is almost a constant with the average value being equal to 0.286 at the primary inflow and 0.289 at the secondary inflow. The maximum deviation of the mean pressure at the inflow from these average values is

less than 0.3 % for the primary side and less than 0.001 % at the secondary side. The reference length scale is chosen as the boundary layer thickness at the inflow plane at the splitter plate top, denoted as $\delta_{99,ref}$ and is equal to 1.54 mm. The reference flow variables are taken as the primary flow freestream variables at the inflow. The measurements of the other three boundary layer thicknesses at the inflow plane are given in terms of $\delta_{99,ref}$ in table 4.18. The reference Reynolds number and the reference Mach number are

$$Re_{ref} = 62251 \quad M_{ref} = 1.58$$

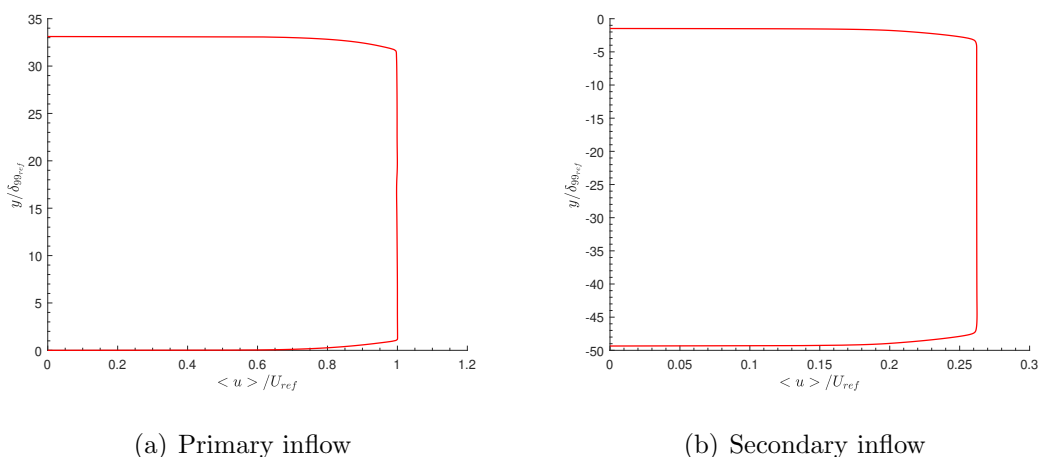


Figure 4.12. Compressible mixing layer : LES calculations : mean streamwise velocity profile at the inflow.

4.3.2 Domain Size

A five superblock Cartesian topology shown in figure 4.15 is used. The primary section extends from $y=0$ to $33.12 \delta_{99,ref}$ and leads into the mixing section. The splitter plate face at the splitter plate tip (which marks the beginning of the mixing section) extends from $y = 0$ to $\sim -0.33 \delta_{99,ref}$. The secondary section has a cross-stream height of $47.87 \delta_{99,ref}$ at the inflow plane to $49.03 \delta_{99,ref}$ at the splitter plate tip, tapered uniformly at its top face (i.e the splitter plate bottom) and leads into the

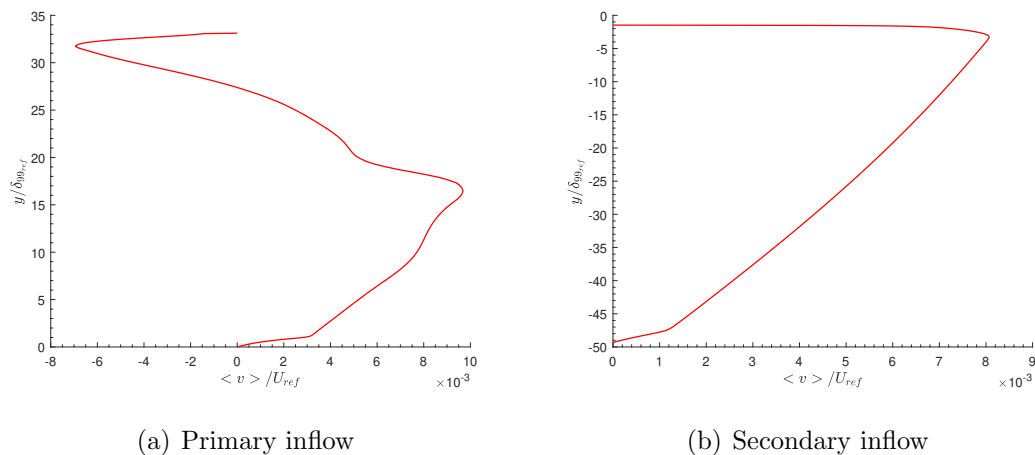


Figure 4.13. Compressible mixing layer : LES calculations : mean cross-stream velocity profile at the inflow. $\langle v \rangle$ is positive near the upper wall at the secondary inflow, since it tapers upwards.

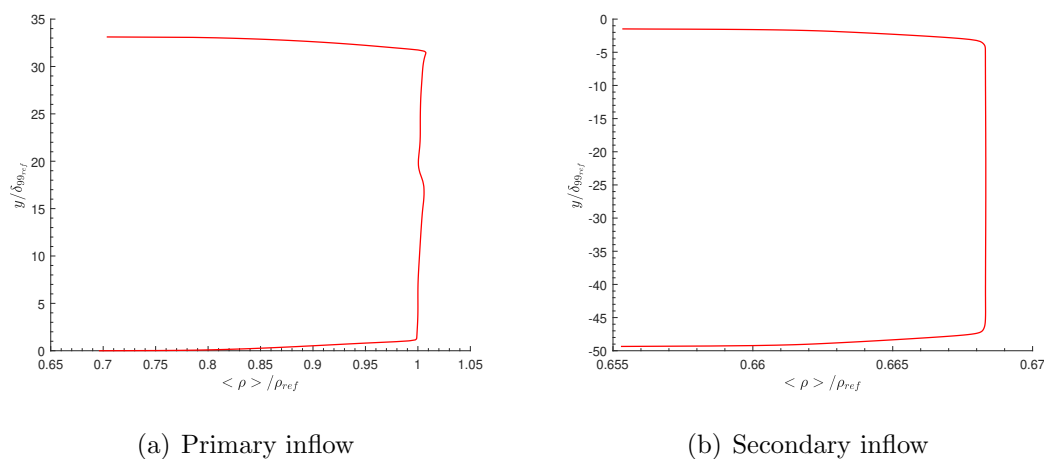


Figure 4.14. Compressible mixing layer : LES calculations : mean density profile at the inflow.

mixing section. Thus the mixing section has a uniform cross-stream height of $82.48 \delta_{99ref}$. All the above domain measurements match with the experimental domain in which the case in table 4.1 was performed.

Because of the turbulent inflow method used in the current study, a redevelopment of about 12 times the initial boundary layer thickness is needed for the turbulent

eddies to develop into realistic structures (though a length of 8 times the boundary layer thickness is found to work well for wall modeled flows, it is better to choose a conservative length of 12 times the boundary layer thickness at the inflow). Thus a constant height section with a streamwise extent of ~ 12 times the boundary layer thickness of the splitter plate top and bottom boundary layers at the inflow is added to primary and secondary sections respectively. It should be noted that these redevelopment lengths may not be sufficient for the primary section top wall and secondary section bottom wall boundary layers. However, the impact of these boundary layers on the mixing layer is minimal and it is essential to keep the simulation costs as low as possible. Thus the streamwise extent of the primary section is from $x = \sim -44.99 \delta_{99_{ref}}$ to $x=0$ and the secondary section extends from $x = \sim -52.99 \delta_{99_{ref}}$ to $x=0$. The streamwise extent of the mixing section (i.e from the splitter tip $x=0$) is $162.34 \delta_{99_{ref}}$ and is based on the considerations mentioned earlier. A buffer zone of length $20 \delta_{99_{ref}}$ is added at the end from $x=162.34 \delta_{99_{ref}}$ to $x=182.34 \delta_{99_{ref}}$, where a sponge zone is employed to damp out the vortices before reaching the outflow boundary that could cause the simulation to fail.

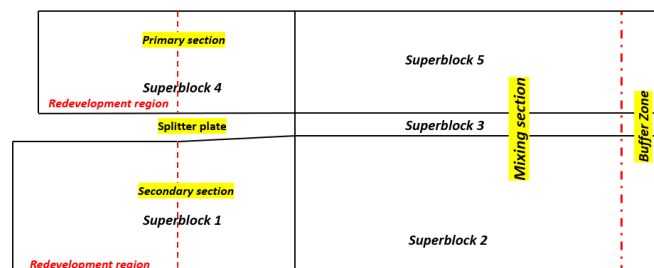


Figure 4.15. Compressible mixing layer : LES calculations : superblock topology (not drawn to scale).

The domain length in the spanwise direction is taken as $20 \delta_{99_{ref}}$ and is approximately equal to 10 times the mixing layer momentum thickness (which is measured

from the RANS calculations using the $k - \epsilon$ model) at the farthest downstream end of the physical domain. This criterion is based on the observations made in references [21, 30].

Table 4.18. Compressible mixing layer : LES calculations : boundary layer thickness at the inflow

Location	δ_{99} (in terms of $\delta_{99_{ref}}$)
Primary section top wall	1.38
Splitter plate bottom wall	1.68
Secondary section bottom wall	1.91

4.3.3 Grid Details

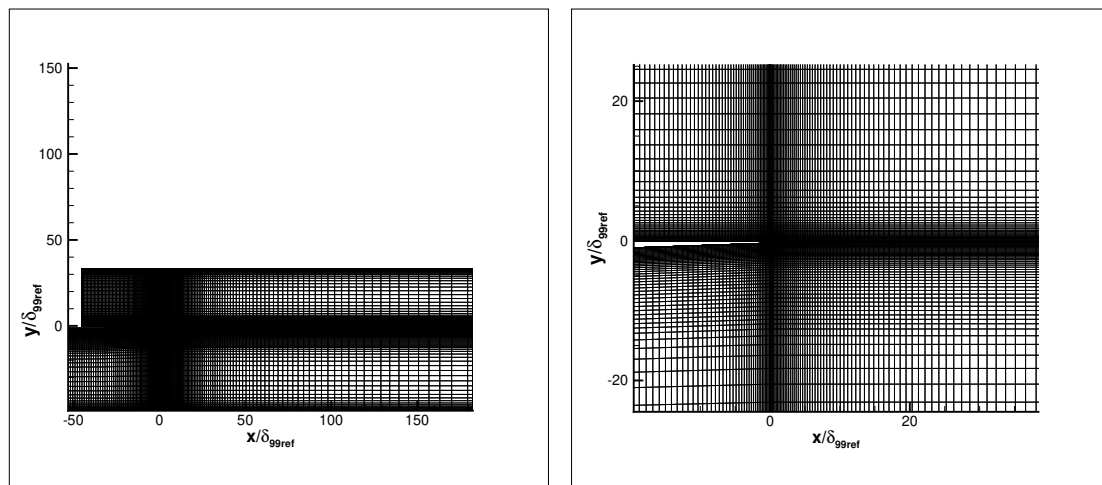
The grid details in each of the superblocks are shown in table 4.19. The grid is formed with the commercial software Pointwise. The grid resolution details in each of the directions will be explained now. It should be noted that some of these values may be slightly coarser than a similar LES study [21] performed at a slightly lower Reynolds number. But this was necessary to keep the computational costs at a reasonable level, especially when simulating two additional boundary layers on the mixing section top and bottom walls, which to the author's knowledge, has never been done before for mixing layers. This is also supported by the fact this is a preliminary simulation aimed at capturing a reasonable amount of physical details and estimating the cost of simulating a laboratory type mixing layer.

Spanwise direction

The grid spacing in the spanwise direction is taken as a constant spacing of $\Delta z = 0.1 \delta_{99_{ref}}$ which is finer than a similar LES study [21] performed at a slightly lower Reynolds number.

Streamwise direction

In the primary stream section, from $x=-44.99 \delta_{99_{ref}}$ to $x=-32.99 \delta_{99_{ref}}$ a constant spacing of $\Delta x = 0.1 \delta_{99_{ref}}$ is used. This is the redevelopment region for the boundary layer on the splitter plate top. This streamwise spacing is consistent with the recommendations for using wall models implemented in the current LES solver [38]. From $x=-32.99 \delta_{99_{ref}}$ (i.e start of the physical section) to $x=0$ (S.P. tip), the grid is smoothly refined from $\Delta x = 0.1 \delta_{99_{ref}}$ to $\Delta x = 0.02 \delta_{99_{ref}}$ with a maximum stretching ratio of ~ 1.006 . Similarly in the secondary stream section, a uniform spacing $\Delta x = \sim 0.17 \delta_{99_{ref}}$ is used from $x=-52.99 \delta_{99_{ref}}$ to $x=-32.99 \delta_{99_{ref}}$ and then the streamwise spacing is smoothly reduced to $\Delta x = 0.02 \delta_{99_{ref}}$ at the splitter plate tip with a maximum stretching ratio of ~ 1.007 . From $x=0$ to $x=162.34 \delta_{99_{ref}}$ (i.e in the test section), the grid is smoothly stretched from $\Delta x = 0.02 \delta_{99_{ref}}$ to $\Delta x = 0.8 \delta_{99_{ref}}$ with a maximum stretching ratio of ~ 1.005 . The Grid is highly stretched in the buffer zone with a maximum stretching ratio of ~ 1.06 .



(a) Entire domain

(b) Close to the splitter plate tip

Figure 4.16. Compressible mixing layer : LES calculations : grid structure: showing every 8th grid point.

Table 4.19. Compressible mixing layer : LES calculations : number of grid points in each superblock (total number of grid points ~ 221 million)

Superblock #	$N_x \times N_y \times N_z$	Approx. no of grid points (in millions)
1	519 x 458 x 201	48
2	819 x 458 x 201	75
3	819 x 16 x 201	3
4	619 x 329 x 201	41
5	819 x 329 x 201	54

Cross-stream direction

In the cross-stream direction, the grid spacing is tailored to refine the regions of the shear layer and the boundary layers. The edges of the shear layer at the end of the physical domain are inferred from the preliminary RANS calculations (based on the $k - \epsilon$ model) and are found to be from $y \sim -11.8 \delta_{99_{ref}}$ to $5.2 \delta_{99_{ref}}$ in the test section. This follows from the fact that outside this region the magnitude of the TKE was very low ($\sim 0.02\%$ of its maximum value in the shear layer at this location). Now the grid spacing in the cross-stream direction at the location of the splitter plate tip will be given. It should be noted that these values are used throughout the test section and are used in corresponding intervals in the primary and the secondary stream sections. From $y=0$ to $1 \delta_{99_{ref}}$, a constant spacing of $\Delta y = 0.02 \delta_{99_{ref}}$ is used. Hence the initial boundary layer on the splitter plate top is resolved with 51 grid points. From $y=1 \delta_{99_{ref}}$ to $5.2 \delta_{99_{ref}}$, the grid is smoothly stretched from $\Delta y = 0.02 \delta_{99_{ref}}$ to $\Delta y = 0.08 \delta_{99_{ref}}$ with a maximum stretching ratio of ~ 1.016 . The splitter plate face is resolved with ~ 18 grid points. Likewise, on the secondary side, from $y=-0.33 \delta_{99_{ref}}$ to $y = -2 \delta_{99_{ref}}$, a constant spacing of $\Delta y = 0.02 \delta_{99_{ref}}$ is used. This implies, that the initial boundary layer on the splitter plate bottom is resolved with about 84 grid points. From $y=-2 \delta_{99_{ref}}$ to $y=-11.8 \delta_{99_{ref}}$, the grid is smoothly stretched from Δy

$= 0.02 \delta_{99_{ref}}$ to $\Delta y = 0.08 \delta_{99_{ref}}$ with a maximum stretching ratio of about ~ 1.012 . The initial boundary layers on the top and bottom walls of the primary stream and secondary stream sections respectively are each resolved with about 31 points (in the cross-stream direction) that are uniformly spaced. Outside these above-mentioned regions, where the flow is likely to be irrotational, the grid is smoothly stretched with a maximum stretching ratio of ~ 1.035 .

It should be noted that it is not attempted here to resolve the boundary layer all the way to the wall. The Δy^+ for each of the boundary layers at the inflow is shown in table 4.20. A wall modeling approach is used to simulate the boundary layers. The wall model employed here, namely the generalized equilibrium wall model, is formulated to allow the location of the first grid point away from the wall to be within or below the log-law region [41].

Table 4.20. Compressible mixing layer : LES calculations : wall y^+ for each of the boundary layers at the inflow

Location	Δy^+
Secondary section bottom wall	~ 21
Splitter plate bottom wall	~ 7
Splitter plate top wall	~ 26
Primary section top wall	~ 62

4.3.4 Boundary Conditions and other Details

The digital filter based turbulent inflow boundary condition [39] is used at the inflow of both the primary stream and secondary stream sections to impose velocity and density fluctuations on the corresponding mean profiles throughout the inflow plane. As mentioned earlier, the mean profiles of the flow variables are taken from the RANS calculations based on the $k - \epsilon$ model. However, since information about the Reynolds stresses is not available from the $k - \epsilon$ model, the anisotropy of the

Reynolds stresses is taken from the RSM simulation and together with the turbulent kinetic energy from the simulation with the $k - \epsilon$ model, is used to construct the Reynolds stress profiles for the turbulent inflow boundary condition used in the LES. Since the boundary layer thicknesses in the RSM case are lower than that in the $k - \epsilon$ simulation, the profiles of the Reynolds stress anisotropy coefficients are stretched in the cross-stream direction by a factor proportional to the ratio of the boundary layer thickness between the two cases, when constructing the Reynolds stresses from the TKE. These Reynolds stress profiles are shown in figures 4.17 and 4.18. Based on previous work with this boundary condition [39], it was recommended that the integral length scales at the inflow be

$$[L_x, L_y, L_z] = [1.6, 0.4, 0.4]\delta_{99} \quad (4.3)$$

where δ_{99} is the boundary layer thickness at the inflow. This is followed in the current work for both the primary and secondary stream sections where δ_{99} in equation 4.3 is taken as the inflow boundary layer thickness on the splitter plate top and bottom walls respectively. Note that these length scales are used throughout the inflow plane and they may not be suitable for the boundary layers on the primary stream section top wall and secondary stream section bottom wall (as their thicknesses are different from the ones on the splitter plate). However, as noted earlier, the impact of these boundary layers on the growing shear layer will be minimal and also the length scales are only imposed approximately in the current inflow condition [39].

A characteristic-based subsonic outflow boundary condition is used at the outflow in the current simulation. It should be noted that the flow field at the outflow in the current simulation is composed of both subsonic and supersonic flows. Therefore, for points on the boundary where the flow is supersonic, the characteristic-based subsonic outflow boundary condition is not applied. Inside the sponge zone close to the outflow, the solution is forced to a smooth target solution which is taken as the RANS solution ($k - \epsilon$ model). This is done to smear out the vortices, which if allowed to reach the outflow plane, is found to cause instabilities. A generalized equilibrium wall model is used for all the walls except the one at the splitter plate face which is

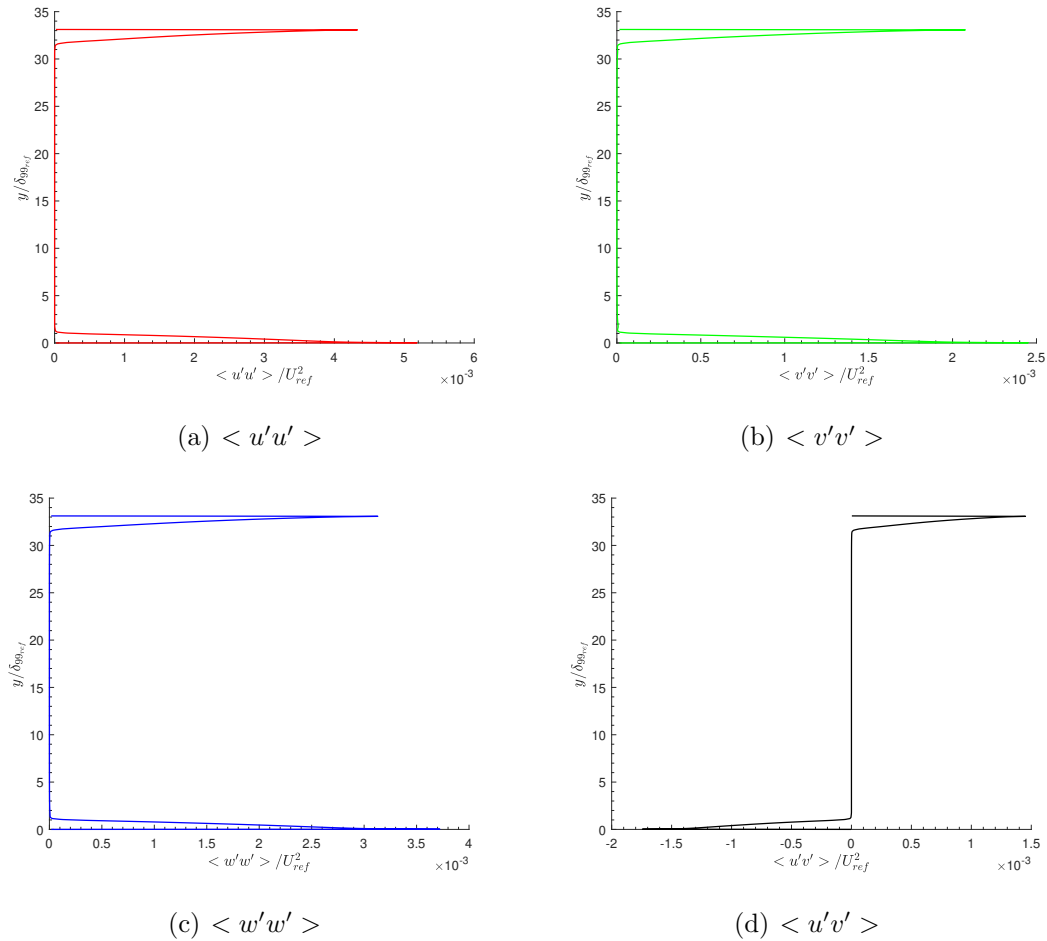


Figure 4.17. Compressible mixing layer : LES calculations : Reynolds stress profiles at the primary inflow.

taken as an isothermal wall with the temperature at this wall set equal to the average temperature at the splitter plate face obtained from the RANS calculations ($k - \epsilon$ model).

The RANS simulation (based on the $k - \epsilon$ model) is used as an initial condition for the LES calculations, as doing so was found to be effective in avoiding any instabilities that occur during the startup of the LES simulation [63]. The RANS solution is non-dimensionalized with the reference variables used in the LES and then it is interpolated on the LES grid to serve as an initial condition for the LES.

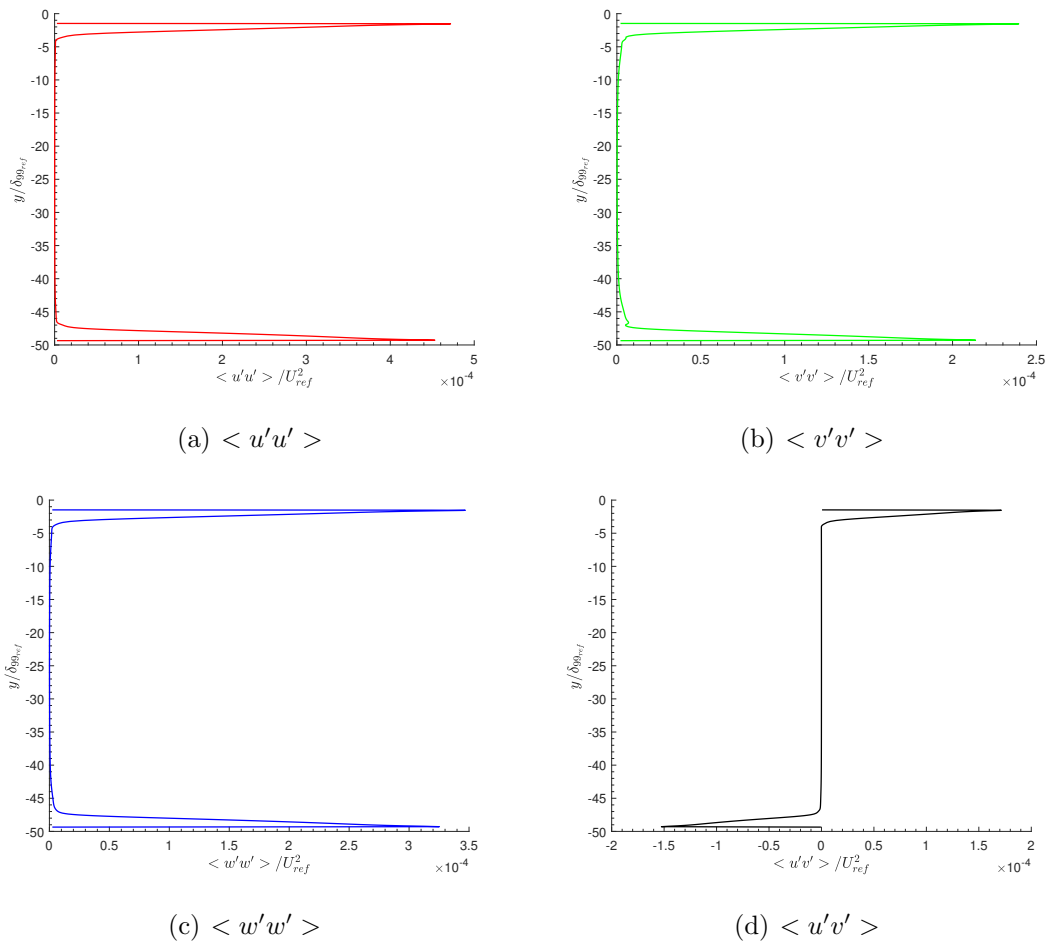


Figure 4.18. Compressible mixing layer : LES calculations : Reynolds stress profiles at the secondary inflow.

The WENO characteristic filters are used for shock-capturing in the present work. During the initial testing, the local application of the WENO characteristic filters caused the simulation to fail. This is probably because the Ducros shock detector was not able to detect the weak shock waves in the simulation to be able to apply the filter locally at those locations. Hence for this simulation, the WENO characteristics filters are applied globally everywhere in the flow field, though this becomes very expensive (by a factor of ~ 1.86). The non-dimensionalized time step (non-dimensionalized using the reference velocity and the reference length scale) chosen here is $\Delta t = 0.0075$. This is because of the explicit time-stepping procedure used

in the current methodology. The CFL number in each of the directions is limited to ~ 1 and the maximum CFL number obtained with this time step for this case is $(\text{CFL}_x, \text{CFL}_y, \text{CFL}_z) = (0.63, 0.48, 1.01)$.

4.3.5 Simulation Cost

The number of timesteps required to flush the initial conditions out of the computational domain is around 120k. It is desirable to collect statistics from this point and the samples are collected every timestep thereafter. The statistics are collected for about 355k timesteps. In this time window, a particle with the convective velocity will travel the mixing section approximately 10 times. This averaging period is based on the recommendations of Mankbadi et al. [64]. The CPU time per timestep using 6384 cores is around 0.37s for the global application of the WENO filters. This results in the simulation cost being around 308K core hours. A part of this simulation was performed on Purdue’s RCAC community cluster “Brown” and the rest was performed on Stampede 2 at TACC through an XSEDE allocation.

4.3.6 LES : Results and Discussion

Instantaneous flow field data

The instantaneous non-dimensional u contours are shown in figure 4.19. There are weak oblique shocks in the test section which interact with the shear layer. The shock wave that originates from the inflow disrupts the boundary layers as inferred through the non-dimensional density contours in figure 4.20. This occurs because the inflow is supersonic and starts with a turbulent boundary layer that disturbs the supersonic flow. Further research needs to be done to avoid this strong shock wave and the consequent SWBLI. This is necessary as it could change the state of the boundary layer on the splitter plate top which plays a major role in the growing shear layer downstream. Furthermore, this shock wave also gets reflected into the mixing section

and eventually interacts with the growing shear layer. It is important to avoid such interactions to be able to get results closer to the reference experiment.

Figure 4.21 shows the instantaneous ω_z contours. The evolution of the turbulent boundary layers on the four walls and the turbulent shear layer in the mixing section could be clearly inferred. The vortex structures present in the shear layer are smeared out in the sponge zone (separated by a red dotted line from the physical domain in figure 4.21) aiding in numerical stability. The mixing of the two turbulent boundary layers, evolving on the splitter plate walls, at the splitter tip could be seen in figure 4.21(b). Additionally, it could also be observed that the vorticity from the outer regions of these turbulent boundary layers is shed directly into the growing shear layer close to the splitter tip.

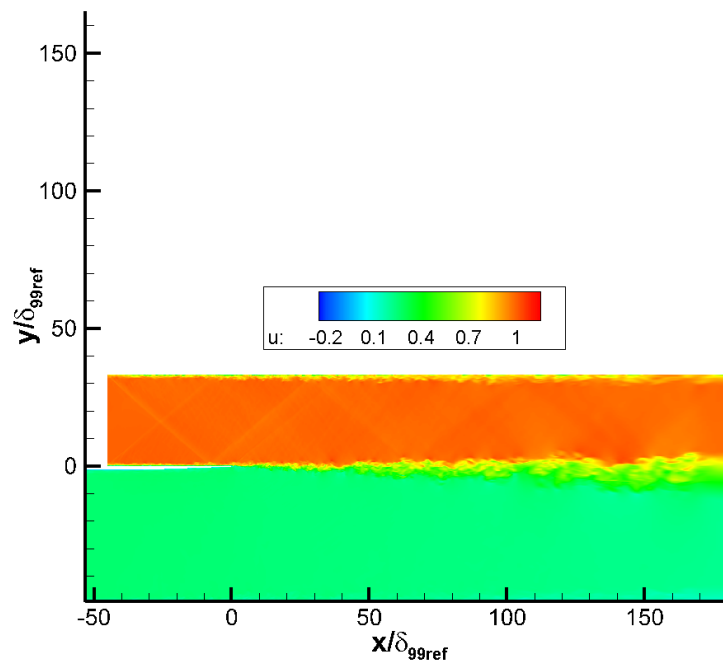


Figure 4.19. Compressible mixing layer : LES : instantaneous u contours.

The second invariant of the velocity gradient tensor, Q is a popular parameter used to visualize the vortex structures present in the flow field. Vortex structures are

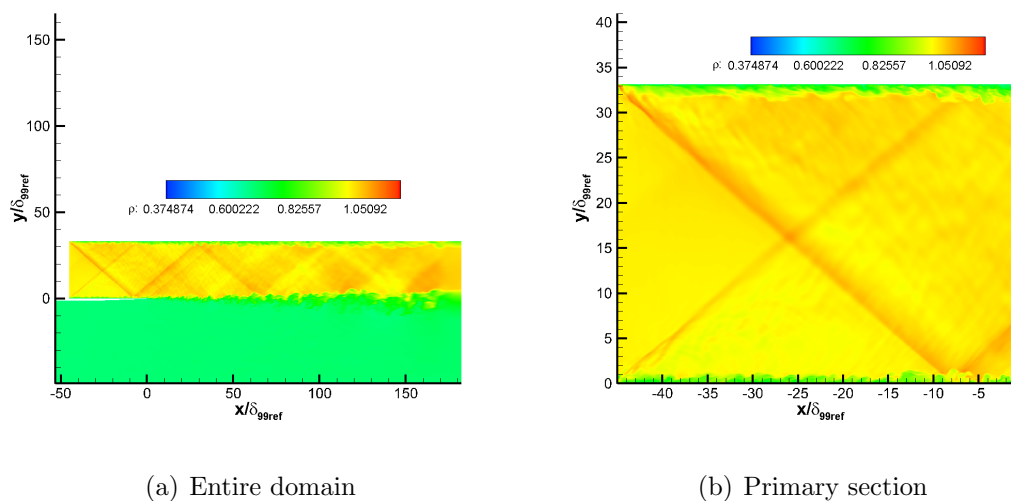


Figure 4.20. Compressible mixing layer : LES : instantaneous density contours.

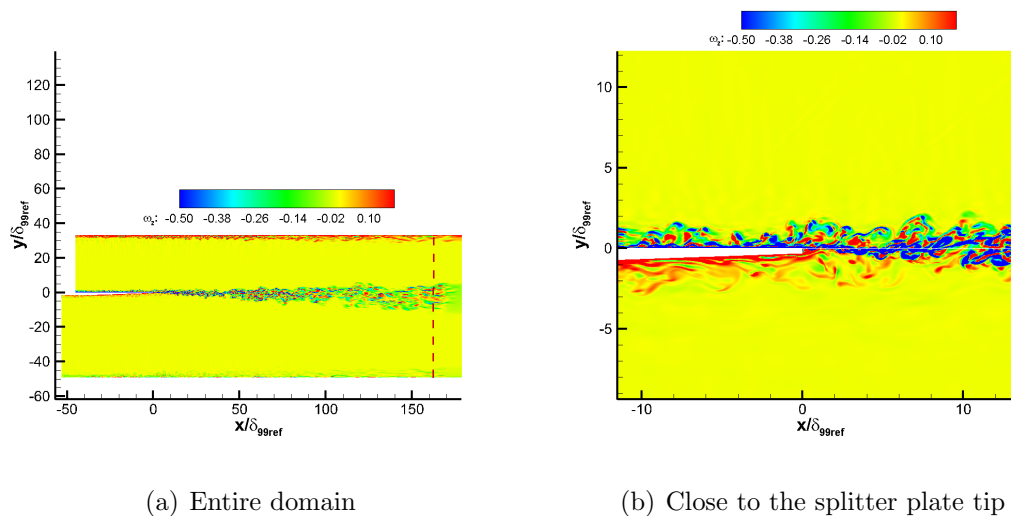


Figure 4.21. Compressible mixing layer : LES : ω_z contours.

identified as regions of the flow field where $Q > 0$, which implies that the vorticity magnitude is higher than the magnitude of the rate of strain in those regions [65]. The iso-surface of Q for the boundary layers on the splitter plate top and bottom walls are shown in figures 4.22 and 4.23 respectively. After a short redevelopment region, a large number of hairpin vortex structures, typical of a turbulent boundary layer, could

be seen in both the cases. Thus, this observation bolsters the fact that the boundary layers mixing at the splitter plate tip are turbulent and consist of flow features that are physically present in turbulent boundary layers. These hairpin vortices are convected into the mixing section as observed in figure 4.24(b) and 4.25(b) and consequently, the near field of the shear layer is largely three-dimensional as opposed to a mixing layer evolving from laminar initial conditions. The size of these hairpin vortex structures become larger further downstream inside the mixing section as seen in figures 4.24(a) and 4.25(a). The streamwise elongated structures present in these boundary layers break down into finer structures past the splitter plate tip [6], as could be observed in figures 4.26(a) and 4.27. This was also reported in the LES of Sharma et al. [6]. The thin region of reduced vorticity magnitude on the splitter plate top observed around $x \sim -8$ (in figure 4.26(a)) is probably due to the shock wave impinging on the boundary layer around this location, as evident from the rise in pressure observed in the pressure contours shown in figure 4.26(b). It is interesting to observe (in figure 4.26(a)) the presence of thin spanwise elongated structures in the boundary layer on the splitter plate top (high-speed flow) near to the splitter plate tip ($x=0$). These structures could also be observed in figure 4.28. Note that these are not present in the boundary layer of the low-speed stream on the splitter plate bottom as could be inferred from figures 4.27 and 4.29. Though the origin of these structures is not clear, they are likely to be the result of the shock boundary layer interaction that occurs upstream of the splitter plate tip (as inferred in 4.20), as they start to appear near this location. The exact mechanism involved could not be clearly studied as the flow is not resolved all the way to the wall but is rather modeled near the wall through the use of a wall model. Though these structures are convected into the mixing section, they get dissipated quite quickly within a short distance from the splitter plate tip as observed in figure 4.28.

The re-circulating region that exists close to the splitter plate face could be observed in figure 4.30. As mentioned earlier, the mixing layer is three dimensional right from the splitter plate tip. In order to visualize the instantaneous velocity field

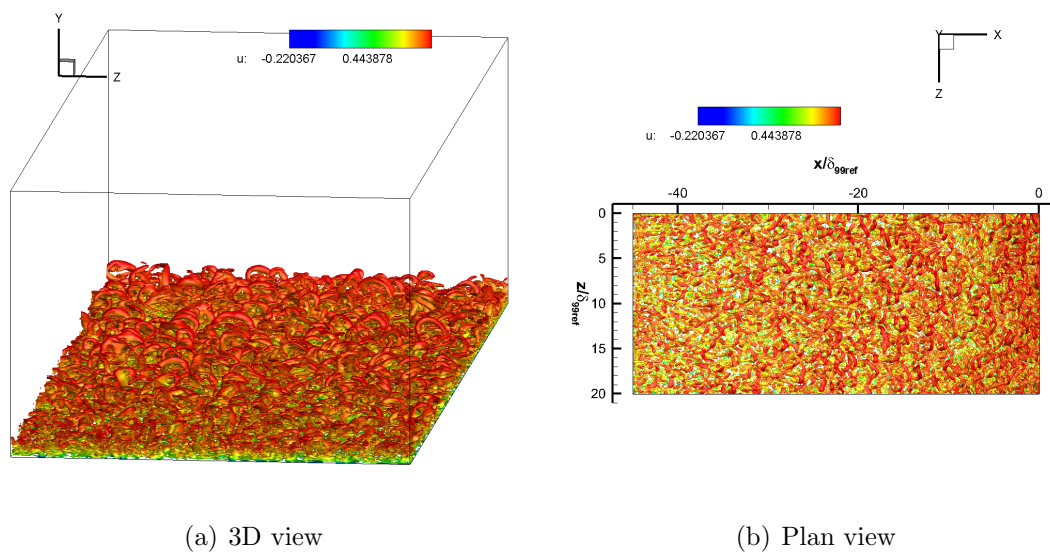


Figure 4.22. Compressible mixing layer : LES : iso-surface of $Q=0.03 \left(\frac{\Delta U}{\delta_{99ref}}\right)^2$ colored by the non-dimensionalized streamwise velocity for the boundary layer on the splitter plate top.

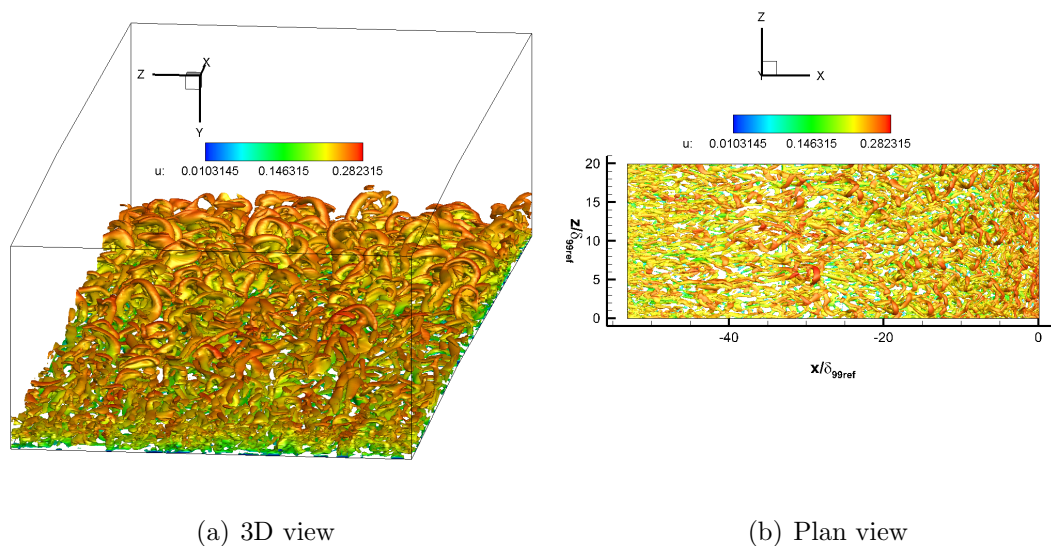


Figure 4.23. Compressible mixing layer : LES : iso-surface of $Q=0.001 \left(\frac{\Delta U}{\delta_{99ref}}\right)^2$ colored by the non-dimensionalized streamwise velocity for the boundary layer on the splitter plate bottom.

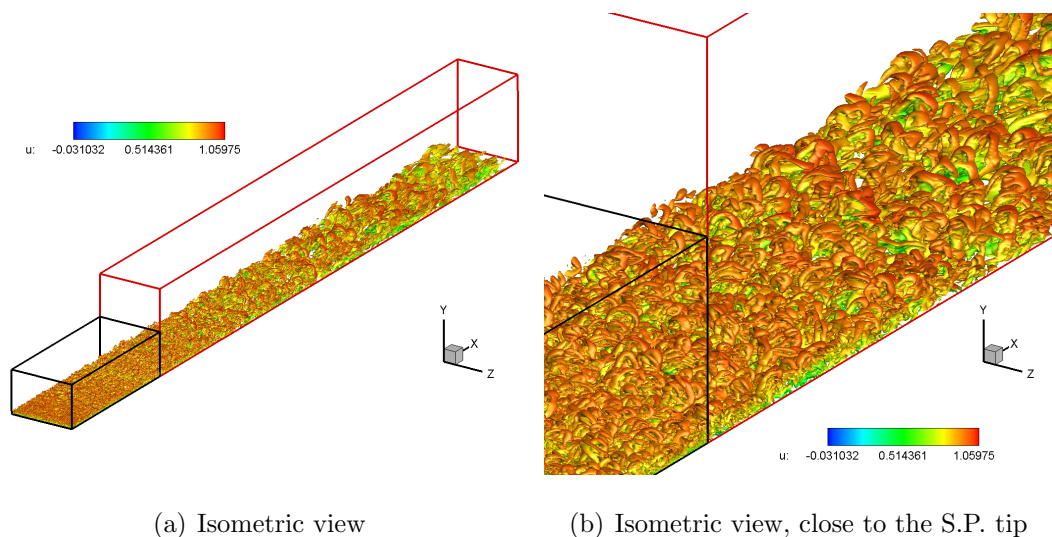


Figure 4.24. Compressible mixing layer : LES : iso-surface of $Q=0.001 \left(\frac{\Delta U}{\delta_{99_{ref}}} \right)^2$ colored by the non-dimensionalized streamwise velocity for the boundary layer on the splitter top leading into the mixing section (high speed side). Only a short portion of the primary (boxed in black) and mixing sections (high speed side, boxed in red) in the cross-stream direction is shown for the sake of brevity.

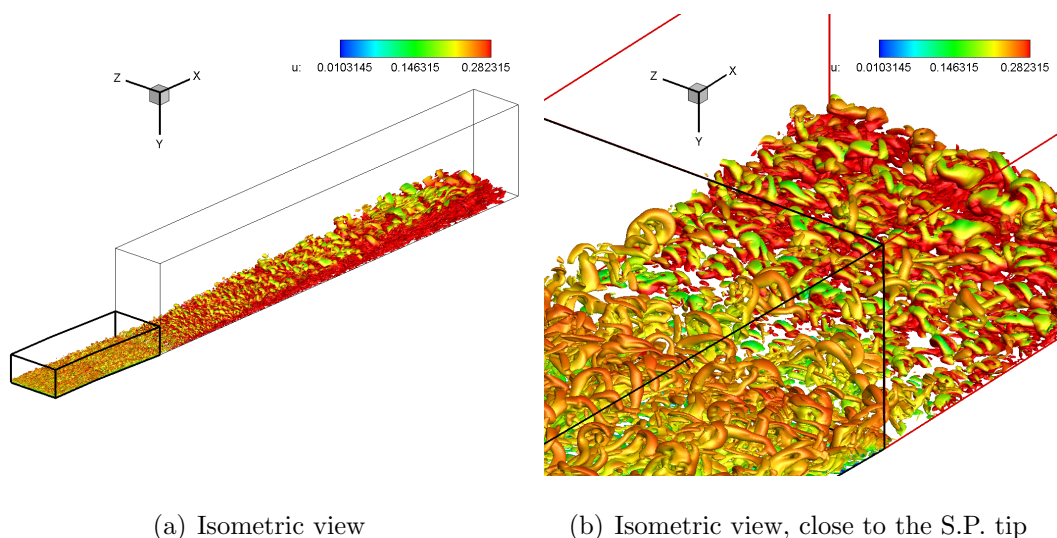


Figure 4.25. Compressible mixing layer : LES : iso-surface of $Q=0.001 \left(\frac{\Delta U}{\delta_{99_{ref}}} \right)^2$ colored by the non-dimensionalized streamwise velocity for the boundary layer on the splitter plate bottom leading into the mixing section (low speed side). Only a short portion of the secondary (boxed in black) and mixing sections (low speed side, boxed in red) in the cross-stream direction is shown for the sake of brevity.

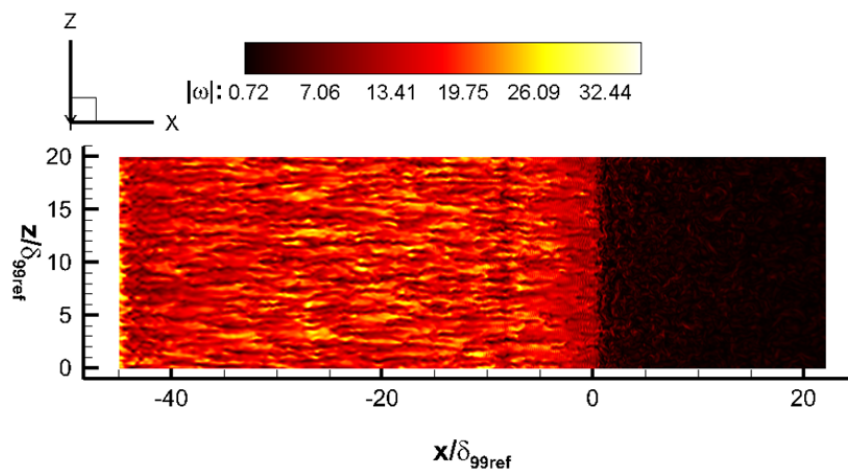
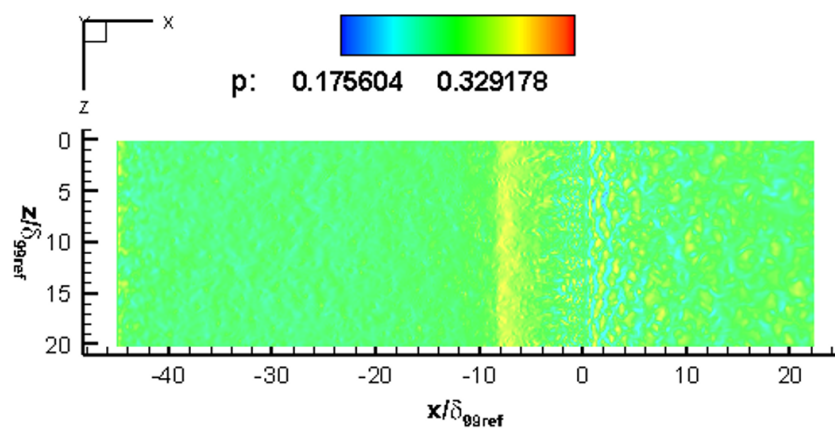
(a) $|\omega|$ (b) p

Figure 4.26. Compressible mixing layer : LES : instantaneous vorticity magnitude, and pressure contours shown for the plane of the splitter plate top and the adjoining plane in the mixing section.

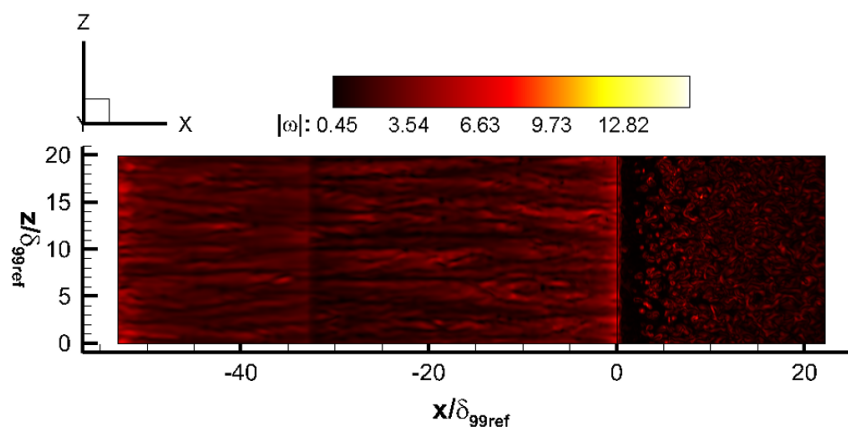


Figure 4.27. Compressible mixing layer : LES : instantaneous vorticity magnitude contours shown for the plane of the splitter plate bottom and the adjoining plane in the mixing section at $y = -0.33$.

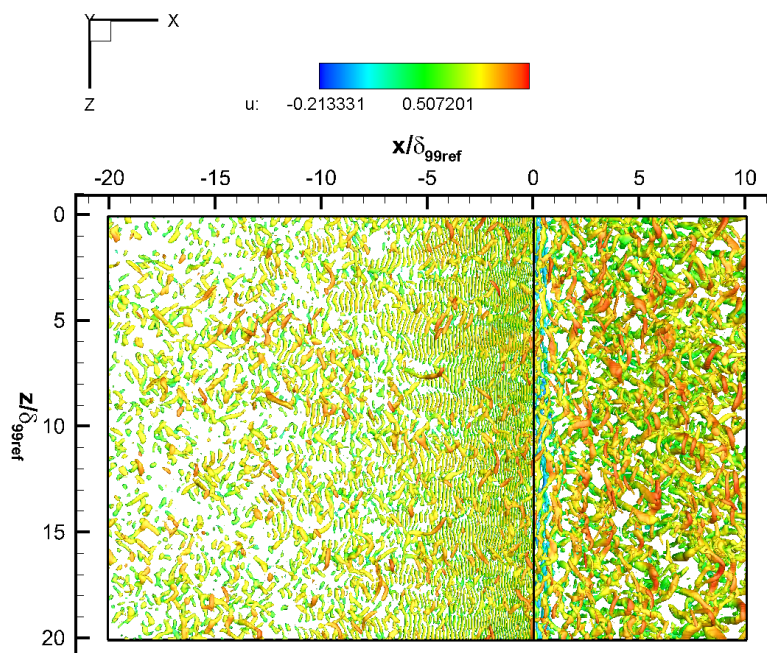


Figure 4.28. Compressible mixing layer : LES : iso-surface of $Q=0.3$ $\left(\frac{\Delta U}{\delta_{99ref}}\right)^2$ (colored by the non-dimensionalized streamwise velocity) shown for the plane of the splitter plate top and the adjoining plane in the mixing section.

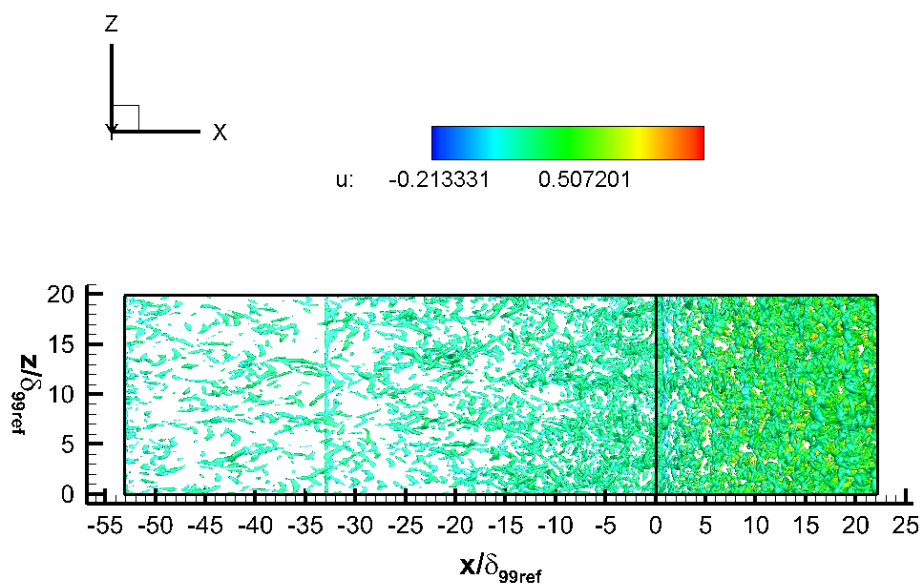


Figure 4.29. Compressible mixing layer : LES : iso-surface of $Q=0.001$ $(\frac{\Delta U}{\delta_{99ref}})^2$ (colored by the non-dimensionalized streamwise velocity) shown for the plane of the splitter plate bottom and the adjoining plane in the mixing section at $y = -0.33$.

relative to the convective structures present in the mixing layer, the convective velocity U_c (defined as in [11]) is subtracted from the instantaneous streamwise velocity and is shown in figure 4.31 at four different streamwise regions. Elliptic structures entraining fluid into the mixing layer from the low-speed and high-speed streams could be clearly seen in the near field region (figure 4.31(a)) of the mixing layer. The entrainment into the mixing layer could be observed through the streamlines with arrowheads indicating the direction of the flow. Further downstream, these elliptic structures appear to grow in size. Note that these observations are in direct agreement with what was observed in the reference experiment [11]. These elliptic structures appear more disorganized in the downstream stations (figures 4.31(b)-4.31(d)) due to the highly three-dimensional nature of the flow field.

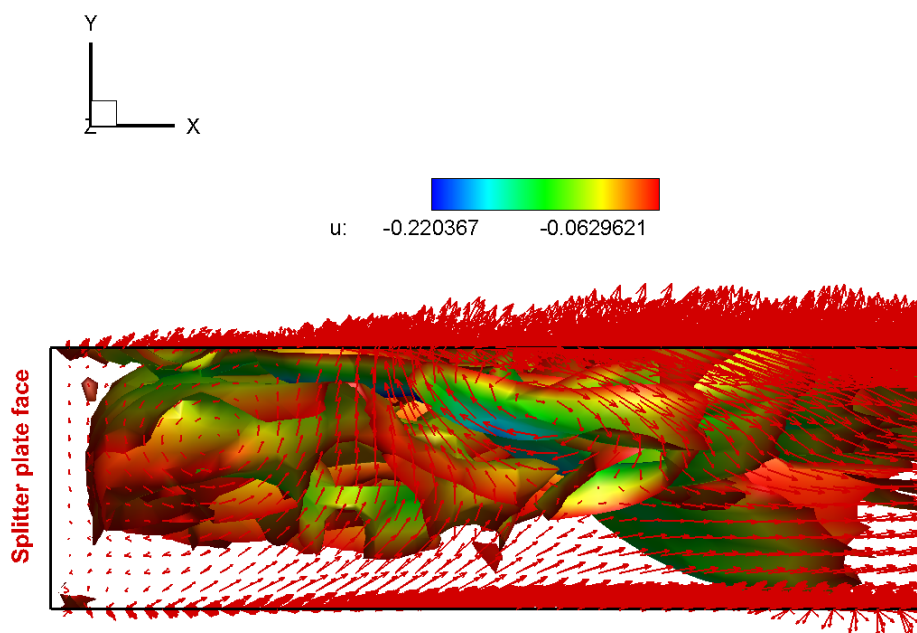


Figure 4.30. Compressible mixing layer : LES : velocity vectors close to the splitter plate face shown together with the iso-surface of $Q=0.1$ $\left(\frac{\Delta U}{\delta_{99_{ref}}}\right)^2$ (colored by the non-dimensionalized streamwise velocity) in regions where the streamwise velocity is negative.

Thus the instantaneous data seem to indicate the presence of fluid structures that are typically present in boundary layers and mixing layers and are in agreement with

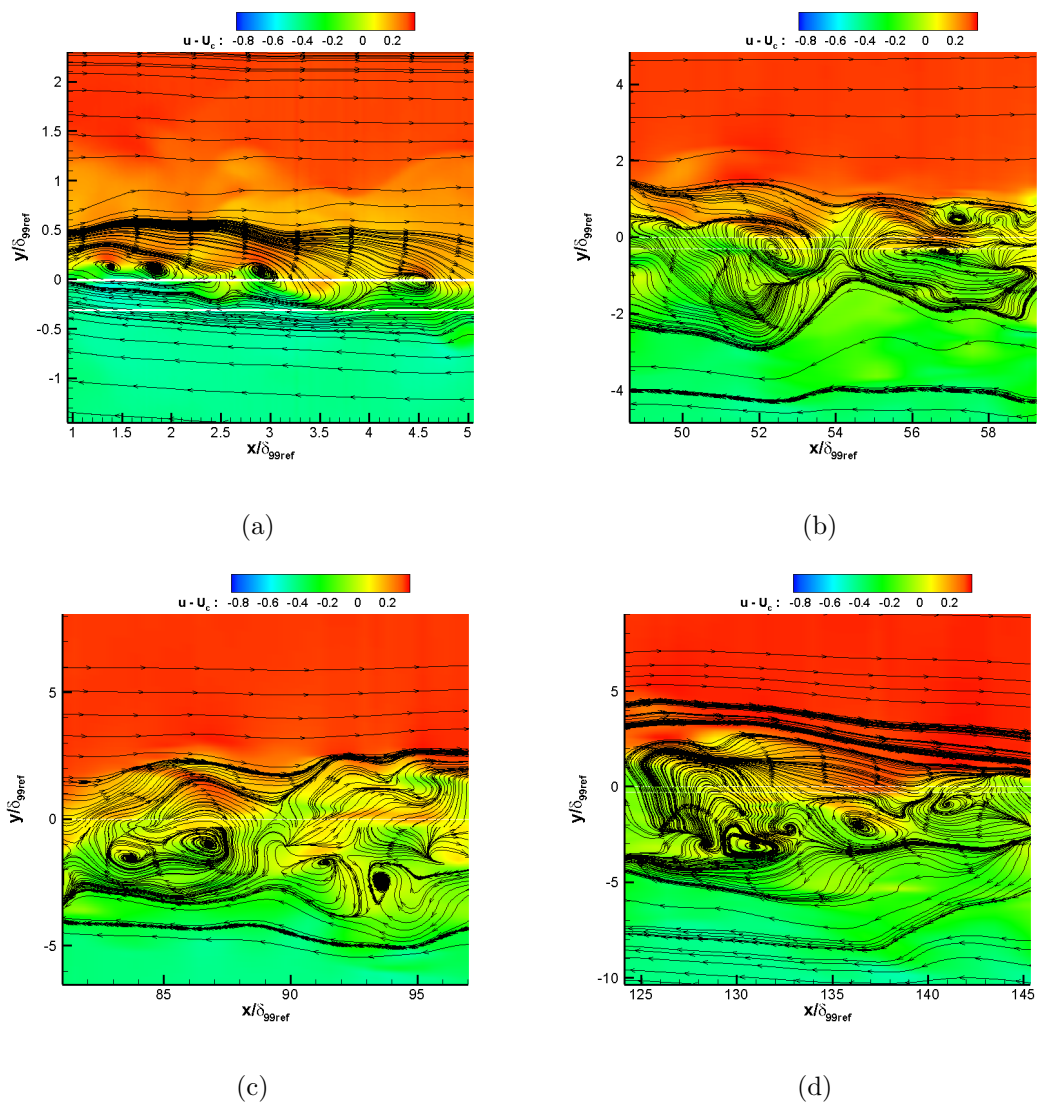


Figure 4.31. Compressible mixing layer : LES calculations : $u - U_c$ contours with streamlines in the growing shear layer, shown at a given spanwise plane.

what is found in the literature. Next, the flow statistics are analyzed and compared with the reference experiment.

Effect of statistical sample size

As mentioned earlier, the statistics are collected for about 355k timesteps. It is important to ensure that the collected statistics are independent of the sample size. Hence for this purpose, the collected statistics are averaged temporally and spatially in the spanwise direction for three different sample sizes as in table 4.21 and is analyzed to ensure that they are converged.

Table 4.21. Compressible mixing layer : RANS calculations : sample sizes for analysis of statistical convergence

Case ID	Sample size (in no. of timesteps)	No. of times a particle with convective velocity traverses the mixing section in this time window
S1	~ 205K	~ 6
S2	~ 275K	~ 8
S3	~ 355K	~ 10

The boundary layer thickness (using the procedure mentioned in section 4.2.2) and the skin friction coefficient (equation 4.2) derived from the mean profiles of the flow variables using the three sample sizes, at a specific streamwise location upstream of the splitter plate tip, are shown in the table 4.22. It should be noted that the wall shear stress is estimated using the ‘Clauser Plot method’ [66] (using the derivative of the velocity profile at the wall to measure the wall shear stress resulted in values that are too small due to the coarse grid spacings used near the wall). This method works consistently for boundary layers at some streamwise stations/walls and not for others. This inconsistency is probably due to the use of a wall model and/or

flow acceleration effects observed close to the splitter plate tip (more on this later). Further research needs to be done on this aspect. It could be seen that the boundary layer properties are almost the same for all three sample sizes, indicating that the statistics are well converged for the incoming boundary layers. The variation of the shear layer thickness (δ_b , obtained using the mean streamwise velocity) inside the mixing section is shown in figure 4.32. δ_b is almost the same for all the three sample sizes. A linear fit to δ_b in the range shown in figure 4.32 gives the growth rate of the shear layer and is shown in table 4.23. The growth rate obtained using all the three samples sizes are very close. These results indicate that the first-order statistics are well converged for all the three sample sizes.

Table 4.22. Compressible mixing layer : LES calculations : δ and C_f at $x/\delta_{99_{ref}} = 0$, obtained using the three different sample sizes

Location	S1		S2		S3	
	$\delta/\delta_{99_{ref}}$	C_f	$\delta/\delta_{99_{ref}}$	C_f	$\delta/\delta_{99_{ref}}$	C_f
Splitter plate top	1.56	0.00137	1.56	0.00137	1.56	0.00137
Splitter plate bottom	1.95	0.00344	1.95	0.00345	1.96	0.00345

The Reynolds stresses obtained using the three different sample sizes under consideration are shown at two streamwise stations, one near the center of the mixing section and the other towards the end in figures 4.33 and 4.34 respectively. At the first station (figure 4.33) it could be seen that the Reynolds stresses obtained using the sample sizes S2 and S3 are almost the same, whereas that obtained using sample size S1 is slightly lower at the peak, though all the Reynolds stresses obtained using all the three sample sizes are reasonably close. At the second station (figure 4.34), though the agreement between Reynolds stresses obtained using samples sizes S2 and S3 may not as good as in figure 4.33 (note that, as mentioned earlier, the turbulent statistics at downstream locations usually take much longer to converge compared to those at upstream locations), the profiles obtained using all the three sample sizes are

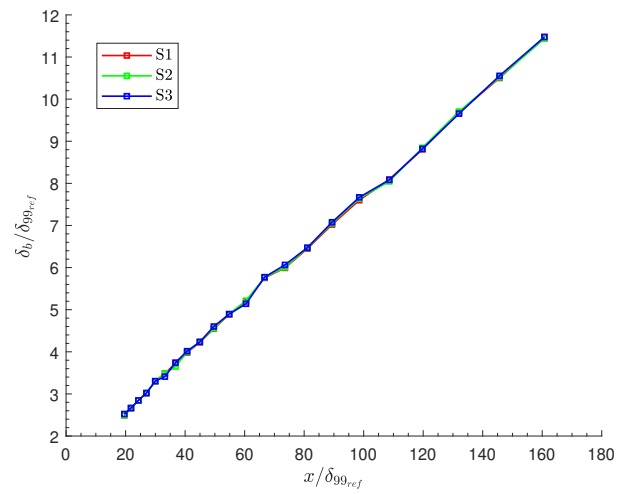


Figure 4.32. Compressible mixing layer : LES calculations : variation of δ_b inside the mixing section obtained using the three different sample sizes.

still reasonably close. Hence, it could be concluded that the second-order statistics are reasonably converged, especially for the larger two sample sizes.

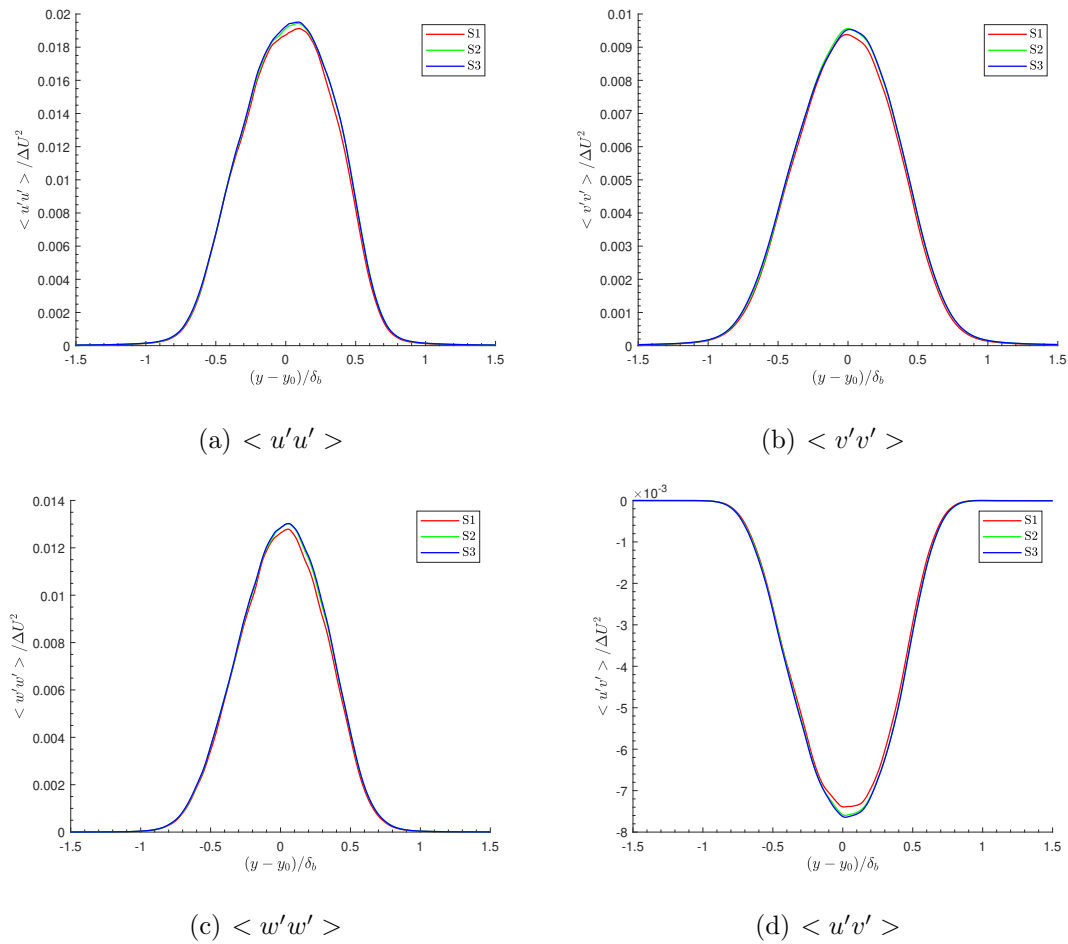


Figure 4.33. Compressible mixing layer : LES calculations : Reynolds stresses at $\frac{x}{\delta_{99_{ref}}} \sim 80$ obtained using the three different sample sizes.

Thus the results presented in this part indicate that the total sampling duration (S3 in table 4.21) used in the present LES calculations is adequate. Hence these collected statistics are averaged temporally and spatially in the spanwise direction and the results are compared against the results of the RANS calculations and the reference experiment and are presented next.

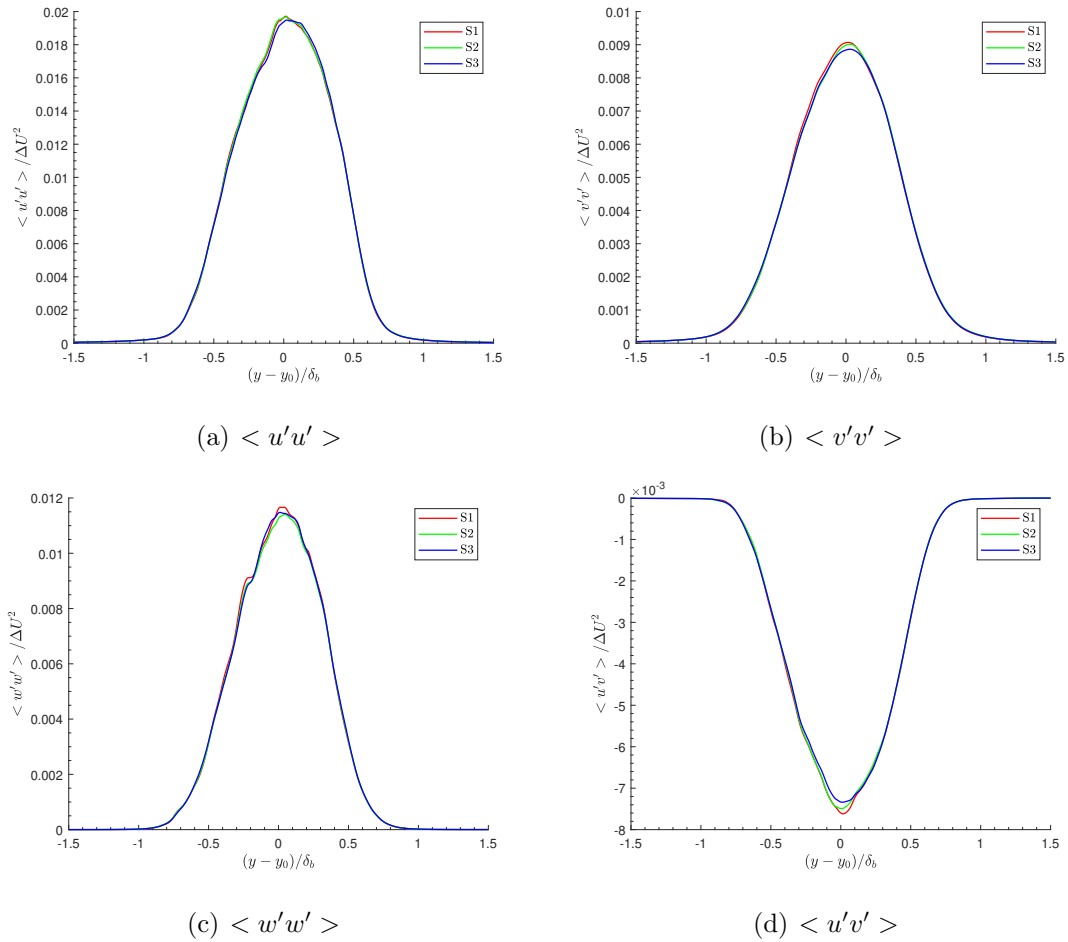


Figure 4.34. Compressible mixing layer : LES calculations : Reynolds stresses at $\frac{x}{\delta_{99_{ref}}} \sim 150$ obtained using the three different sample sizes.

Table 4.23. Compressible mixing layer : LES calculations : $\frac{d\delta_b}{dx}$ obtained using the three different sample sizes

Case ID	$\frac{d\delta_b}{dx}$
S1	0.06276
S2	0.06280
S3	0.06286

Comparison with RANS and the reference experiment

In this part, the results of the LES calculations are dimensionalized (wherever applicable) for the purpose of making comparisons with the reference experiment and the results of the RANS calculations. Tables 4.24 and 4.25 show the boundary layer thicknesses and the skin friction coefficients compared against the reference experiment. Excellent agreement with the experiment is observed for all of the boundary layers except the one on the splitter plate bottom, for which the boundary layer thickness is thinner compared to the experiments. The reason might be that the flow close to the splitter plate bottom accelerates near the splitter plate tip as is evident by the thinning of the boundary layer. Note that this was also observed in the RANS calculations though the flow close to the splitter plate top was also found to accelerate near the splitter plate tip in RANS calculations, an effect which is not observed in the LES. Inferring from table 4.25, the skin friction coefficient in the present LES is in reasonable agreement (at least the ones on the splitter plate) with the experiment though they are being underpredicted. This is probably because of the coarse grids that are used in the present case close to the wall as the flow is modeled near the wall using a wall model.

The length of the recirculation zone that exists close to the splitter plate tip is inferred through the time-averaged and spanwise averaged contours of streamwise velocity embedded with streamlines as shown in figure 4.35. This length is found to be $\sim 0.6 \delta_{99_{ref}}$ or ~ 0.40 times the boundary layer thickness on the splitter top at the splitter plate tip. Unfortunately, no data is available from the experiment for comparing the length of this recirculation zone.

The variation of pressure inside the mixing section at ~ 25 mm below the splitter plate tip is shown in figure 4.36. The pressure variation in the LES case approximately matches that of the RANS simulation with the $k - \epsilon$ model, which is expected since the inflow profiles of the flow variables for the LES case are taken from the latter. Furthermore, this also implies that the variation of pressure in the mixing section in

Table 4.24. Compressible mixing layer : LES calculations : δ compared with the experiment. Here 'l' denotes distance upstream of the splitter plate tip in mm

Wall	δ (mm)				Experiment 0<l<20
	LES				
	l = 0	l = 5	l = 10	l = 15	
Primary section top wall	3.02	2.91	2.72	2.6	2.98
Splitter plate top wall	2.39	2.33	2.19	2.08	2.24
Secondary section bottom wall	4.44	4.32	4.2	4.08	4.10
Splitter plate bottom wall	3.01	3.18	3.18	3.14	4.05

Table 4.25. Compressible mixing layer : LES calculations : C_f compared with the experiment. Here 'l' denotes distance upstream of the splitter plate tip in mm

Wall	C_f				Experiment 0<l<20
	LES				
	l = 0	l = 5	l = 10	l = 15	
Primary section top wall	0.0012	0.0012	0.0012	0.0013	0.0017
Splitter plate top wall	0.0014	0.0014	0.0014	0.0014	0.0021
Secondary section bottom wall	0.0020	0.0020	0.0020	0.0020	0.0034
Splitter plate bottom wall	0.0034	0.0023	0.0022	0.0021	0.0036

the LES is reasonably close to that present in the experiment (ref section 4.2.2). As mentioned before, the freestream velocities and the convective Mach number reported in the reference experiment (given in table 4.1) are measured in the range $200 \text{ mm} \leq x_{spt} \leq 230 \text{ mm}$. The values of U_1, U_2 and M_c in the present LES calculations are shown in table 4.26 in the above mentioned range. Excellent agreement with the experiment is achieved for these quantities, as the values reported in the experiment fall within the range of values presented in table 4.26. This excellent agreement with the experiment is viewed as a consequence of simulating the wind tunnel top and bottom walls, as it helps maintain a pressure gradient similar to that present in the experiments. The variation of U_1, U_2 and M_c in the streamwise direction is attributed to the same reasons mentioned in section 4.2.2.

Table 4.26. Compressible mixing layer : LES calculations : U_1, U_2 and M_c at certain streamwise locations

Location	$U_1 (ms^{-1})$	$U_2(ms^{-1})$	M_c
At $x_{spt} = 200 \text{ mm}$	436.00	99.28	0.543
At $x_{spt} = 210 \text{ mm}$	432.45	98.59	0.538
At $x_{spt} = 220 \text{ mm}$	437.37	97.84	0.548
At $x_{spt} = 230 \text{ mm}$	434.66	97.09	0.544

The streamwise velocity profiles at several locations inside the mixing section are shown in figure 4.37 and is compared against the results of the RANS calculations and the reference experiment. At the first streamwise station, a velocity deficit exists in all the cases. However, at the second streamwise station (figure 4.37(b)) the velocity deficit has disappeared in the LES case, whereas the profiles from the RANS and the experiment shows a slight velocity deficit, as confirmed through the inset in figure 4.37(b). On further analysis (results not shown), it is found that the velocity deficit region ends at $x_{spt} \sim 24 \text{ mm}$ in the LES case, which is much earlier compared to what was observed in the RANS (49 mm in the $k - \epsilon$ simulation and 43 mm in the RSM

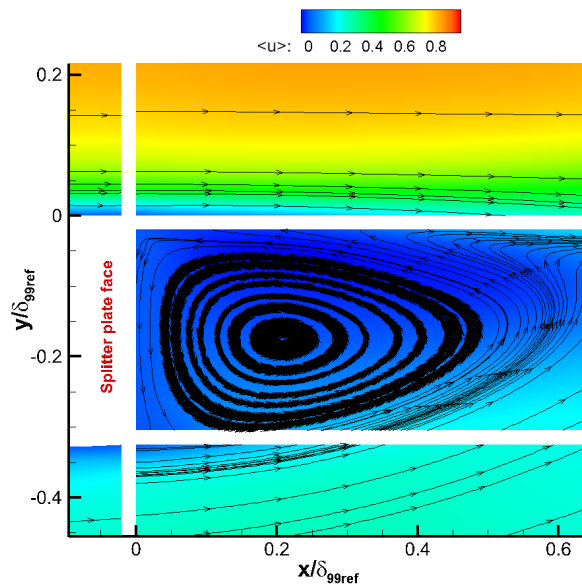


Figure 4.35. Compressible mixing layer : LES calculations : contours of $\langle u \rangle$ with streamlines.

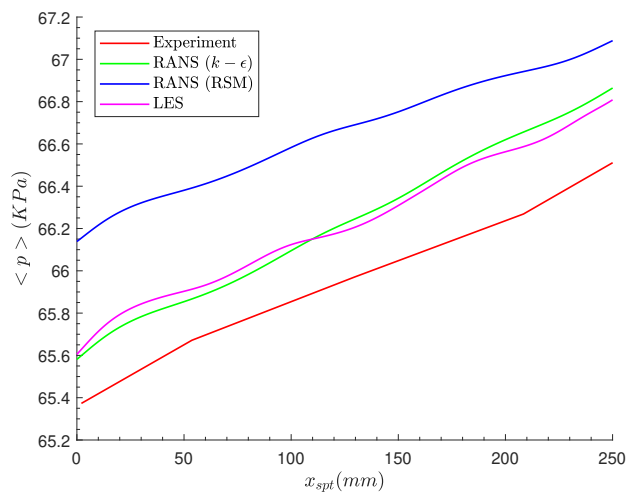


Figure 4.36. Compressible mixing layer : LES calculations : variation of pressure inside the mixing section.

simulation) and in the reference experiment (35 mm [11]). This is interesting since the boundary layer thicknesses at the splitter plate tip in the LES case are comparable with that of the RANS simulations. It may be possible that this is a consequence of the thin spanwise structures found in 4.28, which may provide additional entrainment into the mixing layer, thereby aiding to end the velocity deficit region relatively quickly. Reasonable agreement with the experiment is observed for the streamwise velocity profiles at the initial streamwise stations (figure 4.37(a) - figure 4.37(d)), with the shear layer in the LES case appearing slightly thicker compared to the other cases. However, further downstream, the velocity profiles in the LES case match the experimental data very well. Shortly downstream of the end of the velocity deficit region, the normalized $\langle u \rangle$ profiles (when plotted against the non-dimensionalized cross-stream coordinate $(y-y_0)/\delta_b$) at several streamwise stations start to collapse on top of each other indicating that self-similarity in the mean streamwise velocity is achieved. This is shown in figure 4.38. Excellent agreement with the experiment is achieved for the self-similar streamwise velocity profile. The variation of the mixing layer thickness in this self-similar region is shown in figure 4.39. As inferred earlier through the velocity profiles, the mixing layer starts thicker in the LES case compared to the other cases, though it becomes reasonably close to the experimental and the RANS simulation with the $k - \epsilon$ model results further downstream. A linear fit to δ_b in this self-similar region gives a R^2 value of 0.9991, which indicates the linear growth of the mixing layer in this self-similar region. The growth rate obtained is shown in table 4.27 together with the results from the other cases. The growth rate of the mixing layer is in good agreement with that of the reference experiment.

The non-dimensionalized turbulent kinetic energy inside the mixing section is shown at several streamwise stations in figure 4.40. At the first station, the TKE is in excellent agreement with the experiment. However, further downstream, this agreement deteriorates and the TKE is largely under predicted compared to the experiment and the RANS simulation based on the $k - \epsilon$ model and becomes close to the TKE in the RANS simulation based on the RSM. This under-prediction is

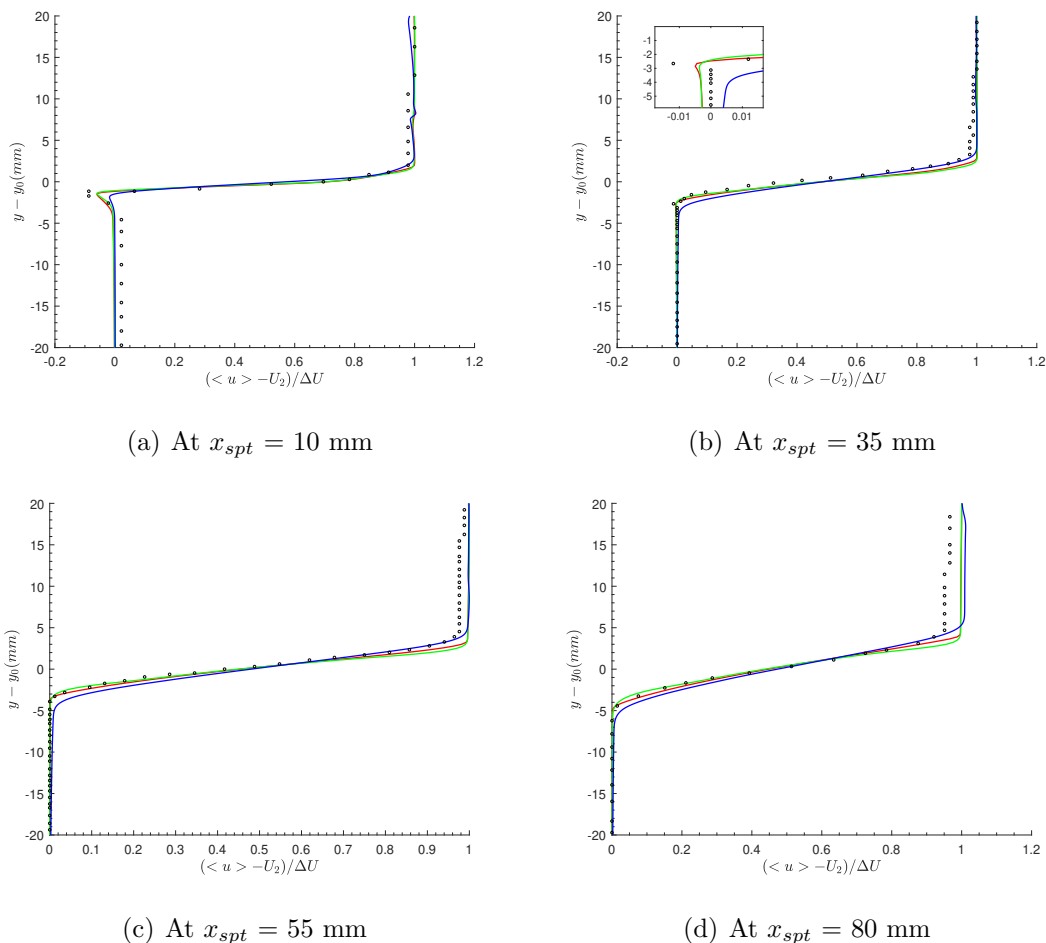


Figure 4.37. Compressible mixing layer : LES calculations : mean streamwise velocity profiles of the LES (blue), $k - \epsilon$ (red) and RSM (green) simulations compared with the experiments (scatter) at several streamwise locations.

Table 4.27. Compressible mixing layer : LES calculations : comparison of $\frac{d\delta_b}{dx}$ with the experiment and the RANS

Case	$\frac{d\delta_b}{dx}$	Percentage error w.r.t the experiment
RANS : $k - \epsilon$ model	0.07000	4.74 %
RANS : RSM	0.05455	18.37 %
LES	0.06286	3.06 %
Experiment	0.06683	-

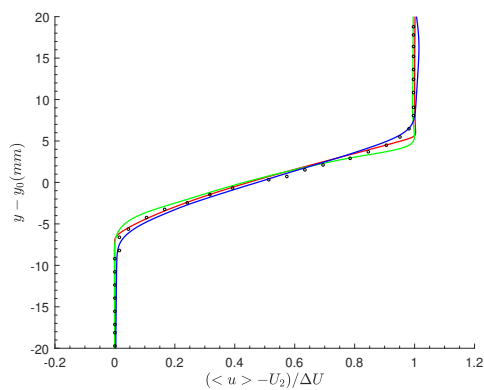
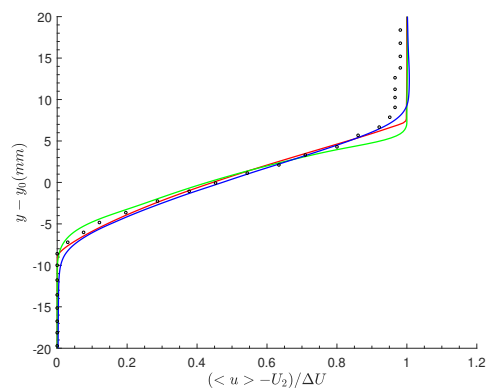
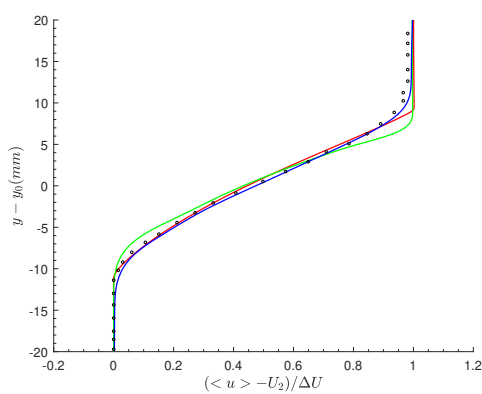
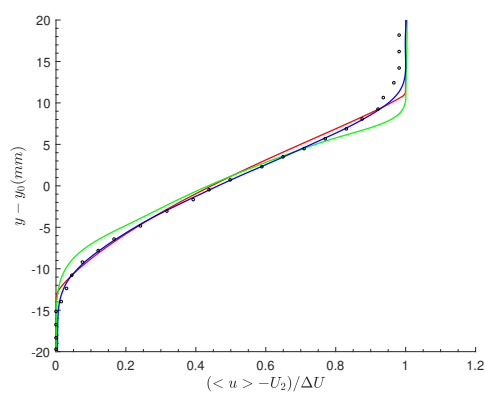
(e) At $x_{spt} = 120$ mm(f) At $x_{spt} = 160$ mm(g) At $x_{spt} = 200$ mm(h) At $x_{spt} = 240$ mm

Figure 4.37 (cont.). Compressible mixing layer : LES calculations : mean streamwise velocity profiles of the LES (blue), $k - \epsilon$ (red) and RSM (green) simulations compared with the experiments (scatter) at several streamwise locations.

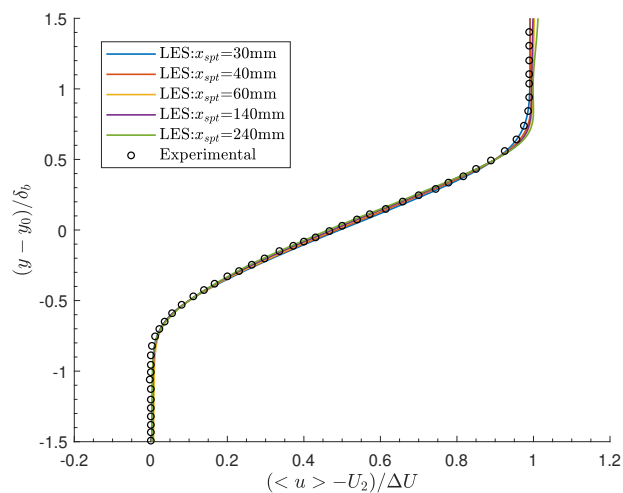


Figure 4.38. Compressible mixing layer : LES calculations : self-similar streamwise velocity profile compared with the reference experiment.

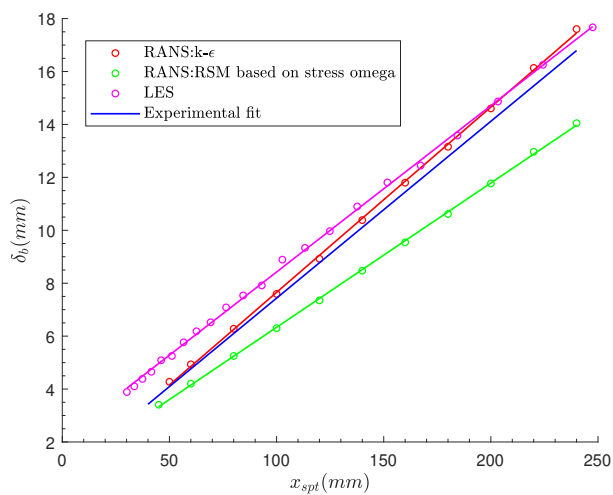


Figure 4.39. Compressible mixing layer : LES calculations : variation of δ_b inside the mixing section, compared against the results of RANS simulations and the reference experiment.

probably due to the application of the characteristic filter globally everywhere in the flow field, which causes too much dissipation in the non-shock turbulent regions of the flow field. The non-dimensionalized Reynolds stresses are plotted (against the non-dimensionalized cross-stream coordinate $\frac{y-y_0}{\delta_b}$) at several streamwise stations and are shown in the figure 4.41. All the components of the Reynolds stresses have attained self-similarity by $x_{spt} \sim 220$ mm (for the transverse Reynolds stress, while the other components attain self-similarity slightly upstream), as the profiles become reasonably close throughout the shear layer. This location of self-similarity is slightly downstream of what was reported in the experiments ($x_{spt} = 200$ mm). The self-similar Reynolds stresses in the range of $220 \text{ mm} \leq x_{spt} \leq 240 \text{ mm}$ are averaged and compared with the experiments and RANS (based on the RSM). This is shown in figure 4.42. All the components of Reynolds stresses are underpredicted reflecting what was observed in the TKE. However, the transverse normal and the primary shear stresses are reasonably close to the experimental data except at the location of the peak which is underpredicted. The other two normal components are underpredicted everywhere inside the shear layer. Also, except for the spanwise normal Reynolds stress, the other components are reasonably close to the RANS results.

The anisotropy coefficients of the Reynolds stress tensor defined as [11]

$$c_{ij} = \frac{\langle u'_i u'_j \rangle - \frac{2}{3} k \delta_{ij}}{2k} \quad (4.4)$$

are plotted in figure 4.43. The anisotropy of the streamwise normal Reynolds stress is positive whereas the other anisotropy values of the other two normal stresses are negative (in the core of the shear layer) for both the LES and the RANS which is in agreement with the experiment. The RANS profiles are reasonably close to the experimental data, though they remain constant across the shear layer as opposed to the trends seen in the experimental data. The anisotropy of the streamwise normal Reynolds stress in the LES case is in good agreement with the experiment. However, c_{yy} and c_{zz} in the LES case are higher and lower respectively when compared to the experiments. c_{xy} is also found to be largely overpredicted in the LES case. The average value of the anisotropy coefficients in the center of the shear layer (-0.25

$< \frac{y-y_0}{b} < 0.25$) is computed for the RANS and LES and is compared with that of the experiments in table 4.28. The anisotropy values from the DNS of Pantano and Sarkar [18] at a convective Mach number of 0.7 is also included in the table 4.28 for comparison. Though this DNS is at a slightly higher convective Mach number than the present case, the authors remark that the effect of M_c on the anisotropy coefficients is weak [18]. Also, the value of c_{zz} is unreported in the DNS. But here it is estimated using

$$c_{xx} + c_{yy} + c_{zz} = 0 \quad (4.5)$$

From the table 4.28 it could be seen that in the LES case, except c_{xx} , the other anisotropy values are largely off from the experimental values. However, in the LES case, the anisotropy values of the normal Reynolds stresses are in good agreement with that of the DNS while c_{xy} is still relatively large. In the RANS case, the anisotropy values are reasonably close to either the experiment or the DNS, for the different components.

The Reynolds stress correlation coefficient defined as [11] is shown in figure 4.44. Both RANS and LES overpredict this correlation coefficient when compared with the experiment, with the RANS results being in relatively good agreement with the experiment than the LES. This is also reflected in the average value of this correlation coefficient near the center of the shear layer as shown in table 4.29, with the result of the RANS being in much better agreement with the experiment than the LES.

Table 4.28. Compressible mixing layer : LES calculations : comparison of Reynolds stress anisotropy coefficients with the experiment, RANS and DNS of Pantano and Sarkar [18]

c_{ij}	LES	RANS (RSM)	Experiment [11]	DNS [18]
c_{xx}	0.16	0.13	0.18	0.15
c_{yy}	-0.11	-0.12	-0.16	-0.10
c_{xy}	0.19	0.16	0.14	0.16
c_{zz}	-0.05	-0.01	-0.01	-0.05

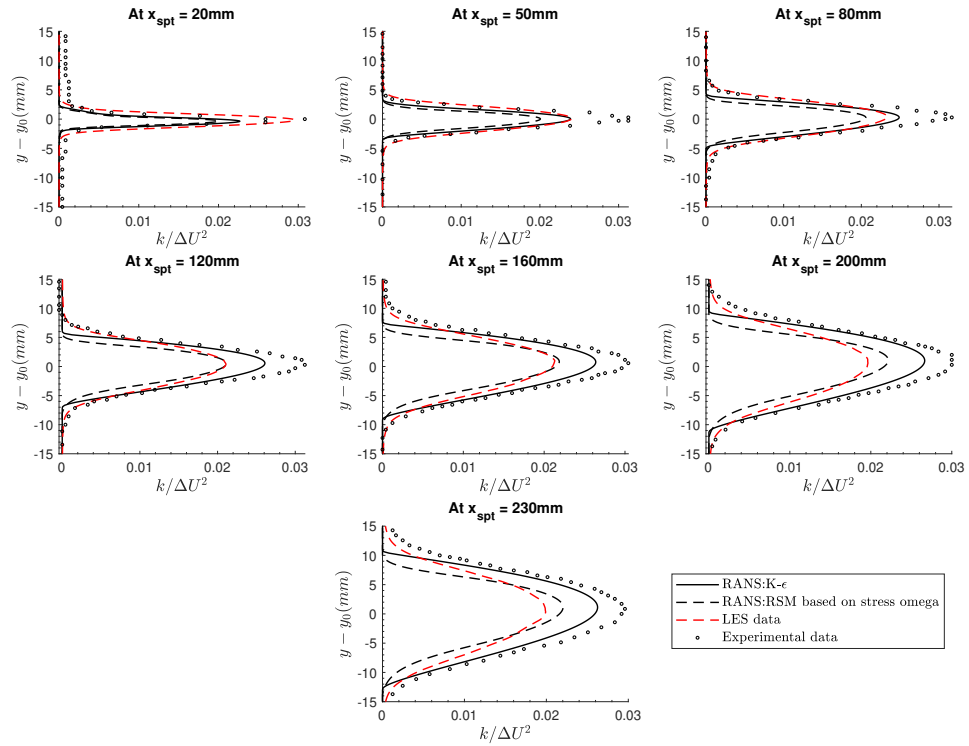


Figure 4.40. Compressible mixing layer : LES calculations : comparison of TKE with the experiment and the RANS.

Table 4.29. Compressible mixing layer : LES calculations : comparison of Reynolds stress correlation coefficient with the experiment and RANS

Case	Average value of $\frac{-Re_{xy}}{\sqrt{Re_{xx}Re_{yy}}}$ near the center of the shear layer ($-0.25 < \frac{y-y_0}{\delta_b} < 0.25$)
LES	0.56
RANS (RSM)	0.51
Experiment [11]	~ 0.47

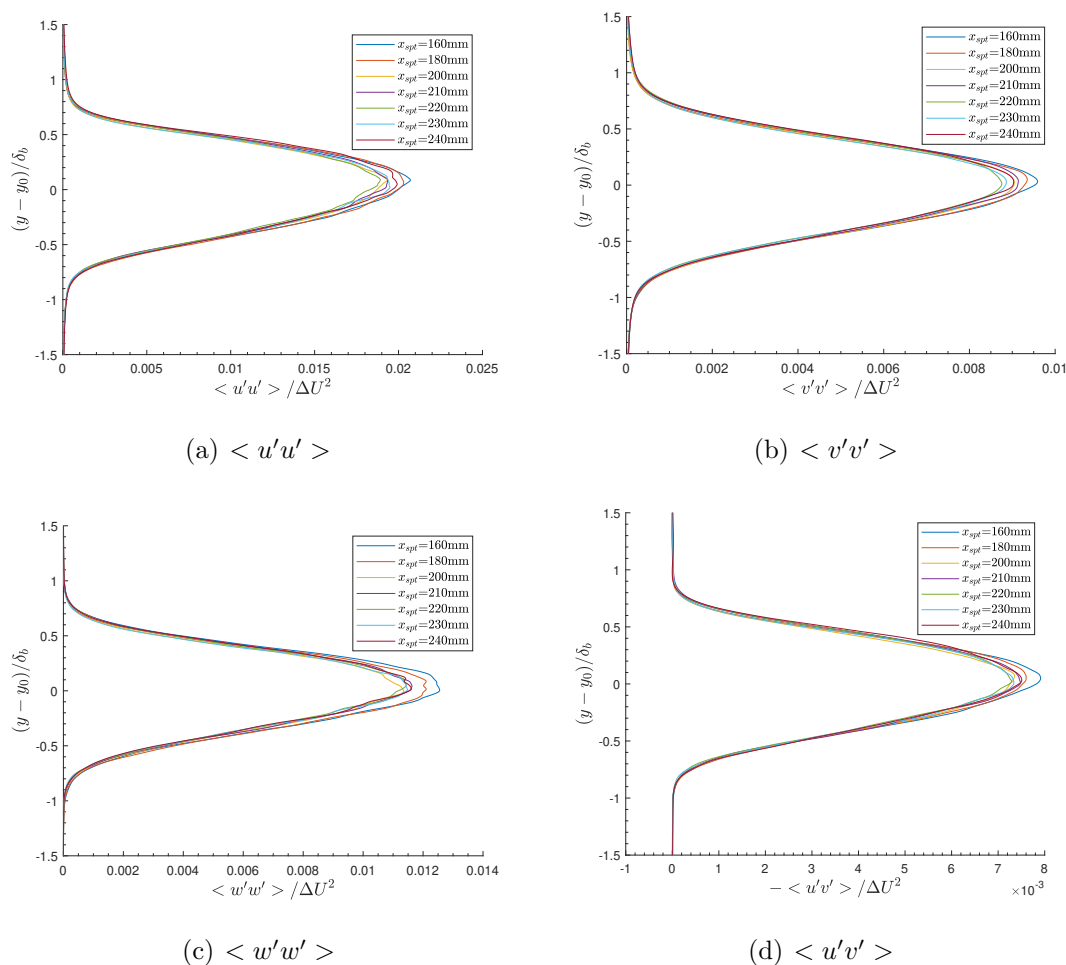


Figure 4.41. Compressible mixing layer : LES calculations : Reynolds stresses at several streamwise stations.

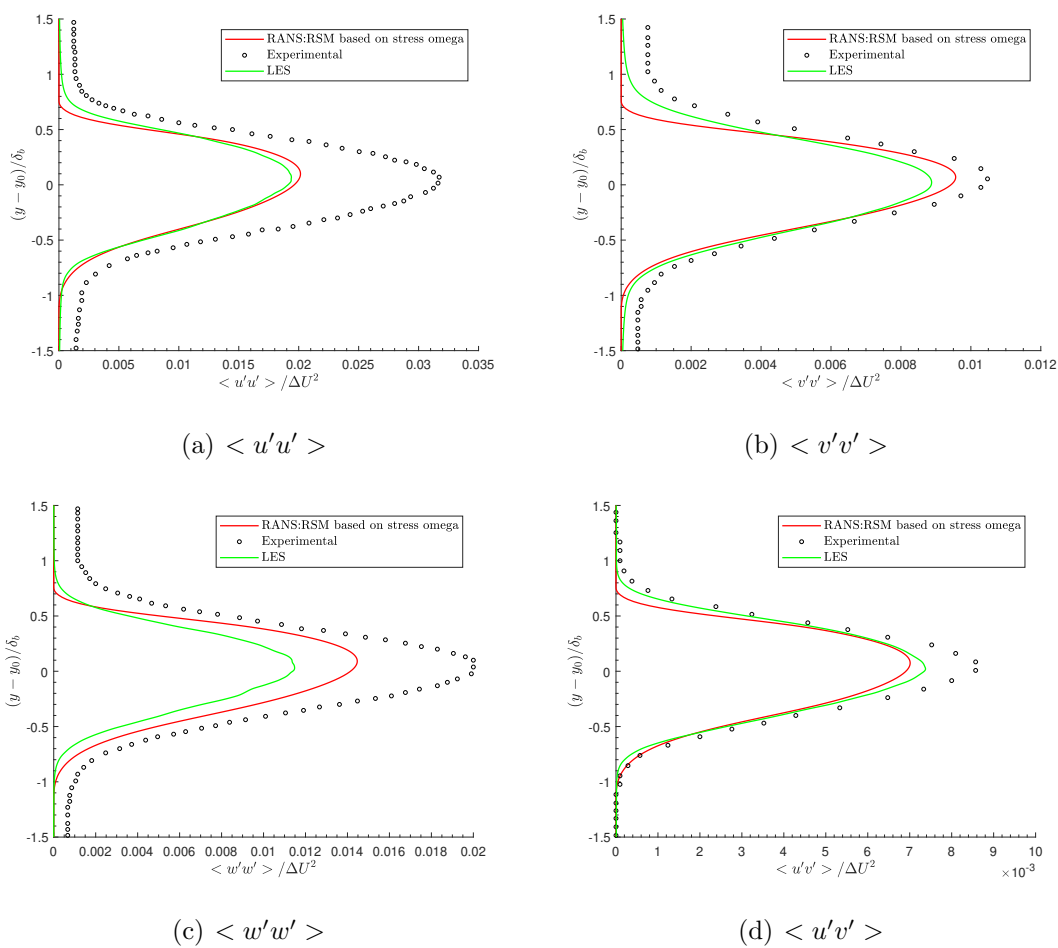


Figure 4.42. Compressible mixing layer : LES calculations : Reynolds stresses compared with the experiment and the RANS (RSM).

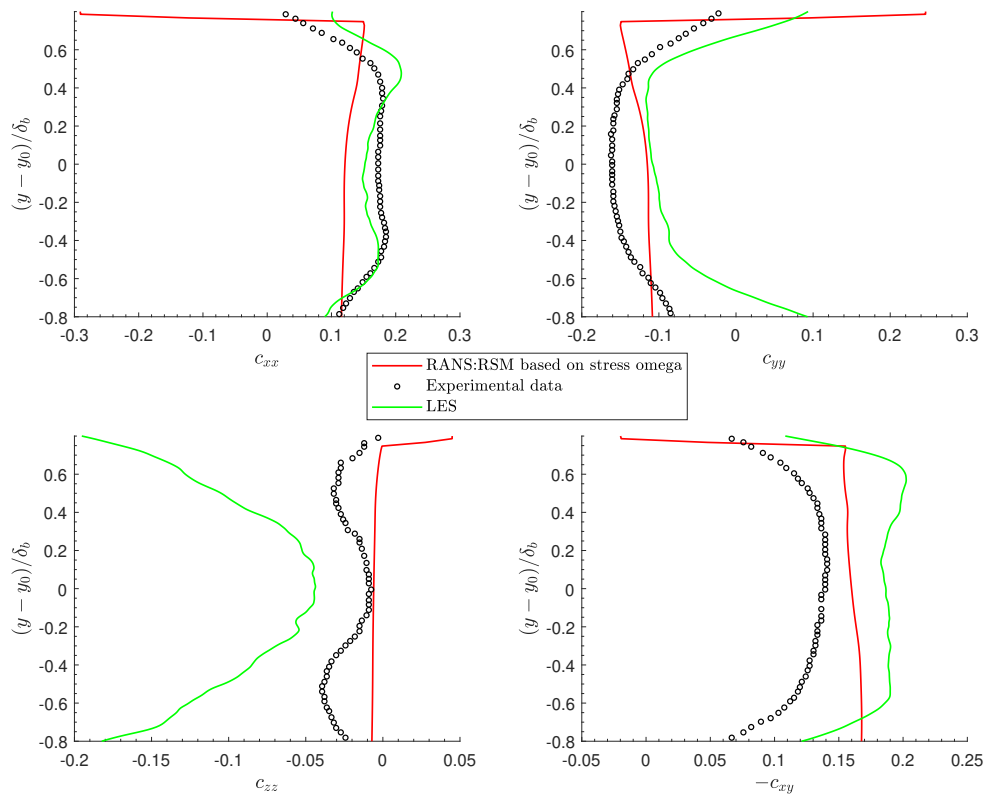


Figure 4.43. Compressible mixing layer : LES calculations : anisotropy of the Reynolds stress tensor compared with the experiment and the RANS.

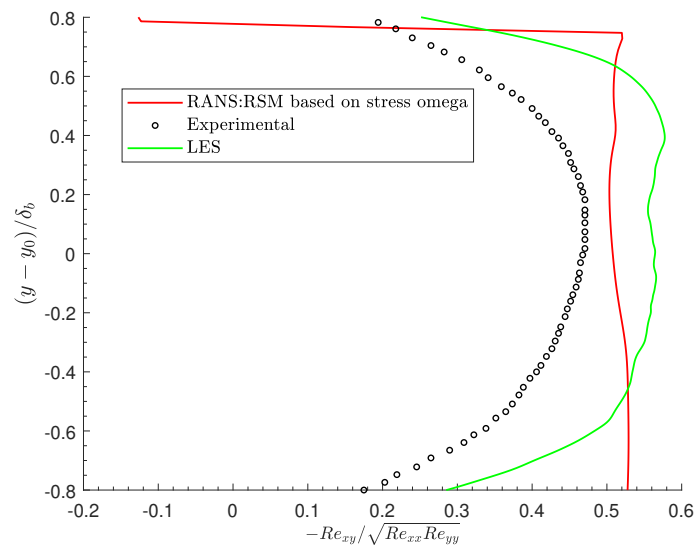


Figure 4.44. Compressible mixing layer : LES calculations : Reynolds stress correlation coefficient compared with the experiment and the RANS.

5. CONCLUSION

A methodology has been successfully developed to perform an LES of a compressible mixing layer of experimental flow conditions where the upstream boundary layers leading into the mixing section were resolved using a wall model approach. This approach was validated by performing an LES of the compressible mixing layer matching the flow conditions of Kim et al. [11] using the in house LES solver and by comparing the results against the reference experiment. Good agreement with the reference experiment is achieved for the upstream boundary layer properties, the mean velocity profile of the shear layer and the shear layer growth rate. The following presents a brief summary of the present work.

5.1 Summary

An in house LES solver previously used to perform simulations of jets was chosen to perform the large eddy simulations in the present work. A few changes were made to the solver's boundary conditions and other settings to enable simulations of two-stream mixing layers. Parallel scaling tests were performed for the solver on a current supercomputer and recommendations on the work size per processor were made for efficient parallel scaling of the simulation runs. The solver was validated and verified for two-stream mixing layer flows by performing simulations of laminar and incompressible mixing layer flows and comparing the subsequent results with the literature.

The inflow velocity profiles for the laminar mixing layer cases were taken from the analytical solutions for a plane laminar mixing layer and the density is set constant at the inflow. The analytical solutions exhibit a streamwise gradient in the freestream for the cross-stream velocity which in turn causes a cross-stream gradient in the pres-

sure. This gradient, however, drops, with distance from the virtual origin. Hence two cases were performed.

Case 1: The inflow profiles were taken from an instance of the analytical solution close to the virtual origin. The pressure profile at the inflow, that was obtained by numerical solving the y -momentum equations, has a pressure gradient in the cross-stream direction.

Case 2: The inflow profiles were taken from a downstream instance of the analytical solution such that the pressure gradient in the cross-stream direction is negligible. The pressure at the inflow was therefore set as a constant.

It was seen that in case 1, there is a cross-stream gradient in the streamwise velocity at the free-streams, which causes the self-similar velocity profiles to deviate from the self-similar profile of the analytical solutions at these regions. This anomaly is attributed to the pressure variation in the streamwise and cross-stream direction in the fluid domain, especially close to the inflow. The vorticity thicknesses of the shear layer at several streamwise stations, in this case, are in excellent agreement with the analytical results whereas the shear layer thicknesses are found to be slightly higher compared to the latter. Case 2, however, exhibited no significant cross-stream gradient in the freestreams and the self-similar profiles are in extremely good agreement with that from the analytical solution. This again is attributed to the pressure variation close to the inflow. Both the shear layer and vorticity thicknesses are found to be in excellent agreement with the analytical solutions. Thus it is concluded that simulations involving laminar mixing layers should start from an instance of the analytical solution that is taken from a location that is far downstream from the virtual origin, so as to avoid any significant pressure gradient effects.

The incompressible turbulent mixing layer simulations performed as a part of the validation match the flow conditions of the DNS of Attili and Bisetti [33]. Three cases were performed:

Case 1: White noise inflow with Tam and Dong outflow boundary condition.

Case 2: White noise inflow with subsonic characteristic outflow boundary condition.

Case 3: Correlated inflow with subsonic characteristic outflow boundary condition.

It should be noted that the DNS employed a white noise type inflow. A statistical sample size of 8 FTC was found to be adequate to obtain turbulent statistics that are statistically stationary. For case 2, very good agreement with the reference DNS is observed for the mean velocity and turbulent stresses. The instantaneous flow field is found to consist of flow structures that are typical to a turbulent mixing layer evolving from laminar initial conditions. The near field is characterized by the presence of spanwise rollers and streamwise structures with the former undergoing pairing. The flow eventually transitions to a turbulent mixing layer that is characterized by the appearance of a large number of small scale structures. For case 1, reasonable agreement with the reference experiment is observed for the turbulent statistics, though the agreement was not as good as with case 2. An unphysical pressure rise close to the outflow is observed for case 1 which could be the reason for this discrepancy. Case 3 was performed to check for the presence of statistically stationary streamwise vortices as a correlated inflow was found to be necessary for the development of these structures [61]. However, it is observed, through the contours of secondary shear stress and the magnitude of the spanwise wrinkle in the mean streamwise velocity, that both case 2 and case 3 are devoid of strong statistically stationary streamwise vortices and this, in turn, is likely to be the reason for the reduction in growth rate observed in the present cases compared to the experimental fit. Though the absence of these structures in the former (white noise type inflow) is well established in the literature [61], the exact reason for the absence of these structures in the correlated inflow case in the present work is not known. Here it is speculated that the reason might be the use of a hyperbolic tangent type inflow, as opposed to a boundary layer type inflow that is typical of experiments. Moreover, the near field region of case 3 is found to have increased turbulence levels compared to case 2, due to the presence of a relatively large number of small scale structures in the former. The approach to self-similarity in the turbulent stresses is also found to be quicker for case 3 compared to case 2.

As validation and verification cases presented results that in are good agreement with that found in the literature, the LES solver is deemed to be of good numerical accuracy to study mixing layer flows. Thus with this confidence, LES of a compressible mixing layer matching the flow conditions of Kim et al. [11] was performed with this solver. First, RANS simulations with the realizable $k - \epsilon$ and stress-omega based RSM models were performed with ANSYS Fluent to obtain the initial conditions and inflow profiles for the LES. A grid convergence study was performed with the RANS calculations to ensure that the results are mesh independent. It was found that the RANS simulation based on the $k - \epsilon$ model better matched the boundary layer and mixing layer properties reported in the reference experiment compared to the one with the RSM. Therefore, the inflow profiles and initial conditions for the LES were taken from the former. Since the information about the Reynolds stresses is not available from the $k - \epsilon$ model, the anisotropy values of the Reynolds stresses were taken from the RANS simulation based on the RSM and together with the TKE from the former, were used to construct the Reynolds stresses at the inflow (required by the turbulent inflow method).

The instantaneous flow field of the LES was analyzed. Shock waves, originating from the inflow of the primary stream, are found to interact with the boundary layer and the growing shear layer which is undesirable and needs to be avoided. The upstream boundary layers are characterized by the presence of hairpin vortices which are very typical of turbulent boundary layers. These were also found to be convected into the mixing section and found to grow in size as they move downstream. Consequently, the near field of the mixing layer is highly three dimensional as opposed to the mixing layers evolving from laminar initial conditions.

The statistics that were collected were analyzed to ensure that they are reasonably converged. The boundary layer thicknesses are found to be in good agreement with that reported in the experiment (except the one on the splitter plate bottom which is slightly lower). The skin friction coefficients, though underpredicted, are in reasonable agreement with the reference experiment. The shear layer is slightly thicker in the

LES compared to that in the reference experiment. This is especially pronounced close to the splitter plate tip. However, the growth rate and self-similar velocity profile in the present case are in good agreement with that from the experiment. The Reynolds stresses in the LES are all underpredicted compared to the reference experiment. This is partially attributed to the global application of the characteristic filters, which probably caused too much dissipation in non-shock turbulent regions. The anisotropy of the normal Reynolds stresses obtained in the present LES, though off from the reference experiment for some components, are found to be in good agreement with that of the DNS of Pantano and Sarkar [18]. The anisotropy of the Reynolds shear stress is, however, found to be overpredicted in the present case.

5.2 Recommendations for Future Work

As mentioned earlier, shock waves were found to originate from the supersonic primary inflow that interact with the boundary layer and the growing shear layer downstream. Further research could be done to avoid such unnecessary SWBLI and shock wave shear layer interaction through an appropriate inflow treatment. Furthermore, in the present work, the WENO characteristic filter (used for shock capturing) was applied globally everywhere in the flow field as the local application of the filter caused the simulation to fail. As speculated earlier, this is probably due to the Ducros detector not being able to detect weak shock waves, to be able to apply the filter locally at those locations. Thus research could be done to improve the shock-capturing scheme to detect weak shock waves to enable local application of the characteristic filters. This is highly desirable to reduce the computational cost and also to avoid unnecessary dissipation in non-shock regions. Additional grid sensitivity studies could be done for this test case to establish a clear LES framework for studying compressible mixing layers with such experimental flow conditions. After such a framework is established, the remaining test cases of Kim et al. [16] could be studied using LES, to provide better insights on the effects on compressibility on shear layers.

REFERENCES

REFERENCES

- [1] Michael M Rogers and Robert D Moser. The three-dimensional evolution of a plane mixing layer: the Kelvin–Helmholtz rollup. *Journal of Fluid Mechanics*, 243:183–226, 1992.
- [2] W Andrew McMullan, Shian Gao, and Christopher M Coats. The effect of inflow conditions on the transition to turbulence in large eddy simulations of spatially developing mixing layers. *International Journal of Heat and Fluid Flow*, 30(6):1054–1066, 2009.
- [3] Garry L Brown and Anatol Roshko. On density effects and large structure in turbulent mixing layers. *Journal of Fluid Mechanics*, 64(4):775–816, 1974.
- [4] William A McMullan, S Gao, and Christopher M Coats. Organised large structure in the post-transition mixing layer. part 2. large-eddy simulation. *Journal of Fluid Mechanics*, 762:302–343, 2015.
- [5] DW Moore and PG Saffman. The density of organized vortices in a turbulent mixing layer. *Journal of Fluid Mechanics*, 69(3):465–473, 1975.
- [6] Arjun Sharma, Rathakrishnan Bhaskaran, and Sanjiva Lele. Large-eddy simulation of supersonic, turbulent mixing layers downstream of a splitter plate. AIAA Paper No. 2011-0208, January 2011.
- [7] RD Mehta. Effect of velocity ratio on plane mixing layer development: Influence of the splitter plate wake. *Experiments in Fluids*, 10(4):194–204, 1991.
- [8] SN Hug and WA McMullan. The influence of velocity ratio on the evolution of streamwise vortices in the simulated plane mixing layer. *European Journal of Mechanics-B/Fluids*, 76:166–177, 2019.
- [9] Sylvain Laizet, Sylvain Lardeau, and Eric Lamballais. Direct numerical simulation of a mixing layer downstream a thick splitter plate. *Physics of Fluids*, 22(1):015104, 2010.
- [10] James H Bell and Rabindra D Mehta. Development of a two-stream mixing layer from tripped and untripped boundary layers. *AIAA Journal*, 28(12):2034–2042, 1990.
- [11] Kevin Kim, Gyu Sub Lee, Blake E. Johnson, Gregory S. Elliott, and J Craig Dutton. Stereoscopic PIV measurements of a turbulent compressible mixing layer for CFD validation. AIAA Paper No. 2017-4129, June 2017.
- [12] Dimitri Papamoschou and Anatol Roshko. The compressible turbulent shear layer: an experimental study. *Journal of Fluid Mechanics*, 197:453–477, 1988.

- [13] DW Bogdanoff. Compressibility effects in turbulent shear layers. *AIAA Journal*, 21(6):926–927, 1983.
- [14] Gregory S Elliott and M Samimy. Compressibility effects in free shear layers. *Physics of Fluids A: Fluid Dynamics*, 2(7):1231–1240, 1990.
- [15] Steven G Goebel and J Craig Dutton. Experimental study of compressible turbulent mixing layers. *AIAA Journal*, 29(4):538–546, 1991.
- [16] Kevin U Kim, Gregory S Elliott, and J Craig Dutton. Three-dimensional experimental study of compressibility effects on turbulent free shear layers. *AIAA Journal*, 58(1):1–15, 2019.
- [17] Albertus Willem Vreman, ND Sandham, and KH Luo. Compressible mixing layer growth rate and turbulence characteristics. *Journal of Fluid Mechanics*, 320:235–258, 1996.
- [18] C Pantano and S Sarkar. A study of compressibility effects in the high-speed turbulent shear layer using direct simulation. *Journal of Fluid Mechanics*, 451:329–371, 2002.
- [19] Sergio Pirozzoli, Matteo Bernardini, Simon Marié, and Francesco Grasso. Early evolution of the compressible mixing layer issued from two turbulent streams. *Journal of Fluid Mechanics*, 777:196–218, 2015.
- [20] Dongdong Zhang, Jianguo Tan, and Xiao Yao. Direct numerical simulation of spatially developing highly compressible mixing layer: Structural evolution and turbulent statistics. *Physics of Fluids*, 31(3):036102, 2019.
- [21] Mina R Mankbadi, James R DeBonis, and Nicholas J Georgiadis. Large-eddy simulation of a compressible mixing layer and the significance of inflow turbulence. AIAA Paper No. 2017-0316, January 2017.
- [22] Hans Wolfgang Liepmann and John Laufer. Investigations of free turbulent mixing. Technical report 1257, Nat. Adv. Comm. Aero., Washington, 1947.
- [23] BG Jones, HP Planchon, and RJ Hammersley. Turbulent correlation measurements in a two-stream mixing layer. *AIAA Journal*, 11(8):1146–1150, 1973.
- [24] D Oster and I Wygnanski. The forced mixing layer between parallel streams. *Journal of Fluid Mechanics*, 123:91–130, 1982.
- [25] James H Bell and Rabindra D Mehta. Measurements of the streamwise vortical structures in a plane mixing layer. *Journal of Fluid Mechanics*, 239:213–248, 1992.
- [26] Lein-Saing Huang and Chih-Ming Ho. Small-scale transition in a plane mixing layer. *Journal of Fluid Mechanics*, 210:475–500, 1990.
- [27] Noel T Clemens and MG Mungal. Two- and three-dimensional effects in the supersonic mixing layer. *AIAA journal*, 30(4):973–981, 1992.
- [28] Robert D Moser and Michael M Rogers. The three-dimensional evolution of a plane mixing layer: pairing and transition to turbulence. *Journal of Fluid Mechanics*, 247:275–320, 1993.

- [29] Y Wang, Mamoru Tanahashi, and Toshio Miyauchi. Coherent fine scale eddies in turbulence transition of spatially-developing mixing layer. *International Journal of Heat and Fluid Flow*, 28(6):1280–1290, 2007.
- [30] William A McMullan. Spanwise domain effects on the evolution of the plane turbulent mixing layer. *International Journal of Computational Fluid Dynamics*, 29(6-8):333–345, 2015.
- [31] William Andrew McMullan. The effect of boundary layer fluctuations on the streamwise vortex structure in simulated plane turbulent mixing layers. *International Journal of Heat and Fluid Flow*, 68:87–101, 2017.
- [32] Qiang Zhou, Feng He, and MY Shen. Direct numerical simulation of a spatially developing compressible plane mixing layer: flow structures and mean flow properties. *Journal of Fluid Mechanics*, 711:437–468, 2012.
- [33] Antonio Attili and Fabrizio Bisetti. Statistics and scaling of turbulence in a spatially developing mixing layer at $Re_\lambda = 250$. *Physics of Fluids*, 24(3):035109, 2012.
- [34] A. Uzun. *3-D Large Eddy Simulation for Jet Aeroacoustics*. PhD thesis, Purdue University, December 2003.
- [35] S. Lo. *Numerical Simulations of Supersonic Jet Flows*. PhD thesis, Purdue University, 2010.
- [36] C. Martha. *Toward High-Fidelity Subsonic Jet Noise Prediction using Petascale Supercomputers*. PhD thesis, Purdue University, May 2013.
- [37] Y. Situ. *Scaling Finite Difference Methods in Large Eddy Simulation of Jet Engine Noise to the Petascale: Numerical Methods and Their Efficient and Automated Implementation*. PhD thesis, Purdue University, December 2014.
- [38] K. Aikens. *High-Fidelity Large Eddy Simulation for Supersonic Jet Noise Prediction*. PhD thesis, Purdue University, West Lafayette, 2014.
- [39] N. Dhamankar. *Boundary Conditions Towards Realistic Simulation of Jet Engine Noise*. Master’s thesis, Purdue University, 2012.
- [40] N. Dhamankar. *An Immersed Boundary Method for Efficient Computational Studies of Nozzles Designed to Reduce Jet Noise*. PhD thesis, Purdue University, 2016.
- [41] Shanmukeswar Rao Vankayala. *Investigation of Wall-Modeled Large Eddy Simulations for Jet Aeroacoustics*. PhD thesis, Purdue University, 2019.
- [42] M. Visbal and D. Gaitonde. Very High-Order Spatially Implicit Schemes for Computational Acoustics on Curvilinear Meshes. *Journal of Computational Acoustics*, 09(04):1259–1286, 2001.
- [43] S. Lele. Compact finite difference schemes with spectral-like resolution. *Journal of Computational Physics*, 103(1):16–42, 1992.
- [44] Datta V Gaitonde and Miguel R Visbal. Pade-type higher-order boundary filters for the navier-stokes equations. *AIAA Journal*, 38(11):2103–2112, 2000.

- [45] Christopher KW Tam and Zhong Dong. Radiation and outflow boundary conditions for direct computation of acoustic and flow disturbances in a nonuniform mean flow. *Journal of Computational Acoustics*, 4(02):175–201, 1996.
- [46] C. Bogey and C. Bailly. Three-dimensional non-reflective boundary conditions for acoustic simulations: far field formulation and validation test cases. *Acta Acustica united with Acustica*, 88:463–471, 2002.
- [47] Jae Wook Kim and Duck Joo Lee. Generalized characteristic boundary conditions for computational aeroacoustics. *AIAA Journal*, 38(11):2040–2049, 2000.
- [48] Guido Lodato, Pascale Domingo, and Luc Vervisch. Three-dimensional boundary conditions for direct and large-eddy simulation of compressible viscous flows. *Journal of Computational Physics*, 227(10):5105–5143, 2008.
- [49] A Fosso P, Hugues Deniau, Nicolas Lamarque, and Thierry Poinsot. Comparison of outflow boundary conditions for subsonic aeroacoustic simulations. *International Journal for Numerical Methods in Fluids*, 68(10):1207–1233, 2012.
- [50] TIM Colonius, Sanjiva K Lele, and Parviz Moin. Boundary conditions for direct computation of aerodynamic sound generation. *AIAA Journal*, 31(9):1574–1582, 1993.
- [51] M. Louis. *Validation of Characteristic Boundary Conditions Implemented in Computational Aeroacoustics Large Eddy Simulations of Wall Bounded Flows*. Master’s thesis, Purdue University, December 2011.
- [52] Eric Polizzi and Ahmed H Sameh. A parallel hybrid banded system solver: the spike algorithm. *Parallel Computing*, 32(2):177–194, 2006.
- [53] Yingchong Situ, Lixia Liu, Chandra S Martha, Matthew E Louis, Zhiyuan Li, Ahmed H Sameh, Gregory A Blaisdell, and Anastasios S Lyrantzis. A communication-efficient linear system solver for large eddy simulation of jet engine noise. *Cluster Computing*, 16(1):157–170, 2013.
- [54] Yingchong Situ, Chandra S Martha, Matthew E Louis, Zhiyuan Li, Ahmed H Sameh, Gregory A Blaisdell, and Anastasios S Lyrantzis. Petascale large eddy simulation of jet engine noise based on the truncated spike algorithm. *Parallel Computing*, 40(9):496–511, 2014.
- [55] ANSYS Fluent Inc. Fluent Theory guide, Fluent 2019 R2 documentation, 2019.
- [56] Sutanu Sarkar and B Lakshmanan. Application of a Reynolds stress turbulence model to the compressible shear layer. *AIAA Journal*, 29(5):743–749, 1991.
- [57] ANSYS Fluent Inc. Fluent User’s guide, Fluent 2019 R2 documentation, 2019.
- [58] MJ Casarella and Y Choo. Displacement effects on the laminar mixing of two parallel streams. *The Aeronautical Quarterly*, 19(4):388–402, 1968.
- [59] M.M. Rogers, P. Moin, and W.C Reynolds. The structure and modeling of the hydrodynamic and passive scalar fields in homogenous turbulent shear flow. Report No. TF-25., 1986. Department of Mechanical Engineering, Stanford University, Stanford, California.

- [60] Michael M Rogers and Robert D Moser. Direct simulation of a self-similar turbulent mixing layer. *Physics of Fluids*, 6(2):903–923, 1994.
- [61] William Andrew McMullan and Stephen J Garrett. On streamwise vortices in large eddy simulations of initially laminar plane mixing layers. *International Journal of Heat and Fluid Flow*, 59:20–32, 2016.
- [62] Gyu Sub S Lee. *Design and development of a wind tunnel for the investigation of turbulent compressible mixing layers*. Master’s thesis, University of Illinois at Urbana-Champaign, 2017. <http://hdl.handle.net/2142/98393>.
- [63] Marco Corderoni. *A Computational Analysis of the Aerodynamics and Aeroacoustics of Jets with Fluid Injection*. PhD thesis, Embry-Riddle Aeronautical University, 2018.
- [64] Mina R Mankbadi, James R DeBonis, and Nicholas J Georgiadis. Comparison of high-order and low-order methods for large-eddy simulation of a compressible shear layer. AIAA Paper No. 2015-2939, June 2015.
- [65] Václav Kolář. Vortex identification: New requirements and limitations. *International Journal of Heat and Fluid Flow*, 28(4):638–652, 2007.
- [66] Tie Wei, Rodney Schmidt, and Patrick McMurtry. Comment on the Clauser chart method for determining the friction velocity. *Experiments in Fluids*, 38(5):695–699, 2005.
- [67] RC Lock. The velocity distribution in the laminar boundary layer between parallel streams. *The Quarterly Journal of Mechanics and Applied Mathematics*, 4(1):42–63, 1951.

APPENDIX

APPENDIX A. ANALYTICAL SOLUTIONS OF THE INCOMPRESSIBLE LAMINAR MIXING LAYERS

In this part, the analytical solutions of the incompressible laminar mixing layers are presented. The equations that govern the steady state incompressible flow between two parallel streams with zero pressure gradient are the boundary layer equations given by

$$u \frac{\partial u}{\partial x} + v \frac{\partial u}{\partial y} = \nu \frac{\partial^2 u}{\partial y^2}, \quad (\text{A.1})$$

$$\frac{\partial u}{\partial x} + \frac{\partial v}{\partial y} = 0. \quad (\text{A.2})$$

A stream function ψ can be introduced to satisfy the continuity equation. Thus,

$$u = \frac{\partial \psi}{\partial y}, \quad v = -\frac{\partial \psi}{\partial x}. \quad (\text{A.3})$$

Now, if ψ is expressed as [67]

$$\psi = \sqrt{\nu x U_1} f(\eta), \quad (\text{A.4})$$

where η is a non-dimensional variable namely,

$$\eta = \frac{y}{\sqrt{\frac{\nu x}{U_1}}}, \quad (\text{A.5})$$

then u and v can be expressed in terms of f and η as

$$u = U_1 f'(\eta), \quad (\text{A.6})$$

$$v = \frac{1}{2} \sqrt{\nu U_1 / x} (\eta f' - f), \quad (\text{A.7})$$

and equation A.1 can be reduced to the following third order ODE,

$$f''' + \frac{1}{2} f f'' = 0. \quad (\text{A.8})$$

The boundary conditions of this problem are

$$u \rightarrow U_1 \quad \text{or} \quad f' \rightarrow 1, \quad \text{as} \quad \eta \rightarrow \infty \quad (\text{A.9})$$

$$u \rightarrow U_2 \quad \text{or} \quad f' \rightarrow \frac{U_2}{U_1}, \quad \text{as} \quad \eta \rightarrow -\infty \quad (\text{A.10})$$

However, equation A.8 is of third order and hence three boundary conditions are needed to solve the problem. In order to tackle this, the solution procedure of Casarella and Choo [58] is followed. Here, the governing equations are first solved in a transformed space given by,

$$\begin{aligned} x_t &= x_p, & y_t &= y_p + S(x_p), \\ u_t(x_t, y_t) &= u_p(x_p, y_p), & v_t(x_t, y_t) &= v_p(x_p, y_p) + u_t(x_t, y_t) \frac{dS}{dx_p}. \end{aligned} \quad (\text{A.11})$$

where the subscript 't' indicates quantities in the transformed space and 'p' indicates quantities in the physical space, by assuming an arbitrary third boundary condition. Then, the correct third boundary condition is satisfied by means of the function $S(x)$ through a compatibility condition. Here $S(x)$ is an arbitrary function of x subject to the condition $S(0) = 0$. The arbitrary third boundary condition used for solving equation A.8 in the transformed space is taken as

$$v_t(x_t, 0) = 0 \quad \text{or} \quad f(0) = 0, \quad (\text{A.12})$$

which implies that $y_t = 0$ or $\eta = 0$ is the equation of the dividing streamline (between the two streams) in the transformed space. Consequently, the equation of the dividing streamline in the physical space is given by $y_p = -S(x_p)$. Now, equation A.8 is numerically solved in the transformed space using the boundary conditions given by equations A.9, A.10 and A.12 as a 3-point boundary value problem, to determine f and subsequently the quantities in the transformed space using equations A.5-A.7. Now, the compatibility condition used to satisfy the correct third boundary condition is

$$U_1 v_p(x_p, \infty) = -U_2 v_p(x_p, -\infty), \quad (\text{A.13})$$

which is the condition of balancing the transverse momentum across the two streams. Thus using equations A.11,A.13 and solution of v_t in terms of f (equation A.7), we get

$$\frac{dS}{dx_p} = \frac{1}{2U_1} \left(\frac{\nu U_1}{x_p} \right)^{\frac{1}{2}} k, \quad (\text{A.14})$$

and therefore

$$S(x_p) = \frac{1}{U_1} \sqrt{\nu U_1 x_p} k, \quad (\text{A.15})$$

where k is given by

$$k = \frac{(\eta_\infty f'_\infty - f_\infty) + \frac{U_2}{U_1} (\eta_{-\infty} f'_{-\infty} - f_{-\infty})}{1 + \left(\frac{U_2}{U_1} \right)^2}. \quad (\text{A.16})$$

Finally, the quantities in the physical space can be obtained using equations A.11, A.14, A.15, A.16 and the quantities in the transformed space. It could be clearly seen from equations A.7, A.11 and A.14 that v_p exhibits a streamwise gradient even in the free streams that is inversely proportional to the \sqrt{x} . In the present work, the coordinate $(x_p, y_p) = (0, 0)$ is termed as the virtual origin, which is the point at which the two streams are first supposed to come into contact with each other [67].